MID-CRUSTAL GEODYNAMICS OF THE SOUTHERN CENTRAL ZONE, DAMARA OROGEN, NAMIBIA

Lucio Colin Poli

A Thesis Submitted for the Degree of PhD
at the
University of St Andrews

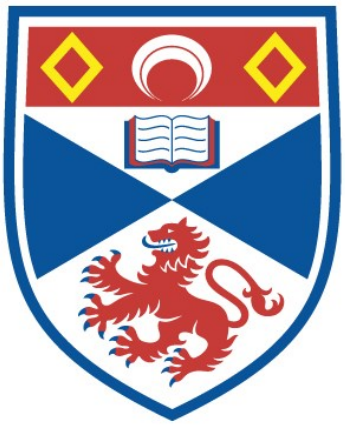

1997

MID-CRUSTAL GEODYNAMICS OF THE SOUTHERN CENTRAL ZONE, DAMARA OROGEN, NAMIBIA

Lucio Colin Poli

Thesis presented in partial fulfilment of the

Degree of Doctor of Philosophy.

October 1997.

The University St Andrews.

I Lucio Colin Poli hereby certify that this thesis has been composed by myself, that it is a record of my own work, and that it has not been accepted in partial or complete fulfilment of any other degree or professional qualification.

Signed.....Date....1.10.97....

I was admitted to the Faculty of Science of the University of St Andrews under the Ordinance General No. 12 on 1st *October 1994* and as a candidate for the Degree of Ph.D. in *October 1995*.

Signed.....Date...21./1..97....

I hereby certify that the candidate has fulfilled the conditions of the Resolution and Regulations appropriate to the degree of Ph.D..

Signed.....Date....1.10.97.....

Copyright

Unrestricted

In submitting this thesis to the University of St Andrews I understand that I am giving permission for it to be made available for use in accordance with the regulations of the University Library for the time being in force, subject to any copyright vested in the work not being affected thereby. I also understand that the title and abstract will be published, and that a copy of the work may be made and supplied to any bona fide library or research worker.

Abstract

Two areas of well exposed mid-crustal structures in the axial zone of the Pan-African Damaran orogenic belt show that basement has formed domes which have amoeboid forms on the scale of tens of km with steep sided overturned non-planar, non-cylindrical geometry. These are surrounded by open to tight synclinal cover envelopes that converge at depressions between the domes. The domes are found in association with a strong regional WSW moderately plunging lineation. Strain analysis demonstrates that domes have formed in a moderately plunging constrictional field. Structural features which normally indicate polyphase evolution such as mesoscale fold interference patterns are rare and inconsistent. Regional structural form, described morphogically by cylindrical domains, is defined by one fabric S_0/S_1. Secondary fabric trajectories and mesoscale fold oreintations are controlled by domain scale structure and not regional deformation trends. Dome formation is thus interpreted as being the result of a simultaneous flow and buckling episode within the middle crust.

Deformation was extremely ductile. *P-T* estimates from thermobarometry with Grt-Bt, Grt-Crd-Bt-Sil assemblages indicate that peak metamorphic conditions during deformation were approximately 3.5kbar and 650°C in the cover envelopes and 7kbar 791°C in the basement domes, approaching the amphibolite-granulite transition. Interactive transpressional collision between three cratons during the latest Neoproterozoic-early Paleozoic: namely the Kalahari, Congo and Rio de la Plata caused constriction and extrusion in the Central Zone. The metamorphic gap between basement and cover occurred when the distance between regional isotherms was reduced by thinning at the basement-cover interface. Higher temperatures where preserved at dome cores. At the cooler margins of the Damara Belt thrust tectonics occurred, albeit obliquely with sinistral transpression. After dome formation granite intruded many domal structures.

Acknowledgements

Sincere thanks to all of the people who have helped in the smooth running of this project. Most of all I wish to thank Grahame Oliver (G) for his supervison and many discussions. His generous advice and critical thought have provided much stimulation and encouragement, especially in the final 'push' for the prompt finish. The project was supported by a NERC studentship, they are gratefully acknowledged, especially for providing additional funds for field assistants.

Thanks to all the staff at St Andrews who helped in the various aspects of the project. Many thanks to Donald Herd for his valuable advice during EMP work. Thanks to Ian Alsop for his help. Thanks to Andy Mackie, Angus Calder, Stuart Alison, G. Sanderman and Andy in reprographics for technical work. Thanks to Judy Kinnaird and Paul Nex for help and advice with maps.

I would like to thank all those in Namibia for making my field work so enjoyable. The Breytenbachs of Namibfontein farm 91 for access and support throughout fieldwork. Martin Hirsch and Hassner Pepler are thanked for helping me to take aerial photographs. Thanks also to Frenus, Fred Soulsby and the Geological Survey for logistical help and accommodation. A special thanks to both field assistants Alan and Tiffany for their generous help in Namibia.

I would also like to acknowledge all of the geologists outside of St Andrews whom I have had discussions with and help from. Firstly, many thanks to Professor J.F. Dewey for his continued interest in this project. Thanks to Dave Waters and Tom Argles at Oxford University for their advice and help with Thermocalc. Professor Brain Windley and D. Cunningham at Leicester University are gratefully acknowledged for their suggestions and consideration of my research. Thanks also to I.W.D. Dalziel and L. Gahagan for providing the basis for Figure 6.11a using 'plates' computer software. Thanks also to F. Spear for his comments regarding the computer program GTB. Finally, thanks to R. Lisle, A. Thompson and H. Fossen for providing manuscripts.

Many thanks to those of you who made life in St Andrews so pleasant principally, Nick, Simon and Al for their humour. Thanks to Slug for making me stop work occasionally. Finally, I would like to thank my parents for their support (especially financial!).

Contents Page

CHAPTER 3 Structural Analysis

CHAPTER 4 Metamorphism

CHAPTER 1

Introduction

1.1 Research Aims

This research has applied the methods of modern structural and metamorphic geology to two areas of the Inland-Branch of the Damara orogen so that the questions raised by the publications of Oliver (1993, 1994 & 1996) may be fully discussed. The series of questions were used as guide line aims to address the process of dome formation:

1. What is the nature of the basement cover contact? Is it a regional scale detachment?

2. If it is a regional scale detachment, what is its relationship to the process of dome formation?

3. Is the process of dome formation polyphase or single phase?

4. Do the regional detachment and domes represent a metamorphic core complex

5. If these are related to core complex development then is there a metamorphic gap between the basement and cover? How might this be accounted for?

1.2 Introduction

St Andrews University Geology Department has initiated a number of recent studies in Africa (Mestres-Ridge 1992, Oliver 1994, Nex 1997). This project was designed by G.J.H. Oliver following reconnaissance mapping between 1990-93 which highlighted the need for increased detailed field knowledge of the dome structures of central Namibia. Oliver (1994 & 1996) drew comparisons between the morphology of domes in the Central Zone with Cordilleran Metamorphic Core Complexes. The areas studied were covered by the large scale maps of Smith (1965), Miller & Grote (1988) and Lehtonen *et al.* (1993).

The presence of complex regional amoeboid fold patterns and domes in the geological record has been documented in many orogens yet still remains largely a matter of subjective interpretation of conventional field observation. Eskola (1949) highlighted the problem of these structures and today still no consensus has been reached as to their origin.

The Damara orogen is no exception and provides some of the best exposed and probably least studied and understood structures of this nature.

1.3 Methodology

Field mapping was carried out over a total period of eight months during 1995 and 1996. Two areas were mapped using a combination of air photographs and enlarged and traced topographic maps at 1: 10000 scale. Mapping was mostly confined to dry canyon and stream sections. Numbered and orientated rock samples were collected for additional laboratory studies. Reference to locations and samples is made by means of a grid system e.g. GR[013,028], this is unique to this study since Namibia has no national grid system. A variety of additional studies were carried out in St Andrews including petrographic and microprobe analysis.

1.4 Location of the study areas

The field area lies in the central and western region of Namibia south west Africa between Usakos and Swakopmund (Figure 1.1). Two areas were studied in detail. Both are accessible from the main route 2/2 and are located along the Khan River where the geological outcrop is particularly good. The first area, the Namibfontein area is situated on both the Namibfontein 91 and Vergenoeg 92 farms 15km west of Usakos. Exposure is best along canyon sections but becomes poorer at the northern margin of the area towards the railway line, where gravel plateau is the main feature. Approximately 200km^2 were investigated from outcrop study. The second study area, The Khan Mine area, is ~ 45km east of Swakopmund and 50km west of the Namibfontein area, exposure is excellent here too although in the north of the area much of the ground is featureless, some 50km^2 were investigated.

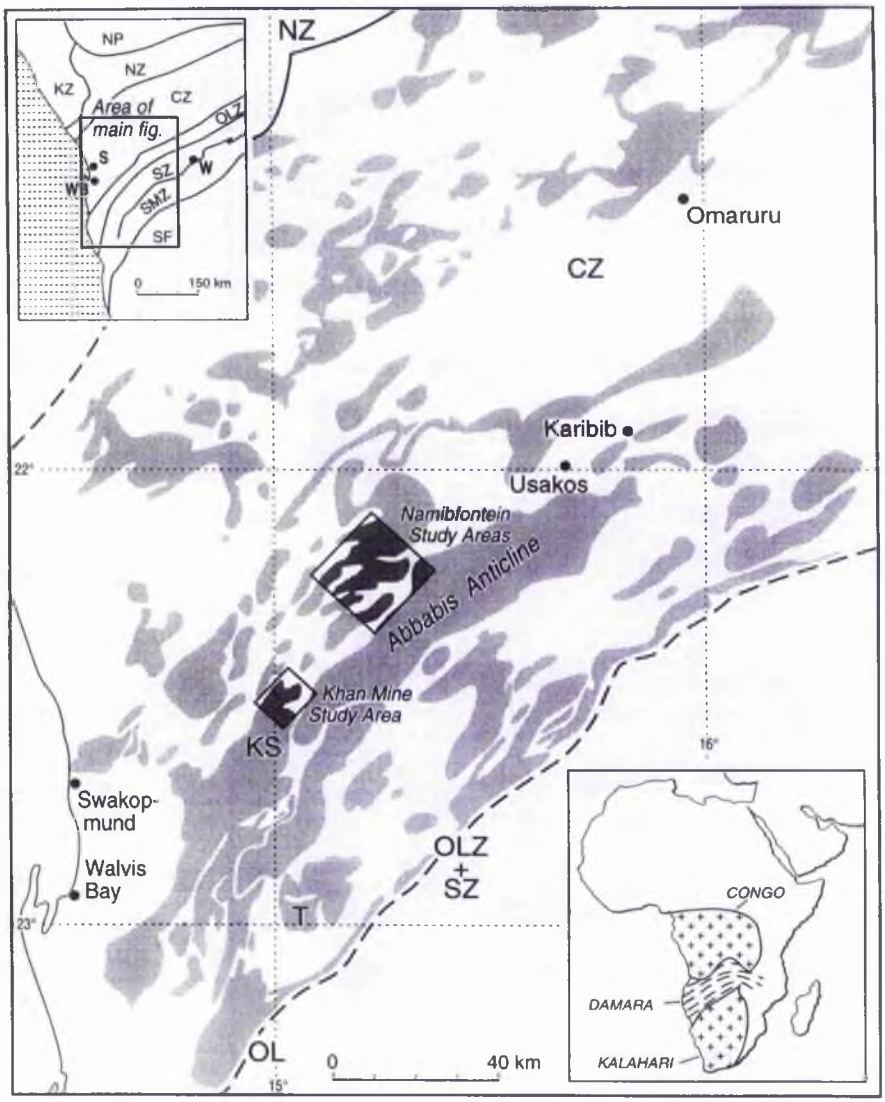

Figure 1.1 Map of the Damara Belt, Namibia showing the location of two study areas in the Central Zone, The Namibfontein Study Areas & The Khan Mine Study Area. Lower inset shows the location of the Damaran belt between the neighbouring Congo and Kalahari cratons. Upper inset shows the major tectono-stratigraphical divisions of central Namibia modified from Miller and Hoffmann (1981): NP=Northern Platform (Congo craton), KZ= Kaoko Zone, SMZ= Southern margin zone, SF=southern foreland and platform (Kalahari craton), S=Swakopmund, WB=Walvis bay, other abbreviations as in the main figure. The main figure shows elongate dome structures of the Central Zone (CZ), the northern zone (NZ), the Okahandja lineament zone (OLZ), and the southern zone (SZ) of the Damaran Belt. T= Tumas Dome.

1.5 Geological Framework

A brief introduction of the geological setting of the study area is presented in this section before the detailed analysis in Chapters 3 & 4. The most striking feature of the area under consideration is that it provides nearly 100% exposure of the highly deformed deep crustal roots of the Damara orogenic Belt caused by collision of the Kalahari and Congo cratons in the Lower to Middle Cambrian (Miller 1983; Unrug 1992; Oliver 1994; Prave 1996) (Figure 1.2) Orogenesis resulted in the metamorphism and deformation of the Damara sequence and reactivation of Pre-Damaran basement to create the complex structures present today.

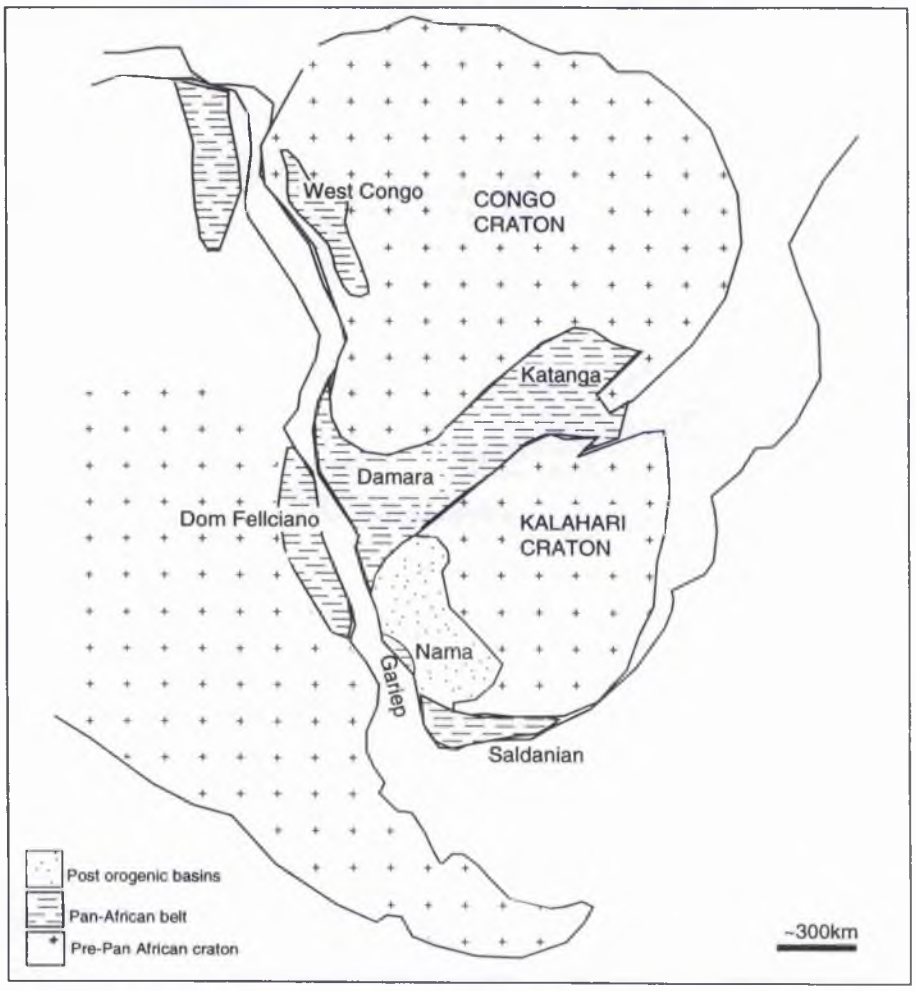

Figure 1.2 Tectonic framework of the Damara orogen after Gresse (1989)

Figure 1.2 shows the tectonic setting of the Damara orogen has a lateral equivalent in the Zambesi belt (Unrug 1992); both have orogenic trends parallel to the cratonic margins and formed part of a the main Pan-African accretion event (Kennedy 1964; Clifford 1967 and Black & Liegeois 1993). The western extent of the Damara is believed to be delimited by the Riebeiro orogen in Brazil (Porada 1979 & 1989).

In detail, the Damara orogen was divided into discrete tectonostratigraphic zones by Miller (1983b) based on the contrasting nature of their various structural, metamorphic and stratigraphic characters. Figure.1.1 shows the location of the Central Zone where complex domal structures and pervasive granite intrusions are the major features; this is in contrast to the Southern Zone, Northern Zone or Coastal Branches where thrust tectonics dominate. It is notable that overall the belt only displays thrust style tectonics at its coastal, northern and southern margins where it is characterised by moderate *T* and moderate *P* metamorphic facies (Ahrendt *et al.* 1978; Coward 1981; Kasch 1983; Ahrendt *et al.* 1983; Stanistreet *et al.* 1991; De Kock 1992). Higher temperature and lower pressure metamorphism are recorded in the Central Zone (Masberg 1996) where domes broadly coincide with the amphibolite to granulite isograd (Nash 1971). The significant difference in *PT* conditions from the Central Zone to the Southern Zone represents the contrasting nature of geological mechanisms that were in operation across the Damara Belt. The Okahandja Lineament separates these two zones and is contrasted by the change from cordierite-sillimanite assemblages to the north of the lineament and staurolite kyanite assemblages to the south. Bühn *et al.* (1994) studied the metamorphic facies changes across these zones and found no evidence of a "coherent isograd", he suggests that the Okahandja lineament represents sinistral oblique strike slip with a down throw of the Central Zone.

The Damaran sequence is sub-divided into two parts: the rift related Nosib Group and the post-rift Swakop Group (Lethonen *et al.* 1993). It is generally accepted that an early rifting stage was involved in Damara orogenesis which involved the generation of oceanic crust (Henry *et al* .1990), during later collision this was subducted. The exact width of the 'ocean' however is not known. A detailed discussion of the geodynamic setting of the Damara orogen is given by Henry *et al.* (*op. cit.*) and Chapter 6. Elements of the stratigraphy are given in Chapter 2.

1.6 Structural History

The earlier work on the nature of deformation history relevant to this study is more appropriately discussed in Chapters 3 & 6; however, a few introductory words are necessary to give a general picture. The Damara orogen has been interpreted by many workers as having undergone three major deformation events. Whether these events can be correlated

throughout the entire belt relies on meaningful and comparable dating which is largely absent (Oliver 1994). Given that the *PT* conditions reflected in mineral paragenesis in the Southern and Central Zones are so different it seems likely that different deformation mechanisms were in operation. On these grounds the rationale of orogen wide correlation seems a fundamentally flawed concept. There is good reason therefore to argue that deformation at the craton margins, i.e. the Southern and Northern Zones, should not necessarily be correlated with the internal zone. This is particularly pertinent since many of the existing structural studies of the Central Zone promote 'polyphase' deformation in a multitude of trends and styles. (Gevers 1963; Smith 1965; Jacob 1974a, 1983; Blaine 1977; Downing & Coward 1981; Kasch 1988; Miller 1983b; Miller & Grote 1988; Bühn 1991; Bühn *et al.* 1994)

1.7 Summary

The origin of dome structures in the Central Zone has largely been based on regional scale 1:25 000 (and greater) mapping studies. Few of the earlier studies have discussed alternatives to polyphase deformation e.g. Oliver's (1994, 1996) Metamorphic Core Complex model which has yet to be rigorously tested. No studies have satisfactorily discussed the relationship of the basement cover contact to the mechanism of dome formation.

CHAPTER 2

Stratigraphy

2.1 Introduction

This chapter gives a brief account of the litho-stratigraphy from the Namibfontein and Khan Mine areas. Major stratigraphic units (shown in Table 2.1) are described as formations. Details of general field characteristics such as thicknesses, composition and assemblages are given in addition to summary logs.

Sequence	Group	Formation	Member	Lithology	Thickness
DAMARA	Swakop	Kuiseb		Bt schist, crd schist, calc silicate rock, marble.	< 3km
		Karabib	Onguati	Impure marble, calc silicate rock, schist	10-150m
			Arisis River	Pure marble	< 200m
			Otjongeama	Impure marble, calc silicate interlayers	40-210m
			Harmonie	Marble calc silicate rock, schist	10-20m
		Arandis	Oberwasser	Biotite Schist	10-150m
			Okawayo	Marble with thin clac-silicate interlayers	2-25m
			Spes Bona	Calc silicate rock, schist	30-430m
			Karub	Marble with calc silicate schist layers	2-60m
		Chuos	unconformity	Mixtite, pebble and boulder bearing schist minor quartzite and marble.	< 700m
	unconformity	Rossing		Marble, minor quartzite, conglomerate, gneiss, calcsilicate rock.	< 200m
	Nosib	Khan		Pyroxene-amphibole feldspathic quartzite Amphibole-pyroxene gneiss, amphibole and biotite schist	<1100m
		Etusis		Reddish feldspathic quartzite, arkose, conglomerate, quartzofeldspathic gneiss sillimanite gneiss; minor biotite schist, marble, amphibolite, calc silicate rock.	< 3500m
Khan River	Detachment				
ABBABIS COMPLEX (Kibaran/ Eburnian?)				Kfs Augen gneiss, biotite sillimanite gneiss, amphibolite, migmatite. Qtzite, marble and conglomerate.	

Table 2.1 Major stratigraphic units for the Damara Sequence showing approximate post-tectonic thickness after Lehtonen *et al.* (1993)

Although many records of Damaran stratigraphy exist it is interesting that this study has noted several new features that have important consequences for structural interpretations. Previously, detailed accounts of the general litho-stratigraphy for the Namibfontein area have been given by Marlow (1981) & Smith (1965) while, for the Khan Mine area, the reader is referred to publications by Nash (1971), Hoffman (1984) and Berning (1986) who studied the SJ area, just 3km to the east of the Khan Dome. More recently Nex (1997) has provided a full account of the stratigraphy in the Goanikontes area. The type locations and nomenclature of Damaran stratigraphic units used in this study are adopted from the South African Committee for Stratigraphy (SACS), (1980a).

In the two study areas the stratigraphy comprises two main parts; a basement called the Abbabis Complex (Lehtonen *et al.* 1993) and a cover sequence called the Damara Sequence. The older Pre-Damaran Abbabis Complex mainly outcrops at the centre of dome structures while the younger unconformable Damaran Sequence usually forms a folded cover envelope (individual domes referred to in this Chapter are described in Sections 3.3.1 & 3.3.2). In the field the distinction between the two is not always easily definable, the difficulty arising because both are intensely deformed and heavily invaded by late tectonic granites. In the course of this study the distinction of the Abbabis Complex from the base of the Damara Sequence was particularly important since this zone has recently been interpreted as a regional detachment spanning the length of the Central Zone (Oliver 1994). The exact nature of the contact was studied at several localities and, in addition, collection of orientated samples enabled geometrically controlled petrographic investigations to be carried out (Chapter 4.)

2.2 Pre-Damaran stratigraphy; the basement

The term basement is loosely used to describe the Abbabis Complex stratigraphy first noted by Gevers & Frommurze (1929) that was eroded to form the Nosib Group (see Section 2.3.1). Its identification depends on the recognition of subtle structural and lithological differences from the younger Damara succession which, due to intensive mobilisation during Damaran orogenesis, can be very similar in appearance. In order to recognise basement in the two mapping areas a detailed log of the upper 600m of the Complex at the type area Abbabis 70 farm ~15° 45'/ 22° 15' was undertaken. The results are in good agreement with the most recent comprehensive study of the basement near Usakos by Brandt (1987) who divided the Complex into three parts shown in Table 2.2.

Narubis Granitoid Complex	ortho (augen) gneiss
Noab Formation	metavolcanic rocks alternating feldspathic quartzite, marble & calc-silicate
	schist and metabasite
Tswasis Formation	schist, para-gneiss, meta-arkose, subordinate marble, calc-silicate, conglomerate

Table 2.2 Summary of the stratigraphy of the Abbabis Complex after Brandt (1987).

2.2.1 Abbabis 70 farm

This section briefly describes the sequence of stratigraphic units recorded at the Abbabis 70 farm (Figure 2.1, Log 1). Foliation and bedding surfaces dip approximately 85° towards 100°, the sequence youngs to the east. The Damara sequence here is separated from the Narubis granitoid complex by 170m of basal conglomerate shown in Plate 2.1a. It appears that at 210m the conglomerate is highly tectonised resulting in a marked reduction of the clast size, the general assemblage in this high strain zone is comprised of [1] Qtz+Msc+Pl+Kfs+Bt with variable composition clasts; the shear zone is not discrete nor confined to this formation alone. The sheared basal conglomerate (Plate 2.1b) defines an obvious ultramylonite zone that separates basement from cover. This also confirms the observations of Oliver and Kinnaird (1996).

Progressively, the metaconglomerate grades downwards into a distinctive coarse ortho-gneiss with augens of potassium feldspar, usually as microcline, this has a similar assemblage as the metaconglomerate with a greater proportion of Kfs. Mafic and dioritc tectonic inclusions (10 by 30cm) that are parallel or at a low angle to the shear fabric are occasionally observed in the augen gneiss and have been interpreted by Brandt (1987) as tectonically thinned intrusive intermediate and mafic dykes. They do not appear in the Damara sequence and provide a useful structural criteria for the defining of basement. An interesting feature at this location is the presence of undeformed aplitic dykes (< 1-2m) composed of Qtz > Pl + Kfs + Bt + Msc (quartz is slightly undulose) which cut both the conglomerate and orthogneiss horizons demonstrating granite intrusions continued after tectonism. These have previously been noted by Oliver and Kinnaird (1996). Lower still (at 220m below the base of the Damara sequence) the ortho-gneiss grades progressively to a fine grained, green-grey dioritic gneiss which is cut by intrusive minor (2m to 10cm) pegmatitic quartz veins with large euhedral Kfs phenocrysts. The dioritic gneiss first appears as minor (< 20cm) horizons parallel to the main schistosity which gradually dominate the sequence. At 400m the darker mafic gneiss forms complex ductile flow structures which pinch and swell (see Plate 2.2). These are defined by two alternating subordinate types of acidic horizons (>10cm); one fine-grained, massive and Kfs-rich and the other coarse grained Kfs-rich with green biotite. At 515m below the Damara sequence the lowest part of the sequence changes to generally massive, white-grey, coarse gabbroic gneiss with plagioclase augens. Some compositional variation occurs and viscous flow banding becomes evident.

---

[1] Mineral abbreviations in this study used after Kretz (1983)

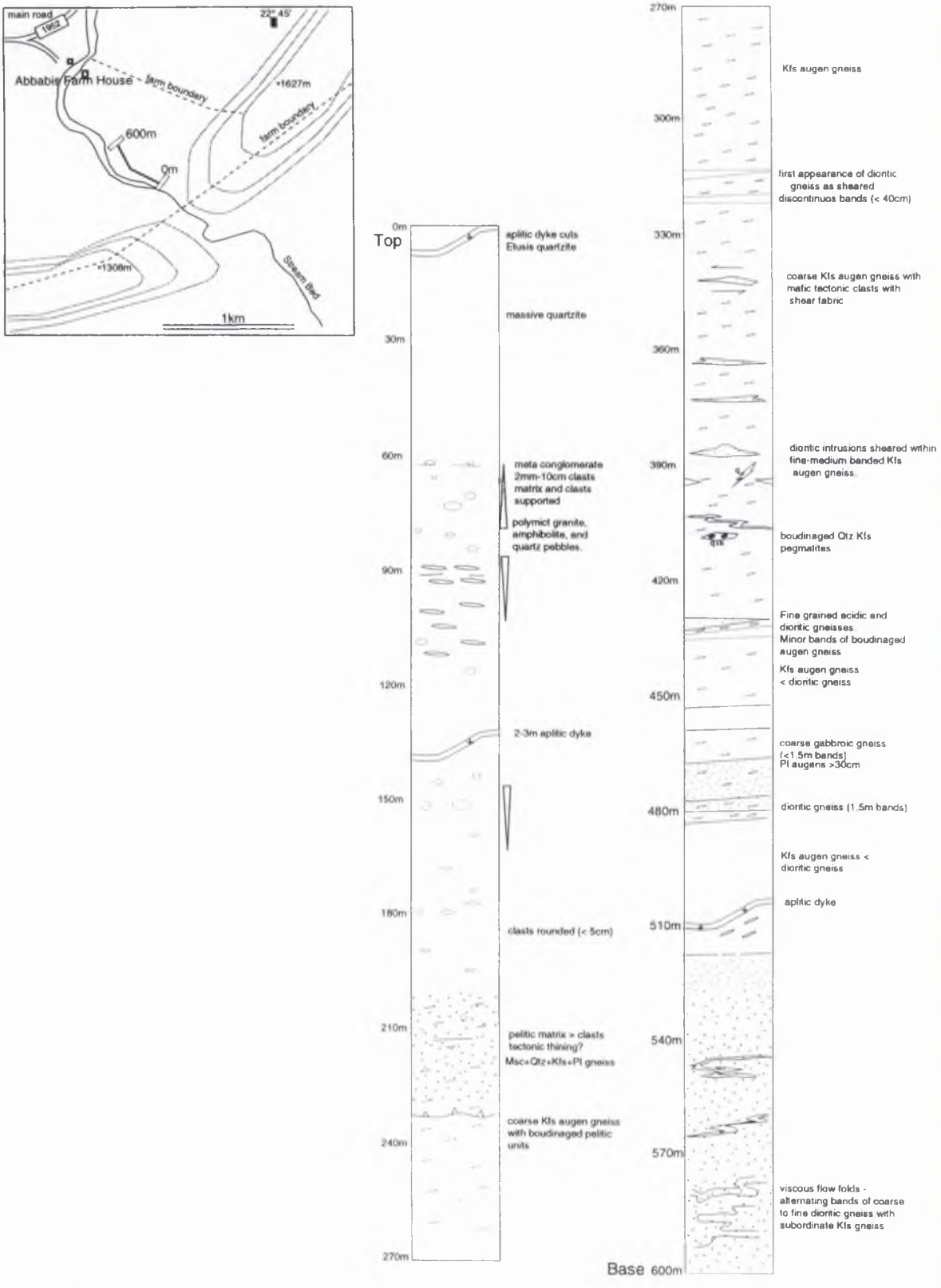

Figure 2.1 Log 1 of the Etusis Formation - Abbabis Complex tranistion at Abbabis 70

Plate 2.1a Photograph of highly deformed basal conglomeratic gneiss at the basement-cover boundary (170m), Abbabis 70 Farm.

Plate 2.1b Photograph of highly deformed basal conglomeratic gneiss with reduced grain size at the basement-cover boundary (210m) , Abbabis 70 Farm.

Plate 2.2 Photograph of complex flow folded mafic and Kfs-gneisses at (400m) in the basement, Abbabis 70 farm.

2.2.2 The Namibfontein area

The presence of extensive granite intrusions at the core of the Namibfontein and Vergenoeg domes precluded the possibility of detailed mapping of basement in these areas. However, in contrast to this area, very good exposure of highly strained basement gneisses is observed in the southern-most part of the Namibfontein area at the core of the Valencia dome. The main lithology here consists of (*c.* 500m) of pinkish-white granitic gneiss characterised by elongate plagioclase microcline augens defining granoblastic linear fabrics, the general assemblage is Kfs+Qtz+Pl+Mc+Bt. Shear bands are commonly displayed (see Section 3.9).

In more detail, two litho-types could be distinguished on the basis of composition and fabric grain size. The first type, at GR[038,014](Location N38.18) forms a thin horizon (< 5m) of banded (grain size, 2-4mm) gneiss composed predominantly of augens of white Pl and Qtz surrounded by green biotite-rich schleiren (Plate 2.3). Below this, the second and most common type, is a coarse banded (grain size, 5-15mm) pink gneiss with augens composed of Mc+Pl (often sericitic)+ Qtz and accessory magnetite; Bt-rich schleiren forms >20% of the gneiss (Plate 2.3). It is notable that this unit contains variably strained (10-20cm) mafic tectonic clasts (*cf.* Ghosh 1993) that are similar to those observed at Abbabis 70 (described in Section 2.2.1); in most of these the amphibole has been altered to biotite.

Plate 2.3 Handspecimens of basement augen gneiss at Location 38.18 GR[038,0/014]. (left) Pl-rich, finer grained gneiss, (right), Common coarse Kfs-augen gneiss. Scale used = two pence coin (25mm).

In all of this area the gneisses are cut by Damaran pegmatite veins and leucogranite veins up to 15 cm-1m wide. At one location N38.20 GR[038,016] the gneiss remains only as lense shaped rafts (3-5m) where late widespread medium-coarse grained granite intrusion dominated. This unit resembles the description of the upper part of the Abbabis Complex described in Section 2. On these grounds it is concluded that the structural level observed here corresponds to the Narubis Complex.

Within the Namibfontein dome, exposure of Pre-Damaran basement was documented in an area forming the south and west overturned culmination, to the east of the Karub Syncline (described in Chapter 3) At N42.23 GR[033,089]for example, there is intermittent exposure of an augen quartzo-feldspathic gneiss with biotite schlieren. The gneissose layering is often folded in a monoclinal open manner and is unlikely to be representative of the Nosib Group since this fold style is absent in the cover. This implies that the same structural level is exposed here as in the Valencia dome, albeit swamped by > 70% late Damaran granite.

Further west, at about the same structural level, at N18.4 GR[072,089] basement is preserved as large migmatitic rafts of a micaceous crenulated gneiss. The gneiss is comprised of Mc+Pl+Qtz+Bt+Sil. Sil is abundant (up to 25% of the rock) and suggests that some facies variation occurs within the Abbabis Complex. Further north and west the equivalent units are largely assimilated with little and no recognisable structure preserved. Plate 2.4 shows a typical example of a highly assimilated gneiss. The Geological Survey of Namibia (1980) have correlated Red granite that swamp the basement with the Abbabis Complex. These granites are traceable into the cover at GR[075,085] and therefore cannot be Pre-Damaran.

Mapping of the western most part of the Vergenoeg dome shows a *c.*10-20m band of dark brown, highly migmatitic foliated gneiss composed of Qtz+Kfs+Bt+Sil±Mag. Within the gneiss microscale banding (>2-4cm) of quartzo-feldspathic segregations define rootless intrafolial folds and symmetrical fish structures shown in Plate 2.5. Sillimanite, as fibrolite, forms patches (2-3cm) on foliation surfaces, sometimes randomly orientated but otherwise aligned. Lehtonen *et al.* (1993) propose a sedimentary origin for this unit whilst suggesting it is part of the Noab Formation.

In view of the general account given here, it appears that at least two units of the Abbabis Complex outcrop in the Namibfontein-Vergenoeg domes while the exposure in the Valencia dome presumably correlates with location N42.23 GR[033,089].

Plate 2.4 Photograph showing assimilated basement gneiss at Location N20.18 GR[063,100].

Plate 2.5 Photograph showing basement exposed in the Vergenoeg dome. Note folded rootless isoclinal Kfs bands parallel to schistosity. Location N48 [MAP 2].

2.2.3 The Khan Mine area

In general, a large area of Abbabis Complex rocks is exposed in this region and a great variety of litho-types are present suggesting that relatively deep structural levels are exposed. For the sake of simplicity two areas of basement outcrop have been defined which effectively split the Abbabis Complex here into a structurally lower and higher part. In the following account the lowest part has been documented in Figure 2.2, Log 2 GR [045,010 to 047,016] where the litho-stratigraphy comprises a series of complex sequences punctuated by Damaran granitoids. The upper sequence GR[021,037] is rather more straightforward, comprising (*c.*600m) of augen gneisses cut by large volumes of Damaran granitoids. There appears to be no systematic variation within the structurally higher part although important local facies changes exist.

2.2.3i The lower part of the Abbabis Complex- The Tsawisis Formation

During the course of structural mapping a distinct *c.*400m sequence of lithological units was documented in Log 2 shown in Figure 2.2. This near complete sequence was noted at GR[026,060] (Location K31.12). It begins here with a prominent thick (>20m) banded calcitic marble horizon and several thin, subordinate, medium-grained amphibolitic schists. The sequence cannot directly be traced structurally higher at this point but resumes about 2km west along strike at GR[045,010] (Location K31.19). It continues with a buff coloured, gritty monomict conglomeratic gneiss composed of Bt+Qtz+Pl with variable Bt contents and distinctive Qtz pebble augens that make up < 10-15% of the unit (Plate 2.6a). The size of Qtz augens varies from ~45cm to ~5cm. The conglomeratic gneiss exhibits compositional heterogeneity, thin 20-30cm bands of Qtz-Bt-rich gneiss and more felsic material which are flow folded occur 25m above the base (Plate 2.6b) (Figure 2.2). This is contrasted by a 10m thick, intensely flow folded dioritic ortho-gneiss. The ortho-gneiss is a grey to pinkish coloured equigranular crystalline rock.

Plate 2.6a Photograph showing coarse monomict metaconglomerate at Location K31.19 GR[045,010].

Plate 2.6b Photograph showing flow folded Bt-gneisses and Kfs-rich gneisses above monomict metaconglomerate at GR[045,010].

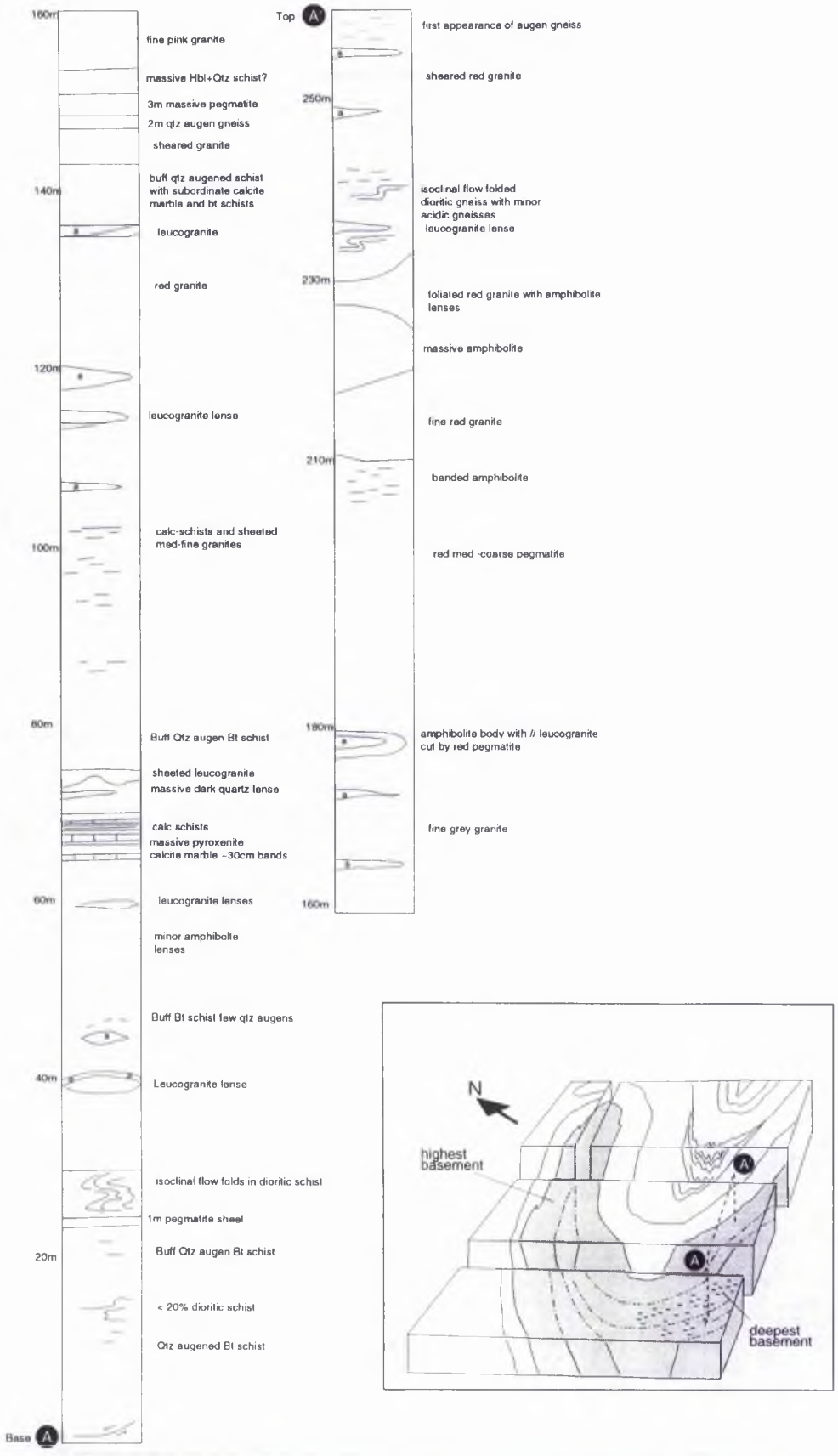

Figure 2..2 Summary litho-stratigraphic log for basement, south-west of Khan mine area

At 50m above the base of the Log 2 (Figure 2.2) amphibolite is included in the sequence. It first appears as thin (1-2m) meso and microscale pods and lenses with variable lateral extent. These have sharp conformable contacts with the surrounding gneisses and unfolded granites. Sheeted pegmatitic granitoid veins (30-40cm) also become quite common.

At 70m above Location K31.19 GR [047,011] a second calcitic unit occurs. A prominent series (> 10m) of thin (30-40cm) calcite marble bands and subordinate calc-schists breaks the sequence of Qtz augened gneiss. Above this (20m higher) massive, megacrystic red granite dominants the sequence. Large *insitu* amphibolite units are interspersed amongst this middle section of the log which preserve compositional banding and exhibit interbedded Qtz-rich schistose layers that form internal boudinage structures. These pods were correlated and traced to the amphibolites described above in section 2.2.3.i. Two of these units are traceable along strike up to 2km west.

At 230m gneisses (that resemble the flow folded dioritic gneisses at Abbabis 70) mark a transition to Kfs-augen gneisses and structurally highest basement. This forms approximately 400m of strata below the Etusis quartzites in Log 2. No sharp junction is observed between basement and cover but rather nondescript highly sheared Bt gneiss.

2.2.3.ii Origin of the Tsawisis Formation

The age of this unique series of lithologies has so far been speculated as Pre-Damaran. An alternative supposition to this is that the sequence represents the inverted limb of a large overturned nappe of the Damara sequence. During the course of mapping however, three features mitigated against this. Firstly, despite the presence of some similar litho-types, it may be argued that the relative arrangement of the units within the sequence is too dissimilar from that of the cover, only large lateral changes of facies could explain this which seems unrealistic when the simple stratigraphy of the cover is considered. Secondly, the style of microscale features, particularly sheared quartz pegmatite veins are not present in the cover strongly suggesting that rather than syn-tectonic Damaran pegmatites (that would post-date nappe formation) they are Pre-Damaran. Thirdly, a comparison of the total thickness of the basement (*c.* 260m including the contribution of granitic sheets) with the cover (*c.*1000m) clearly shows the sequence is more than half as thick as the cover. Thus, if correlation with the cover is made a substantial thinning of the lower limb occurred such that it remains as a tectonic sliver. Since this has not been observed elsewhere and because of the stratigraphic dissimilarities the rocks in Log 2 may be assigned to the Tsawisis Formation.

Plate 2.7 Photograph of Qtz pegmatite in the basement at GR [051,021] (MAP 3).

It should be borne in mind however that these arguments can only be verified by age dating. What is clear from the internal structure and composition of the units is that they represent protoliths derived from siliclastic and carbonate deposition (despite the absence of primary structures) and that even the most unusual litho-types, such as massive boudinaged amphibolite lenses with interbedded Qtz-rich layers are laterally continuous and suggestive of a sedimentary/volcanic origin.

2.2.3.iii The upper basement- The Narubis Granitoid Complex

The structurally highest part of the basement outcrops at the centre of the Nose Structure Anticline (see Figure 2.2). The entire outcrop is highly strained and variably migmatised. Unfoliated leucogranite sheets are emplaced at all levels and associated with vein hosted mineralization. Magnetite and hematite is found ubiquitously as mesoscale veins (< 25cm) and small anhedral patches (>5cm) oxidized to a dark brown-black colour.

Plate 2.8 Photograph of typical augen gneiss cut by post tectonic red granite dyke.

The majority of the Nose Structure Anticline is comprised of coarse Kfs augen gneiss similar to the Valencia dome. There is considerable compositional inhomogeniety within the gneisses reflecting the variable Qtz, Kfs, Pl and Bt assemblage. The most notable compositional difference however, is the occasional occurrence of Hbl+Pl augen gneisses (for example GR[027,044] Location K19.5). This amphibolitic gneiss appears white-grey in colour with small (< 2mm) black hornblende porphyroblasts. The presence of hornblende may suggest that some gneisses are highly strained equivalents of the dioritic gneisses at Abbabis 70. They were considered as potentially useful for thermobarometric studies, the results of which are shown in Chapter 3.

Other minor lithologies present in the upper basement, at GR[020,039] Location K20.5 for example, include a large (>10-20m) lense of well foliated and folded dark brown gneiss included within the Kfs gneiss. The contact of this horizon with the Kfs gneiss is parallel to the foliation and discrete. The gneiss is composed of Qtz+Bt+Kfs+Pl +Sil and is migmatitic.

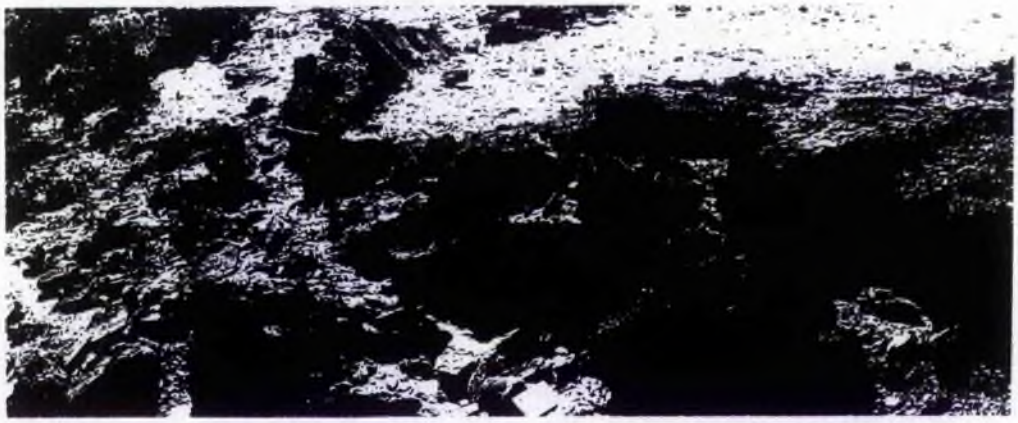

Plate 2.9 Photograph showing well foliated L-S gneiss at location K20.5 GR[020,039].

It is probable that this unit represents a lower part of the Abbabis Complex exhumed during the intense deformation of the Nose Structure anticline (see Chapter 3). Further west the 'hornfelsic' gneiss is more prolific, in particular at locations along the tributary stream that cuts the Nose Structure, individual outcrops at GR[012,025] Location K27.9 display complex mesocscale fold patterns.

In contrast to the feldspathic gneisses, structurally lower at GR[021,012] Location K31.6, a rare fine grey-white quartzite is recorded. The unit appears as a thin (< 30m) horizon with subordinate rotated olive-green amphibolite pods which distinguish it from leucogranite. 50m below this the outcrop is dominated by coarse red granites which are punctuated by boudinaged dark black amphibolite pods (> 5m thick and > 50m long). Plate 2.10 shows an outcrop of amphibolite which is traceable along strike. The mafic horizons are in marked compositional contrast to the Damara granites and have remained unassimilated during intrusion, only recrystallising and thinning, Kfs-rich gneisses, on the other hand, have been completely assimilated leaving only amphibolite pods. This unit mark a transitional zone between the upper and lower sequences.

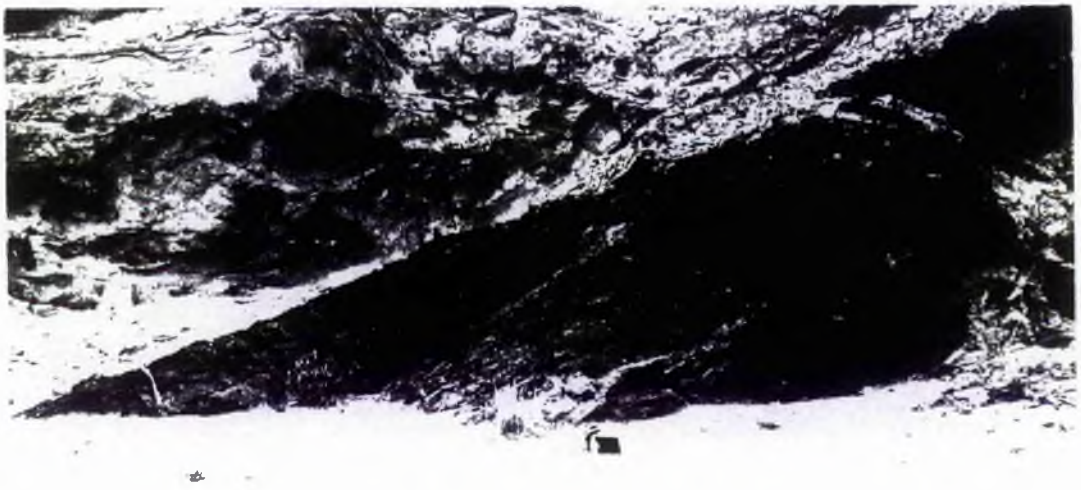

Plate 2.10 Amphibolite in the basement at Location K31.8 [023,011], unit dips to the NE.

In summary, the basement in the Khan Mine area may be split into two structurally and compositionally distinct parts. The structurally lowest part is assigned to the Tsawisis Formation. The structurally highest part is assigned to the Narubis Granitoid Complex. Basement exposed in the Namibfontein area is also assigned to the Narubis Granitoid Complex. This appears to have an igneous origin (Brandt 1987).

2.3 The Damara Sequence

This section outlines information obtained from outcrop mapping and measured sections from the Damara Sequence (see Section 2.1). Full accounts of the litho-stratigraphy of the Damara Sequence in the Central Zone are given by Hoffman (1984), Brandt (1985), Badenhorst (1992) and Nex (1997). Despite the intense deformation and metamorphism of the sequence, good examples of primary features such as cross bedding and compositional banding are preserved; the seminal work of Henry (1992) gives a full account of these sedimentological aspects.

2.3.1 The Nosib Group

In the areas studied the Nosib Group consists mainly of terrigenous siliciclastics and volcanics. The Group is split into two Formations. The lowest, the Etusis Formation, has a basal conglomerate and arkose-arenites (now quartzo-feldspathic gneisses) presumably from a granitic source. The upper, the Khan Formation, is composed of amphibole-rich dark green gniesses.

2.3.1.i The basal conglomerate

The Nosib Group overlies the Abbabis Complex where it is marked by a basal conglomerate. Evidence of the mylonitic basal conglomerate, similar to that at Abbabis 70, was recognised in two locations. The conglomerate is much thinner at GR [032,085] Location. N42.21, than at Abbabis 70, forming *c.*20m thick outcrops (Plate 2.11).

Plate 2.11 The basal conglomeratic gneiss at Location N42.21 [032,085].

In detail, it occurs as a matrix supported polymict-metaconglomerate with variably sized white coarse gneissose pebbles (with the assemblage Qtz+Kfs+Pl+Bt). The unit marks a probable basement-cover contact in an area where exposure is limited.

In the Khan Mine area no definitive exposure of basal conglomerate was noted. An observation of small (2-cm) quartz-rich pebbles in a raft of grey quartz-biotite schist at GR[032,020] K11.1 in an area that approximately corresponds to the basement-cover junction was obscured by granite intrusions, thus little detail was preserved.

Comparison of conglomerate clasts between the limited exposure in the two study areas and Abbabis Farm shows that clasts are composed almost entirely of Qtz+Kfs+Bt gneiss. Oliver (*pers. comm.*) reports Hbl, Bt gneisses in basal conglomerate in the Abbabis area; Hbl bearing gneisses were not noted in the two study areas suggesting they are more monomict. A further comparison shows that the matrix in the Abbabis area contains up to 15% Msc, in the Namibfontein Msc is absent, rather Bt is common. In the Khan Mine area preservation of a basal conglomerate is poor, instead a highly tectonised mylonite zone exists, (see Section 3.9) .

2.3.1.ii The Etusis Formation

The Etusis Formation is composed of fine to very coarse arkosic to quartz-rich arenaceous meta-sediments with >25% Kfs. In hand specimen the gneiss is a distinctive orange-red colour with the general assemblage Kfs+Qtz+Pl+Bt+Sil.

A notable feature of these gneisses are large 2-5cm sized orientated sillimanite porpyhroblastic masses, that constitute up to 20% of the rock. Gevers & Frommurze (1929) first recorded these and commented on their 'torpedo' shape (see Chapter 3). The abundance of sillimanite presumably is due to the high aluminium content of the original sediments. Sillimanite knots are also formed along joint surfaces and cross-cut bedding planes (see Plate 2.12, GR[080,075] Location N23.16).

Plate 2.12. Photograph showing sillimanite growth on a cross-bedding plane. GR [080,075]

In much of the Namibfontein area, weathered minor (< 50m) mafic amphibolite-rich (usually altered to biotite) horizons are included in the formation. In some outcrops, at GR[066,099] Location N20.19 for example, pure amphibolite (tremolite) horizons can be seen. It is possible that skarn-type effects have contributed to the basic nature of these horizons since intrusive granite pegmatites are always found near to them (Nex 1997).

The formation varies in thickness greatly in the Namibfontein area where it is composed almost entirely of true meta-arkoses. The thickest part, *c.*1.5km, outcrops at the north east closure of the Namibfontein dome and thins to *c.*200m along the north of the dome (Lehtonen *et al.* 1996). The formation appears to remain of constant thickness along the southern rim ~ 500m GR[055,065].

Arkosic gneisses are much less common in the Khan Mine area. Outcrop is limited to impersistant thin (10-20m) bands immediately above the basement along most of the basement-cover boundary. The thickest unit in the Etusis Formation is found structurally above the minor meta arkoses and composed of Qtz-Bt rich banded quartzites. In hand specimen they are pale yellow-white in colour coarse-grained and have a hard sugary texture. Banding is defined by biotite (< 5%) and Fe-Ti oxides (< 15%) and always asymmetrically boudinaged.

2.3.1.iii The Khan Formation.

The Khan Formation outcrops in both study areas. It is comprised of four stratigraphic units shown in Table 2.2 after (Berning 1976) and the South African Committee of Stratigraphy (SACS) (1980). Oliver & Kinnaird (1996), in the SJ area (Figure 1.1), have proposed a revised informal stratigraphy, they place the highest member of the (SACS) Etusis Formation in the Khan Formation. This is because the unit has a finer grain size than underlying schists and is calcareous.

Formation	Berning (1976)	SACS (1980)	Oliver & Kinnaird (1996)
Khan	Biotite-amphibole schist	Lower Banded Gneiss	
	Upper pyroxene-hornblende gneiss	-Mottled Gneiss -Amphibolite -Mottled Gneiss	
	Pyroxene-garnet gneiss/ amphibole	Upper Banded Gneiss	
	Lower pyroxene-hornblende gneiss	Amphibole schist & basal conglomerate	Basal Biotite Schist
Etusis	Basal Biotite Schist		

Table 2.2 Sub-division of the Khan Formation after Berning (1976), SACS (1980) with modification after Oliver and Kinnaird (1996).

The Khan Mine area is dominated by the Khan Formation which forms the dominant 'Blauer Heinrich' mountain and much of the outcrop in the north of the area. The base of the formation is exposed at GR[038,029] Location K11.8 where meta-conglomerates interspersed between amphibolitic schists are in contact with the Etusis Formation below. The basal conglomeratic horizons are monomict and between 10-12m thick. Clasts are comprised only of dark grey quartz that commonly display quartz-mica pressure solution shadows in a coarse grey-green matrix schist composed of Qtz+Bt+Pl. Clast sizes from various locations have been recorded for use in strain analysis in Chapter 3. Pytgmatically folded magnetite veins < 3cm thick were also noted in this location.

Above the basal conglomerates litho-types were recorded in a Log 3 GR[054,018 to 057,032] Figure 2.3. They form a monotonous series of banded grey-green coarse to medium-

grained gneisses with the general assemblage Qtz+Bt+Pl±Hbl±Kfs. At 500m from the base of the Log 3 (Figure 2.3) a gneiss unit comprising a massive granoblastic assemblage of Cpx+Pl+Grt+Qtz±Kfs was recorded. The granoblastic texture creates a mottled appearance. The same unit is also clearly exposed at the same level on the northern limb of the Blauer Heinrich Syncline. Comparison of Table 2.2 suggests this correlates with the Upper pyroxene hornblende member of Berning (1976). It is notable that skarn mineralization is spectacularly displayed within this formation. For example at GR[051,046] (Location K7.8), Plate 2.13, country rock in contact with leucogranite form complex assemblages, typically (Tre+Cz+Mag+Kfs &Tre+Cz+Bt).

Plate 2.13 Photograph showing a complex skarn-type dioptase-Kfs assemblage in the Upper pyroxene hornblende Member.

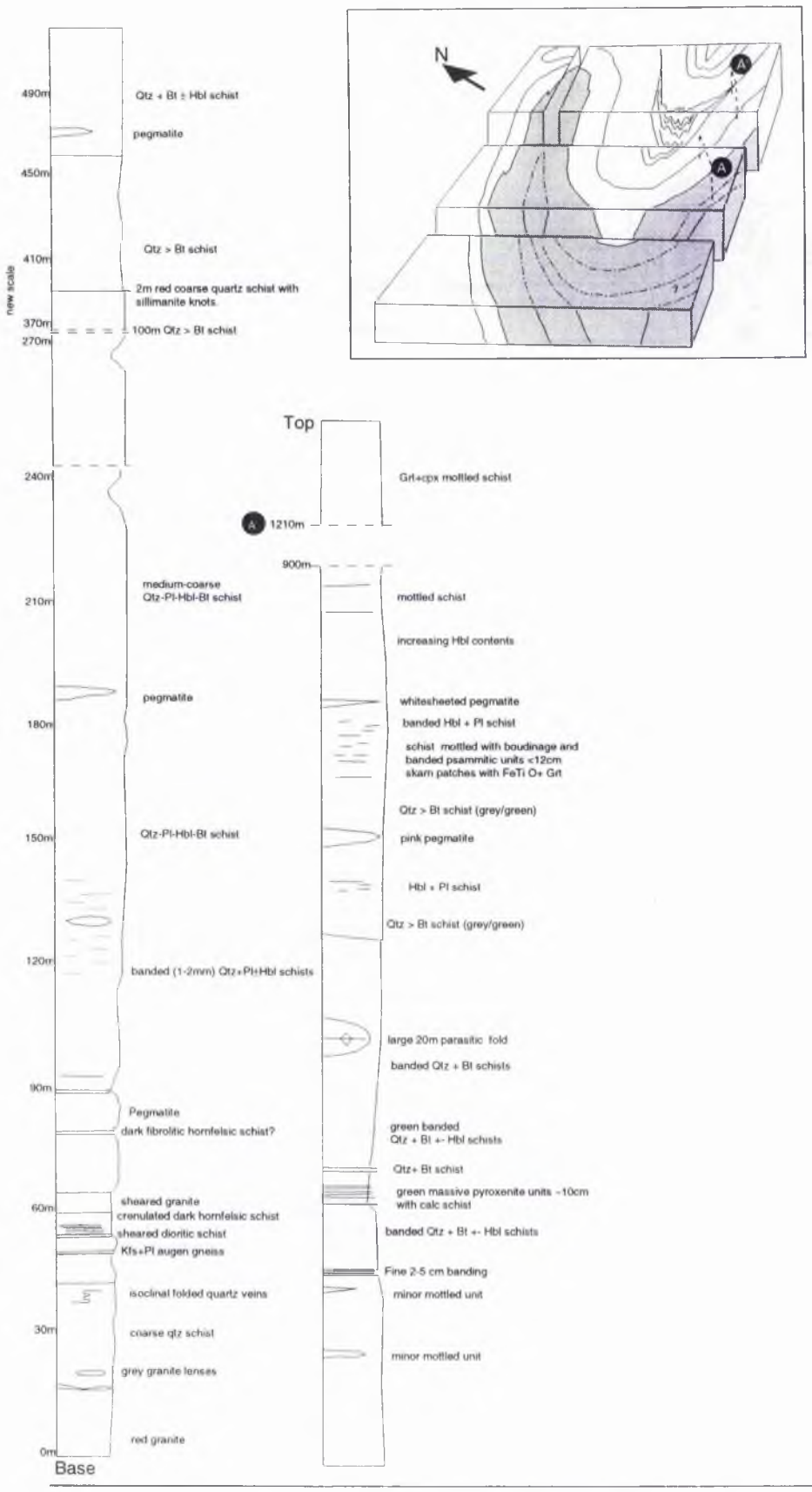

Figure 2.3 Summary log for basement- Nosib Group transition, Khan mine area

The Khan Formation is comprised of two distinct members in the Namibfontein area. The largest exposure of the first member is south of the Namibfontein dome where a thickness of *c.*500m outcrops around the Blauerberg dome and forms the high 830m peaks that overlook the Khan River to the north. A *c.*50m thick conglomeratic gneiss horizon at GR[034,027] (Location N37.3, 278m) on the south side of the Khan river, is virtually identical to the basal conglomerates in the Khan Mine area. The second and largest member (*c.*200m thick) is comprised of heterogeneous deep green gneisses with the general assemblage Pl+Qtz+Bt+Hbl+Kfs. Hbl is present in both the matrix and as large (1x3cm) randomly orientated euhedral porphyroblasts. Centimetre scale Bt-rich and Qtz-rich bands are common within the gneisses. Gneisses are typified by migmatite and ductile foliation boudinage, especially towards the core of the dome, this is best seen at GR[034,027] Location N37.3 (610m). As in the Khan Mine area skarn type assemblages are common typically including dioptase and fibrous tremolite intergrowths e.g. sample N48.4, GR[029,012]. Apart from the main banded gneisses thin units of 'mottled' gneisses were observed at GR[023,100] (Location N3.2b).

2.3.2 The Swakop Group

The Swakop Group is comprised of carbonaceous and argillaceous sediments which are more uniform and laterally persistent in nature towards the top. The group is made up of five formations; the Rössing, Chuos, Arandis Karabib and Kuiseb Formations.

2.3.2.i The Rössing Formation

The Rössing Formation outcrops discontinuously throughout the study areas. In the Khan mine area it forms the base of the Swakop Group, paraconformably overlying the Khan Formation (Lehtonen *et al.* 1993). This is marked by a basal conglomerate which overlies the Khan Formation GR[050,040]. Outcrop of the formation is confined to a maximum *c.*225m thick sequence around the symmetrical kilometre scale Blauer Heinrich Syncline where it defines a spectacular series of parasitic folds along the limbs; further east the formation thins eventually becoming completely absent. The formation is made up of a series of intercalated marbles, calc-schists, pelites and meta-conglomerates, many of these units are <1m thin and make this the most compositionally varied of all the formations studied. It is evident from other studies in the Khan-Swakop area e.g. Lehtonen *et al.* (1993; 1996) and Nex (1997) that there is considerable lateral variation within the formation; because of this a detailed description of the formation is presented in Log 4 shown in Figure 2.4 GR [050,040 to 052,038 and 058,035 to 058,035]. In the SJ area the formation is divided into five units (Table 2.2) by Hoffman (1984), while Berning (1986) has split it into six members . In detail comparison of Table 2.2

with Figure 2.3 confirms the highly variable nature of the Formation since few similarities are apparent.

Log 4 shows that the base of the formation grades from a 6m thick conglomeratic unit with smooth rounded quartz pebbles to a variable sequence of thin marble bands (< .5m), calc-dolomite schists, amphibolite and amphibolitic schists. Above this, *c.*2m horizons of thin conglomerates with Qtz clasts mark the start of a *c.*95m thick sequence of banded grey-buff coloured calcite marbles and subordinate calc-schists. This may correlate with the upper marble unit in the SJ area (see Figure 2.3). The sequence becomes dominated by pelitic units higher up, starting with a 30m thick unit of garnet bearing schists overlain by a *c.*10-15m thick unit of calcite marble bands and calc-schists (< 40cm). The formation terminates with a second pelitic (>55m) unit. This unit is deep brown in colour and comprised of the assemblage Qtz+Bt+Pl+Kfs+Grt+Crd±FeTiO. Garnet and cordierite are common porphyroblasts; garnet occurs as extremely large (15 x 20cm) almandine veins and segregations.

Hoffman (1984)			Berning (1976)	
Unit	Thickness (m)	Lithology	Unit	Thickness (m)
Quartzite	> 100m	Medium-grained quartzite.	Feldspathic quartzite	50
Upper pelitic gneiss	40 -50m	Diopside-biotite gneiss grades into Crd+Grt gneiss.	Upper Bt-Crd gneiss	50
Upper marble	50-70m	Serpentine marble and Cpx+Qtz marble with gritty-conglomerate base.	Upper marble	60
Lower pelitic gneiss	30-40m	Migmatised Crd+Sil gneiss locally Grt bearing grading to Hbl+Bt schist.	Conglomerate	5
Lower Marble	20-50m	Serpentine marble and subordinate graphite marble.	Lower Bt-Crd gneiss	40
			Lower marble	40

Table 2.3 Subdivision of the Rössing Formation in the SJ area after Berning (1976) and Hoffmann (1984).

There is a contrast between the Rössing Formation in the Khan Mine area and the Namibfontein area. It is represented by two 30m thick horizons of grey calcite marble on the northern flank of the Valencia dome GR[035,025]. The formation only occurs in this southern region and is notably absent in the stratigraphy around the Namibfontein and Vergenoeg domes (Lehtonen *et al.* 1996). In detail the marble is coarse-grained and commonly graphitic.

Banding is conspicuous and in some cases defined by green <30cm thick pyroxene-rich bands. At GR[019,063], Location N33.10, skarn assemblages have developed at the junction of the marble and Khan Formation where unfolded leucogranite sheets have intruded marble. The characteristics of the marble make it indistinguishable from the Arises member marble (see Section 2.3.3.ii). The stratigraphic position however, which places it structurally above the Khan Formation, clearly delimits it to be the Rössing Formation.

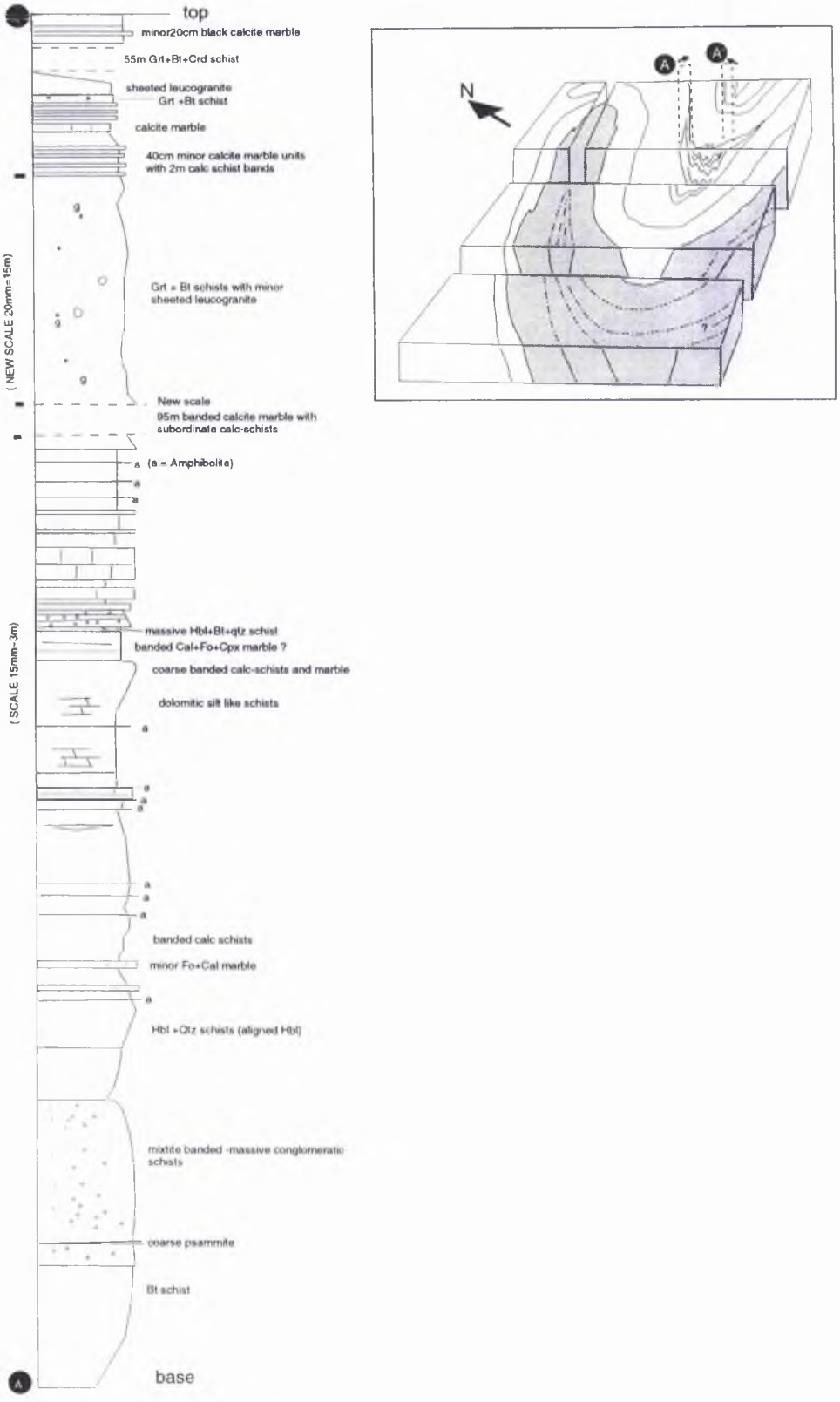

Figure 2.4 Scale log of Rossing Fm. for Khan mine area

2.3.2.ii The Chuos Formation

The Chuos Formation is exposed in both study areas. It is comprised of various horizons of impure arenaceous cross-bedded psammite units, metaconglomerates and ironstones. In the Khan Mine area the formation has a more or less constant thickness (*c.*500m) while in the Namibfontein area thickness is more varied. Here the formation is exposed in two structural settings. In the first setting it forms a thin (*c.*70m) horizon immediately above the Nosib Group in the core of the twin domes while in the second case it forms a continuous (*c.*100m) horizon south of the Khan River. In the southern-most exposure, across the large synclinorium the formation is much thicker; is made up of five horizons which can be mapped approaching the summit at GR[103,098] (Location N15.8, 870m), Table 2.4 summarises the main features.

A)	(10-15m)	Pure white friable fine grained quartzite. Inverted cross bedding is preserved indicating the wrong way up.
B)	(~20m)	Meta-conglomerate / mixtite with large clasts (> 30 x 10cm <) of granitic and gneissose compositions
C)	(~20m)	Meta-conglomerate / mixtite with few clasts (< 20%?)
D)	(~5m)	White Quartzite
E)	(~20m)	Meta-conglomerates with matrix and clasts of mixed compositions

Table 2.4. Summary of litho-types present in the Chuos Formation south of the Khan River at Namibfontein 91.

Outcrop of the formation around the twin dome structures and has been logged in a section from GR[087,085] to [090,081] shown in Figure 2.5, Log 5. In contrast to the outcrop near GR[103,098] the formation is markedly different, it consist of thin horizons of grey impure very coarse quartzite with far fewer (< 5%) strained pebbles (Plate 2.14). It is notable that compositionally pebbles are composed of white quartzite and not varied.

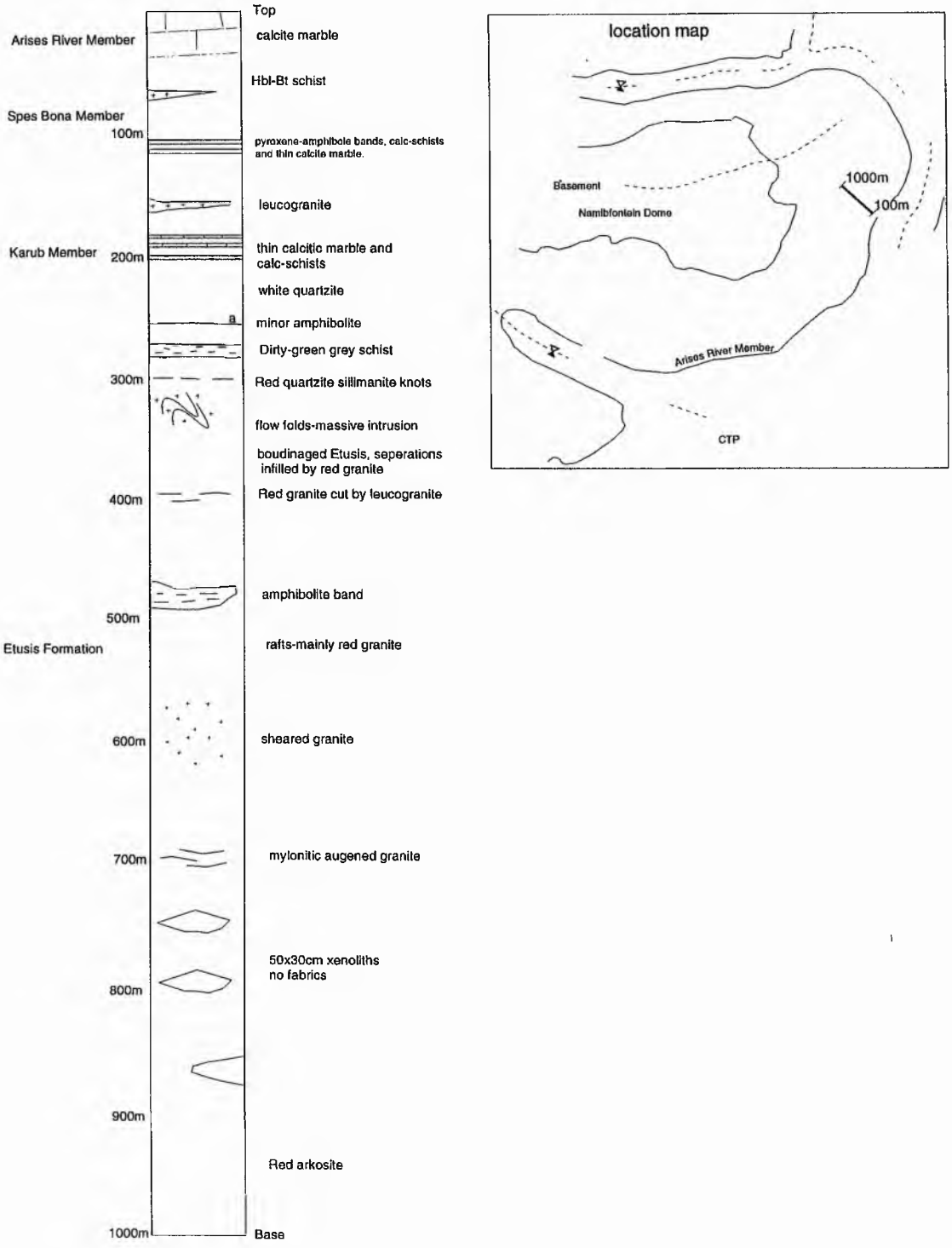

Figure 2.5 Log 5 summary of Damaran Stratigraphy at Location N14.6

Plate 2.14 Photograph of the Chuos Formation at N44.3[072,112] showing rare qtz-rich pebbles. Clast size ~2-5cm.

At GR[087,085] it was noted that the Chuos Formation occurs as rafts within late Damaran red granite. This is consistent with observations made by Kröner (1984) who suggested that 'red granite' did not intrude above the Nosib Group.

In the Khan Mine area the Chuos Formation is more uniform in nature, it lies over both the Khan and Rössing Formations and may be unconformable. Ordinarily, the formation is made up of *c.*3m thick units of schistose and more massive mixtite and metaconglomerate. Towards the top of the formation at GR[060,040], Location K34.2 for example, these become centimetre thick, forming interbedded Fe-rich horizons.

In detail, the schistose matrix is comprised mainly of quartzo-feldspathic arenaceous material; with the assemblage Qtz+Bt+Pl+Kfs. Clasts within the matrix are of varied composition, commonly Kfs+Pl+Qtz+Bt gneisses and Qtz+Pl+Kfs+Bt adamellitic granitic material, quartzite pebbles are also common. Clasts are predominantly matrix supported. Original clast shape has not been preserved during Damara orogenesis (see Chapter 4) while individual pebble size can be extremely large; at GR[063,046] Location K34.4 for example, matrix supported grey gneissose granite clasts are up to boulder size (30 x 120cm).

In rare instances, the main quartzo-feldspathic matrix is contrasted by poorly banded ironstone (< 1m), such as at GR[063,046], with sub-parallel discordant contacts to the schistose units. The ironstone is fine-grained and dark brown in appearance with iron oxide (magnetite) as small euhedral patches. Internally, the units contain thin (< 2cm) pytgmatically folded leucogranite veins that are generally more highly strained than those in the quartzo-feldspathic matrix (see Plate 2.15).Discussions as to the origin of the Chuos Formation have been comprehensively covered by Schermerhorn (1974) & (1975), Martin *et al.* (1985), Henry *et al.*

(1986) and Badenhorst (1992). The Chuos matrix supported mixtites with their exotic clasts are generally thought to have a glacio-marine origin.

Finally, it should be noted that the Chuos Formation is not always conformable, in some areas the Rössing Formation is absent and it rests on the Khan Formation e.g. the northern limb of the Blauer Heinrich Syncline. Previously, this has been regarded as evidence of i) an unconformity surface or lateral changes of facies (Downing 1983) ii) as remnants of early thrusts (Barnes 1981) and iii) as tectonic thinning of the cover (Oliver 1996). The later two cases appear unlikely. Strain analysis in Section 3.7.1 suggests quite uniform deformation across cover formations. The existence of major thrust is not supported by field mapping, although stratigraphic units are absent in some sections, the sequence is not inverted. Thus, the Khan-Chuos Formation and Kuiseb-Chuos Formation boundaries are interpreted as unconformable. Furthermore, examination of cross-sections (from Maps 1 & 3) show that Khan and Etusis Formations are diachronous.

Plate 2.15 Photograph showing dark brown Fe-rich Chuos Formation at K34.4 GR[063,046] interpreted as ironstone formation.

2.3.3.iii The Arandis Formation

The Arandis Formations is dominated by carbonate sequences. The formation consists of four members (Badenhorst 1992), which are present in both of the mapping areas and form important marker horizons shown below in Table 2.5.

Formation	Unit	Lithology
Karabib	Onguati Member	Marbles, calc-silicates and quartz biotite schists.
	Arises River Member	Pure calcitic marble.
	Otjongeama Member	Calc-silicate layers.
	Harmonie Member	Alternating calc-silicate, thin marble and schist.
Arandis	Oberwasser Member	Grey Grt+Bt schist
	Okawayo Member	Thin grey marble and calc-silicates
	Spes Bona Member	Green micaceous schists and calc-silicates
	Karub Member	Marble and calc-silicates

Table 2.5 Summary of sub-units within Arandis and Karabib Formations from Lehtonen *et al.* (1993).

In the Namibfontein area the Arandis Formation was mapped as a *c.*500m thick sequence below the Karabib Formation which broadly comprises two members. The first thin but more distinctive member consists of interlayered green pyroxene and thin grey (<15cm) calcitic marble bands, the banding is stretched exhibiting complex pinch and swell type foliation boudinage, this is assigned to the Karub Member (Lehtonen *et al. op. cit*). The second member is *c.*300m thick and composed of well foliated, green micaceous schist which is highly weathered. It has a general assemblage of Bt+Qtz+Pl±Kfs. According to Lehtonen *et al.* (1996) this corresponds to the Spes Bona Member (see Figure 2.5)

In the Khan Mine area the Arandis Formations outcrops around the Blauer Heinrich syncline where, like the Chuos Formation, they form complex parasitic folds. Details of the component lithologies of the Arandis Formation were recorded from GR[062,040 to 065,040] in addition to the Karabib Formation described below, these are summarised in Table 2.6.

2.3.3.iv The Karabib Formation

In the Namibfontein area the Arises River Member dominates the Karabib Formation, it is spectacularly exposed around the twin domes and in particular around the Karub Syncline. Due to its ductile nature its outcrop thickness is extremely variable; at the north-east closure of the dome it is *c.*50-100m thick, however following the marble to the north it thins to ~10m GR[088,117]. In general the marble horizon often defines steep curving ridges being of considerable use in mapping. In the Khan Mine area the Karabib Formation outcrops around the Blauer Heinrich syncline recorded at GR[065,040], summarised in Table 2.6.

The marble member is coarse-grained, blue-grey and calcitic in appearance (Lehtonen *et al.* 1996), less commonly it is dark green or yellow near to leucogranite sheets and segregations. Plate 2.16 shows Location N10.16 at GR[086,110] where medium-grained white leucogranite forms sharp seriate contacts with the overlying marble. It is notable that large (3 x 1m) granite segregations have been boudinaged within the marble in addition to calc-silicate horizons. These often appear as chocolate tablet structures within the marble; individual horizons of calc-silicates comprise numerous thin bands of massive green diopside. These have been described by Lehtonen *et al.* (1993) who assign them to the Otjongeama Member. In this study they do not appear confined to a single stratigraphic horizon. In most areas it is clear that the Arises Member Marble acted as a barrier to melt intrusion so that leucogranite sheets are extremely common below the Karabib Formation; under the southern limb of the Karub Syncline, for instance, multiple sheeted garnet (>2cm) leucogranites (> 10m thick) formed local contact skarn, this phenomena is absent from the overlying Kuiseb Formation.

Plate 2.16 Photograph showing outcrop of the boudinaged calc-silicate horizons at Location N10.16. Note that large (3 x 1m) granite segregations have also been boudinaged within the marble.

The zone between the Kuiseb Formation and Karabib Formation was termed the Onguati Member by Badenhorst (1992). These transitional schists are clearly exposed at

GR[099,105] Location N9.1 in a narrow gorge section (Plate 2.17) and at GR[019,074] Location N32.2, along a small track that leads into the closure of the Karub Synform. It is generally denoted by thin calcite marble horizons and minor biotite and calc-schists horizons.

Lithology	Member	~ thickness
	KARABIB FM.	
Calc-schists and biotite schists.	Onguati Member	>20m
Massive grey calcite marble.	Arises Member	>100m
Pyroxene Qtz banded calc-silicates.	Otjongeama Member	5-10m
	ARANDIS FM.	
Dark Cherty horizons (>30cm).	?	5m
Bt schists with conglomeratic horizons.	?	100m?
Crd + Grt schists.	? 50m?	
Minor marble band with subordinate Hbl and Grt schists.	Karub Member >10m	

Table 2.6 Summary of the Karabib and Arandis Formation lithologies in the Khan Mine area.

2.3.4.v The Kuiseb Formation

The Kuiseb Formation is widespread in the Namibfontein area where it forms large areas of synclinoria south of the twin domes. It was not present in the Khan Mine area. The formation is composed of pelitic to semi-pelitic material, usually a brown-grey colour and frequently weathered. The schist is often migmatized with abundant centimetre to metre-scale leucogranite veins which cut foliation or form parallel and boudinaged layers. (Details of the leucogranite field relations are discussed in Chapter 5).

In outcrop it is banded and has a parallel foliation, banding is often on a scale of tens of centimetres reflecting primary compositional variation. Graded bedding is quite commonly preserved , despite the intense deformation of the formation. An extremely good example of metre-scale graded bedding occurs at GR[059,054], Location N25.6. According to Henry (1992) this is evidence of the turbiditic origin of this Formation. In fresh hand specimens the schist is a purple-grey colour with cordierite as a common index mineral. These form parallel elongated porphyroblastic growths on foliation surfaces (see Plate 2.19). Garnet is also a common porphyroblastic phase, it is notable that in the Karub Synform almandine garnet is a ubiquitous major phase and suggests that here the formation is perhaps more iron-rich. Qtz and

Kfs constitute < 30% of the matrix in most samples. The general assemblage is Qtz+Bt+Pl+Kfs+Crd±Grt.

In exceptional instances carbonate-rich calc-silicate units were mapped. These were noted within the schists at GR[081,120] Location N11.4 at the centre of the northern synform. The lithologies included thin (40cm) calcitic marbles and quartz-diopside bands forming ~20% of the total outcrop. Lehtonen *et al.* (1993) have noted that similar calcareous lithologies within the Kuiseb Schists east of Hentis Bay

Plate 2.19. Photograph showing elongate Crd porphyroblasts on foliation surfaces in Kuiseb Schist, Location K24.4 GR[075,056]

2.3.5 Cenozoic

A 5-10m thick polymict calcite cemented breccia was observed at Location N46.5 overlying rocks of the Khan and Rössing Formations. The breccia is unfolded and clearly forms an angular unconformity with the Damara sequence. According to Wilkinson (1990) these locally preserved units are representatives of Tertiary surface processes.

CHAPTER 3

Structural Analysis

3.1 Introduction

The Central Zone provides complete examples of structures exhumed from the ductile mid-crust. In this Chapter a detailed account of the geometry of these structures is presented. The description is deliberately set out in an unconventional manner since it is the intention to highlight the unusual non-planar and non-cylindrical morphology without pre-empting a polyphase origin. Conventionally, notation used to describe complicated fold geometries implies polyphase deformation, thus pre-supposing their origin. Furthermore, chronological subscripts imply deformation has effected an entire area, however, Tobisch & Paterson (1988) state:

"If one can document the progressive relationship of structures on a regional scale, the deformation should be considered as *one composite deformation,* consisting of various components (e.g. morphologies) which represent different deformational stages in the evolution of that rock body. Since the different morphologies may form at various times in different parts of a progressively deforming mass, they may be more realistically viewed as penecontemporaneous rather than representing discrete pulses of deformation separated by geologically meaningful periods of time."

3.1.i Aim

It is therefore a central aim in this Chapter to present a balanced description of all important mesoscale structures while allowing an open overview of the regional picture but without pre-supposing their origin.

3.2 Structural description conventions

The structures described below appear to display 'spatial chaos' in their geometries (*cf.* Hunt *et al.* 1996) both at the macroscale and mesoscale. They challenge descriptive technique and established geological modes of formation. The labels used to describe structural elements therefore do not refer to chronological regional events but describe the succession of structural elements observed at outcrop scale. Structural investigation has focused on the interpretation of bedding/compositional layering (S_0), tectonic foliations (S_1 & S_2), lineation (L_1), defined by mineral orientation data, and fold axis orientation data $F_{(1\text{-}2)}$.

Data are presented for minor *cylindrical structural domains* delineated on maps and plotted on equal area stereograms for structural domains. This procedure is used normally to interpret polydeformed terranes by defining β axes where changes in axial trace angles occur. A β axis is a regional fold axis defined by the plotted poles of a folded axial surface. (*cf.* Ghosh 1993). Here it is used to define regional scale fold geometry, bends in fold axial traces are not necessarily regarded as subsequent fold phases. This approach permits an open comparison of macro-scale structural elements with the mesoscale outcrop features on a purely geometric basis. Table 3.1 lists the symbols and orientation convention used to describe structural elements in the field.

The main fabric throughout the study areas is a regional composite, bedding/compositional layering tectonic fabric (S_0+S_1), S_1 defined by coarse biotite and quartz ribbons. The origin of S_1 is interpreted as mimetic since it is parallel to S_0 in all lithologies. Barnes (1981p.51) noted that other tectonic fabrics are rarely found in the Central Zone. The subscript S_{1C} is used to denote tectonic foliation in the cover and S_{1B} for basement. (definition of basement and cover is given in Section 2.2). A regional stretching lineation L_1 is defined by aligned micas or aligned elongate mineral porphyroblasts that lie on the plane of S_1.

Element (examples)	*Orientation convention*	*Symbol*
Bedding surface	Dip/Dip Direction	$=S_0$
Defined by compositional banding and metamorphic phase variation.		
Tectonic foliations	Dip/Dip Direction	$=S_{1(B)/(C)}$ - S_2
Defined by schistose biotite, S_2 usually sub-parallel to S_1.		
Lineation	Plunge/Plunge Azimuth	$=L_1$
Aligned metamorphic minerals including matrix Bt, porphyroblasts of Crd, Sil and Hb. Also aligned Kfs augens.		
Fold hinge	Plunge/Plunge Azimuth	$=F_1$-F_2

Table 3.1 List of structural elements and orientation convention.

3.3 Regional Scale Structure

The areas studied consist of a *c.* 50km wide network of domal structures with varying morphologies. Barnes (1981) recognised three types of domes; he termed these granite domes, metasedimentary/migmatite domes and 'Pure' metasedimentary domes. This work describes four dome structures and their surrounding cover envelope. The Khan Mine area consists of the Khan Dome and its easterly cusp the Nose Structure Anticline; this is a metasedimentary basement dome. The Namibfontein area consists of 'twin domes' the Namibfontein and Vergenoeg Domes, so called 'granite domes', and the Valencia dome, a metasedimentary ridge like dome.

3.3.1 The Khan Mine area

The Khan Mine study area, shown in Figure 3.1 and Plate 3.1, is dominated by a well exposed tight anticlinal dome called the Khan Dome. The north-east part is called the Nose Structure Anticline (Smith 1965). The Nose Structure Anticline forms part of a curved anticlinal cusp which extends from the main body of the Khan Dome to the south-west where it apparently partly encircles an open to tight synclinal domain, called the Blauer Heinrich Syncline. The Blauer Heinrich Syncline (Figure 3.1) trends NE-SW and converges towards the east with three other synclinal axes at the Khan Mine Convergence Point (see Section 3.3.1i); it has a 1-2km span and contains numerous second order folds.

3.3.1.i 'Convergence Points'

A 'convergence point' is a point where major fold axes meet and bifurcate. The term is used to describe a significant feature of the non-planar and non-cylindrical regional scale structure in the Central Zone (Barnes 1981). Points where kilometre scale folds bifurcate at convergence points are a common feature of dome crests and synclinal domains (see Section 3.5.1.ii, Figure 3.10)

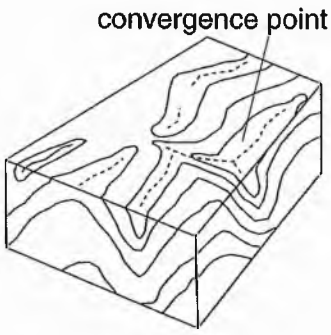

Plate 3.1 Aerial photograph (10 000ft) of the Khan Mine area showing the Nose Structure Anticline. Overlay shows main Formations and spatial extent of basement outcrop. Faults and dolerite dykes trend approximately east-west.

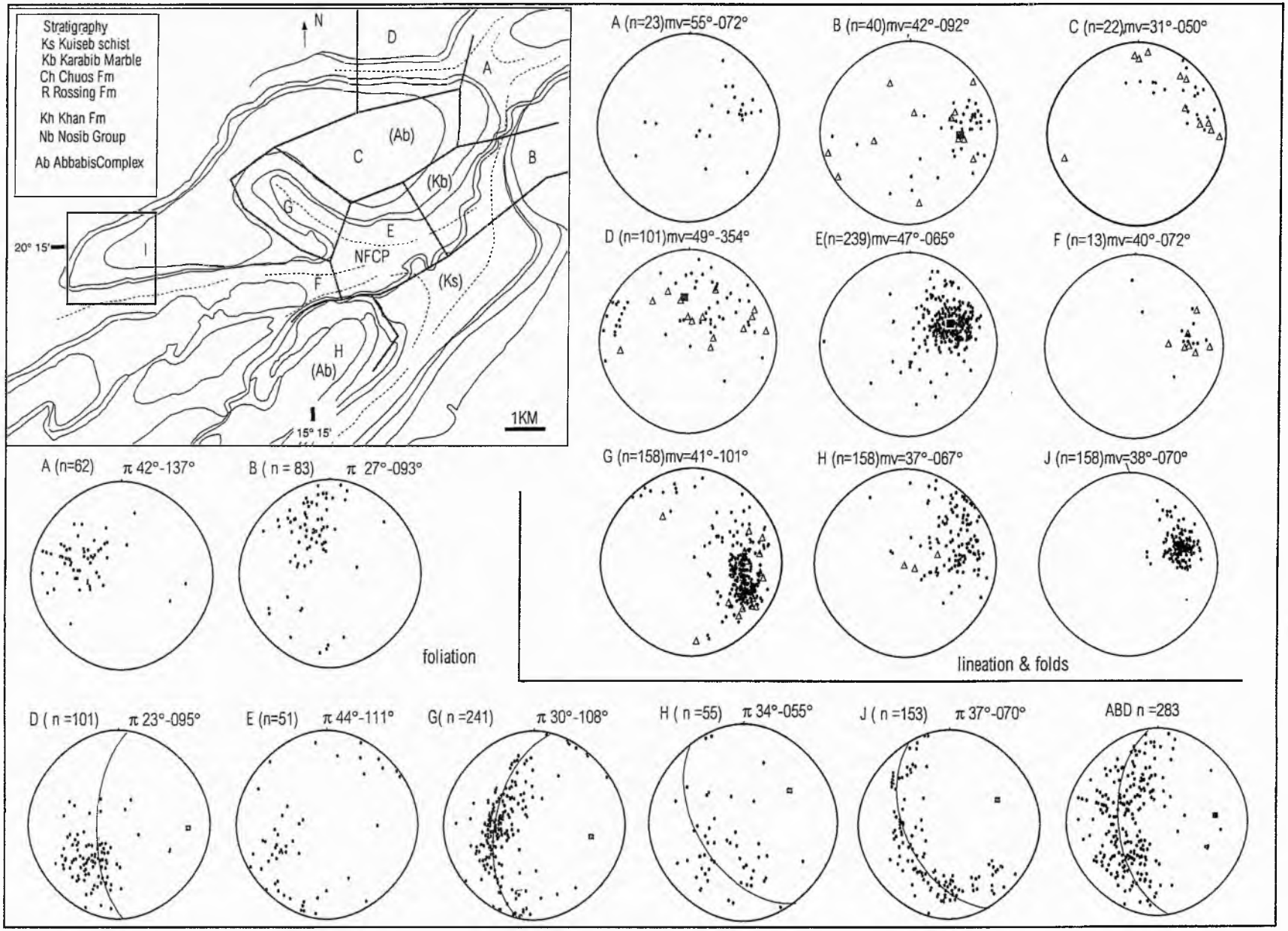

Figure 3.1 S_1 /S_0 foliation plotted as poles (lower inset) and L_1 lineation data (upper right inset) for the Namibfontein area plotted by domain on equal area stereonets (right inset map shows domains). (Δ= fold axis plunge and azimuth, m.v.=mean L_1 vector, π= girdle axis.)

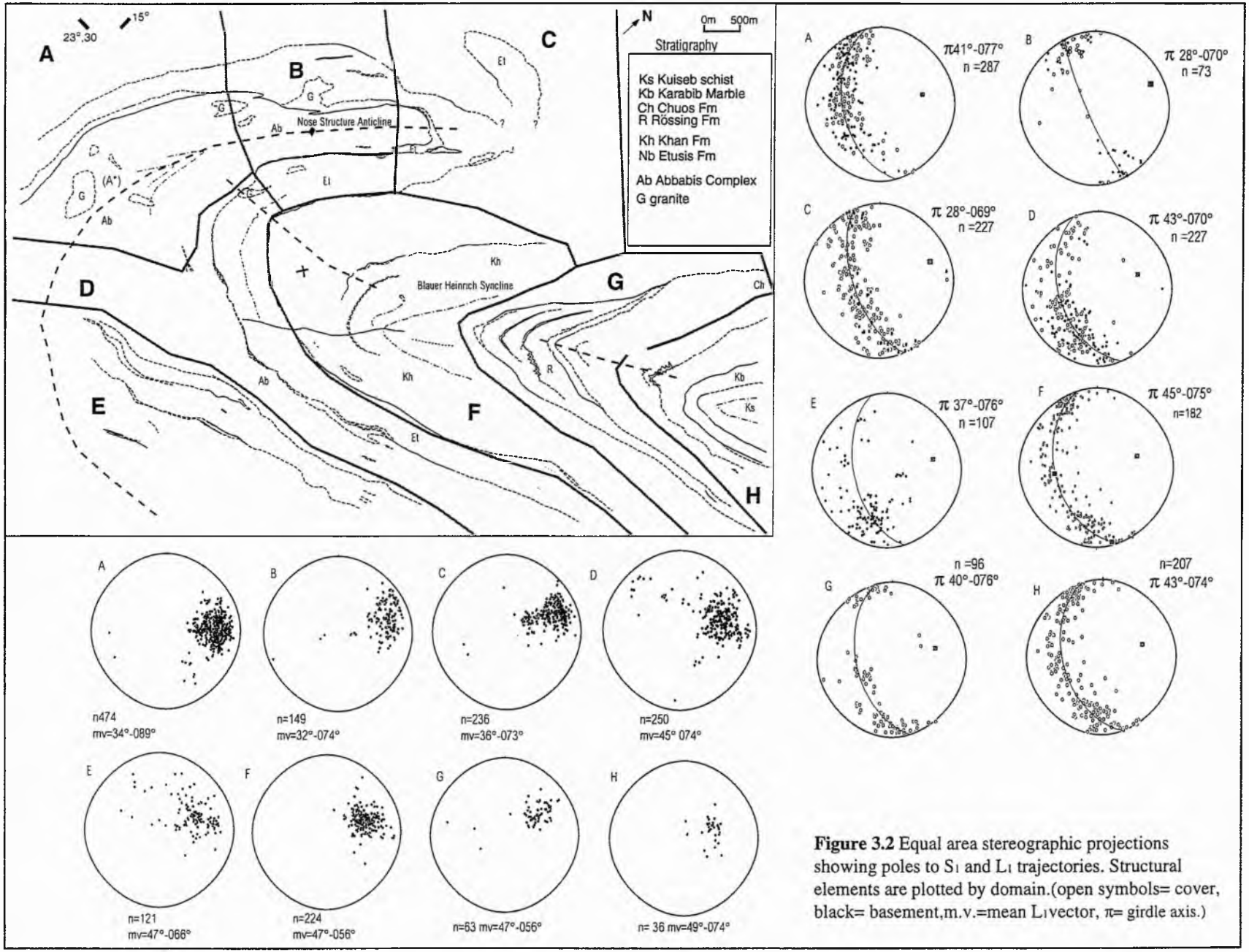

Figure 3.2 Equal area stereographic projections showing poles to S_1 and L_1 trajectories. Structural elements are plotted by domain.(open symbols= cover, black= basement,m.v.=mean L_1vector, π= girdle axis.)

3.3.2 The Namibfontein area

The Namibfontein study area is shown in Figure 3.2, it is 50km further east of the Khan Mine area and exhibits a 20km elongate structure exposing the Namibfontein and Vergenoeg twin domes. An intra-domal subsidiary syncline termed the Karub Syncline (Smith 1965), separates the domes. The Karub Syncline joins part of a wider open to tight synclinal domain that bends around the twin domes. The axial trace of the syncline is curvilinear and similar in form to a rim syncline. It consists mainly of phyllosilicate-rich Kuiseb schists and minor leucogranite intrusions. The southern part of the synclinal rim is a 5 by 10 km structural depression where at least three synclines merge. This is termed the Namibfontein Convergence Point (Figure 3.2). The NE closure of the Valencia Dome, south of the main Namibfontein Convergence Point, exhibits a well exposed highly strained mobilized Kibaran age basement. Migmatised augen gneiss in this area, sampled by Kröner *et al.* (1991), gives a SHRIMP U-Pb zircon age of 1038±58Ma, they interpret this as the age of the granite protolith in the basement.

3.4 Mean lineation and girdle axes

Figures 3.1 & 3.2 show the plotted poles to S_0 and S_1 with π girdle axes orientations for each domain (π girdle axes define a cylindrical fold axis from poles plotted from a folded surface e.g. S_1). The π girdle axes broadly coincide with mean L_1 orientation for each domain; Table 3.2 shows that most domains, with the exception of domains NF(A) and NF(E) have statistical maximum 10-15° deviation between the mean L_1 trend and the associated π axis; this pre-supposes a genetic link between lineation and domain structural trend. Exceptions are domain NF(A) and NF(E) where S_{1C} forms a synclinal convergence point so that a truly cylindrical domain is not defined.

Orientation of π girdle poles and π girdle axes show that regional fold geometry is non-planar and non-cylindrical to sub-cylindrical (Ramsay & Huber 1987a & 1987b). The variability of the mean lineation for each domain compared to the total mean lineation at 44°-069° does not indicate successive generations of lineation as all lineations seen in the field are chronologically L_1. This pattern requires a mode of generation that can produce variation around the general trend.

Domain	*mean L1*	*π Axis*	*variance (trend)*
NF(A)	55°-072°	42°-137°	+65°
NF(B)	42°-092°	27°-093°	+1
NF(C)	31°-050°	*	*
NF(D)	49°-354°	23°-100°	+106°
NF(E)	47°-065°	44°-111°	+46°
NF(F)	40°-072°	*	*
NF(I)	37°-067°	40°-054°	-13°
NF(J)	38°-070°	37°-070°	0
NF(G/H)	41°-101°	30°-108°	+7°
KM(A)	34-089°	41-077°	-12°
KM(B)	32-074°	28-070°	-4°
KM(C)	36-073°	28-069°	-4°
KM(D)	47-056°	43-070°	-14°
KM(E)	47-066°	37-076°	+10
KM(F)	47-056°	*	+10°
KM(G)	47-056°	40-076°	+20°

Table 3.2 Domain π girdle axes and mean lineation shown for Khan Mine area and Namibfontein areas. (* indicates insufficient data to acquire meaningful values)

3.5 Mesoscale fold relations

In order to gain a sense of the 'composite deformation' and bulk strain this section gives an account of the style, orientation and distribution of outcrop scale folds with reference to detailed maps, sketches and stereographic projections. Data are presented separately for the Namibfontein and Khan mine areas.

In general, comparison of fold style and orientation between outcrops shows few similarities (Plate 3.2 A-E). Where it is clear S_0 and S_{1C} are folded, the term F_2 is used to denote a fold, this does not imply a regional F_1 fold event occurred, it merely defines folding of the S_{1C} surface at some stage.

The form and hinge angles of F_2 folds varies from open rounded to near isoclinal, F_2 folds in the Karub Syncline (Plate 3.2B) have been tightened and limbs attenuated, indicative of progressive strain (Lisle 1991). S_{1C} is locally tightly pinched at fold cores where it is sub-parallel to S_2 forming micro-domains of composite transposed foliation (*cf.* Tobisch & Paterson 1988), this is shown in Figure 3.3 and Plate 3.3.

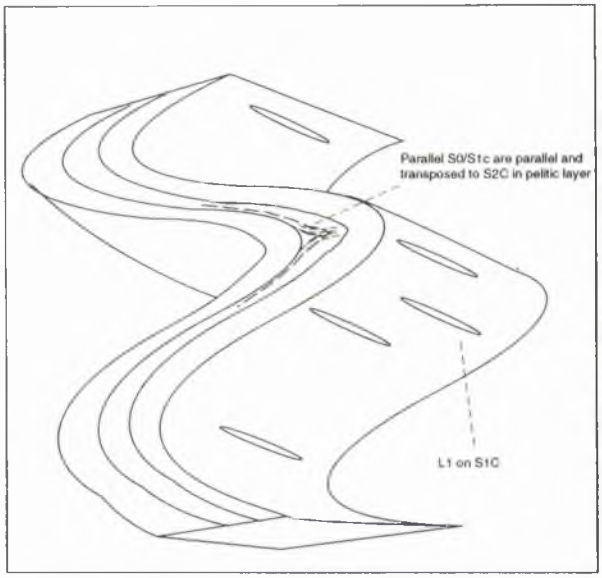

Left Figure 3.3 Schematic drawing to illustrate the relationship between S_{1C} and S_{2C} in F_2 fold cores.

Right Plate 3.3 Photograph showing parasitic F2 fold with S2 developed in fold hinge.

Major porphyroblasts such as garnet and cordierite often have quartz and biotite inclusion trails that are typically straight to gently sigmoidal; there is no remnant evidence of early crenulated tectonic fabrics (see sketches in Section 4.2.3), there is therefore no need to upgrade S_{1C} to S_{2C} i.e. an early tectonic fabric has not been transposed regionally. The strong parallel nature of S_{1C} and S_0 in all strata except F_2 fold cores is diagnostic of mimetic foliation growth parallel to bedding planes and not of an axial planar D_1 fabric (*cf.* Turner & Weiss 1963).

Plate 3.2

A Parallel F_2 folds at location N11.4 formed in psammite from the Kuiseb Formation .

B Tightened rootless isoclinal F_2 folds formed in psammite and surrounded by pelite at location N29.7 at the core of the Karub Syncline.

C Angular tight F_2 folds formed in pelites from the Kuiseb Formation at location N28.2 (292m).

D Angular flexural slip type F_2 folds formed in pelites from the Kuiseb Formation at location N36.15.

E Open to tight moderately plunging F_2 folds formed in pelites from the Kuiseb Formation at the in the nose of the Karub Syncline.


A


B


C


D

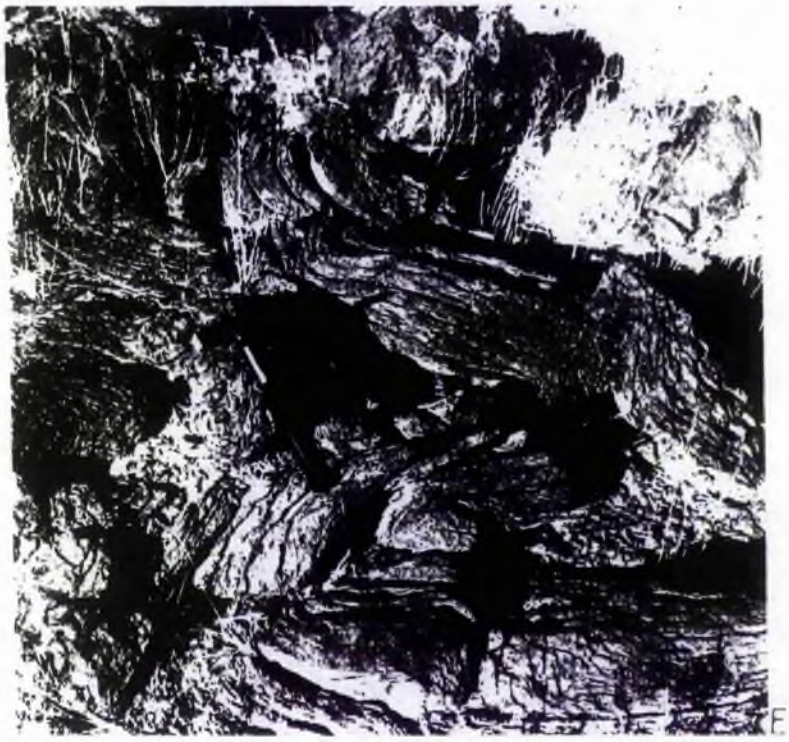
E

3.5.1 Mesoscale folds in the Namibfontein area

Equal area plots in Figure 3.1 show representative fold hinge orientations in the Namibfontein area plotted against lineation trends L_1 (see data in Appendix 3.1). Fold axes are observed to be parallel to sub-parallel to mineral lineation. This observation is supported by close inspection of lineation in the core and on the limbs of F_2 folds where L_1 is always coaxial to the hinges. Furthermore, L_1 trajectories on limbs surrounding F_2 folds are also coaxial suggesting the same geometric relationship to the finite X direction even where mineral lineation is not developed in fold cores. Generally, lineation is more common in fold cores formed in the pelitic-units.

The distribution of fold hinge azimuth about the total mean L_1 orientation is shown in a frequency distribution histogram (Figure 3.4) following the method of Alsop (1993). Fold orientations are grouped into 45° intervals about the principle finite elongation (X) direction (-069°). The histogram shows near normal distribution, bulk fold hinge distribution is slightly anticlockwise and oblique to mean L_1.

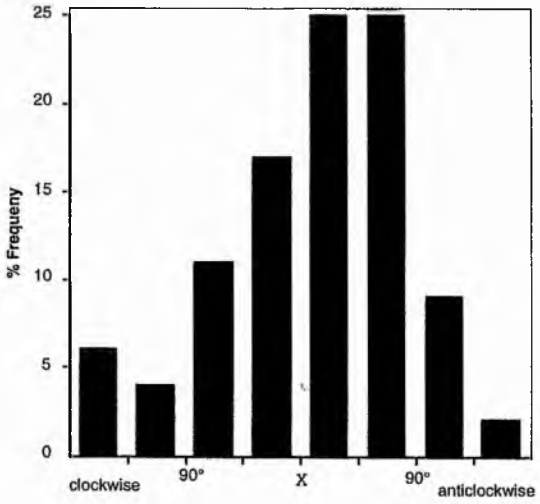

Figure 3.4 Frequency distribution histogram for all F2 fold hinges (n=100) plotted in 45°intervals from mean L1(44°-069°) (X direction).

Small scale folds exist over most of the area, they are most evident in the pelitic and semi-pelitic schists of the Kuiseb and Arandis Formations and less common in the Nosib Group. Examples of typical fold profiles from the Namibfontein area are shown in Figure 3.5. These have been plotted using the morphological classification of Ramsay (1967) where t'_α is plotted as ordinate and α as abissca.

$$t'_\alpha = \frac{t_\alpha}{t_0}$$

t_α= orthogonal thickness

t_0= hinge thickness where α=0

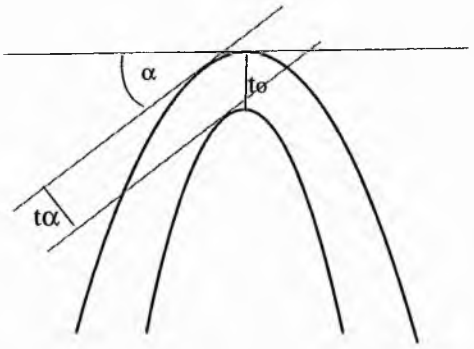

These plots show that folds developed in well-foliated phyllosilicate rich rocks have class 1C to class 2 profiles, which suggests progressive strain (Ramsay & Huber 1987a). (A description of strain in folds is presented in Section 3.7.3). More competent quartz-rich layers form concentric class 1B folds (Plate 3.2 A). Substantial 'differential thinning' of fold limbs (Lisle 1991) which is characteristic during simple shear deformation rarely occurs, thus this might be ruled out as a major fold forming mechanism. Minor folds in the Namibfontein area plunge moderately to steeply and are commonly moderately inclined to the south west. Mesoscale F_2 folding in the Namibfontein area is present in a great variety of styles. The predominance of particular fold styles and, by inference, fold mechanisms can be assigned to three broad settings:

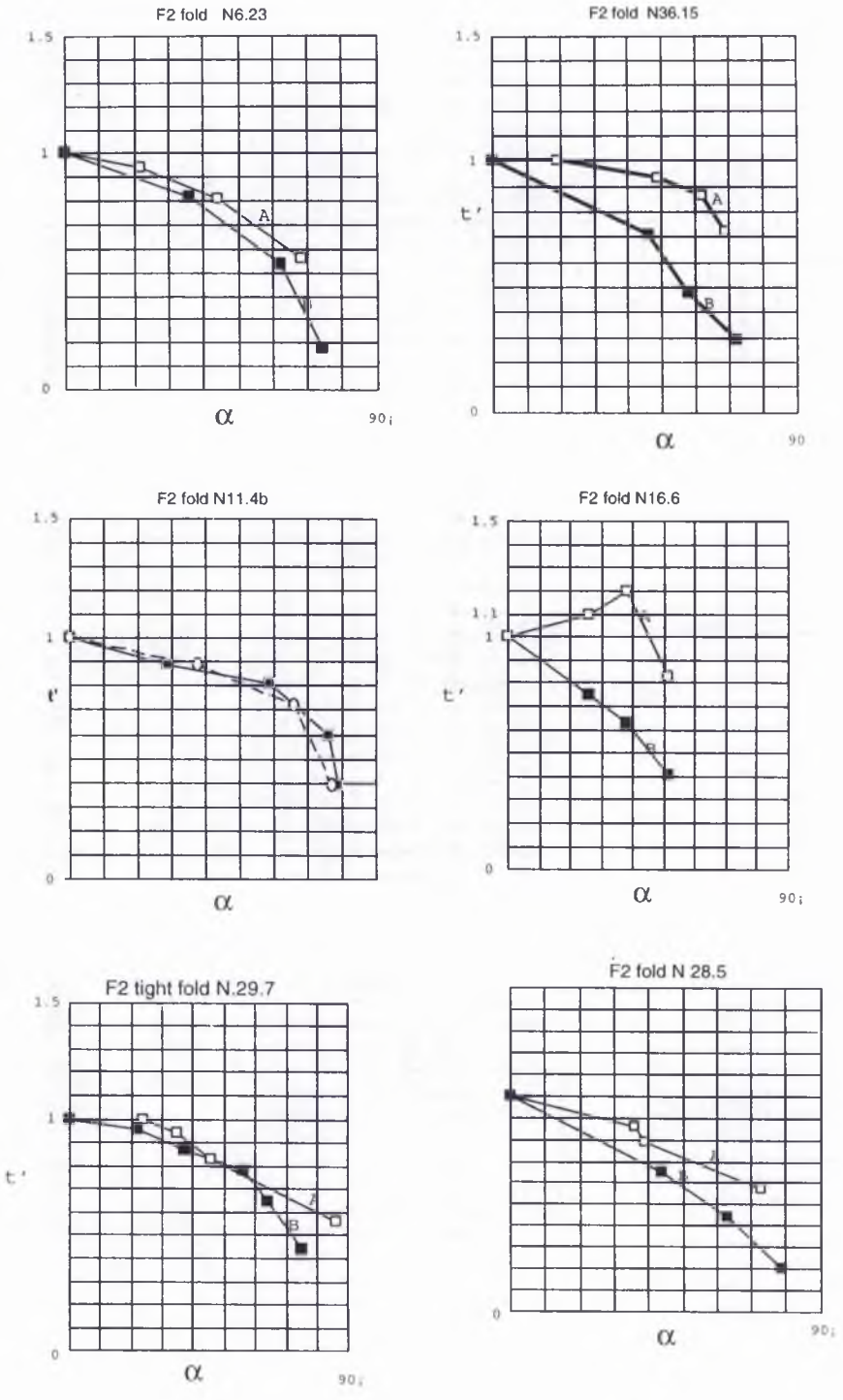

Figure 3.5 Various t' a fold profiles from the Namibfontein area classified according to (Ramsay 1967)

3.5.1.i Folds in the cover

Geometrically, F_2 folds formed in the cover in the Namibfontein area are uncomplicated. Examples of fold geometries have been plotted individually on equal area stereonets to assist description and in order to relate them to the domain scale. In addition two well exposed outcrops were mapped at ~1:2000. These locations provide an insight in the nature of the minor folding at the core of the rim syncline that surrounds the Namibfontein Dome. In the first location, at N11.4 GR[081,120] (shown in Figure 3.6) an *c.* 200m^2 area displays a mesoscopic syncline with a *c.*10m span. This second order fold, is sub-parallel to the regional axis of the rim syncline. It plunges moderately at ~50° to the NE, more steeply than the major syncline. The hinge is rounded and open. Parasitic third order folds form angular hinges in pelitic units and parallel rounded hinges in the more competent quartz pyroxene units (shown in Plate 3.2A). Stereoplot data in Figure 3.6 shows that these minor folds are sub-parallel to the second order fold axis and outcrop lineation; no axial planar cleavage is observed.

The second location, N28.5 at GR[037,053] shown in Figure 3.7, is ~200m south of the Arises Member Marble at the edge of the synclinal domain south of the Namibfontein dome. Two moderately plunging folds with *c.* 3m spans outcrop. The first as a sub-angular box like syncline and the second an angular anticline with a rounded psammitic core. The fold hinges are sub-parallel to regional L_1. The folds are defined by parallel S_0 and S_1. In the fold cores however S_{1C} is pinched towards parallelism of the axial surface of the folds. This strikes ~280°-100° in the anticline, S_{1C} is transposed to form S_2 and transects the axial plane in a clockwise sense by ~20°.

Individual mesoscale F_2 fold data are presented as equal area stereographic projections in Figure 3.8. Fold hinge shape is indicated as minor arcs (axial trace and S_{2C} data are referred to in Section 3.5.4). At first glances two points may be deduced from this figure; firstly, that F_2 fold hinge angles range from open to tight and are therefore quite varied. Secondly, fold hinge plunge and azimuth is variable. The spread of fold hinge trajectories within domains is markedly scattered, comparison of these between domains shows that this spread varies systematically, close to the spread of L_1.

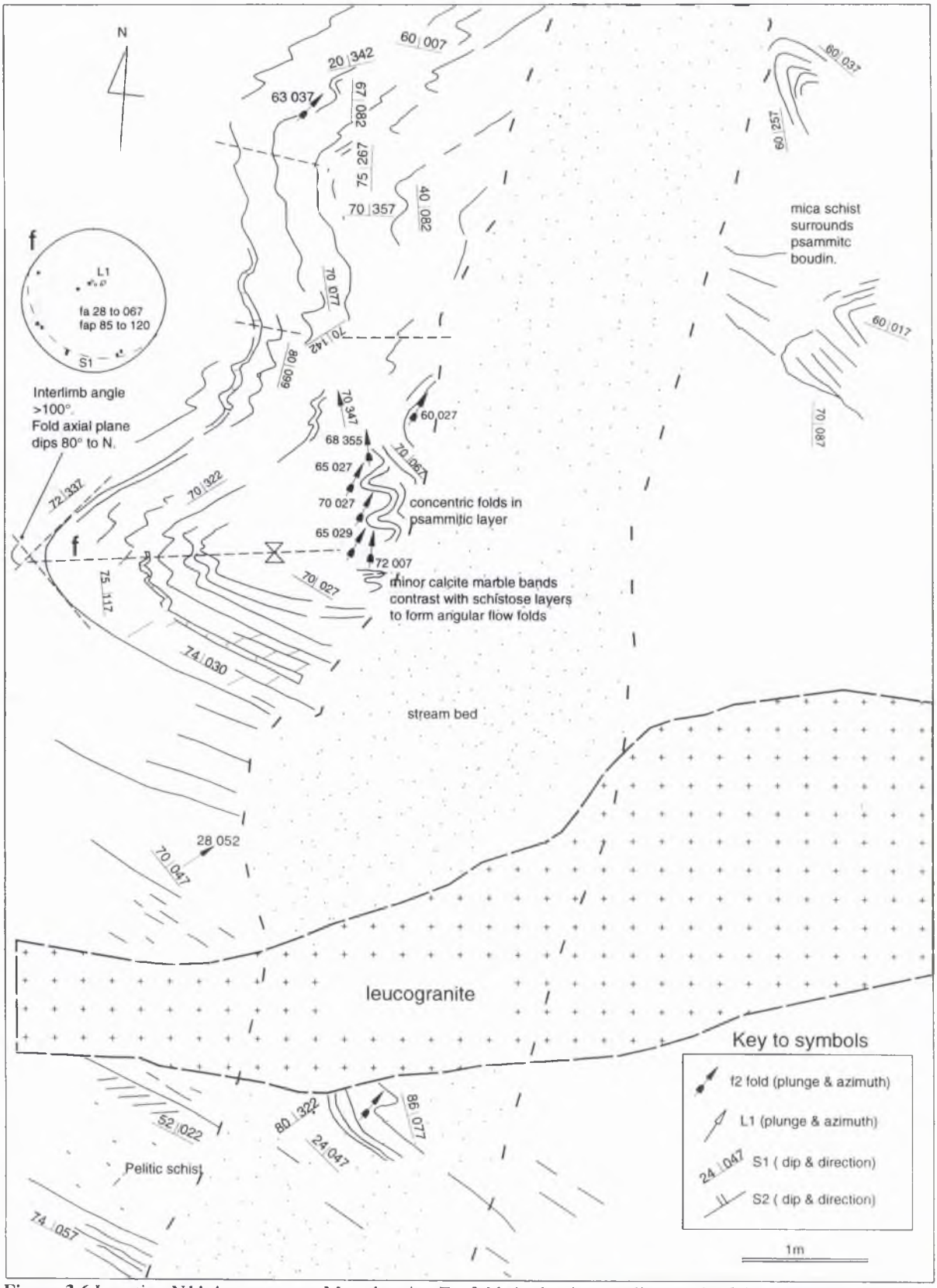

Figure 3.6 Location N11.4 [12,0,0/8,2,0]. Map showing F_{2c} folds in the rim syncline north of the Namibfontein Dome.

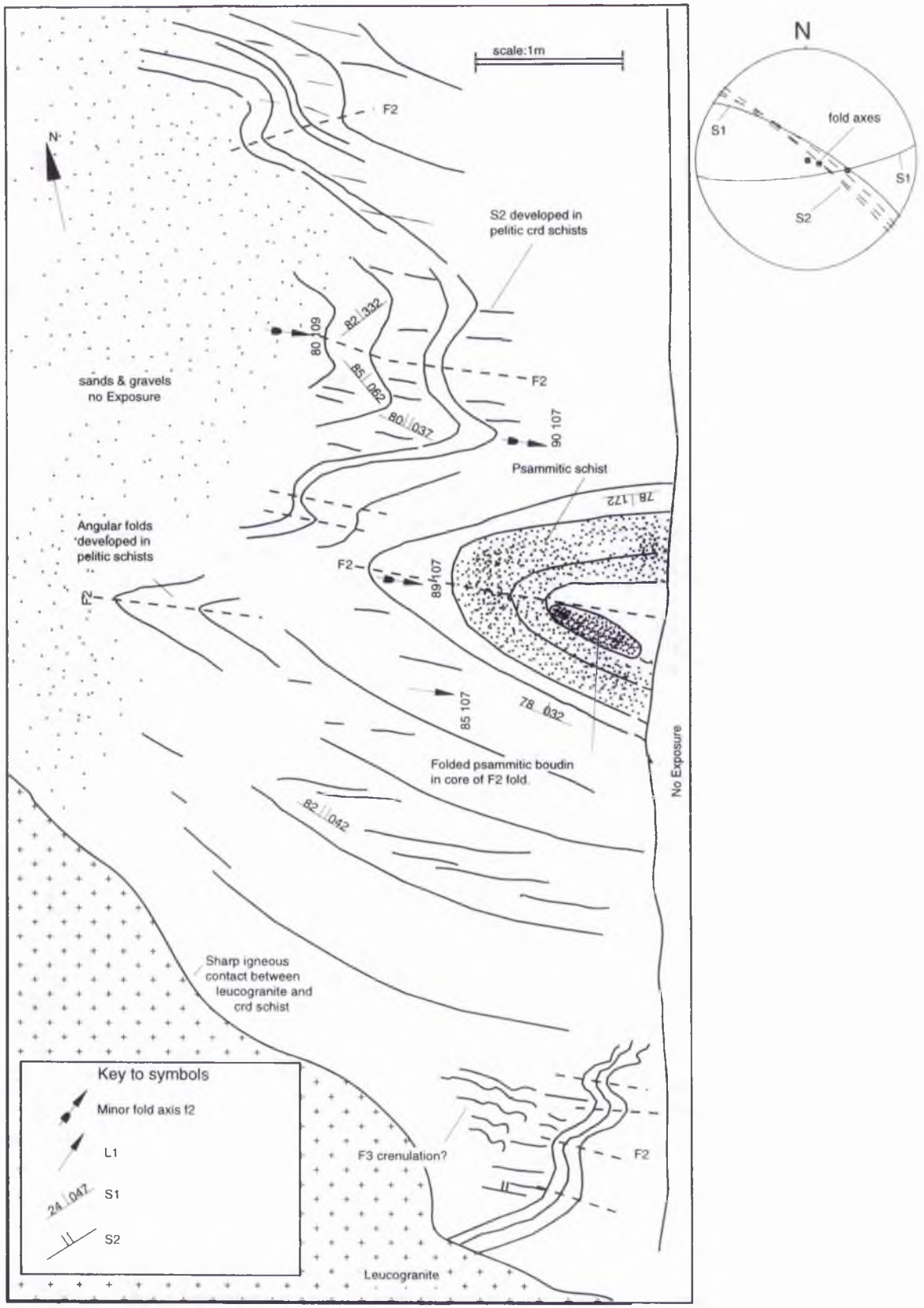

Figure 3.7 Map showing second order F2 fold outcrop at location N28.5 [6,5,0/5,8,0].

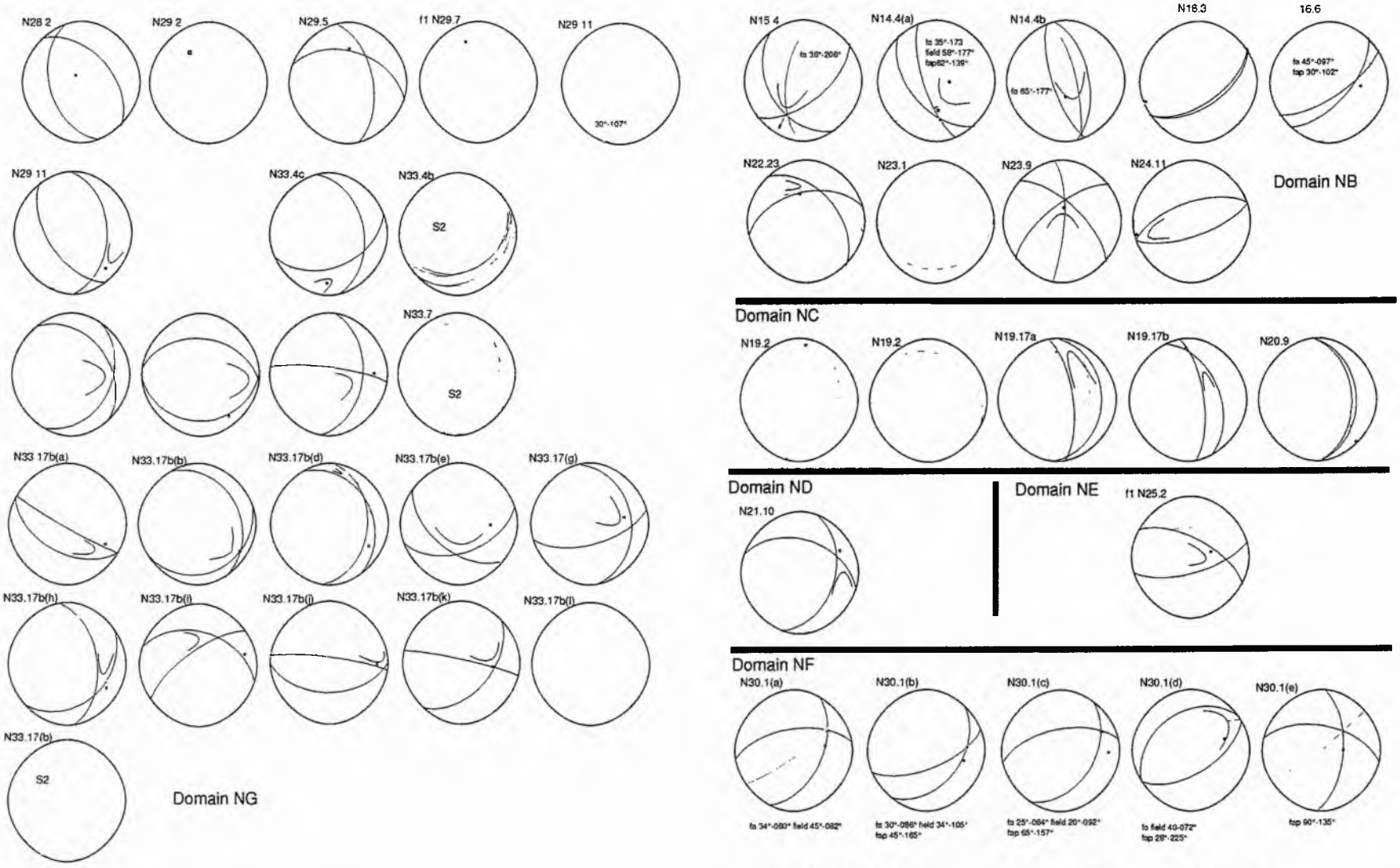

Figure 3.8 Selected mesoscale fold information plotted by domain as individual stereonets. Blue dashed great circles= measured S_2, red great circle= estimated axial plane (fap). purple= measured axial plane. Approximate interlimb angle indicated by solid black curves. All localities from Map 1.

3.5.1.ii The Karub Syncline

Observation of fold and lineation relations in the macroscale Karub syncline, domain N(G), are of great importance to the overall interpretation in this study. Barnes (1981) stated that refolded folds are present in this region in the Arises River Marble. The Karub Syncline, shown in Plate 3.4, was mapped at 1:5000 (1mm=5m) (Figure 3.9). The ~1km wide syncline is defined dramatically by the Arises River Marble. The structure is overturned to the south-west, the lower limb dips ~30° to the NE and the upper limb ~50° to NE. The axial trace is curvilinear. An offset is marked at point A in Figure 3.9. This may have occurred from flexural slip along S_0 and S_1.

Lineation and folding is well developed in the biotite-garnet schists of the Kuiseb Formation throughout the syncline core . The syncline closes to the NW, S_0 and S_1 are steep (>70°) in the transition from the lower limb to the upper limb, the axis of the closure is envisaged as non-cylindrical and 'cup' shaped (Figure 3.11 A&B). At depth the hinge zone axis is likely to become shallower (<60°). L_1 is steeper and more northerly trending around the closure of the Karub syncline (measured in the Arises River Member marble at 85°-026°) compared to the general east-west trend in the limbs. F_2 fold hinge orientations are sub-parallel to outcrop L_1 throughout the syncline and the mean axis trend.

It is notable that equal area stereoplot in Figure 3.1 N(G) shows that L_1 forms a weak girdle distribution around the π axis of the syncline (π=30°-108°). This may be diagnostic of reorientation common in shear folding (Weiss 1955), however, refolding of an early lineation should result in 'differently orientated lineations on fold limbs' (Ghosh 1993). A careful analysis of L_1 in the field, shown in Figure 3.10) reveals that L_1 trajectories are quite constant from the steeper (50°) north-western limb into the shallower eastern limb (30°). Furthermore, this is true at several positions in the fold core e.g. point (A) & (B). The only exception is at (C). Lineation here is preserved in the Arises River Member calcite marble. L_1 departs from the general trend recorded in pelitic units. This may be explained in two ways. Firstly, S_1/S_0 plunge over 80° in the fold core, therefore lineation has had to adjust to the evolution of the fold core, its trajectory does not necessarily indicate refolding, rather it is due to a greater strain in the steep fold core. Secondly, lineation at point (C) is recorded in calcite marble, the competence contrast between this and surrounding pelites may have resulted in differential strains and a steeper lineation trajectory. In either case it is clear that lineation is generally consistent throughout the Karub Syncline axis and not differently orientated across the limbs.

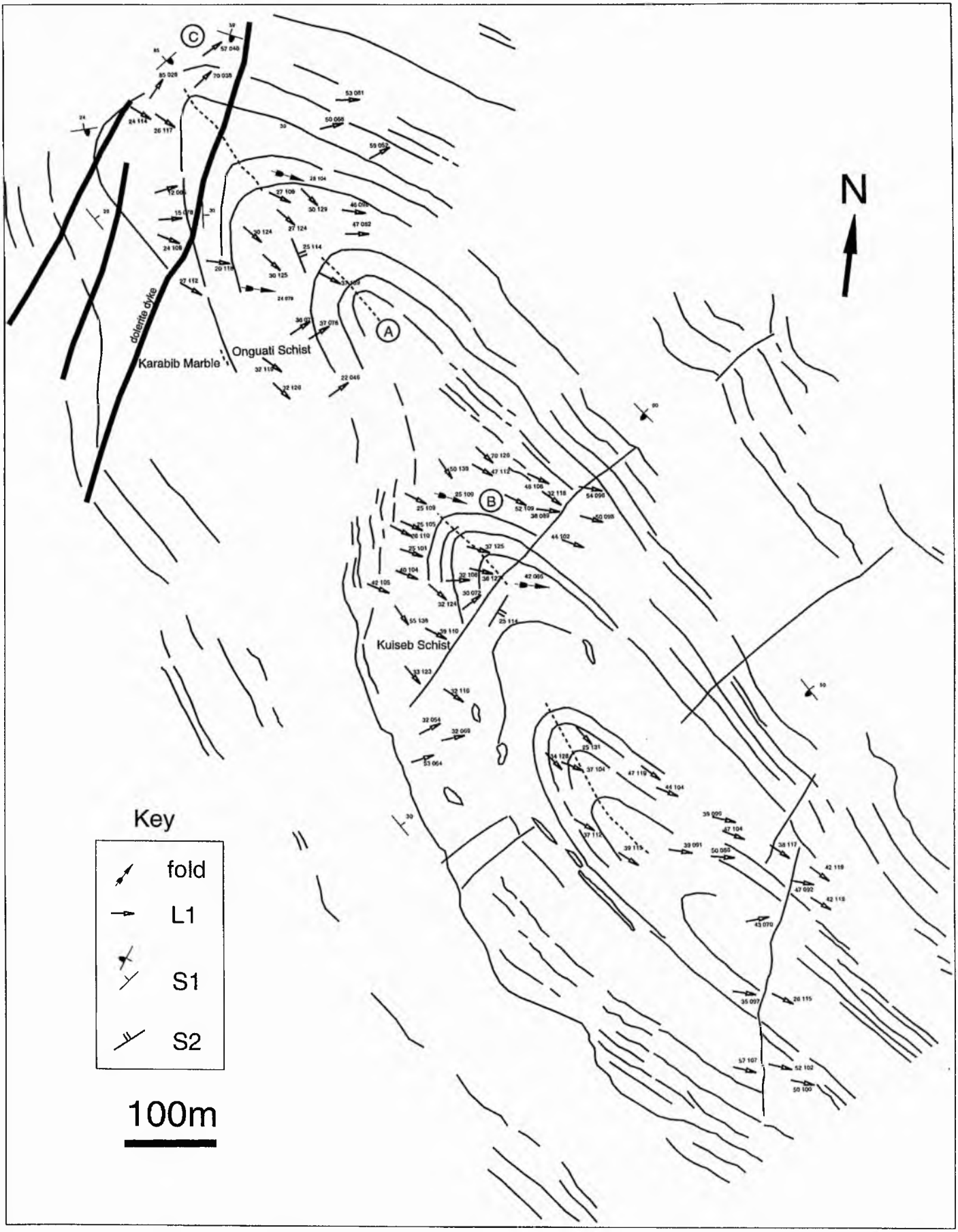

Figure 3.9 Structural map of the Karub syncline showing L1, selected S1 and F2C orientations

Plate 3.4 Aerial Photograph of Karub Syncline. Taken with 50mm lense from 10 000ft.

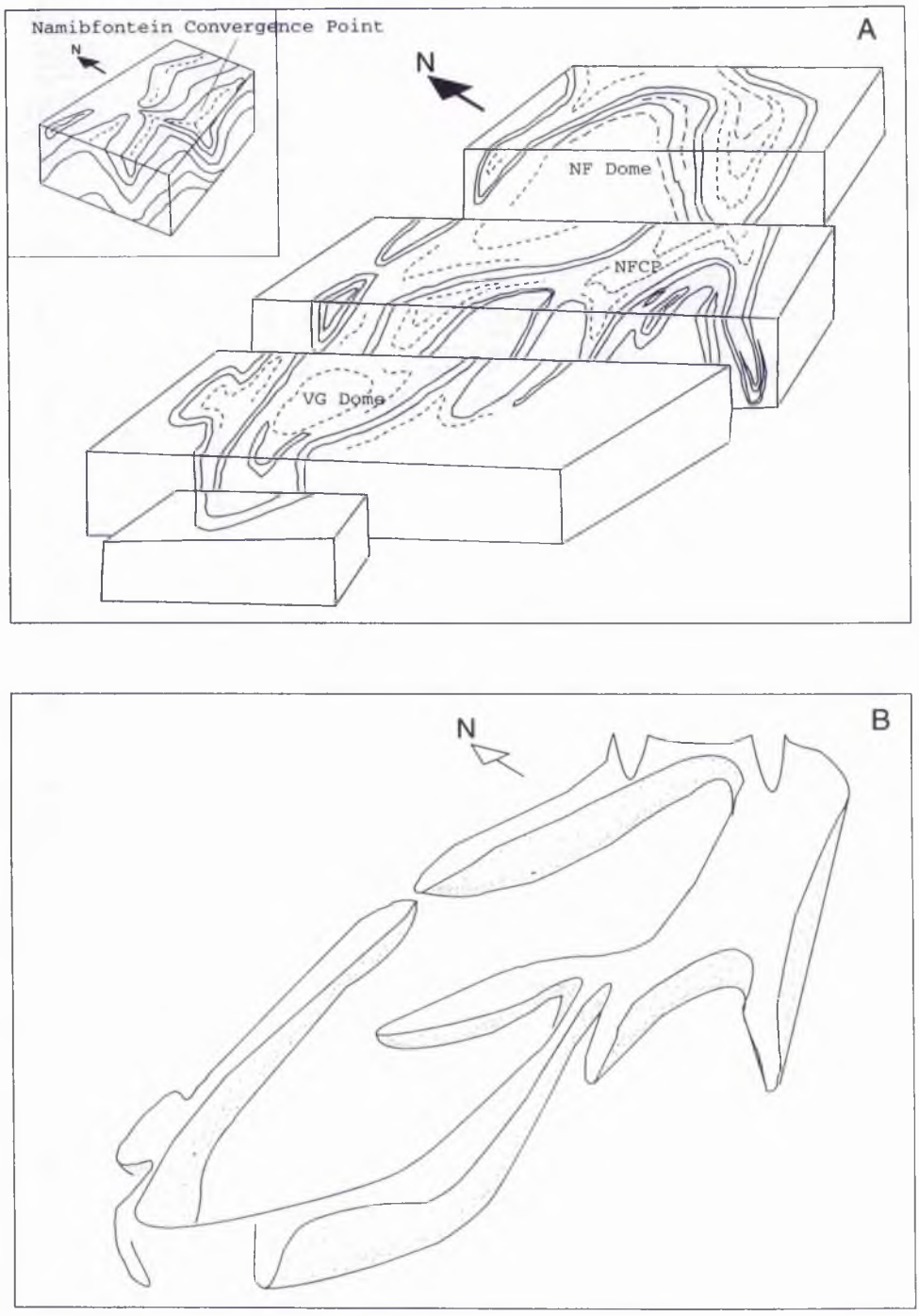

Figure 3.10. Block diagram to show the interpreted 3 dimensional geometry of the geological structure of the Namibfontein and Vergernoeg domes. The Namibfontein Convergence point is shown in upper right inset by converging dashed lines.

Figure 3.11 A Block diagram to show non-planar nature of the cover envelope around the Namibfontein and Vergenoeg domes. Note the 'cup' shaped morphology of the Karub Syncline

3.5.1.iii Pre-Damara folds in the Namibfontein area

Mesoscale folds in pre-Damara basement gneiss are distinct geometrically from those in the cover. Folds in this setting are confined to two outcrops; the first, at N47.1 [MAP 2] in the Vergenoeg Dome, and the second at GR[070,088]N18.4, in the north-east portion of the Namibfontein dome. In the first location, shown in Plate 3.5a, small 10-20cm mesoscale irregular isoclines were found parallel to basement S_{1B}. Although this fabric (S_{1B}) is parallel to S_{1C} (in the cover) there is no observable evidence of compositional layering S_0. The main fabric observed is the S_1 Pan-African fabric, however, assuming a pre-Damaran age it is chronologically a composite second generation tectonic fabric. (Plate 2.5 also shows a evidence of a refolded pre-Damaran fabric). To avoid confusion the terms (S_{1B}) for the basement and (S_{1C}) for the cover are used .

In the second location, N18.4 in domain N(C), mesoscale folds were found in large *c.* 20m long rafts of coarse sillimanite gneisses between the twin granite koppies (Figure 3.12). These folds form at least two complex fold interference patterns. Plate 3.5a, for example, shows a crenulated schist with crenulation hinges that are open to tight which form type 3 interference patterns (Ramsay 1987b). Observation of four minor folds in this area (Figure 3.12) demonstrate that fold axes plunge gently to the east and north-east.

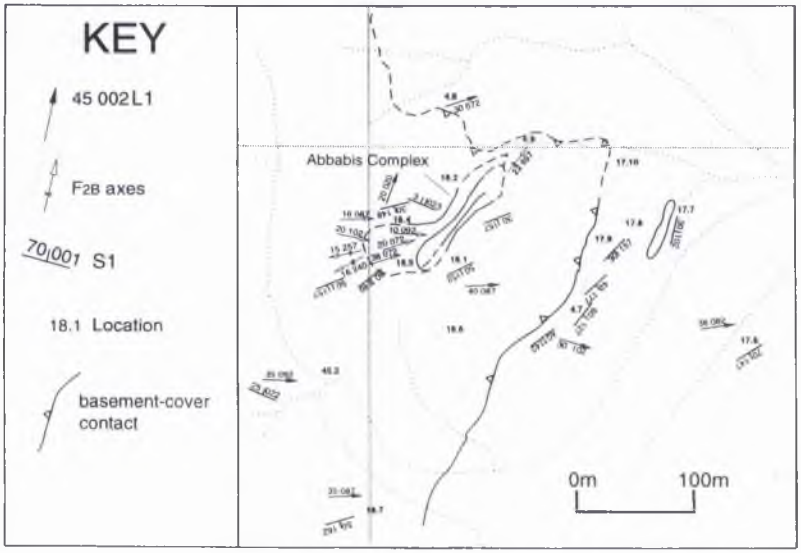

Figure 3.12 Map of area containing F2b folds preserved at location N18.4. (dotted lines=dry stream sections ,vertical grey line=north grid lines from MAP 1)

Despite the complex superposed deformation here, a geometric relationship to the macroscopic structure appears likely as fold hinge orientations mapped in this location are within < 10° of the outcrop lineation and Damaran trend. This is interpreted as fold hinge reorientation during Damaran deformation and overprinting.

Plate 3.5a. Mesoscale pre-Damaran isoclinal fold preserved in basement Bt+Kfs+Pl+Qtz+Sil gneiss, location N47.1 MAP 2.

Plate 3.5b Crenulated Kfs+Bt+Sil+Qtz gneiss preserved as rafts in post-tectonic damara red granite, location N18.4 showing type 3 interference. View looking north-east.

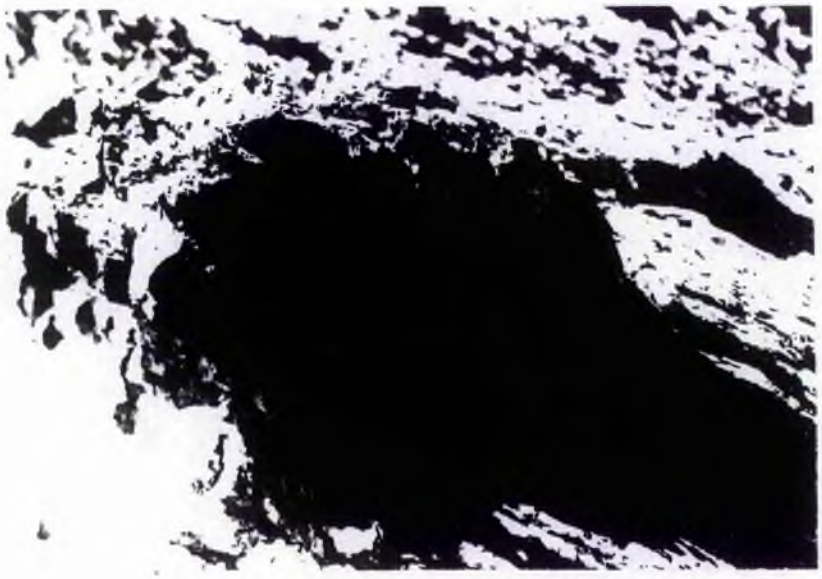

Plate 3.5c Crenulated Kfs+Bt+Sil+Qtz gneiss preserved as rafts in post-tectonic damara red granite, location N18.4.

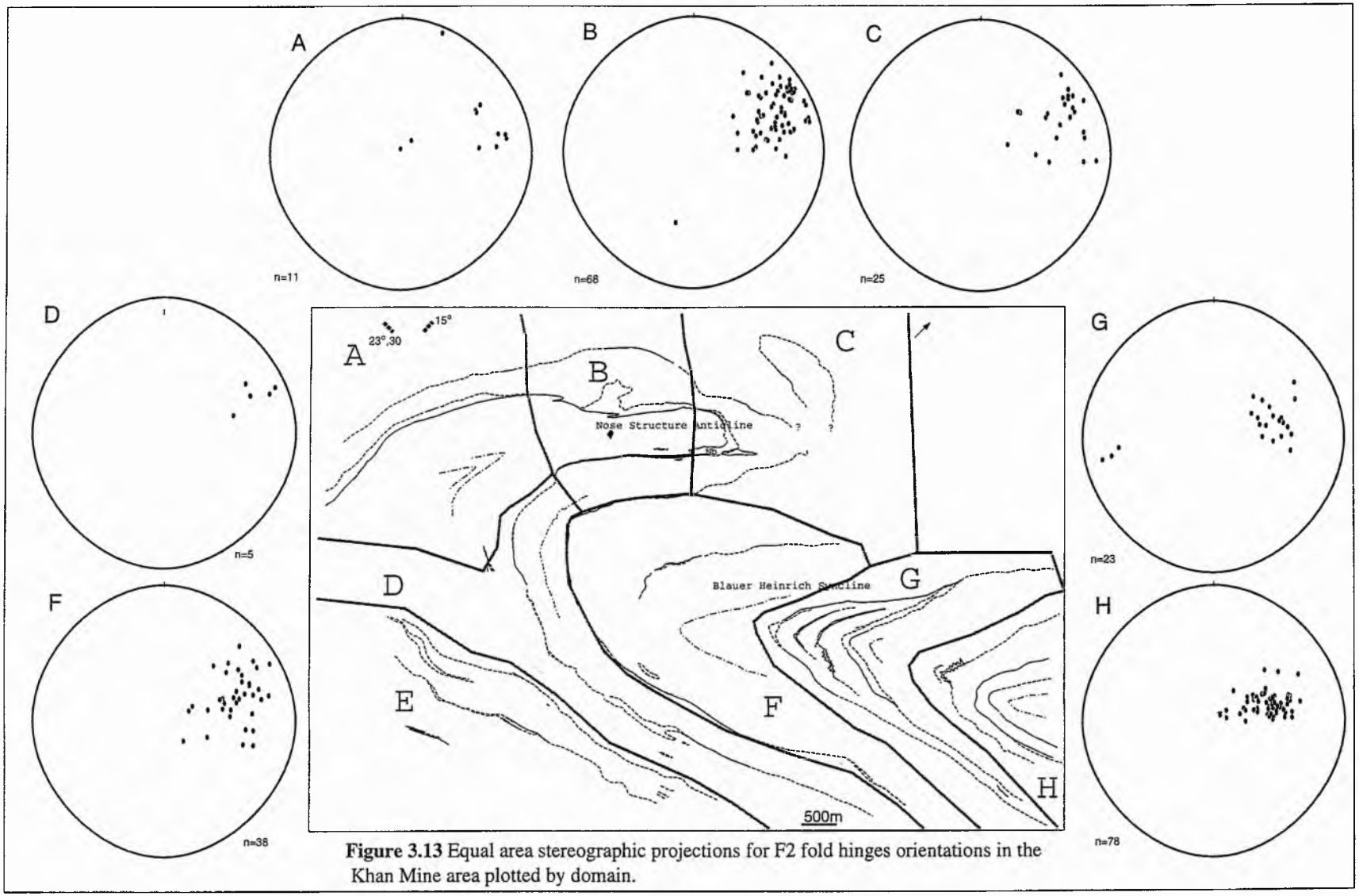

Figure 3.13 Equal area stereographic projections for F2 fold hinges orientations in the Khan Mine area plotted by domain.

3.5.2 Mesoscale folds in the Khan Mine area

There are four settings of folds in the Khan Mine area: equal area stereographic projections of representative F_2 hinge orientations in the Khan Mine area are plotted in Figure 3.13. Fold axes are observed to be parallel to sub-parallel to outcrop lineation and mean lineation shown in Figure 3.2. A comparison of L_1 and F_2 fold axes trajectories shows these data cluster closely around the domain π axes in all domains. Although most mesoscale F_2 fold hinges are parallel to L_1 their shape and style is quite varied. Most small F_2 folds are cylindrical, only a few are non-cylindrical and non-planar. Broadly, outcrops of F_2 folds correspond to the same settings as those of the Namibfontein area. An important additional setting contains folds that are non-cylindrical and non-planar folds developed locally at the basement-cover transition.

3.5.2.i Folds in the cover

The first setting falls within the cover, these are mostly synclinal areas which plunge moderately to steeply. Large order folds in the Blauer Heinrich Syncline commonly contain many metre-scale parasitic folds with broad based, 'M'- like, hinges parallel to outcrop lineation. These are evident along the Rössing-Chuos Formation boundary at Location K34.1, GR [061,039], and the Chuos-Karabib Formation boundary at K10.1[062,042]. Type examples are shown in Figure 3.14a (Plate 3.6) where two map-scale F_{2B} folds have been drawn from a series of second order folds that lie on the macroscale northern limb. The figure shows a *c.* 2m span syncline and anticline defined by folded S_{1C}+ S_0. Limb thickness in the profile plane is uniform, a weak secondary fabric is observed in fold cores. The folds are almost neutral with limbs parallel, S_1 dips ~060°, hinges plunge steeply to the north-east (~66°-067°), slightly less than the π axis (43°-074°) for domain K(H). All parasitic folds are sub-parallel to the larger fold axes. 500m further west the same relationship is shown by second and third order F_2 folds in the Kuiseb Formation in the Blauer Heinrich Syncline core (Figure 3.14b). It is clear that second and third order folds here are a result of progressive compression of S_1+S_0, line length restoration of bed A-A', which is parallel to the finite Y direction represents at least 38% inhomogeneous shortening. Detailed inspection here shows folds which have a range of interlimb angles (~70°-30°) with axial traces that are sub-parallel to the domain K(H) π axis. Commonly, the fold hinges are box like and plunge steeply to the north-east.

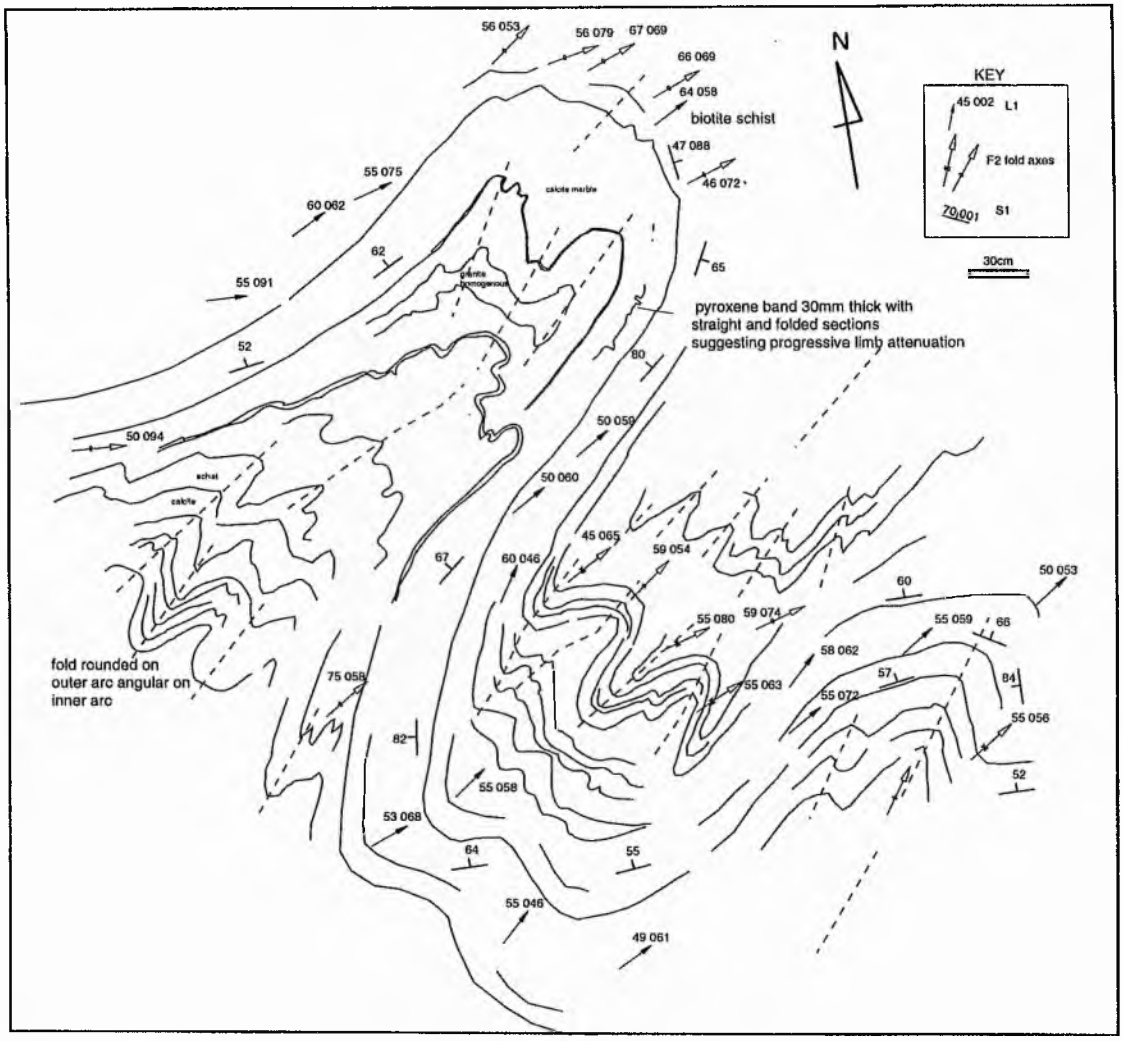

Figure 3.14a Plan view showing typical F2C folds at the core of the Blauer Heinrich Syncline at K10.1.

Plate 3.6 Photograph showing type fold. (Scale shown by note book). orientation Top=north, bottom=south.

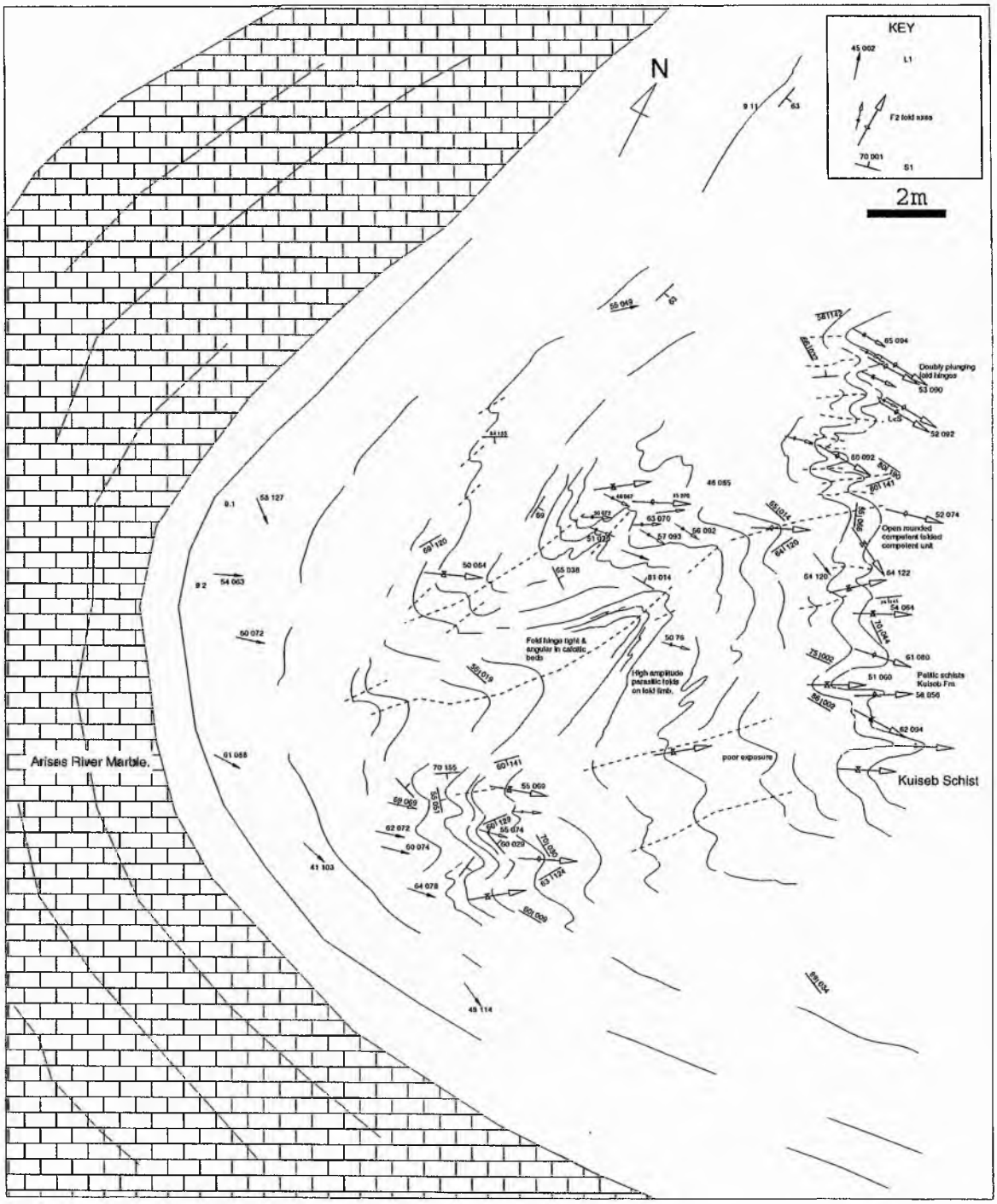

Figure 3.14b Structural map of Kuiseb Formation in the core of the Blauer Heinrich Syncline.

3.5.2.ii Folds near the basement-cover contact

In the second setting, marginal to the basement-cover contact, folds are dominantly tight curvilinear sheaths, notably at K26.11 GR[031,046] and K22.32 GR[021,040]. Figure 3.15 shows a spectacular example at location K22.32 with a tubular geometry (Skjernaa 1989). The tubular fold eye is parallel to L_1 and has a hinge angle < 20° (Plate 3.7). In addition, the fold pattern shows fold closures in the finite X Y and Z directions, these plunge gently at < 30°. These folds may be attributed to higher strains in this area where sheath fold type mechanisms have been able to develop. Tubular folds mainly develop in three ways: i) where the stretching of a layer perpendicular to the y axis of the finite strain ellipsoid has taken place ii) within sites of ductile simple shear and iii) constrictional environments (Kobberger & Zulauf 1995). The presence of prolate shaped sillimanite knots around these folds is suggestive of a constrictional setting in this case. It is significant that the regional geometry of the Khan Mine dome (see Section 6.2.3) resembles that of a tubular sheath.

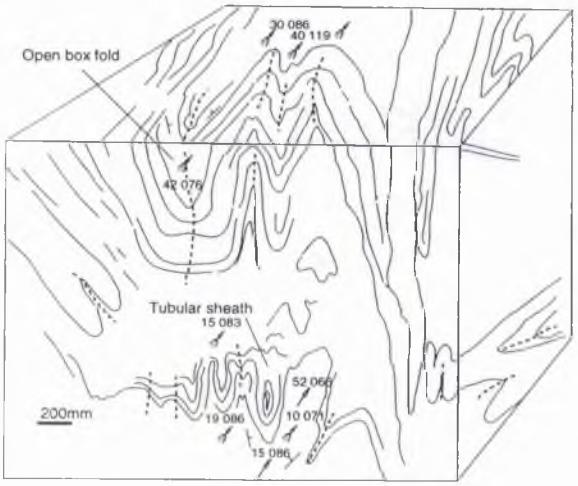

Figure 3.15 Block diagram showing 3 dimensional field sketch of tubular sheath fold development at Location K22.32

Plate 3.7 Photograph showing tubular fold eye (front face of Figure 3.15), at Location K22.32. View looking to the north-east, GR[021,040].

Over most of the basement-cover transition there are few folds. In addition to sheath, folds however, a small number of cylindrical folds were recorded at location K21.15 GR[026,053] (Plate 3.8), and K23.37 GR[017,039]. The folds are formed in quartz-rich Etusis schists, they have tight hinges, angular profiles and plunge gently to the east. Figure 3.16 shows the hinge orientations plotted on an equal area stereonet. In both locations they are dispersed symmetrically over an arc of ~90° along a great circle, the arc bisects the domain axial trend; this may be indicative of fold axis rotations in this region.

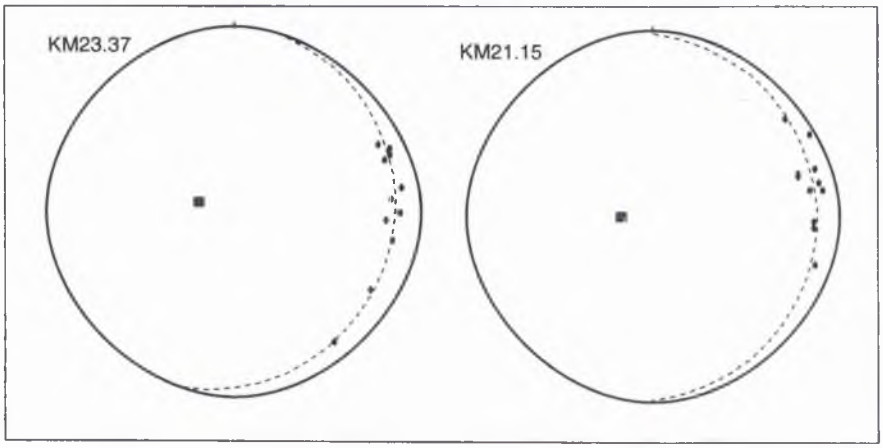

Figure 3.16 Equal area stereographic projections for F2 cylindrical folds at K23.37 and K21.15.

Plate 3.8. Photograph showing complex non-planar folds near the basement-cover contact at location K21.15.

3.5.2.iii Pre-Damara folds

This setting is confined to the Pre-Damara basement gneisses in domains K(A) and K(B), at the core of the Nose Structure Anticline. Foliation and lineation in these domains is the product of a strongly transposed pre-Damaran fabric, it is denoted as S_{1B} & L_{1B}. Understandably, remnants of pre-Damaran mesoscale folds are rarely found. Two areas were observed with clearly exposed pre-Damaran structures.

The first area, around location K29.1 GR[011,024]. Gneisses in this area exhibit a large number of fine scale crenulation axes (Figure 3.17a). Tight and isoclinal crenulations are bounded by S_{1B} typically spaced at 2cm. 50 axes plotted on an equal area stereographic projection, shown in Figure 3.17b cluster tightly with a statistical mean orientation of 42°-072°, approximately 17° anticlockwise of the mean domain L_1 (34°-089°).

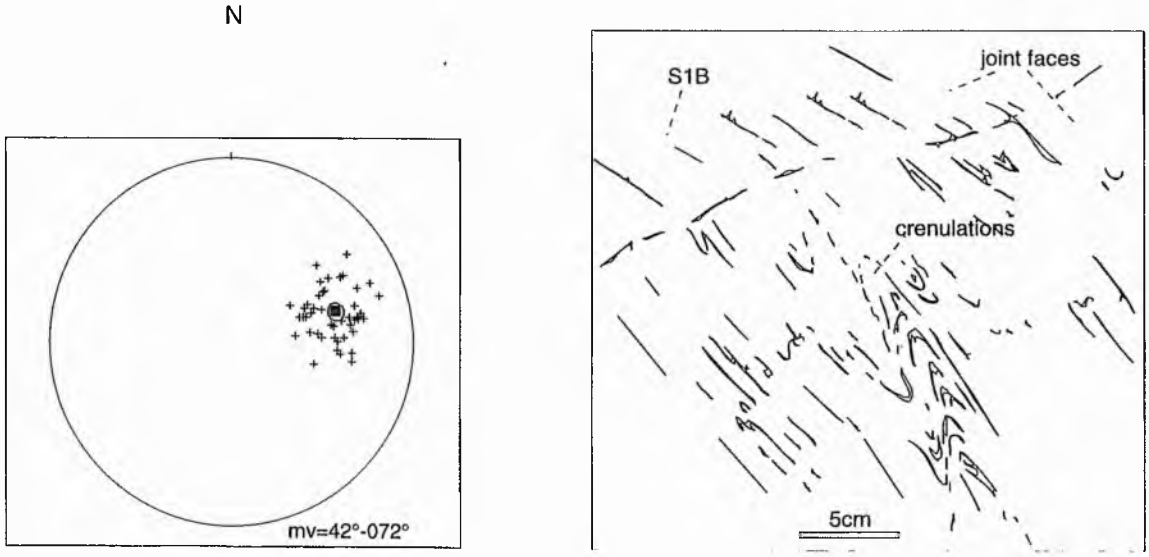

Figure 3.17a(RIGHT)Sketch of photograph showing medium and fine crenulations in basement Kfs+Bt+Pl+Qtz augen gneiss at location K29.1.

Figure 3.17b (LEFT) Equal area stereographic projection showing crenulation axis trajectories in basement gneiss at location K29.1.

Examples of larger 2-3m fold structures are also common in this area, notably at locations K27.9 & K29.3. Coincidentally this area corresponds to the *axial zone* of the Nose Structure Anticline. Location K29.3 GR[013,027], shown in Figure 3.18, exhibits a *c.* 2m long segment of an isoclinal fold. The axial plane of the fold is visibly curviplanar where S_{1B} forms a box like closure at the core of the fold. Parasitic monoclinal folds are present on the limbs. L_{1B}, defined by sillimanite on the surface of S_{1B}, plunges gently to the east and south-east.

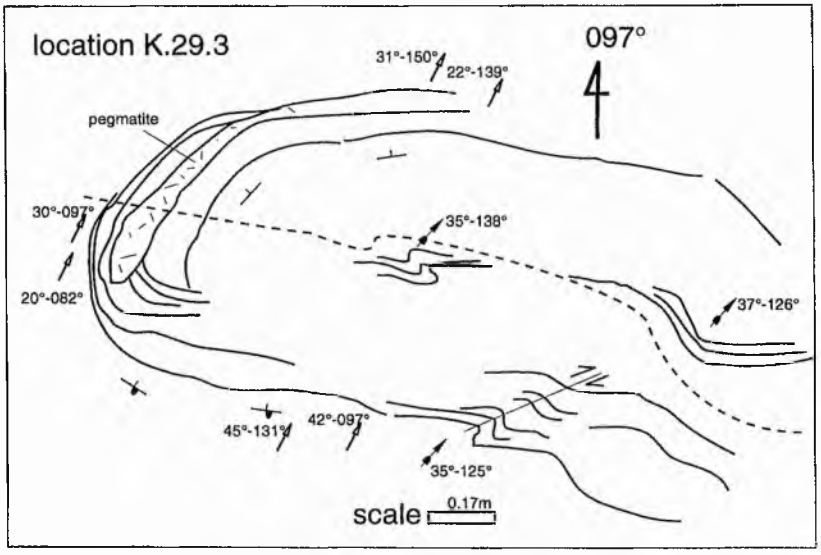

Figure 3.18 Cross sectional sketch to show metre-scale refolded isocline in the basement at location K29.3.

Seen towards 097°.

A second outcrop of mesoscale F_{2B} folds exists in this area at location K27.9 (Figure 3.19). S_{1B} is warped into an open and steeply plunging fold which spans 2m. S_{1B} exhibits centimetre-scale reclined and subhorizontal crenulations; larger parasitic folds are subparallel to the main open fold hinge (~ 74°-089°). A weak non-axial planar S_{2B} crenulation cleavage transects the folds dipping moderately to the south-west. Equal area stereographic projection in Figure 3.13 shows poles plotted for S_{1B} and mesoscale (*c.*<1m) F_{2B} fold hinge orientations. Poles to S_{1B} form a girdle distribution which has a β axis 31°-071°, pitching slightly shallower than the general trend of π axis for domain K(A) (π 41°-077°).

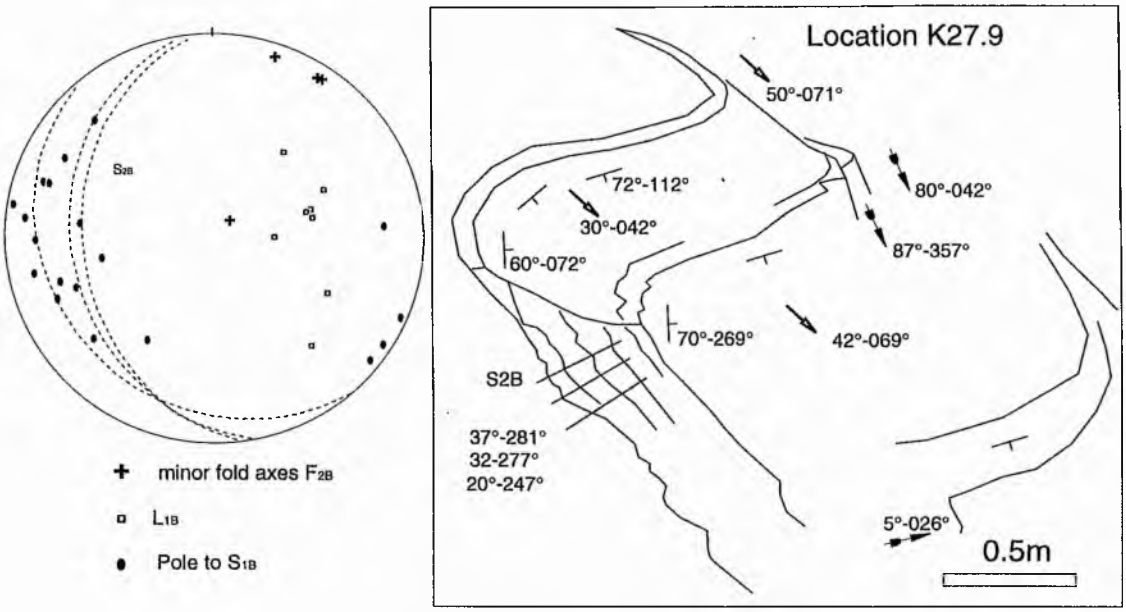

Figure 3.19 Cross sectional sketch of F2B fold segment from locality K27.9. Equal area stereographic projection shows structural elements S1 poles, L1, F2B hinges and S2B. View looking east-north-east.

Finally, pre-Damaran folds were mapped in a second area at location K20.5 GR[020,039], domain K(B). Figure 3.20 shows a series of tight angular to open rounded upright folds. Note that at point A the fold axial trace bifurcates suggesting tightening of an earlier recumbent fold. Both open and tight fold hinges plunge moderately to the north-east.

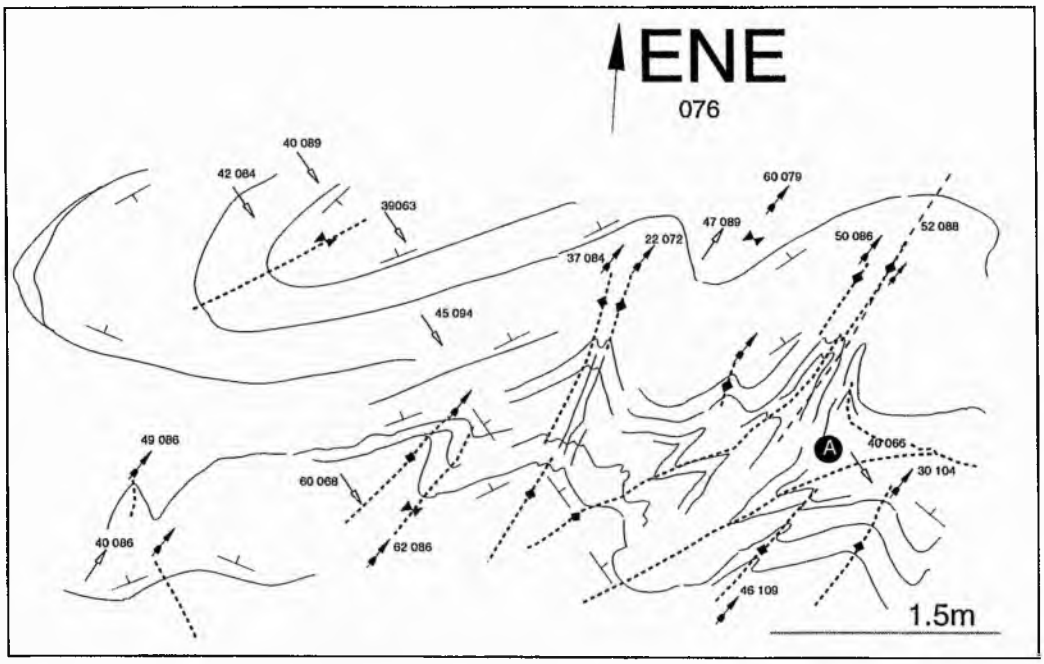

Figure 3.20 Cross sectional sketch to show complex F2B folds in the Nose Structure Anticline K20.5. (Blank arrows = lineation, black arrows = fold axes (plunge and azimuth), dashed lines= synformal and anticlinal axial traces. Viewed towards 076°.

The structural complexity of most fold geometries in this setting leaves little doubt that early pre-Damaran structures have been superposed by Pan-African tectonic events. Most fold hinges appear to have been rotated towards the main Pan-African L_1 trend, folding has resulted in at least two interference fold patterns. While it is tempting to suggest all fold patterns in this setting are the result of interference mechanisms it is also possible that some folds in the basement are contemporary with those in the cover. Deformation in the axial zone of the Nose Structure Anticline for example would most likely record the highest strain and, combined with initial fabric heterogeneity, could have produced fold forms quite diverse from the cover.

3.5.3 Summary of mesoscale folds

1. Overall three distinct fold settings have been recognised; folds are formed in the basement, near the basement cover transition and the cover.

2. Folds in the cover appear to have formed by i) flow with thickened hinges and attenuated limbs. ii) flexural slip folds in angular folded phyllosilicate rich layers iii) Buckle folding in some lower strained quartz-rich layers is rare.

3. In both study areas and all settings, fold amplitude decreases away from the core of synforms and antiforms.

4. Mesoscale folds formed in the basement are the result of sequential fold events. These folds show a range of interference styles.

5. All small scale folds are broadly sub-parallel to mean statistical domain lineation. D2 reorientation of an L_1 lineation seems unlikely given the absence of secondary lineation and sub-parallel relationship of L_1 to F_2. The similarity of F_2 orientation with lineation may have resulted from either strong migration of an early lineation or simultaneous fold hinge extension with mineral growth. Variation of fold hinge direction from the mean domain lineation is accounted for by poor discrimination between reorientated Pre-Damara folds in parts of domains N(E) & N(D). At least three mesoscale fold mechanisms have operated concurrently to form the variety of F_2 folds in the three settings described.

3.5.4 Secondary foliation and axial trace relationships

In most of the study areas crenulation fabrics and secondary fabrics associated with F_2 folds are sparse and poorly developed. S_2 data for the Namibfontein area are shown in Figure 3.19. This documents clearly that the orientations of S_2 and axial traces do not reflect a regional fold trend but rather mesoscale fold environments. This suggestion is also indicated by Figure 3.21 which shows S_2 data plotted as poles and 1% area contour plot, these show data scatter considerably over 180° between the south-east and north-west. However, at the domain scale, S_2 data shows a slight systematic orientation, for example in domain N(G) it is 45° to NE-ENE, in domain N(E) 45° to ENE and in domain N(D) 50° to NNE; the number of measurements precludes a precise estimation of domain trends. S_2 fabrics are not all axial planar: in parts of domain N(E) a second foliation transects the fold hinge clockwise by 10°.

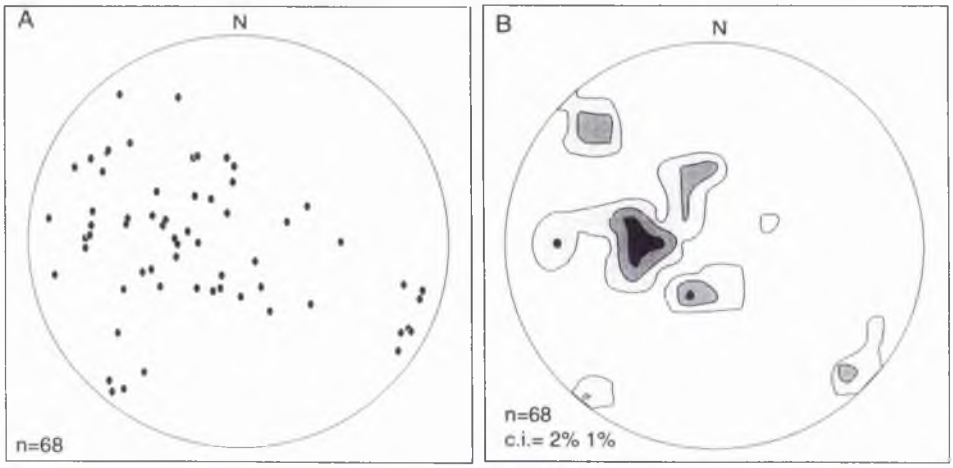

Figure 3.21 Equal area stereographic projection for all S2 data. Planes plotted as poles(A) 1% area contour plot (B).

Two conclusions may be derived from S_2 data. Firstly that secondary foliations did not necessarily form everywhere at the same time from a strong D2 event because S_2 development does not have a consistent regional orientation (Refolding of S_2 by a subsequent deformation is unlikely since L_1 which predates S_2 is consistent). They formed by a mechanism that created inhomogeneous strain and diverse fold orientations. Secondly, S_2 fabrics are not always axial planar to folds.

3.6 Qualitative Strain Analysis

Understanding of the regional strain environment is fundamental to the discussion of a model of dome formation. This section documents qualitative descriptions of finite strain type by means of shape analysis from various strain marker data; these were mostly pebbles and porphyroblasts measured as simple axial lengths (x:y:z), Plate 3.9 shows a typical pebble from the Chuos Formation and Plate 2.17 (see Chapter 2) Crd from the Kuiseb Formation.

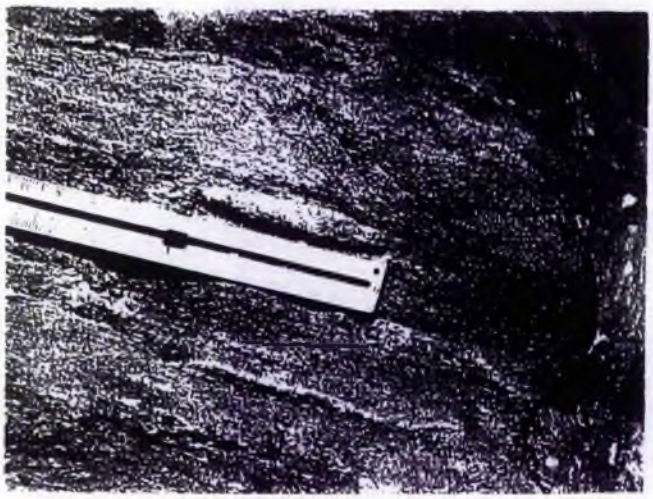

Plate 3.9. Photograph showing typical strained pebble from the Chuos Formation.

3.6.1 Flinn Plots

Initial qualitative estimation of finite strain type in the study areas is made by reference to a series of conventional linear Flinn diagrams (Flinn 1956 & 1965), these are shown in Figure 3.22a-e. Flinn diagrams represent three basic strain types by plotting the ratio (a=x/y) as ordinate and the ratio (b=y/z) as abissca, points lie either above or below the line a=b; prolate shapes lie above the line a=b and oblate shapes below. The plotted points on the diagrams are taken from the axial lengths of pebbles, Sil knots and Crd knots in the cover and Kfs augen shapes in the basement. These show a range of shapes, but generally indicate constrictional prolate strains. In the Khan Mine area most values cluster in the constrictional field; in the Namibfontein area values spread across both the flattening and constrictional fields.(These are discussed in detail in Section 3.6.3).

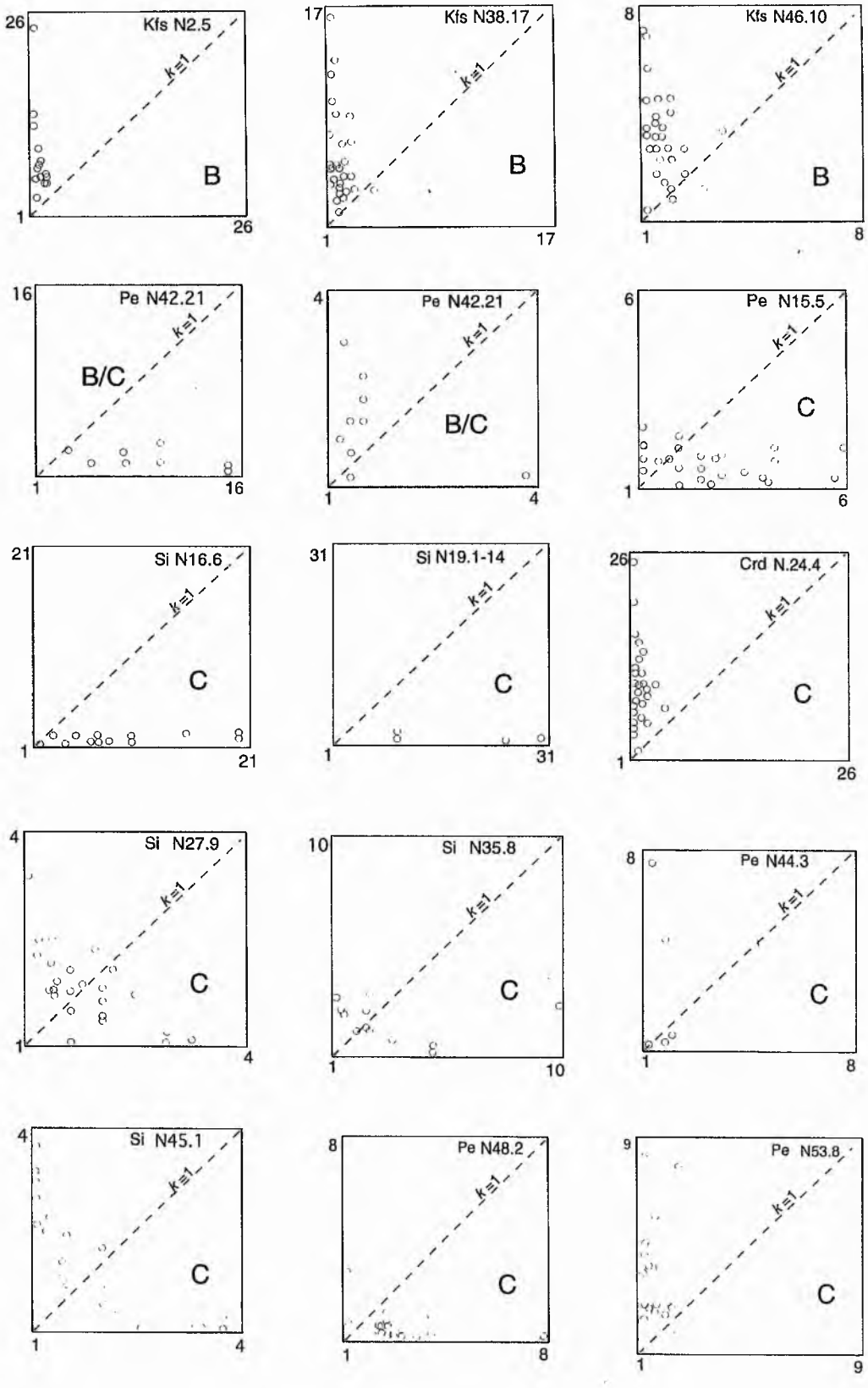

Figure 3.22a Linear Flinn Plots for the Namibfontein area shown for three settings by location. B=basement, B/C=basement-cover transition, C=cover. Strain marker types: Pe=pebbles, Si= sillimanite knot, Crd= cordierite knot, Kfs= potassium feldspar augen.

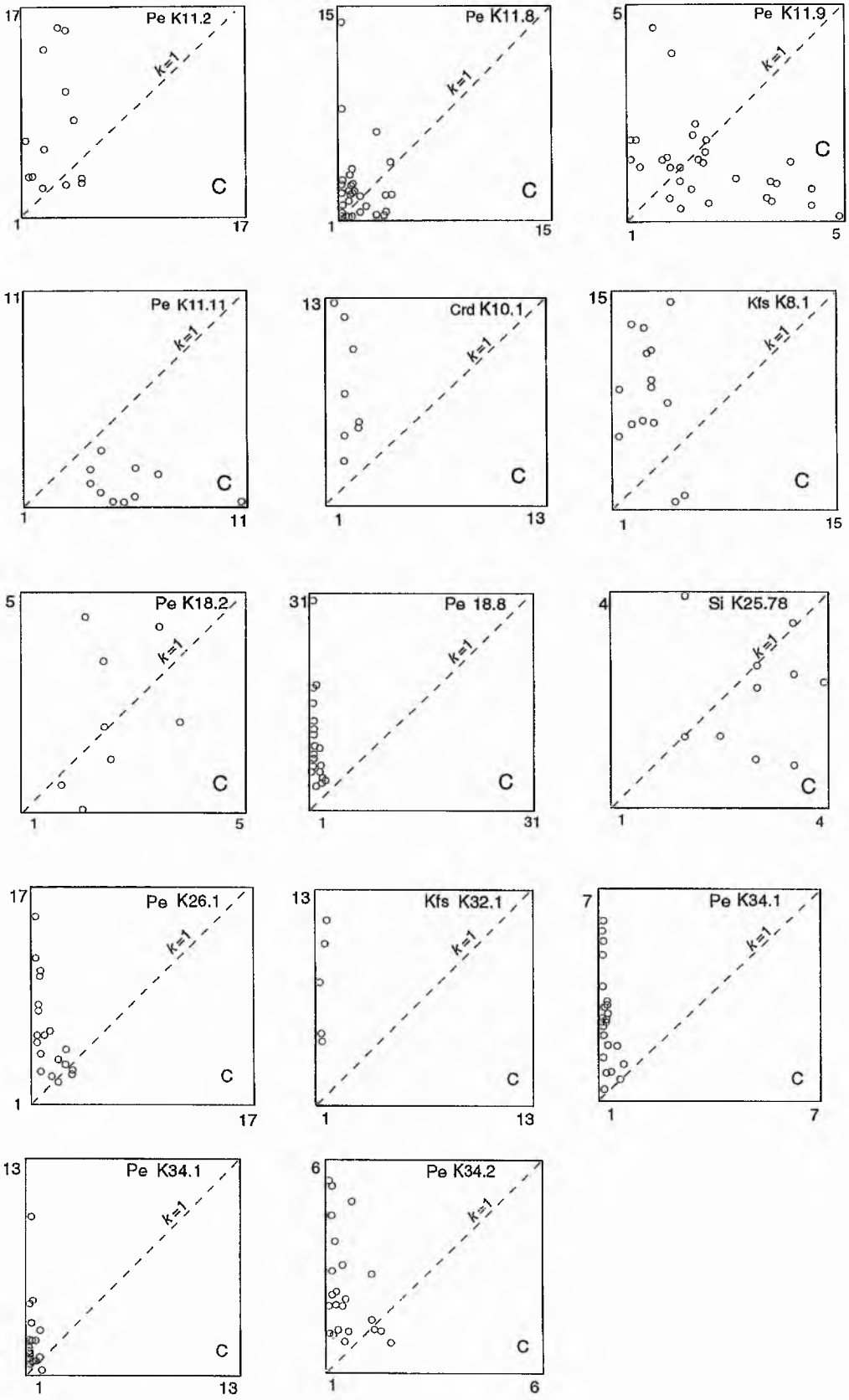

Figure 3.22b Linear Flinn Plots for Khan Mine area shown for the cover (C) by location. Strain marker types: Pe=pebbles, Si= sillimanite knot, Crd= cordierite knot Kfs= potassium feldspar augen.

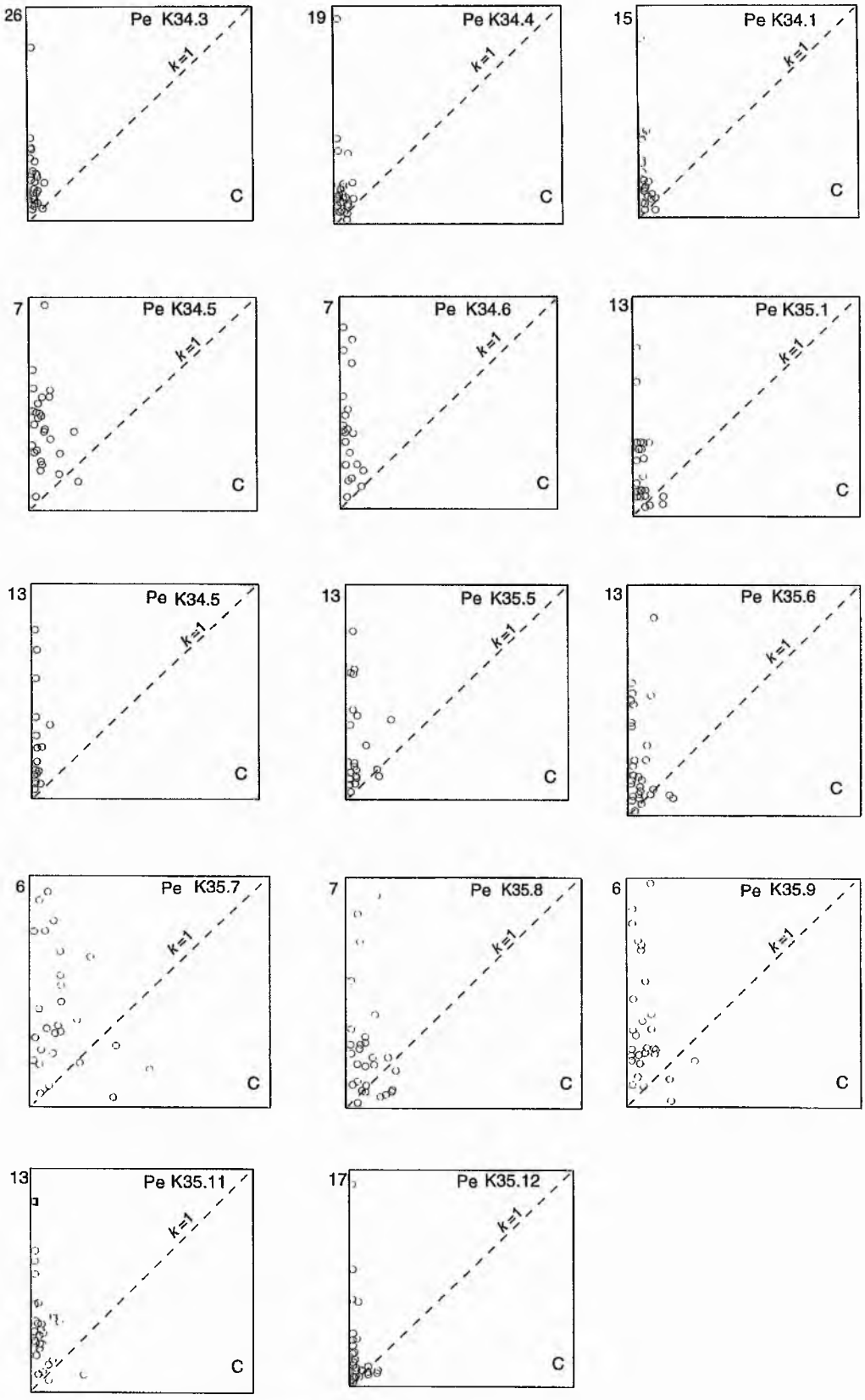

Figure 3.22c Linear Flinn Plots for Khan Mine area shown for the cover (C) by location. Strain marker types: Pe=pebbles, Si= sillimanite knot, Crd= cordierite knot Kfs= potassium feldspar augen.

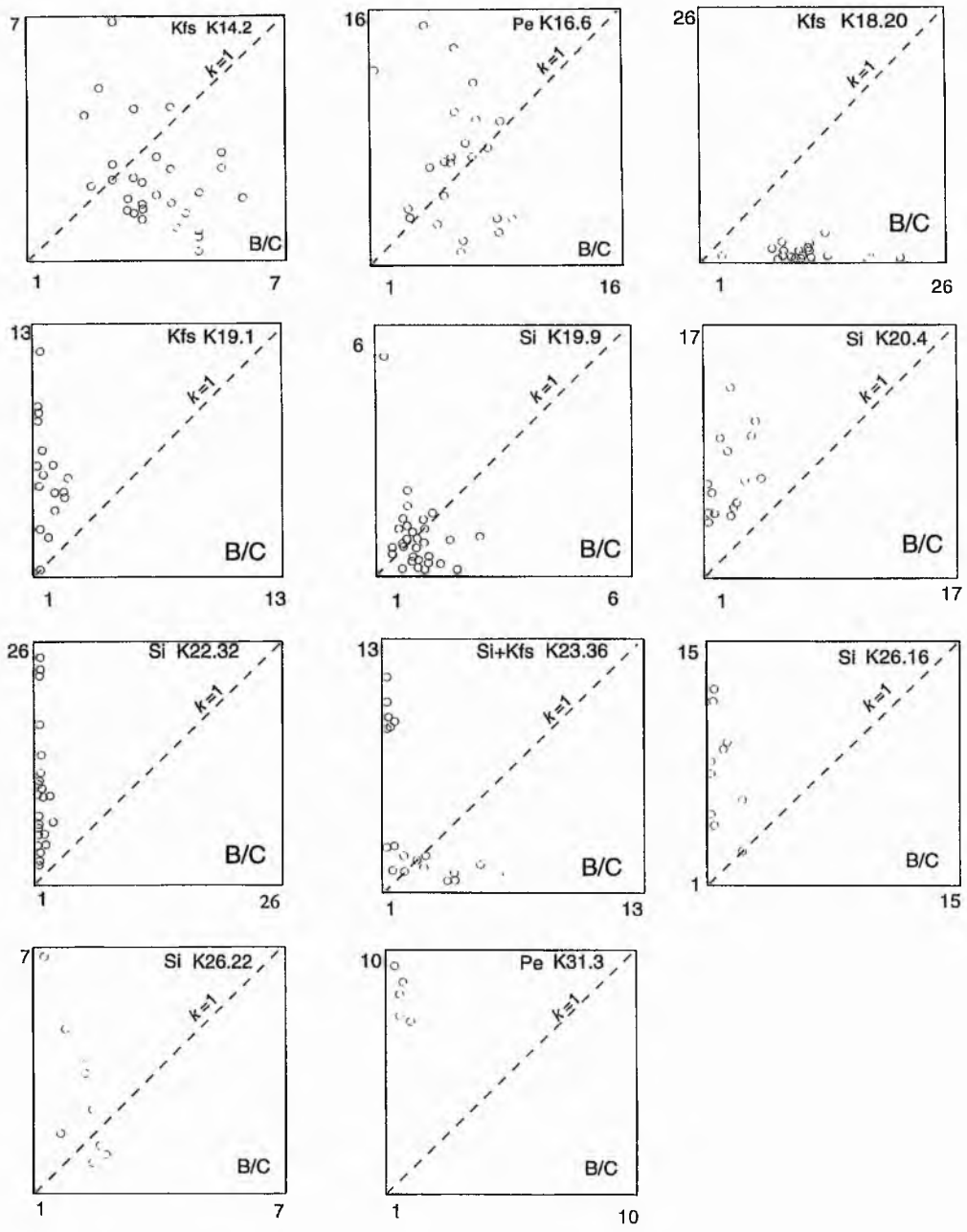

Figure 3.22d Linear Flinn Plots for the Khan Mine area basement-cover transition (B/C) shown by location. Strain marker types: Pe=pebbles, Si= sillimanite knot, Crd= cordierite knot Kfs= potassium feldspar augen.

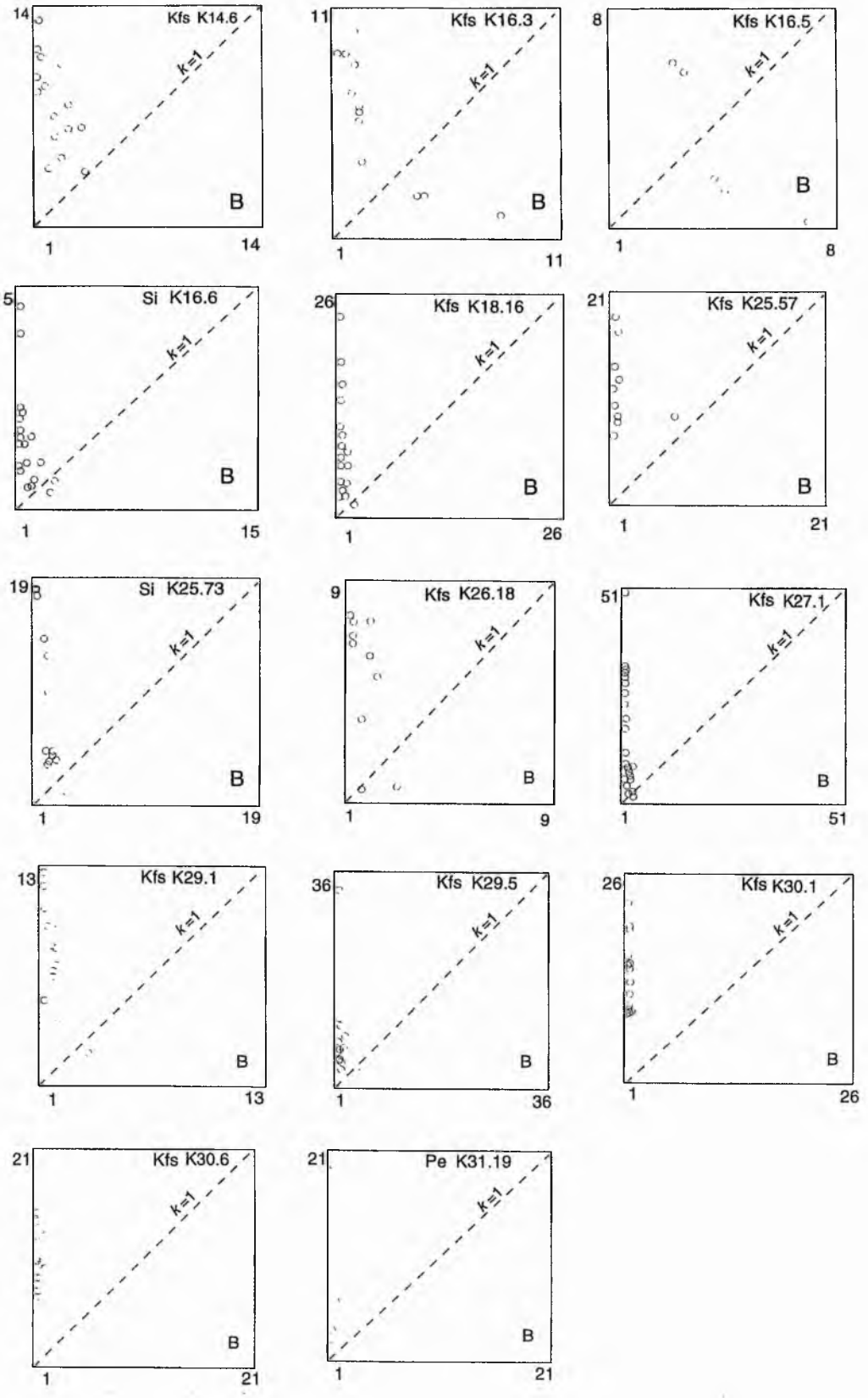

Figure 3.22e Linear Flinn Plots for the Khan Mine area basement (B) shown by location. Strain marker types: Pe=pebbles, Si= sillimanite knot, Crd= cordierite knot Kfs= potassium feldspar augen.

3.6.2 Fabric Analysis

For each outcrop fabric was assessed visually according to the classification scheme of Flinn (1965). Fabric is defined as the 'geometric organisation' (Ramsay & Huber 1987a) of structural elements S_1, S_0 and L_1 i.e. 'L' and 'S' components. These observations are shown on both main maps using the five categories of Schwerdtner *et al.* (1977): L, L>S, L=S, L<S, and S. In the cover mixed, planar-linear (L=S) and linear-planar (L>S) fabrics are most common, they exhibit a strong alignment of metamorphic minerals. In some areas deformed pebbles form an integral part of the tectonic fabric; their long axes are always parallel to sub-parallel to L_1 on S_0 and S_1 surfaces. Rock fabrics in the cover range from L to L=S. In contrast to the cover, linear (L) and (L>S) fabrics are dominant in basement outcrops (mostly at dome cores). This suggests that finite strain in the basement has produced linear fabrics. An absence of primary 'S' surfaces in the granite protolith (Kröner *et al.* 1991) may have facilitated the predominance of L fabrics. Qualitative observations of mixed L-S fabrics are supported by the spread of points in Flinn diagrams.

3.6.3 Regional *k*-value variation

In order to show the spatial variation in finite strain type within the regional structure axial length data (x:y:z) were used to calculate Flinn's *k* parameter:

$$k = \frac{R_{x/y} - 1}{R_{y/z} - 1} \qquad \text{(from Ramsay \& Huber 1987a)}$$

k-values were calculated for every strain marker at each location, values correspond to five shape types; ($k = 0$) uniaxial oblate, ($1 > k > 0$) general oblate, ($k = 1$) boundary prolate-oblate, ($\infty > k > 1$) general prolate and (∞) uniaxial (perfect) prolate. The mode shape is represented by five ellipse types shown in Figures 3.23a & 3.23b, in this way finite strain type from the plots in Figures 3.22a-e can be represented in meaningful manner. Each ellipse is orientated to show the statistical mean orientation of the finite X-direction, this was computed from stereoplot analysis of x axis pebble orientations (see Appendix 3.2). Composite strain shapes are shown in locations where a more or less equal spread of *k*-values exists between two types.

Observation of the *k*-value map for the Namibfontein area (Figures 3.23a) shows that general prolate shapes are more widespread than oblate shapes although it is evident that general oblate-prolate strains exist all around the Namibfontein dome. Prolate strains are indicated at the core of the Valencia dome and also at the Namibfontein Convergence Point. The orientation of finite X-direction is moderately consistent trending north-east south-west and plunging moderately to the north-east.

In the Khan Mine area (Figure 3.23b) prolate strains are ubiquitous in and surrounding the Nose Structure Anticline. Only a small area of oblate strains occurs, this is at the junction of the cover and basement gneisses in the south west core of the Blauer Heinrich Syncline (K25.78); a sub-area of $k<1$ is contoured in Figure 3.23b. This probably occurs because S_1 in this area is steep and almost perpendicular to the bulk regional X-direction.

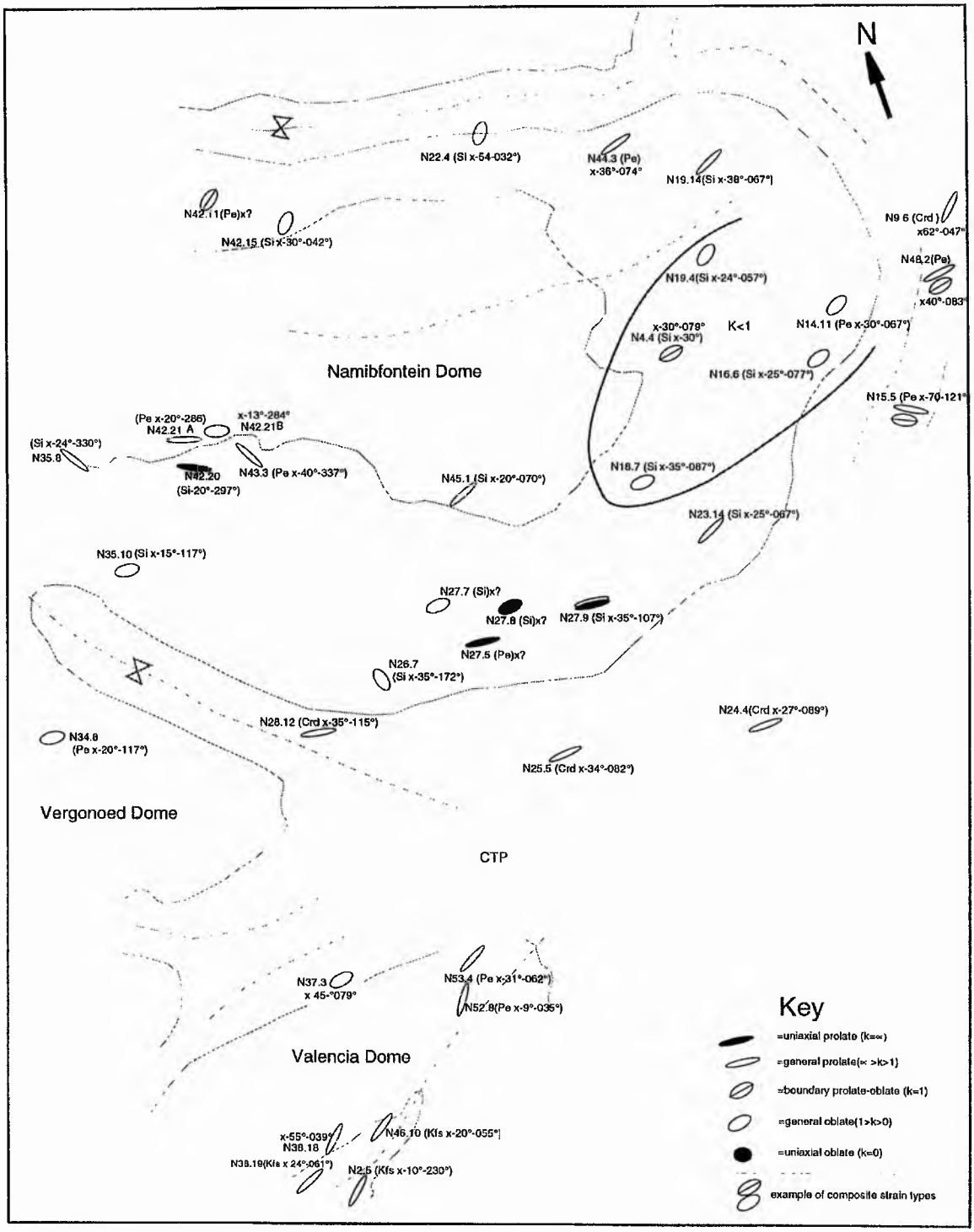

Figure 3.23a Schematic map representing finite strain type in the Namibfontein area with mean *k* parameter values.

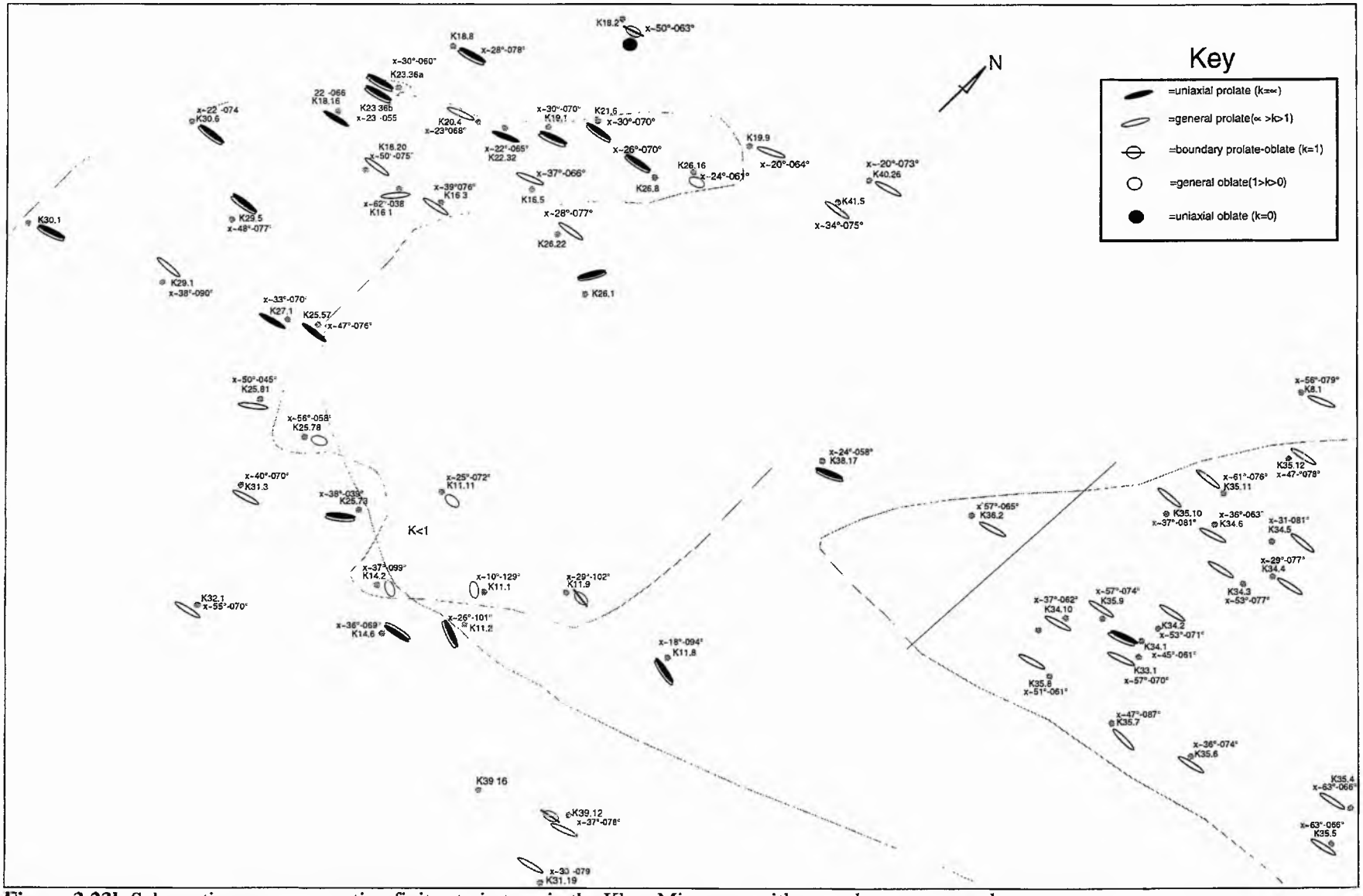

Figure 3.23b Schematic map representing finite strain type in the Khan Mine area with mean k parameter values.

3.6.3.i Limitations of *k*-value method

It is conceded that observation of mineral porphyroblast shapes is not an ideal means of finite strain determination; however cordierite, sillimanite knots and Kfs-augens all tend to show 'general prolate' shapes; furthermore, pebbles commonly form perfect uniaxial prolate shapes. Therefore, overall porphyroblasts and deformed pebbles suggest finite general constrictional strain. Field samples cut in the y/z and x/y planes do not reveal cross cutting cleavages and suggest that $k > 1$ & $k = \infty$ shapes were the result of a single deformation and not the superposition of two separate flattening deformations; if two deformations did occur the primary fabric appears to have been obliterated. The presence of oblate shaped pebbles may be due to matrix flow or perhaps more likely, due to the inhomogeneous nature of strain. Alternatively some pebbles may record original shape (this is discussed in Section 3.7.1.i).

In summary, constrictional fabrics are ubiquitous in both areas indicating shortening in two directions of the finite strain ellipse occurred in the Central Zone. This strain regime corresponds to Ramsay's (1967 Figure 3.54) field 3 ($\lambda_1 > 1 > \lambda_2 > \lambda_3$), where λ_1 is the principle strain. A finite constrictional strain of the bulk crust therefore occurred, a general 44-55° plunge of the X-direction of most strain markers suggests moderately plunging extension within a moderately plunging constriction field.

3.7 Quantitative and Semi-quantitative strain analysis

Quantitative estimates of finite strain intensity are made from laboratory study of fold profiles, boudinage and pebble data. Results are presented from:

i) elongation and shortening from pebble axial ratio measurements.

ii) R_T ratio from R_f/ϕ analysis

iii) R_s strain ellipses from fold profiles and

iv) minimum extension (e) from boudinage structures

3.7.1 Finite strain determination from deformed pebbles

A simple approximation of bulk finite extension and finite shortening has been attempted from the measurement of pebbles around the dome structures in both areas. In the Khan Mine area pebbles are found commonly in the Chuos Formation around the Blauer Heinrich Syncline and less commonly in the Khan Formation and Rössing Formation. Approximately 30 pebbles per location were used in the method adopted from Anhaeusser (1969a). The method is only semi-quantitative as it assumes the following: that no volume change has occurred in the pebbles, that initial shape is spherical and that quartz pebbles and quartzo-feldspathic matrix have negligible viscosity contrast. The method is very simple, its use may be justified when pebbles have such high axial x:y ratios (*c.*1:50) that the effect of original clast shape is comparatively very small. Orientation of the pebble major axes (x) is in every location is sub-parallel to mineral lineation. The fluctuation determined from R_f/ϕ plots is generally low < 20° (*cf.* Hutton 1979) (see Section 3.7.2). Equation (1) below was used to obtain volume (mm^3), equation (2) to calculate the radius of the original pebble and equation (3) to calculate an initial diameter of the original pebble. The tectonic strain ellipse (e1+e2+e3) is then calculated by comparing the initial diameter to the deformed state; reducing the x:y:z ratios to unity (*cf.* Heubeck and Lowe 1994). The results are listed in Appendix 3.3.

$$\text{volume } (V) = \frac{(4\pi)\times(\frac{xyz}{2})}{3} \quad (1)$$

$$\text{radius}^3\ (r^3) = \frac{V}{\frac{4}{3}\pi} \quad (2)$$

$$\text{diameter of initial sphere } (1^0) = \sqrt[3]{r^3} \quad (3)$$

Figure 3.24a shows the range of values finite strain e1+e2+e3 obtained in domains K(G) & K(H) around the Blauer Heinrich Syncline. The highest value obtained, in the core of the syncline at the Chuos and Karabib junction, was 3.38(e1), the lowest value along this junction was 2.38(e1). This suggests that higher strain is recorded at the fold core. Mean values of strain throughout the Chuos, where 1=unity (undeformed state) are: 2.55 (e1), 0.80 (e2) and 0.65 (e3).

Estimates of finite strain magnitude made from pebbles in the Khan Formation are shown in Table 3.3. Values are more varied than those shown in Figure 3.24, values of (e1) are similar except for locations K8.1GR[060,051] and near K18.GR[016,045] in domain K(B) and location K11.2/3 GR[034,019] in domain K(F). It is notable that these high values are near to the basement-cover transition. Mean oblate ellipses (k<1) are recorded near the junction of the cover and basement gneisses in the south-west core of the Blauer Heinrich Syncline supporting the idea that deformation was inhomogenous (see Section 3.6.3 Figure 3.23b).

	domain	e1	e2	e3	k
K8.1	K(G)	5.88	0.80	0.25	6.04
K11.2/3	K(F)	5.36	0.80	0.29	5.31
K11.8	K(F)	2.62	0.95	0.48	1.26
K11.9	K(F)	2.10	1.08	0.48	0.49
K11.11	K(F)	2.79	1.45	0.26	0.74
K18.2	K(B)	2.56	1.04	0.42	0.97
K18.18/19	K(B)	5.40	0.57	0.35	7.8

Table 3.3 Calculated mean finite strains recorded by pebbles in the Khan Formation. (e1,e2,e3 = deformed ellipse axes)

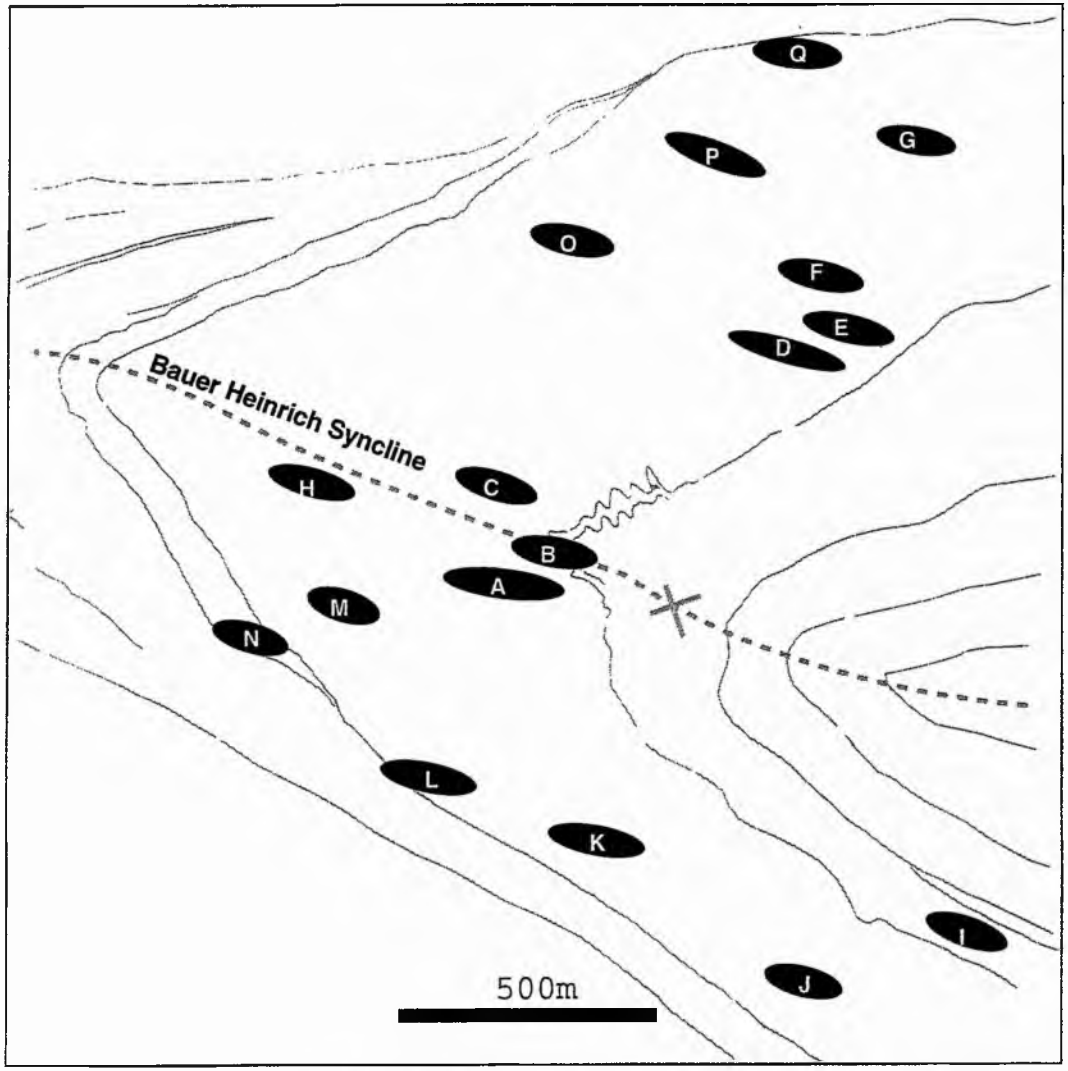

location	x	y	z
A 33.1	338	81	40
B34.1	244	82	56
C 34.2	235	80	56
D 34.3	337	66	49
E 34.4	260	77	57
F 34.5	242	78	56
G 34.6	223	76	62
H 34.10	248	78	56
I 35.4	238	82	57
J 35.5	221	83	60
K 35.6	273	81	52
L 35.7	273	81	52
M 35.8	209	89	59
N 35.9	216	82	61
O 35.10	238	82	57
P 35.11	298	75	49
Q 35.12	249	82	56

Figure 3.24 x/y strain ellipse map for pebble data from the Chous Formation around the Blauer Heinrich Syncline.

In the Namibfontein area outcrops with numerous pebbles are rare. However, Figure 3.24b shows representative finite X/Y strains after analysis of all available data (see Appendix 3.3). It is notable that similar strains are recorded by pebbles in the Chuos Formation at N48.2 GR[110,104] and N15.5 GR[104,850] to those around the Blauer Heinrich Syncline. The highest strains are recorded at the core of the Valencia dome at locations N53.4 =3.62 (e1), 0.49 (e2), 0.45 (e3) and N52.8 3.2(e1),0.84(e2), 0.42 (e3) GR[053,037] & GR[055,030].

3.7.1.i Error in the calculations

The values obtained clearly contain a degree of error as pebbles where not originally perfect spheres, estimates of strain are probably higher than actual strain. A reasonable approximation of an undeformed pebble shape with a compactional strain is a=1.07, b=1.02, c=0.92 from the Moodies conglomerate (Huebeck and Lowe 1994) suggesting in fact that estimates of strain for y, which is orthogonal to L_1 and parallel to S_0, could be too low. Constrictional strains may also be overestimated due to original compactional strains (Freeman & Lisle 1987). Despite these limitations the observed strains appear to be compatible with the development of regional scale tubular folds (see Section 6.1.3).

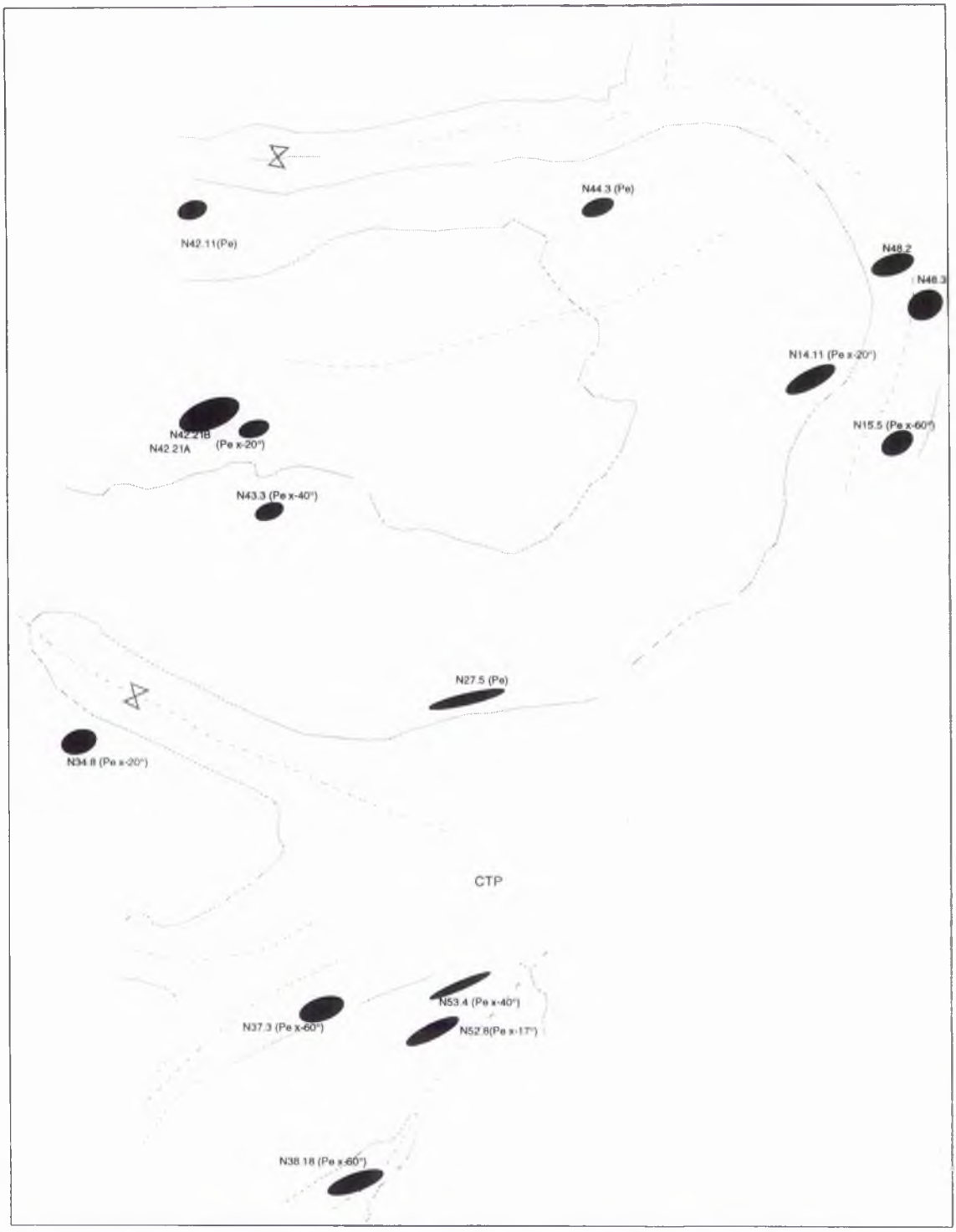

Figure 3.24b Representation of X/Y strain ellipses calculated from deformed pebbles in the cover, in the Namibfontein area.

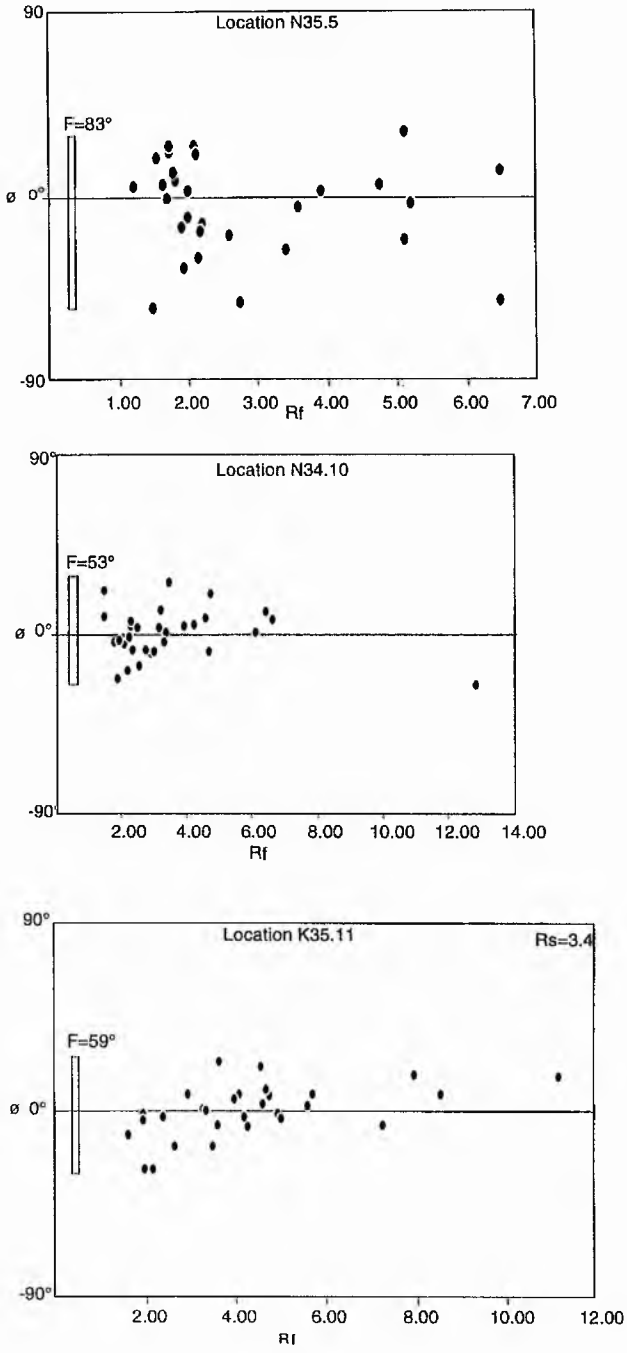

Figure 3.25 Rf/ø Plots calculated from pebbles around the Blauer Heinrich Syncline.

3.7.2 Tectonic strain from R_f/ϕ

The tectonic strain ratio (R_T) is obtained from the relationship $R_T = R_{max}/R_{min}$. (Ramsay 1967). The values R_{max}/R_{min} are taken directly from R_f/ϕ plots which plot the final axial ratios (R_f)of deformed pebbles against their arithmetic mean orientation, termed ϕ. Pebble data from three locations around the Blauer Heinrich Syncline were used to construct R_f/ϕ plots in Figure 3.25, one location from the syncline core K34.10 at GR[060,037], one from the northern limb K35.11 at GR[059,047] and one from the southern limb K35.5 at GR[070,046]. These yield R_T ratios of 5.4 at K35.5, 10 at K34.10 and 7.31 at K35.11 (mean =7.57). High R_T ratios are more characteristic of constrictional deformation i.e. where the tectonic strain produces X>Y=Z suggesting moderate elongation in the finite X-direction and shortening in the finite Y direction.

It is also notable that the data spread in R_f/ϕ plots in Figure 3.25 are not skewed. When data are skewed it is diagnostic of significant compactional strain i.e. non-random initial distribution (De Poar 1980). In this case compactional strains appear to have been negligible or more likely tectonic strain was very large. Therefore, finite strain is due mainly to the tectonic deformation.

3.7.3 R_s analysis from fold profiles

The shortening modification of a flattened buckle fold may be estimated from either t/α method after Ramsay (1967) (Section 3.5.1) or the inverse thickness method of Lisle (1991). A strain ellipse is constructed by plotting the ratio 1/t from a mid point on a reference line against the dip of layer tangent. In this case the smallest width of the ellipse corresponds to the fold hinge. Examples of finite strain ellipses are plotted in Figure 3.25 for various F_2 fold profiles in the Namibfontein area.

R_s ratios are generally >3, suggesting moderate strains. Comparable R_s ratios in Caledonian nappes of north-west Ireland (Alsop *et al.* 1996) shows that strains were high enough to permit sheath fold type mechanisms to operate. A second noteworthy point is that strain ellipses constructed for corresponding limbs at N11.4 GR[081,120] suggest no differential thinning has occurred.

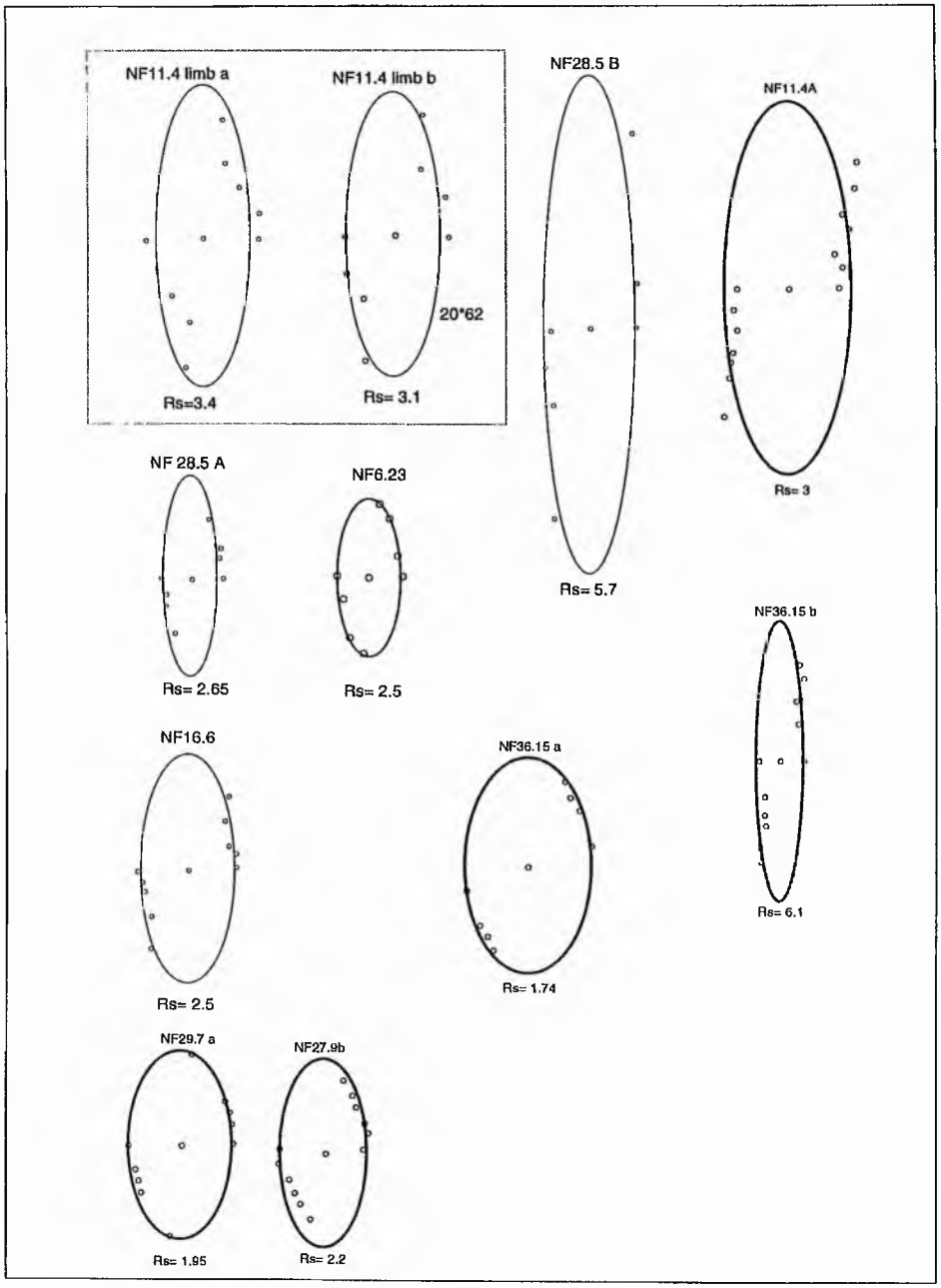

Figure 3.26 R_s ellipses from folds in the Namibfontein area after Lisle (1991).

3.8 Boudinage

Boudinage structures are common throughout both study areas. Four boudinage types were recognised:

i) ductile foliation boudinage;
ii) extension fracture boudinage;
iii) shear fracture boudinage and;
iv) pinch-and-swell structures.

These are described using the terminology of Wilson (1961): examples are shown in Plates 3.10A-C. As a general rule boudin long axes ($B_{1)}$ are parallel to L_1 in outcrop, suggesting they formed parallel to the bulk X-direction. Pinch-and-swell type boudinage and foliation boudinage (often associated with granite patches) are the most common boudinage structures. Layer parallel extension was therefore probably coeval with high temperature metamorphism (see Chapter 4). In units where competence contrast is high, brittle extension fracture boudinage has developed. This is largely confined to the Karabib Formation between calcitic marble and competent pyroxene-rich bands.

Foliation boudinage is displayed in highly foliated and moderately homogeneous units where there are low competence contrasts between the extending units (Ghosh 1993); good examples are found in the core of the Valencia Dome in the Khan Formation (Plate 3.10A) and from the Arises River Member (Plate 3.10B). Plate 3.10A shows a longitudinal section of thinly banded amphibole gneisses form 1m-0.5m boudinage lengths (parallel to L_1). These pinch evenly before the longitudinal separation where small granitic patches are developed. The granite is associated with small conjugate shear bands that cut the thinnest point of the pinch zone. Shear bands normal to the foliation and boudins appear to be genetically linked. The most striking example of this relationship is seen in the Khan Mine area. Plate 3.11 shows an outcrop of the basement-cover contact (Location N18.15 GR[0131, 0367]). The stratigraphy is highly strained and rodded (L-tectonite) it is comprised of prolate leucogranite boudins and quartz-rich micro-boudins usually >30cm long, they appear to represent a zone of tectonic thinning. The relationship between shearband and boudinage is shown in Figure 3.25, L_1 is parallel to the boudin long axes, conjugate shear planes dip ~30°. Movement along these shear planes appears to have been slightly oblique to the boudin long axes as they are offset, curving gently they are displaced ~30° from L_1; deformation was therefore ductile and progressive.

Plate 3.11 Boudinage structures at basement-cover contact in Khan Mine area. Location 18.15 [0131,0367]

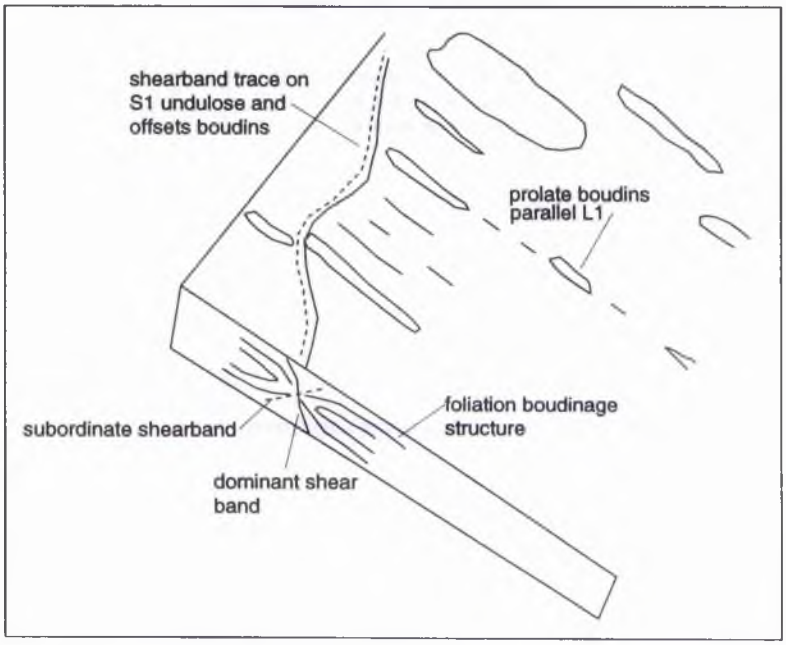

Figure 3.27 Sketch of photograph above to show relationship between boudinage and minor shear bands at location K18.15.

In some areas the outcrop permitted the aspect ratio of boudins to be determined, measured perpendicular to boudin axis (B_1) as width/thickness. Ratios are related to the compressional stress the layer underwent. Stress across the competent layer is reduced when it splits. A layer that splits sequentially (Ferguson 1981) should reach an optimum aspect ratio. In the Namibfontein area ratios are quite low (≤ 2).

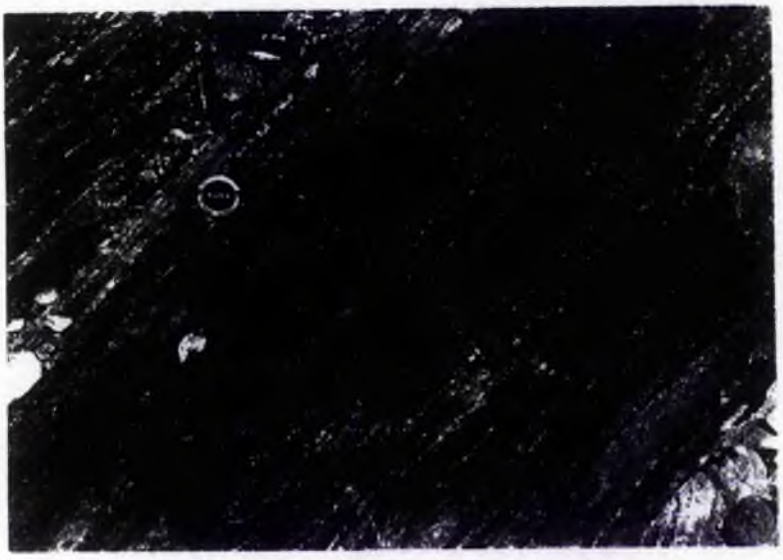

Plates 4.10 A-C

Plate A (Top) Foliation boudinage/ pinch-and-swell structures in the Arises River Member. GR[095,094]. Note boudinage is symmetrical. View looking north-east.

Plate B. (Middle) Foliation boudinage in Khan Formation at GR [035,026]. Note boudinage is symmetrical. View looking south-west.

Plate C (Bottom) Combination pinch-and-swell boudinage and extensional fracture boudinage at location K15.1. Layered leucogranite is parallel to S_1 within basement amphibolite. View looking south-west. Note boudinage is asymmetrical. View looking south-west.

3.8.1 Modified boudins

The occurrence of boudinage has so far been grouped into 4 simple types. However, one rare additional group of boudinage structures occurs in some areas which are folded. These modified boudinage structure are defined only by leucogranite veins, two kinds of modification were found, the first, type 1) slight and the second, type 2) intense.

The first type is found in the Khan mine area, where boudin lengths are warped slightly, forming curved crescent shaped half waves (Plate 3.12) orthogonal to L_1. The most striking area is shown in Figure 3.28, location K27.19. This is on the overturned limb of the Nose Structure Anticline directly below basement augen gneiss. Good three dimensional outcrop here shows folded leucogranite boudins parallel to and orthogonal to L_1.

Plate 3.12a Folded half wave boudins at K27.19 [045,022]

In the Namibfontein area two outcrops exhibit type 2) folded boudins. The first, at N29.11 GR[031,070] is *c.*300m east of the Karub Syncline. Plate 3.12b shows a small outcrop of boudin lengths *c.*10cm long folded around a westerly verging F_2 fold. The second, location N33.7 GR[025,065], (Plate 3.12c) shows an isoclinally folded 2.5cm thick leucogranite vein wrapped by a cordierite schist in the core of the Karub syncline. These two types of modification would normally be suggestive of polyphase deformation, normally boudinage strains are non-recoverable and are good indicators of superposed strains. Lines of extension i.e. boudinage, cannot enter a field of compression in a single deformation. Thus, conventionally, descriptions of the later structures would be explained by a two stage history: 1) intrusions of granitic veins during S_1 growth (D1), 2) folding by a subsequent and separate D2 event. An alternative explanation is given in Section 6.3.

Plate 3.12 b & c

Plate 3.12b (Top) Modified leucogranite boudins at N29.11. Note σ type folded boudin with top to south-west sense of shear.

Plate 3.12c (Bottom) Modified leucogranite boudins at N33.7. Note boudins are almost parallel.

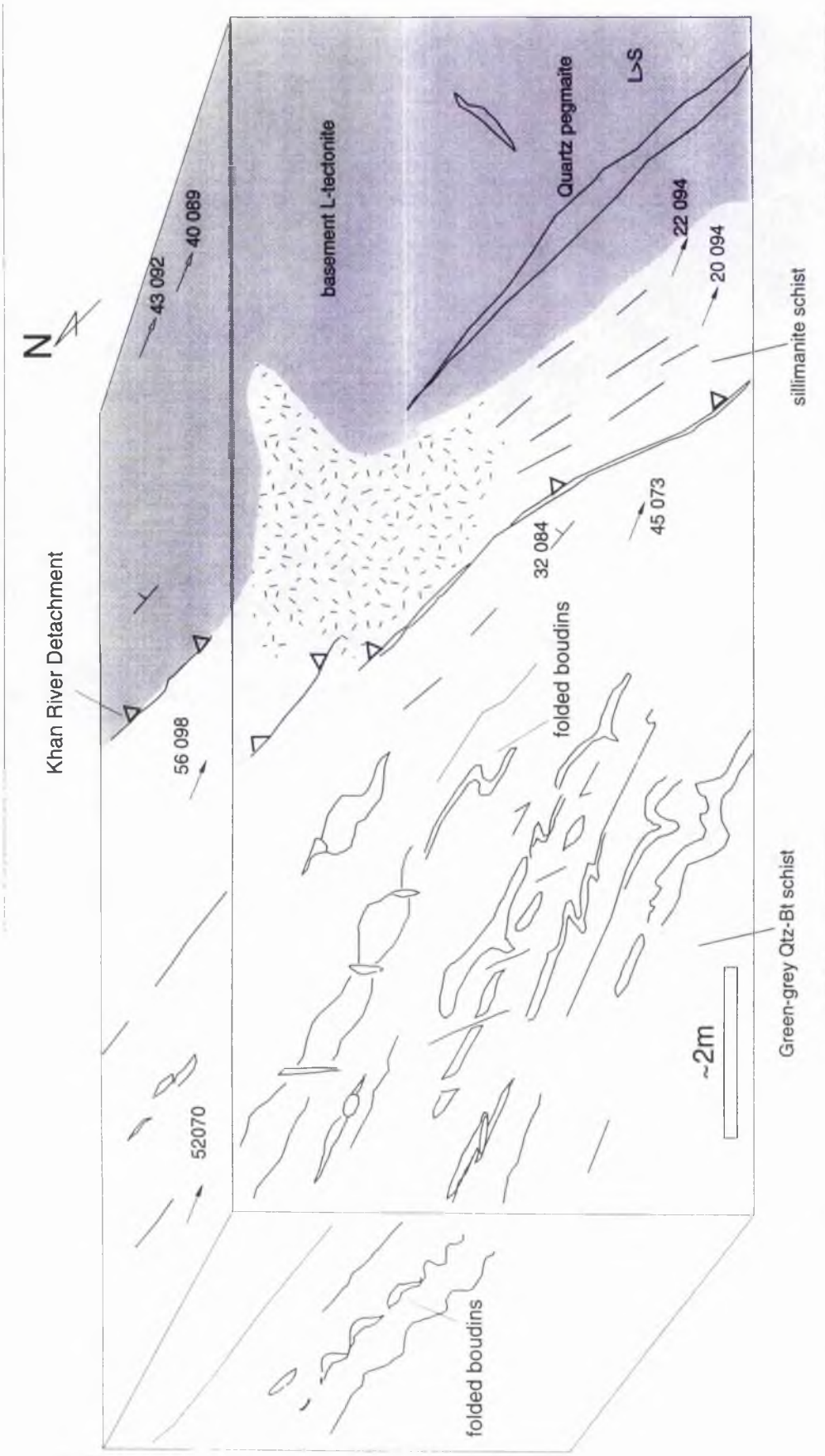

Figure 3.28 Sketch showing orientation of lineations, foliation and boudins at location N27.19. Grey indicates basement augen gneiss, dashes indicate pegmatite.

3.8.2 Quantitative strain measurement from boudinage

An estimation of extension (e) was made from boudinage lengths and separations shown in Table 3.4 The parameter (e), the extension is obtained from the equation:

$$e = \frac{l_A' - l_A}{l_A} \qquad \text{(after Ramsay)}$$

l_A' = the final length

l_A = the original length

According to Ferguson (1981) this standard method of strain determination (e) underestimates actual strain because it does not account for sequential separation of individual boudins. By plotting 'true extension' against estimated extension and using linear regression Ferguson (*op. cit.*) suggested the transform e^*= 1.564 (e-3.22) for estimates of e<70%.

Location	Formation	lithology	type	strain (e)	strain (e*)
N5.8	Kuiseb Fm.	Leucogranite	P&S	87%	131%
N7.10	Karabib Fm.	Pyroxenite	EFB	300%	-
N14.9	Arandis Fm.	Leucogranite	P&S	50%	73%
N10.16	Karabib Fm.	Pyroxenite	EFB	307%	-
N17	Arandis Fm.	Schist	FB	42.90%	62%
N25.10	Arandis Fm.	Pyroxenite	FB/P&S	51%	75%
N28.2	Kuiseb Fm.	Leucogranite	P&S	43.40%	62.80%
N33.2	Karabib Fm.	Schist	EFB	800%	-
N5.3(96)	Rössing Fm.	Leucogranite	P&S	24.40%	33.10%
K15.1	Basement	Leucogranite in amphibolite	P&S	41%	59%
K18.16	Etusis Fm	Basal schist?	P&S	96.70%	146%
K18.16	Etusis Fm	Basal schist?	P&S	91%	138%
K18.16	Etusis Fm	Basal schist?	P&S	147%	224%
K27.19	Etusis Fm	Basal schist?	P&S	100.00%	151%
K32.5	Basement	Qtz vein	P&S	42.90%	62.00%
K42.17	Etusis Fm	Basal schist?	P&S	51%	75%
K42.17	Etusis Fm	Basal schist?	P&S	110%	167%

Table 3.4 Estimates of strain e and e^* from boudinage structures in the Namibfontein and Khan Mine areas.

Two observations may be drawn from these data. Firstly, the greatest strains are recorded in marble-pyroxenite units. This is not surprising because competent pyroxenite bands fracture during extension rather than flow. Leucogranite veins also flow, recording lower strains (assuming low competence contrasts). This suggests strain has been distributed preferentially into the Karabib Marble (*cf.* Wells & Allmendinger 1990). This is supported by the outcrop pattern of the Karabib Formation along the Namibfontein dome where S_1 is sub parallel to the finite X

direction, it apparently thins to <10m (location N22.25), an apparent shortening of 10% from the initial thickness to the east.

A second important observation may be drawn from Table 3.4. In the Khan mine area strain has resulted in boudinage at the basement-cover contact. Rodded and boudinaged basal schists at the basement-cover transition record high strains (>120%). (Actual strains are probably even greater than (*e*) since deformation was ductile and internal extension of boudins cannot be measured). It may be concluded that the nature of boudinage and magnitude of strains appears to be controlled by the location of the deforming layers in relation to the regional structure; maximum extension is confined to the basement-cover transition.

3.9 Mylonites at the basement-cover transition

One of the key aims of this study was to determine the significance of mylonites at the basement-cover transition. These were first recorded by Steven (1992), near Usakos at Sandmap Noord, who attributed them to magmatic ballooning deformation. Oliver (1994) later recognised mylonites as a widespread phenomenon around the domes in the Central Zone and suggested that the contact was a site of tectonic shearing, probably due to the inherent weakness of the basement-cover unconformity. Oliver (*op. cit.*) termed this the Khan River Detachment. Values of *k* and variation of fold styles between domains demonstrate that deformation was not homogenous. Higher strains may have been exclusive to this discrete site within the regional structure. Fabrics in the field were given a qualitative value to indicate variation in strain intensity from 1-5 i.e. L/S^1 to L/S^5. Visual observation of $L>S^5$ mylonites in cover rocks 10-50m above the basement-cover contact (shown on Map 1 & 3) support the hypothesis that this was a zone of higher strains than rocks above or below. Furthermore this is consistent with observations made from semi-quantitative strain estimates from deformed pebbles and boudinage.

Previously the basement cover contact was regarded as a regional erosional unconformity. This was evidenced first by Gevers & Frommueruze (1929) who noted discordant basal conglomerates in contact with distinct augen gneisses. The age of the rocks below the unconformity in the Namibfontein area is supported by a zircon SHRIMP age of 1038±58 (Kröner *et al.* (1991). Regionally the unconformity surface has a complicated folded geometry and is obscured by Damaran granite intrusions. It is evident from mapping that the basement was not a passive rock mass (*cf.* Argand 1922) because both cover and basement have undergone Damara deformation. It is unlikely therefore that mylonites at the basement-cover interface resulted solely from displacement of the cover over the basement.

In this study mylonites were identified in both the cover and basement consistent with the findings of Oliver (1994). In the Namibfontein area mylonites were recorded in three sub-areas. In the first area mylonites were observed as orthorhombic L & L/S tectonites in the core of the Valencia Dome. Figure 3.29 shows this area corresponds to the axial zone of the Valencia Dome.

Mylonites at the contact grade from $S=L^2$ mylonites to $L>S^4$. This is best observed from location N38.19 GR[038,014] where a *c.* 5m zone of S=L mylonites grades progressively into ubiquitous L>S tectonites. Plate 2.3b (see Chapter 2). shows a typical L tectonite cut in the z/y plane. In this dimension the Kfs augens tend to have a circular cross section such that Z=Y and $k=\infty$, foliation is weak and disjunctive while lineation is pronounced. In the Y/Z plane augens are extremely elongated with typical x:y ratios >1:10. Augens form ϕ type porphyroblasts with symmetric wings and simple shear sense cannot be deduced from these rocks. Cataclasis is not observed, Kfs feldspar is deformed plastically (*cf.* White & Knipe 1978). Deformation was therefore by diffusion creep and not dislocation creep (Tullis & Yund 1991), probably at temperatures >650°C.

In the second area mylonites outcrop along the northern flank of the Namibfontein Dome at the transition of the Basement and Etusis Formation, at location N42.15 GR[038,109]. Mylonites in this area display a 2-3mm spaced foliation which is both discrete and continuous. The fabric defines an S>L tectonite. Kfs augens and Qtz ribbons form symmetrical ϕ type porphyroblasts. It is notable that at N42.15 outcrop is only 300m thick, considerably less than the southern flank of the Dome between location N14.10 GR[093,095] and N19.1 GR[079,096]. This is interpreted as a result of tectonic thinning.

In the third location, N17.9 near Twien Koppie (Figure 3.12). the basement-cover transition can be traced around a large granite koppie. The contact is discrete and defined by a strong *c.* 5m zone of L/S tectonites. The granite is intruded into and above this zone; above and below the contact the granite is unfoliated. The basement-cover transition dips at 45°-60° to the north-east, L_1 plunges 35°-060°. The contact here can be traced west to location N42.21 GR [032,085]where a deformed basal conglomerate defines a highly deformed L-S mylonite.

In the Khan Mine area the tectonic nature of the basement cover contact is displayed clearly along its entire length. The surface is folded around the main macroscale structure. In addition it forms mappable mesoscale folds along the Nose Structure Anticline. The general nature of the transition is seen clearly at location K14.3 where a type section of the contact was mapped at a scale of 1-1000. Figure 3.30 shows a 100m transition from L tectonites in the basement to S>L tectonites of the Etusis Formation. Fabric strength generally increases towards a zone marked by a band of sillimanite schist, i.e. the basement-cover interface. This is demarcated as a major shear zone in Figure 3.27 which dips 42°-060°. Minor shear bands are observed cutting the quartzite 40m north of the major shear zone, suggesting that the main shear zone anastomises or is bounded by anastomising shear zones. Both top up to the south-west and top down to the north-east shear sense can be deduced.

In the Nose Structure Anticline the basement-cover interface is folded and overturned. The general form of the surface is indicated in Figure 3.31, two geometric types of folds are found: i) reclined and ii) subhorizontal. Decimetre scale reclined folds were mapped in three locations, at GR[016,039], GR[021,040] K26.19 and GR[029,042]. Fold hinge plunge directions are subparallel to the π axis of the Nose Structure Anticline. Close examination of the fold form at location K26.19 shows they are defined by folded S_1-S_0 and that mylonitic lineation L_1, ~55°-074°, is unfolded and subparallel to the mesoscale F_2 axis ~52°-074°. This relationship is interpreted as syn-kinematic progressive folding of the basement-cover interface. Subhorizontal folds in Figure 3.31 are implied from minor monoclinal gently plunging folds seen in the quartzites at location K21.1 GR[020,044].

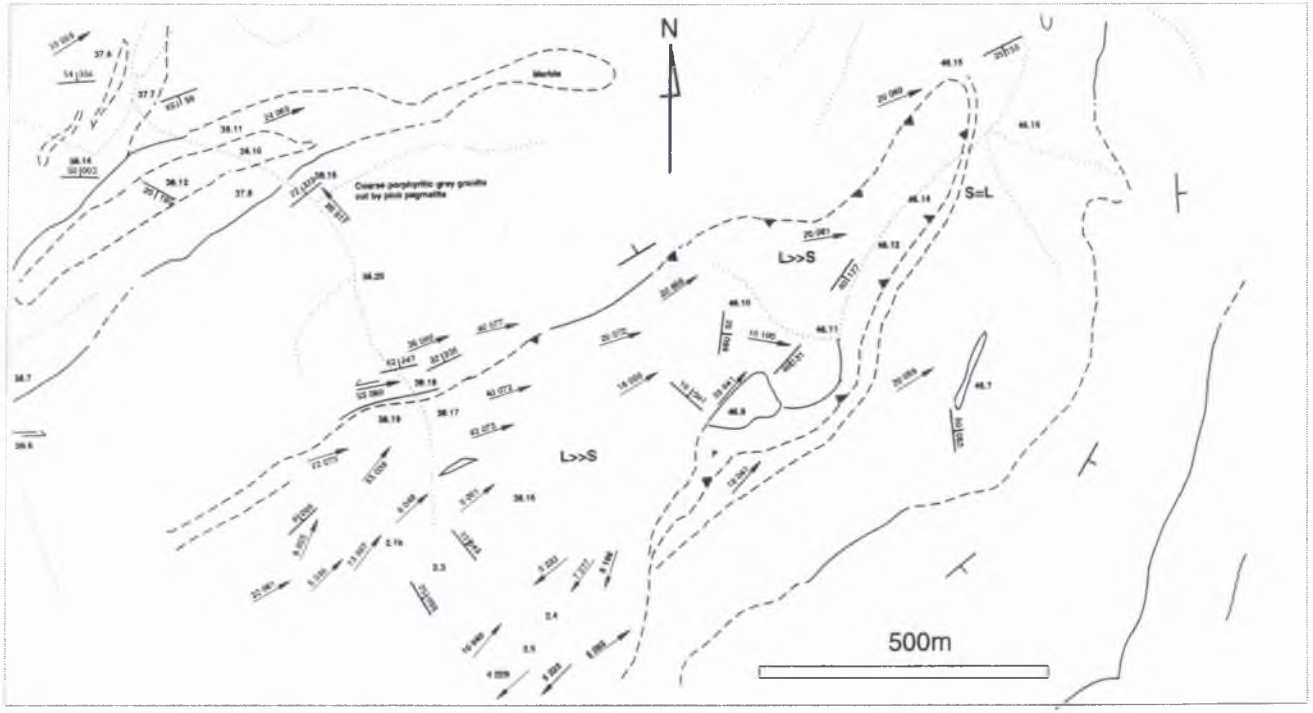

Figure 3.29 Structural geology map of the core of the Valencia dome showing the relative positions of L & S tectonites.

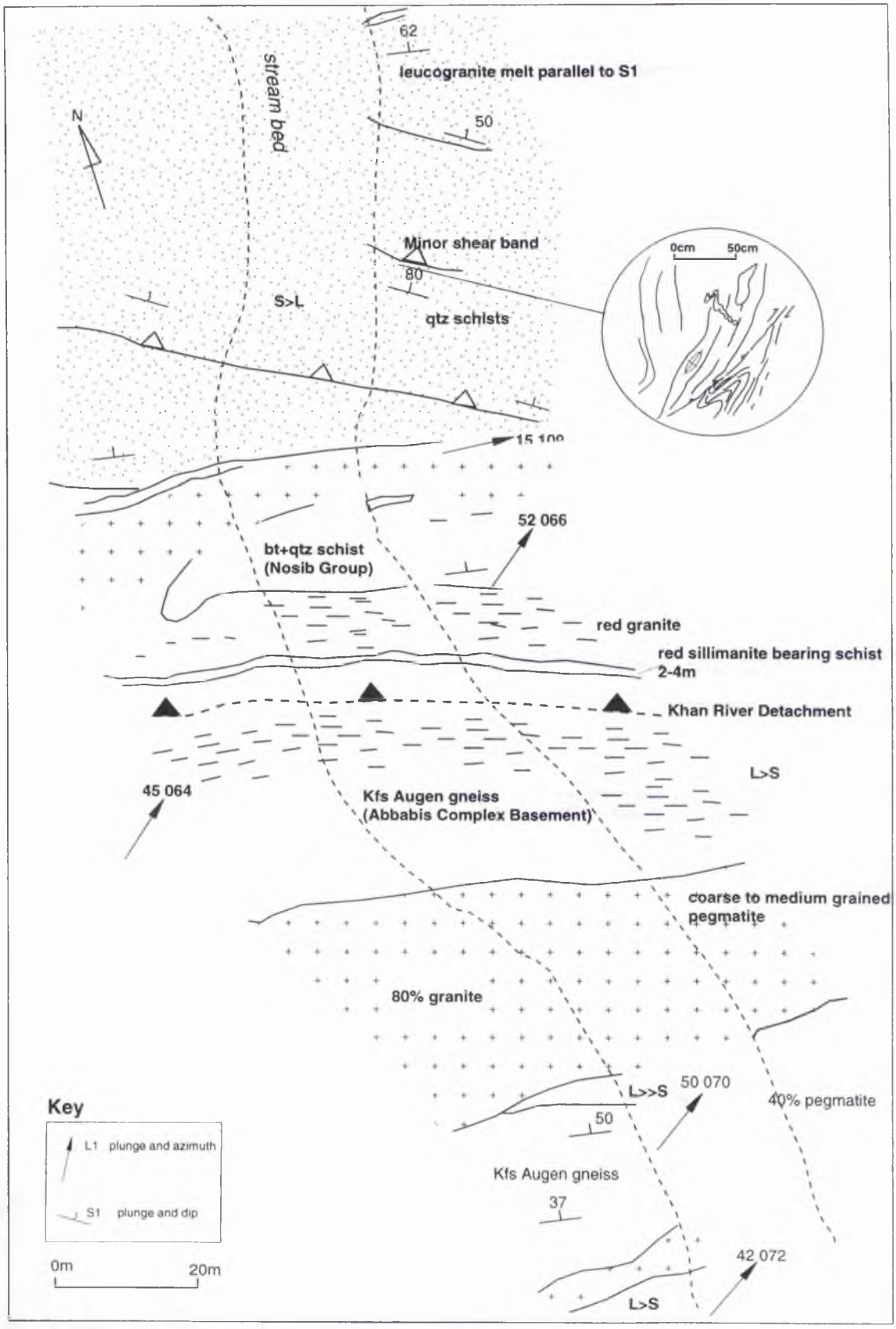

Figure 3.28 Structural geology map of the basement-cover transition at location K14.1. Inset (circle) showing cross section sketch of minor shear band. L and S fabrics indicated.

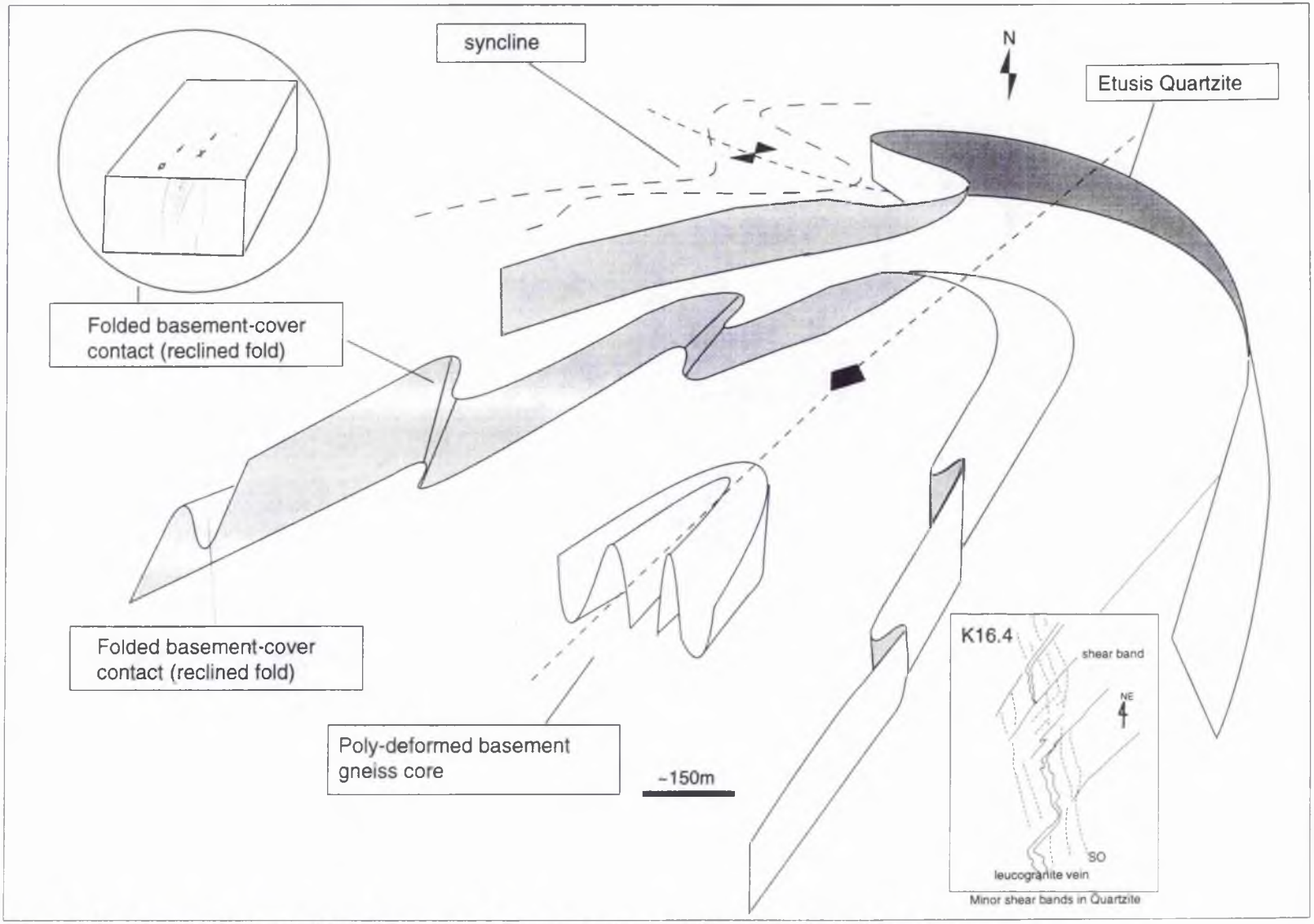

Figure 3.31 Schematic 3D sketch of The Nose structure Anticline showing a possible solution for the NE section.

Inspection of the plunge direction of both reclined and subhorizontal folds shows that they are all subparallel to domain K(B) π axis. Since the only geometric difference is the amount of plunge, the folds are interpreted as contemporary.

In summary several lines of evidence suggest that the basement-cover interface is a tectonic shear zone. Firstly, it is evident that mylonites, mainly L-tectonites, are ubiquitous at the interface. According to the classifications of Ramsay (1980) and Shimamoto (1989) the basement-cover interface or Khan River Detachment is a heterogeneous and ductile shear zone; no boundary constraints can be applied to the Khan River Detachment and it is defined as a non-discrete zone of more intense strain. Secondly, semi-quantitave estimates of finite strain from boudinage and pebble data support the notion that higher strains have occurred along this zone. Thirdly, sheath folds are recorded in this zone and probably originated from the focusing of strain in horizons near the interface. These folds may have resulted from pure shear since sense of shear markers within this zone are symmetrical. Asymmetrical structures may have been obliterated by late annealing due to thermal metamorphic effects but more likely due to the dominance of pure shear. Pressure solution shadows around some garnet porpyhroblasts do indicate a top to the south-west sense of shear. Plate 3.13 shows complex σ–δ type garnet porphyroblast (Figure 3.32) west of the Karub Syncline, S_1 dips to the east , sense of shear indicated top to the south west. Often, however, shear sense is ambiguous with near symmetrical quartz shadows occurring very commonly. A component of differential shear cannot be ruled out along the basement-cover interface since evidence of shear bands is occasionally seen (shear sense directions are shown in maps 1 & 2 Appendix).

Plate 3.13 Photograph showing δ–grt porphyroblast east of the Karub Syncline in the Kuiseb Formation. Sense of shear is top to the south west.

Figure 3.32 Sketch to illustrate various shear sense indicators after Mawer (1987) Passchier and Simpson (1986)

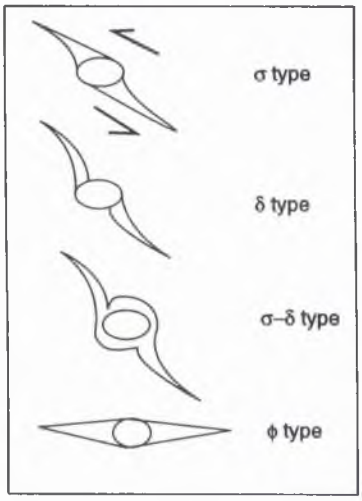

3.9.1 Shear bands and shear strain (γ)

Shear bands have so far been noted in the cover and associated with boudinage near to the Khan River Detachment. Shear bands and minor conjugate shear bands are also present within the basement L-tectonites. At location N44.1 GR[044,102] (Plate 3.14) at the core of the Namibfontein dome, a 3m shear band dips at 25° normal to L_1 and displaces highly sheared basement augen gneisses. Location N2.1b from the core of the Valencia dome and K32.14 from the Khan dome have been studied in more detail and are shown in Figure 3.33 a/b.

At location N38.18/N2.1b GR[039,014] (Figure 3.33a) strain has been partitioned into mesoscale 1-2m long shear bands which are not laterally continuous. These minor shear bands are highlighted by convergence of the Kfs augens into *c.* 10cm wide zones and displaced granite veins. In the Khan mine area at Location K32.14 GR[050,018] (Figure 3.33b) Qtz vein have been displaced by subsidiary shear bands. In both outcrops the dip of the mylonitic fabric is >40° while in the shear bands the dip is 22°-24° (subhorizontal).

An estimation of shear strain (γ) was made in both areas from the displacement of the veins measured as (α'). The parameter (γ) defines the shear strain of an initial marker. This is calculated from equation (1), α represents the initial orientation of a line marker (i.e. the veins) and α' the displaced angle.

$$\cot\alpha' = \gamma + \cot\alpha' \qquad (1)$$

where

$$\gamma = \cot\alpha - \cot\alpha'$$

From this analysis γ at the centre of the bands = 3.5 & 7 for veins A & B at Location N2.1b and 7 for the Qtz vein at Location K32.14. In addition to this method γ was measured from the orientation of the finite strain trajectories (θ), this is taken as the pitch of the Kfs augens relative to the shear zone walls. Equation (2) is used to give γ. In both areas θ=10° which gives γ = 5.5.

$$\gamma = \frac{2}{\tan 2\theta} \quad \text{(after Ramsay 1980)} \qquad (2)$$

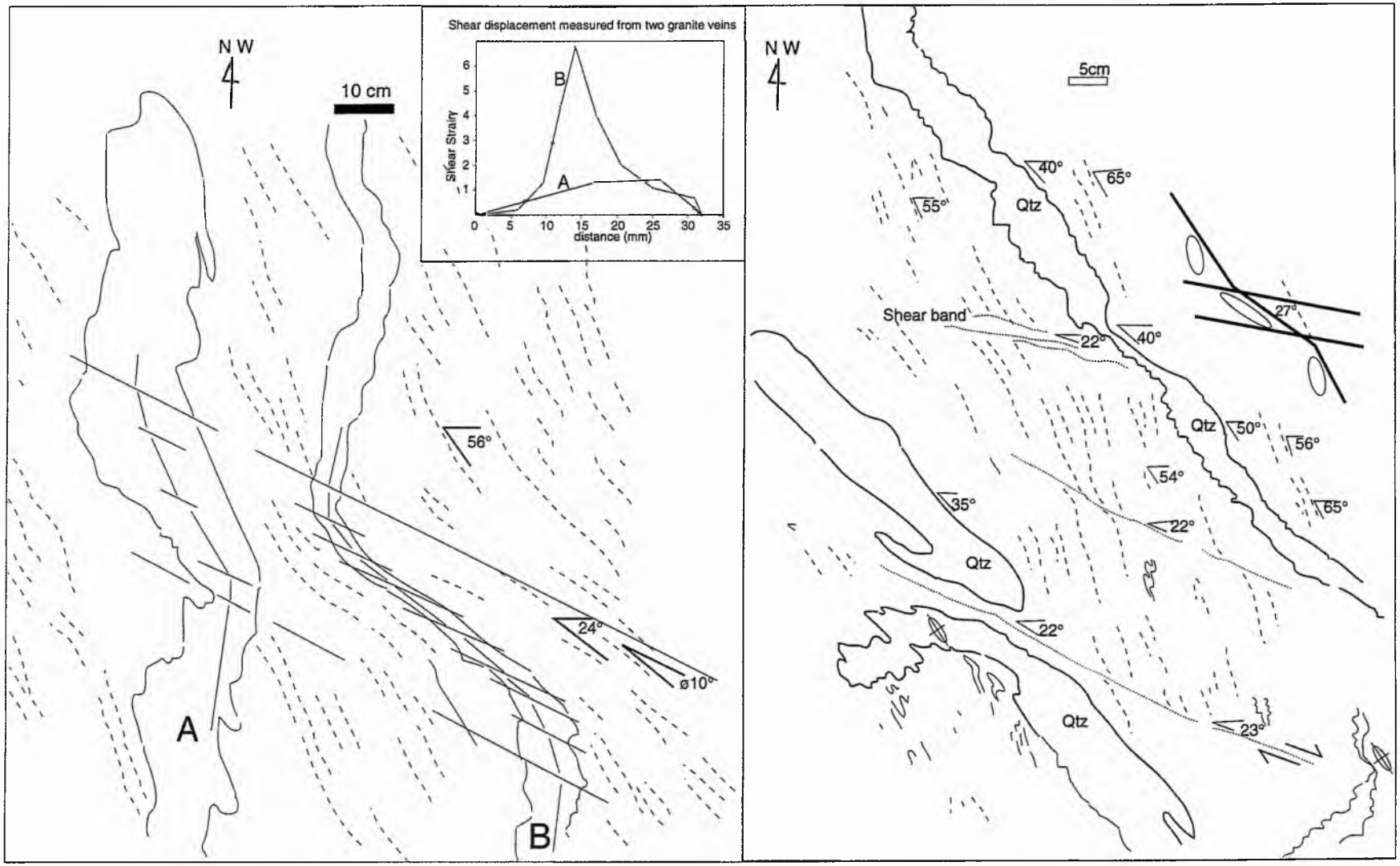

Figure 3.33a (left) Sheared granite veins in basement augen gneiss (N38.18). Upper right inset shows shear strain across each vein.
Figure 3.33b (right) Sheared qtz pegmatite in basement augen gneiss (K32.14).

The total displacement across these shear bands can be estimated (assuming simple shear) by the integral;

$$s = \int_0^x \gamma dx \qquad \text{(after Ramsay 1980)}$$

From the graphs of shear strain against distance across the shear zone (Figure 3.33a) the area under the graphs equates to the total shear displacement <1m for both locations.

3.9.2 Origin of the shear zone and mylonites

Development of mylonites is, in general due to i) superplastic deformation ii) geometric softening and iii) reaction softening (White & Knipe 1978). Observation of mineral paragenesis at in the Abbabis area (Kfs+Msc+Qtz) suggests that reaction softening has occurred in at least some areas. However mylonites at the basement-cover interface in the two study areas do not contain large amounts of Msc (Tullis & Yund 1991). The temperature of mylonitization was certainly around 650°C as feldspar is plastically deformed. It is therefore likely that at least two mechanisms have occurred which led to the formation of mylonites.

What led to the development of the shear zone may be explained in several ways. In the first case it is a conventional idea that strain (constrictional in this case) is nucleated to a point of natural weakness or domain of strain concentration (Oliver 1994). In the second case the basement may have behaved in a static manner while the cover deformed at a faster rate causing shear zones to develop at the margins of domes . Alternatively the basement may have deformed faster than the cover (*cf.* Alsop 1994 figure 10 page 132). This is more likely since the basement is highly deformed. In either case, however, differential shearing would have resulted. This suggests that the mylonites (L-tectonites Plate 3.15) in the core of the domes were produced by pure constriction while those at the dome margins are effected by simple shear i.e. differential movement in some areas is more significant. This may explain why sillimanite appears above the basement-cover contact as both 'general oblate' and 'general prolate' shapes. This spread in *k*-values is not easily explained in terms of a single bulk constriction. The possibility of localised flattening strains is highly likely. In some cases these may post-date constriction, mylonite development therefore continued after S_1 and into S_2. At location N42.21 GR[032,085] for example pebbles in the basal conglomerate display two distinct shapes. Plate 3.16 shows an outcrop of recognisable conglomerate which grades into intensely sheared oblate pebbles.

Plate 3.14 Shear band in basement gneiss at GR[044,102], view looking north-west.

Plate 3.15 L-tectonite mylonite at the core of the Nose Structure Anticline, GR[0125, 0232]. View looking south.

Plate 3.17 location N42.21. Photograph showing basal conglomerate with two increments of strain. Area right and above of hammer shows a pebbles with greater strain.

3.10 Structural summary

1. It has been demonstrated that the structure in the Central Zone is typified by amoeboid basement domes and sinuous synclinal cover domains. These have fold patterns which are not easily explained in terms of sequential formed folds.
2. It has been shown that folds in the cover (mainly synclines) are open to tight and have sharply curved axial traces. Macroscale folds are non-planar and non-cylindrical.
3. It has been stated that synclinal domains have formed convergence points where several synclines merge. These are not adequately explained by a dominant deformation trend within a sequence of deformation events.
4. It has been shown that F_2 fold style is varied and that correlation of folds from one domain to another is not possible by standard means.
5. Most F_2 hinge trends follow domain π axis trends. There is no evidence of refolding of F_2 folds, F_2 are in some instances formed during progressive strain.
6. Since S_2 fabrics have no preferred orientation it does not appear to represent a regional D_2 trend. S_2 is poorly developed and not always axial planar.
7. The similarity of L_1 orientation to mesoscale F_2 hinge orientation shows fold axes are parallel to finite X-direction stretching.
8. Deformation has occurred in a moderately plunging general constrictional field.
9. Finite strains were moderately high and inhomogenous, strain appears to have been partitioned to the basement-cover transition.
10. High strains at the basement-cover transition have resulted in ductile mylonite development around domal structures.

3.11 Interpretation

Fold style and strain analysis suggest general constriction as the principle cause of dome formation in the Central Zone. The structure is similar to Ramsay's (1967 Fig. 3.54) field 3. A new three-stage geodynamic model is proposed:

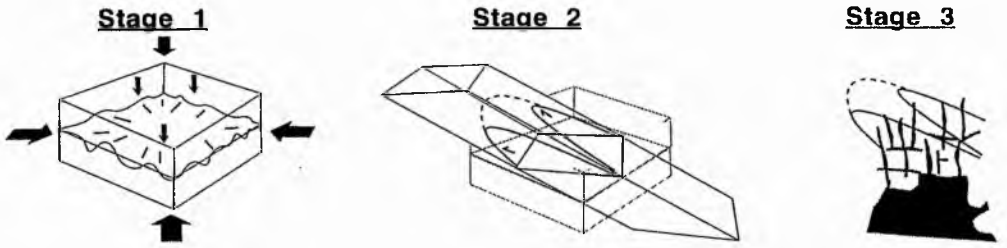

Stage 1

S_1 forms by mimetic growth parallel to S_0 as metamorphism proceeds. Unequal simultaneous shortening in at least two directions initiates constriction; gentle domes form.

Stage 2

This is the main dome forming stage. Dome amplitude reaches its maximum state. L and S tectonites develop. Open to tight synclines develop axial traces that curve tightly. In the case of the Namibfontein dome a rim syncline forms; in contrast, in the Khan mine area the Khan dome curves around the Blauer Heinrich Syncline. In this interpretation the curvature of the synclinal and anticlinal hinges does not define a subsequent deformation but rather indicates continued constriction of the early structure. In domain NF (A) (Figure. 3.2) intersection of the E/W and N/S trending parts of the surrounding syncline might define an F_2 axis generation using conventional terminology. Ghosh (1995) uses the terms F and f folds (Figure 3.31) to invoke a morphological hierarchy to describe the curvature of the axial surface, and thus avoid a chronological description. The hinge line of the syncline NF (ABD) (Figure 3.2) is therefore an F fold subdivided by f folds. Plot NF (ABD) defines a f fold axis. F_2 mesoscale folds therefore evolve and tighten progressively. Fold style is controlled by tightening of local structure, not by a subsequent separate regional D_2 event. The folds in the Karub Syncline, for example, become tight to isoclinal. More open folds are found on the margins of the Namibfontein Convergence Point. Flexural slip, buckling, flow folding and differential shearing operate simultaneously to form mesoscale folds.

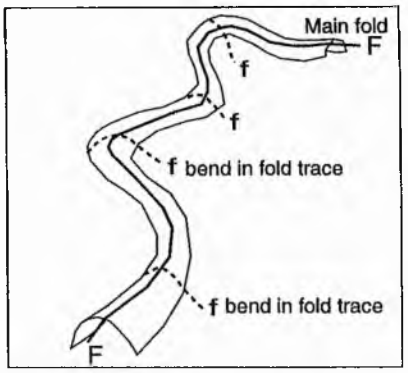

Figure 3.34. Sketch to show morphological classification of fold outcrop after Ghosh *et al.*(1995)

The general trend of F_2 hinges reflects bulk finite X direction (λ_1) at the last stage of constriction. Domain NF (G) and KM(D) (Section 3.6.3) however is controlled dominantly by local progressive tightening of structure. The orientation of finite X direction and prolate fabrics did not reflect the regional kinematic axis because deformation was inhomgeneous in these local domains. This change in the strain field occurs as the rock mass responds to local stress systems. Partitioning of strain becomes increasingly heterogeneous as structure becomes more complicated. Contemporary deformation resulted in lineations that are sub-parallel to fold hinge trends as they developed coincidentally with late mesoscale folds. The progressive amplification of domes creates the Namibfontein and Khan Mine Convergence Points by continued tightening of the surrounding cover envelopes. S_2 fabric form is restricted by local domain trend and form, it does not reflect the regional bulk strain ellipse but local stress systems.

Stage 3

Strain is partitioned into mylonites at the basement-cover contact as domes reach optimum amplitude and maximum extension occurs, at least 155% with ~ 20% shortening . At the final stage granite magma is emplaced without significantly changing the fold geometry.

CHAPTER 4

Metamorphism

4.1 Introduction

This Chapter focuses on the nature of local metamorphism in the study areas (Figure 4.1) and its implications for Damara Orogenesis.

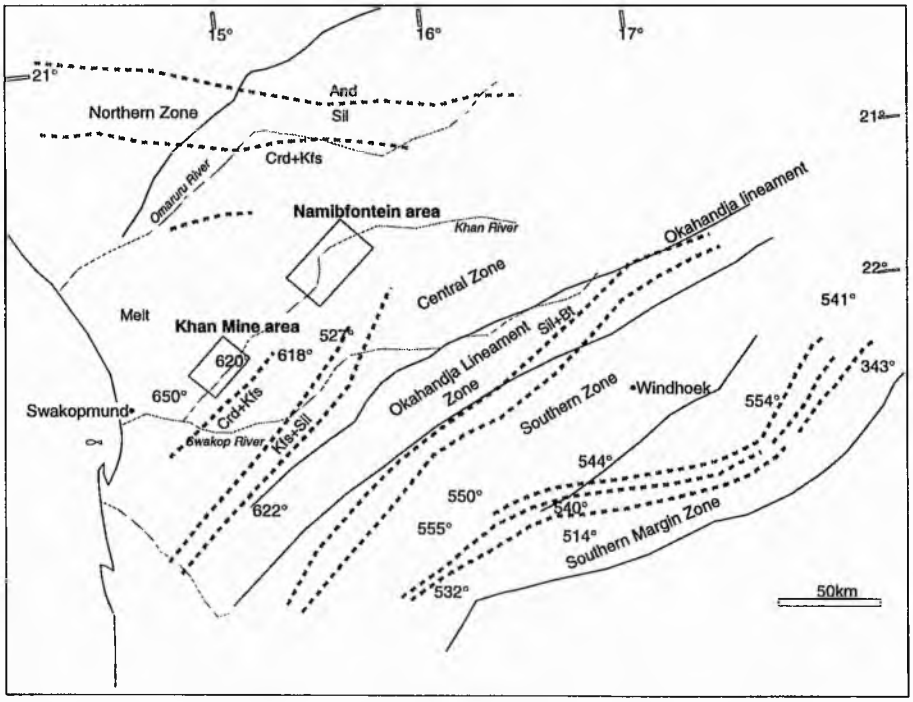

Figure 4.1 Location of the two study areas with reference to tectono-stratigraphic zones. Map modified from Kasch (1983). Grey dashed lines indicate regional isograds after Kasch (*op. cit.*)

Presently, two hypotheses exist concerning the metamorphic evolution of the Central Zone: 1) Single-phase metamorphism is advocated by Martin (1983a), Hartmann *et al.* (1983), Haack (1983), Puhan (1983), Haack & Martin (1983), and Hawkesworth (1986) and 2) multiphase metamorphism is advocated by Kröner (1982), Barnes & Sawyer (1980), Kasch (1983), Ahrendt *et al.* (1983) Oliver (1995) and Nex (1997). These studies do however agree that the Central Zone was essentially a high temperature and low pressure terrane. The areas that were investigated in this study are situated between the Kfs+Sil and migmatite isograds of Hoernes and Hoffer (1979) & Kasch (1983) who considered that metamorphic grade increases from

east to west (see Figure 4.1). This is supported by the occurrence of maximum migmatite generation in an area north of Swakopmund (Masberg *et al.* 1992 & Masberg 1996).

4.1.1 Statement of Aims

1) To quantify the nature and timing of metamorphism in the basement and cover, i.e. is there a metamorphic gap seperated by a high strain zone? (Oliver 1995)

2) To review physical conditions associated with dome formation ;

3) To assess whether metamorphism was episodic or single-phase;

4) To compare the findings of this study with previous metamorphic studies;

5) To construct a *PTt* evolution path of the study area.

4.1.2 Methodology

Samples were given a location number that corresponds to locations on the location numbers on Maps 1 & 2. Samples were cut and selected for thin section preparation to permit a detailed study of mineral parageneses and micro-textural relations (see Section 4.2). From this study various mineral reactions were proposed. Composition data was obtained from EMPA analysis of mineral phases in polished section using the JEOL Superprobe at St Andrews. These data allowed quantitative and semi-quantitative estimates of pressure and temperature to be made using various ion exchange equilibria thermobarometers. These were then tested against each other.

4.2 Petrology of the rock types

This section lists the petrographic features of the main litho-types present in the cover and the basement. Sub-sections list, in table form, the assemblages and textures found in thin section. Visual investigation of thin sections showed that the coarse grain size and heterogeneity of the samples precluded meaningful quantitave estimation of phases present. Instead, qualitative estimation of the relative abundance of phases are listed in decreasing order (e.g. Qtz+Kfs+ etc.).

Four cover rock categories are recognised, these are:

1) pelites and semi-pelites;
2) arkosites and psammites;
3) calc-silicates and marbles;
4) amphibolite and amphibolites.

Generally there are fewer lithologies in the basement i.e. the Narubis Granitoid Complex (Brandt 1987) than in the cover. Three categories were recognised:

1) Semi-pelites (uncommon)
2) Quartz-feldspathic gneisses
3) Amphibolites

4.2.1 Petrology of the Basement rocks in the Namibfontein area

A summary of the assemblages and textures of four representative samples of basement rocks in the Namibfontein area are shown in Table 4.1. Samples have been selected from the twin domes and the Valencia dome. The main textural feature is an inequigranular-interlobate arrangment of matrix mineral grains, typically amoeboid and sutured. Quartz and feldspar are recrystallised forming a ~3-4mm in diameter mosaic while aligned biotites define a weak fabric. In samples from the high strain zone however, (see Section 3.9) the general texture departs from perfect 120° contacts and instead a discrete foliation has developed. It should be noted however, that thinsection cut is important when considering textures. Most sections were cut in the x-z plane to show the extent of strain fabric development, sections cut in the y-z plane on the other hand appear more granoblastic.

N18.4	Qtz + Kfs + Bt + Sil	.basement raft
Texture	Interlobate quartz and microcline form an inequigranular-amoeboid migmatitic texture. Corroded biotite with lobate edges and quartz blebs, is overgrown by sillimanite.	GR[070,088]
NP43.15	Qtz+Bt+Kfs+Pl+Grt+Mz	basement semi-pelite
Texture	A granoblastic coarse gneiss. Garnet is corroded and appears to reacting with potassium feldspar evident from a quartz rim and embayed texture between the two. Inclusions of zircon and monazite are found in garnet and biotite. Euhedral zircons have a corroded growth rim seen with EMP.	GR[034,098]
NP44.11	Kfs+Qtz+Bt+FeTiO+Pl	basement augen gneiss
Texture	Coarse granoblastic schist with aligned biotite. Quartz and microcline and perthitic orthoclase have interlobate grain contacts. Bt is corroded. FeTiO oxides are pinkish-grey in reflected light with grey exolution lamaellae(Mag-Ilm).	GR[066,105]
NT38.17	Kfs+Pl+Bt+Qtz	basement augen gneiss
	Fabric is granoblastic. Large microcline augens define a linear fabric. Microcline has large oligoclase/andesine patches, orthoclase is perthitic. Biotite is weakly aligned. Plagioclase grains have many small quartz blebs..	GR[039,014]
NT43.4	Mc+Qtz+Sil+Bt+Crd+Mag	basement gneiss
Texture	Migmatitic interlobate texture. Fibrolite overgrows all phases forming bow-tie structures. Twinning in microcline bends.	GR[036,089]

Table 4.1 Summary of assemblages and textures of selected samples from the basement in the Namibfontein area.

4.2.2 Petrology of basement rocks in the Khan Mine area

The textural and phase relations of four samples of basement gneisses from the Khan Mine area are shown in Table 4.2. Acidic gneisses are characterised by the general assemblage Kfs+Pl+Qtz+Bt±Mag while more basic gneisses are characterised by the assemblage Qtz+Pl+Mc+Hbl+Bt+FeTiO±Chl. In the basic gneisses amphibole is hornblendic, its content varies between 10-15%. Feldspar is mainly Kfs constitues ~30% of most acidic gneisses and form elongate augens. Perthitic and antiperthitic textures are common.

KP21.6	Kfs > Pl + Qtz +Bt	augen gneiss
Texture	A inequigranular polygonal texture. Bt envelopes opaques. Opaques are zoned. Inner zone as Magnetite with exolution lamellae with a grey corona. Biotites contain zircons and apatites.	GR[024,042]
KP27.19	Qtz > Pl + Hbl + Bt (Chl)+ Fe Ti O (Chl)	
Texture	Granoblastic-lobate textures. Hornblende grains large (1-3mm) within the matrix.	GR[052,022]
KP42.19	Pl+Qtz+Bt+Chl+(Sphene)	mylonite
	Finely banded and mylonitic texture, partly annealed. Opaques are elongate fish structures. Opaque (magnetite) enclosed by sphene.	(directly below cover) GR[060,026]

Table 4.2 Summary of assemblages and textures of selected samples from basement in the Khan Mine area.

4.2.3 Petrology of cover pelites in the Namibfontein area

The textural and phase relations of twelve representative pelitic samples from the Namibfontein area are shown in Table 4.3. The majority of pelitic samples were collected from the Kuiseb Schist. The general assemblage observed is Qtz+Bt+Pl+Kfs±Crd±Grt. Two frequently coexisting porphyroblastic minerals occur, these are1) ferro-cordierite (comprising ~20% of most samples) and 2) garnet (< 10%). All garnet analysed is almandine-rich with minor proportions of grossular, spessartine and pyrope (see Appendix 4.1).

1) Figure 4.2 B&E shows examples of cordierite in thin section. It is commonly enveloped by a well defined external fabric (S_1) and contains straight inclusion fabrics of quartz and biotite. Porphyroblasts in Figure 4.2B exhibit σ-type relationships with aysmmetrical quartz-biotite pressure solution shadows (Passchier & Simpson 1986). This relationship is not common in all samples but clearly shows the growth of cordierite is syntectonic and involved some kinematic rotation. According to Nash (1971) who studied the SJ area and Nex (1997) who studied the Goniakontes area potassium feldspar also grew simultaneously with cordierite as both are partly 'rotated' within matrix biotite folia and contain similar inclusions. This is consistent with the observations in this study.

2) Garnet porphyroblastesis on the other hand is somewhat ambiguous. This is partly because the original matrix-porphyroblast relationship is obscured by coarse gnessose fabrics and because garnet is observed in two textural modes i) syn-tectonic and ii) post-tectonic:

i) In some thin sections post-tectonic growth is demonstrated, in Figure 4.2 A for example, it is apparent that garnet has overgrown biotite that is both aligned and in continuity with the external fabric (S_1).

ii) Syntectonic growth, however, is more common. In some sections (e.g. N10.1 Plate 4.1) garnet is enveloped by biotite and quartz, clearly diagnostic of coeval matrix-porphyroblast development. In section NT34.1 garnet, cordierite and biotite form a semplectite texture.(Plate 4.1B), suggesting growth was coeval with syn-tectonic cordierite. Furthermore, in section NP28.14, both garnet and cordierite exhibit σ-type relationships suggesting syntectonic growth.

Sillimanite is the only Al_2SiO_5 polymorph observed and appears only rarely (e.g. sample (N34.7c, N34.1 & N3.2) as inclusions in cordierite and less commonly, in garnet and quartz. Two varieties of sillimanite have been found. Prismatic and fibrolitic sillimanite is found in the cores of cordierite oriented parallel to the main folia and constitutes ~2% of those samples. In section NT34.7c it is notable that matrix prismatic sillimanite appears to be

replacing biotite parallel to the 001 cleavage trace i.e. biotite appears to have been consumed at the expense of sillimanite.

Accessory phases are numerous in pelites. Euhedral zircon clusters were seen in biotites in sample N9.4 displaying radiation halos. Phosphatic phases are common notably (0.5mm) apatite and small size monazite crystals. Semi-quantative EMP analysis showed that xenotime (YPO_4) is a widespread accessory mineral. In sample NP 34.7c clean non-inherited euhedral zircons are found with monazite and anhedral ilmenite within a single biotite grain whilst parallel monazite and sillimanite inclusions are found as inclusions in cordierite and garnet. Curiously, monazite in cordierite exhibits radioactive halos whilst in garnet these are not seen. Secondary alteration of cordierite and feldspar to sericite is frequently observed. Hematite and ilmenite usually occur as inclusions in biotite. In sample NP9.2 accessory Fe-tourmaline and flourite was observed. Steven & Moores (1995) reported abundant tourmalinite mineralization in the Kuiseb Formation 30km west of Omaruru, they attribute this to an abundance of diagenetic boron-rich fluids.

(Opposite) Figure 4.2 (A-E)

A. N3.2 Small (~1mm) post S_1 (syn S_2?) garnet in an annealed fabric. Note that biotite folia are cut by garnet.

B. N9.4 σ type Syn-tectonic cordierite (top left and right) and quartz domains. Note biotite and quartz form asymmetrical pressure shadows. Sense of shear top up to the south west.

C. N29.5 Poikilitic garnet within granoblastic matrix.

D. N42.5 Syn-tectonic, probable Φ type, elongate Kfs porphyroblasts with quartz and biotite inclusions. Section cut parallel to L1 (30-072).

E. N42.5 Syn-tectonic, probable Φ type, cordierite porphyroblasts (< 4mm) enveloped by biotite folia. Note that parallel biotite and quartz inclusions in lower cordierite have an opposite sense to those above.


A
~1mm

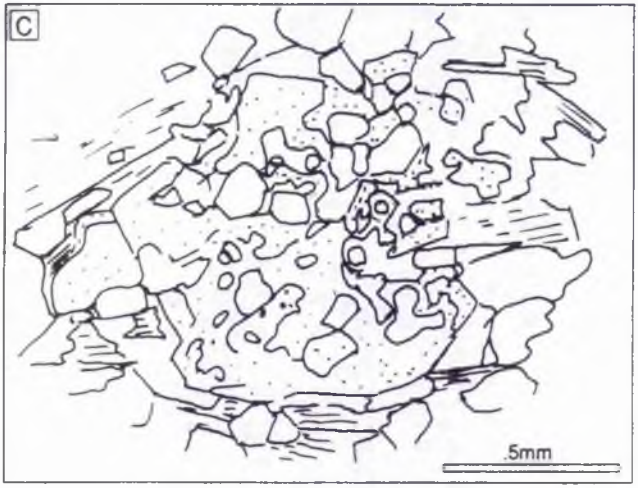
C
.5mm

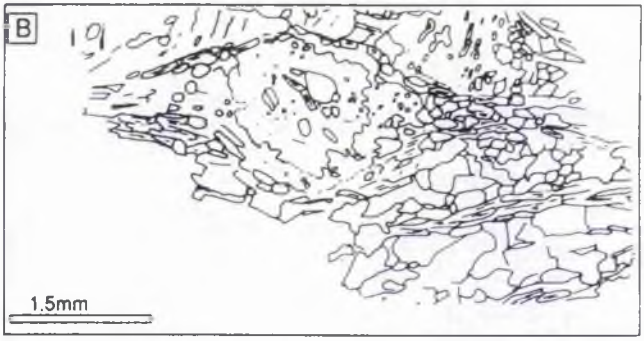
B
1.5mm


D
4mm

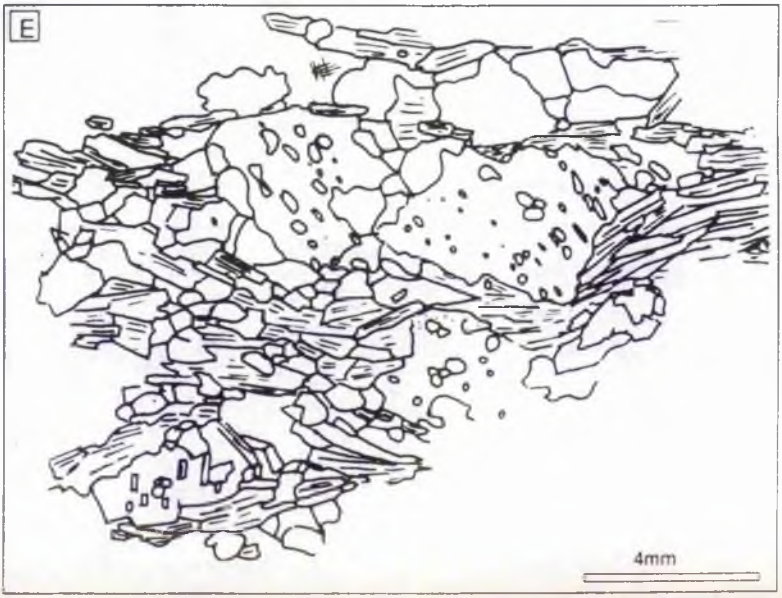
E
4mm

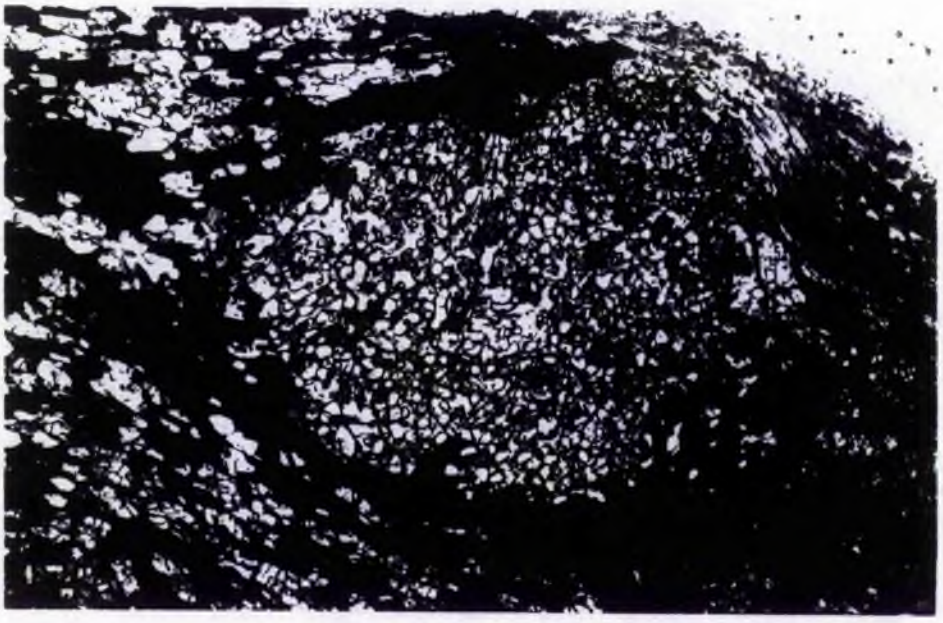

SCALE ---------2mm---------

Plate 4.1A Photomicrograph of N10.1 showing garnet enveloped by matrix bioite. Section cut parallel to L1 (15-102). Photo= inverse image, sense of shear= top up to the south-west.

SCALE ---------1mm---------

Plate 4.1B Photomicrograph of NT34.1 showing garnet cordierite, biotite semplectite. Note also that garnet contains inclusions of tourmaline.

NP3.2	Qtz+Bt > Pl+Kfs+Crd > Grt+Sil+Fe TiO	K.Fm.
Texture	Granoblastic quartz and aligned biotite form matrix. Garnet small < 3mm euhedral and in contact with cordierite, overgrows S1. Cordierite and microcline appears to be replaced by randomly orientated acicular sillimanite and, contains biotite that is obilque to S1	GR[032,057]
NP9.2	Qtz + Bt > Pl + Kfs + Crd > Grt +Tm +Fl Fe TiO	K.Fm
Texture	Fabric is defined by polygonal quartz and plagioclase and aligned biotite. Anhedral garnet blebs are found with lobate quartz and corroded biotite grains. Accessory Fe Tourmaline is enclosed by biotite. Accessory fluorite is enclosed by quartz. Cordierite is not in contact with garnet and pinnitized.	GR[100,106]
NT9.4b	Qtz+Bt > Crd+Pl+Kfs	K.Fm
Texture	A polygonal texture with biotite strongly aligned	GR[101,105]
NP10.15	Qtz+Bt+Grt+Pl+Kfs	K.Fm
Texture	Stromatic gneiss with large > 9mm subhedral poikilioblastic garnets enveloped by biotite coronas. Feldspars and quartz form granoblastic inequigranular texture	GR[087,118]
NP28.14	Qtz+Bt+Pl+Crd+Grt+Spn+Zrn+Fe Ti O	K.Fm
Texture	Anhedral garnet contains biotite inclusions that are parallel to matrix biotite. Garnet and cordierite are not in contact. Main fabric coarse and polygonal with foliation defined by biotite. Accessory xenotime and apatite are common.	GR[035,059]

NP29.5	Qtz+ Bt + Pl + Grt	K.Fm
Texture	Medium granoblastic Qtz-Pl matrix. Aligned Bt defines S1. Grt 2-3mm poilkilitic overgrows matrix Qtz-Bt.	GR[029,064]
NP31.5	Qtz + Bt + Pl + Crd + Grt	K.Fm
Texture	A banded (5-6mm) schist with cordierite rich and garnetiferous horizons. Small subhedral <2mm garnet porpyhroblasts that contain quartz inclusions are enveloped by quartz along with larger 6-9mm poikiloblastic garnets. the main fabric is polygonal. Cordierite contains quartz blebs and straight biotite inclusions.	GR[040,048]
NT31.4	Qtz + Bt > Pl + Kfs + Crd + Grt + Tm +Fe TiO	K.Fm
Texture	Subhedral poikilitic garnet<3mm that contains tourmaline and quartz inclusions is in contact with biotite and cordierite. A quartz biotite garnet semplectite occurs where the three phases meet.	GR[040,049]
NP34.6	Qtz + Bt + Pl + Grt + Fe Ti O	Ar.Fm
Texture	Inequigranular-polygonal texture. Garnets are subhedral 1-2mm with small garnet blebs. Garnet is enveloped by quartz and biotite.	GR[013,059]
NP34.7c	Qtz+Grt +Bt +Pl +Sil	Ar. Fm
	Large > 20mm poikilitc garnets contains quartz blebs, biotite and sillimanite inclusions. Sillimanite inclusions are also present in matrix quartz. Biotite inclusions are in optical continuity with matrix biotites. Garnet and biotite form semplectite.	GR[014,058]

Table 4.3 Summary of pelitic assemblages and textures in the Namibfontein area.

4.2.4 Petrology of cover pelites in the Khan Mine area

Rare pelitic horizons from the Khan Mine area were sampled at the base of the Karabib Formation and, at the Rössing and Chuos Formation boundary. Two samples were analysed; KP10.1 (Qtz+Bt+Grt+Ms+Tm+Kfs) from the base of the Karabib Formation and KP35.11 (Qtz+Bt+Crd>Grt+>Kfs+Mz+(Ser) from the base of the Chous Formation. Garnet forms large (>5mm) and poikilitic porphyroblasts. In Plate 4.2 garnet is seen to have a poikilitic growth core and inclusion free rim. This may suggest a second garnet growth stage has occurred. Cordierite and potassium feldspar in contrast have aligned inclusions of biotite and quartz and are enveloped by biotite folia., their growth is syntectonic. Sillimanite is the only Al_2SiO_5 polymorph present.

SCALE -------0.5mm-------

Plate 4.2 Photograph of EMP compositional image showing Grt with an inclusion free rim. Sample NP35.11.

4.2.5 Meta-arkoses and psammites in the Namibfontein area

A summary of the assemblages and textures of five meta-arkose and psammitic samples is shown in Table 4.5. Compositionally these rocks are have rather simple assemblages, generally: Qtz+Kfs+Pl+Bt+Sil+FeTiO+Ms±Chl±Crd. In the Namibfontein area samples generally have >25% Kfs and are thus termed meta-arkoses.

Grains generally form amoeboid and lobate textures accompanied with quartz blebs (see Plate 4.3). These are interpreted as local migmatitic textures. Feldspar, usually microcline, is anti-perthitic, also noted by Nash (1971). Fibrolite which forms ~20% of most samples was observed in some cases to have formed around 3-4mm hematite blebs. These form the sillimanite knots used in strain analysis (see Section 3.6.1). Importantly the sillimanite within these knots in thin section is quite randomly orientated suggesting that knot shapes, but not individual needles, were controlled by tectonic stress. FeTi oxides are also widespread throughout the matrix. They form elongate symmetrical fish structures in zones near the tectonized basement-cover contact.

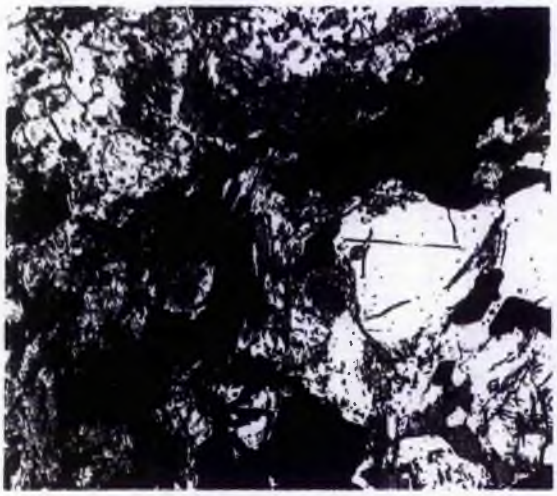

SCALE ------1mm------

Plate 4.3 Photomicrograph showing granoblastic texture in Etusis meta arkose sample NP43.21. Black phase = FeTiO. Top left = Kfs, note sil sub-parallel to bt.

N42.17b	Qtz+Pl+ Kfs+Bt+Sil+FeTiO+Mc +(Chl)	Et Fm
Texture	Granoblastic gneiss with aligned biotites. Large twinned cordierite is extensively replaced by fibrolite. Microcline envelopes cordierite with biotite inclusions. Accessory muscovite and chlorite occurs.	GR[032,086]
N45.1	Qtz+Crd+Pl+Kfs+Bt+Sil+FeTiO+Mc+(Chl)	Et Fm
Texture	Granoblastic-lobate texture. Crd with coarse fibrolite contains quartz blebs.	GR[074,079]
NP42.15	Qtz+Kfs+Pl+Bt+Crd+Sil+FeTi O	Et. Fm
	The fabric is mylonitic. Qtz, Pl, Crd and microcline have been stretched in a ductile manner whilst having seriate-interlobate grain boundaries. Fibrous sillimanite is parallel to the elongation direction in some grains whilst overgrowing Crd+Kfs. In other phases sillimanite has no preferred orientation Fe Ti O form fish-shaped structures. Albite rims form around pyrite.	GR[038,109]
NP22.9	Grt+Sil > Bt+Qtz+Crd	Et. Fm
Texture	Sillimanite envelopes both garnet and cordierite very small biotite grains are in contact with euhedral (> 10mm) garnets	GR[550,113]
NT42.21b	Mc+Qtz+Pl+Bt+Fe TiO	
Texture	Polygonal granoblastic texture	GR[032,087]
NT43.21	Sil+Kfs+Qtz+Bt+Mag	Et. Fm.
	Migmatitic texture grains are extensively corroded and form interlobate fingers. Extensive melt patches and micro-flow folding.	GR[035,109]

Table 4.5 Summary of assemblages and textures of selected samples from the Etusis Fm.

4.2.6 The basic association in the Namibfontein area

A summary of the assemblages and textures of six basic rocks is shown in Table 4.6. Basic samples were collected from three stratigraphic situations. Firstly, they occur as minor *c.*10m units in the Etusis Formation where they contrast sharply with surrounding arkoses (see Section 2.3.1ii). These are substantially altered from Hbl to Bt. Secondly, they occur as Hbl-rich units as described in Section 2.3.1.ii in the Khan Formation. These display a stable granoblastic arrangement of grains (Plate 4.4). Finally, minor units were noted in parts of the Arandis Formation and Kuiseb Formations which contained minor amounts of hornblende. The general assemblage is Qtz+Pl+Hbl+Bt±Kfs+FeTiO.

The amphibole contents of basic gneisses is variable, in the Etusis Formation for example amphibole may constitute as much as 80% of the rock, while in the Khan Formation it ranges from ~10-30%. Generally, amphibole occurs as Fe-rich, dark green pleochroic hornblende. A simple classification of amphiboles is made in Section 4.4.3.ii.

Individual plagioclase composition ranges from Ab 0.15 to Ab 0.67. Comparisons of Ab contents of individual grains (see Appendix 4.2 & 4.3) shows significant differences between individual grains. However, core-rim compositions do not vary greatly.

Accessory phases include ulvospinel, magnetite and apatite. In section NP39.2 ulvospinel forms ~1mm euhedral sub-grains, magnetite is exsolved along cleavage surfaces as minor lamellae. Apatite is a common accessory phase in basic gneisses.

Plate 4.4 Photomicrograph showing granoblastic arrangement of Hbl+Pl+Bt gneiss, sample NP42.12.

NP8.15	Qtz > Pl + Hbl + Fe TiO	Et Fm.
Texture	Granoblastic coarse schist.	GR[087,107]
NP39.2	Pl + Qtz + Hbl + Fe Ti O	Kh. Fm
	Granoblastic inequigranular texture. Irregular hornblende grains > 4mm with complex spinel inclusions. Ulvospinel surrounded by ilmenite then magnetite which is contact with apatite.	
NP42.12	Hbl+Pl+Qtz+Cal(Chl) FeTiO (Mag+Ilm)	Ar. Fm.
Texture	Coarse granoblastic texture. Quartz fingers form irregular contacts with 2-5mm hornblende porpyhroblasts. Magnetite, spinel and ilmenite are in contact with hornblende.	GR[035,113]

Table 4.6 Summary of assemblages and textures of basic association schists from cover rocks in the Namibfontein area.

4.2.7 The basic association in the Khan Mine area

A summary of the textures and assemblages of four samples from basic rocks within the Khan Formation is shown in Table 4.7. Two assemblages are commonly found, these are: 1)Qtz+Pl+Hbl±Kfs±FeTiO and 2)Qtz+Pl+Cpx+Grt+Kfs±FeTiO. For a detailed account of the petrology of the Khan Formation the reader is referred to Nash (1971) Hoffmann (1984a). In general grains form a polygonal texture indicating a degree of equilibrium of the assemblages. In rare instances amphibole overgrows the main fabric (Tack *et al* 1995). Comparison of amphiboles in Section 4.4.3.ii from basement and cover rocks shows no significant compositional differences.

KP21.16	Qtz > Pl > Mc + Hbl + Bt + Fe Ti O ±Chl	L-tectonite augen gneiss.
Texture	Strongly aligned Qtz+Pl+Hbl,granoblastic inequigranular texture	GR[026,053]
KP37	Qtz+Pl+Hbl+Fe Ti O	Kh Fm.
Texture	Granoblastic polygonal	GR[051,031]
KP38.18	Qtz+Pl+Hbl+Bt+Fe Ti O	Kh. Fm.
Texture	Granoblastic inequigranular arrangment of grains. Small deep green Hbl grains commonly form 120° contacts. Larger grains cluster and envelope polygonal feldspar and Qtz. Hbl and Pl have common boundaries.	GR[038,027]
KP8.16	Qtz+Pl+Hbl+Mc+FeTiO	Kh. Fm.
	Granoblastic inequigranular texture. Hbl has oblique xtinction and high relief. Hbl commonly forms 120° contacts with Mc.	GR[065,058]
KP70	Qtz+Pl+Cpx+Grt+Kfs+FeTiO	Kh. Fm.
Texture	Granobalstic polygonal arrangment of all grains. Garnet forms xenoblastic growth in contact with clinopyroxene.	GR[058,051]

Table 4.7 Summary of basic assemblages and textures studied in the Khan mine area

4.2.8 Calc-silicates and marbles in the Namibfontein area

Examples of the assemblages and textures of four calc-silicate samples are shown in Table 4.8. Calc-silicate assemblages were found within most formations as minor and major, massive, non-foliated units. The Arandis Formation and parts of the Khan Formation are dominated by calc-silicate assemblages. Calc-silicate horizons were also present in the Etusis Formation . Calcite-marbles with grains > 10mm were found as minor units in the Arandis Formation and the Arises River Member as nearly pure coarse calcite marble. The assemblage in calc-silicates typically includes Cal+Cpx+Gr±Cz e.g. NT50.4 and NT49.1.

In thinsection siliceous carbonate lithologies are typified by the presence of green diopside (e.g. NT49.1). In NP15.7, however, two pyroxene types were analysed, <10% orthopyroxene of an intermediate orthoferrosillite-enstatite composition was observed in addition to diopside. In NP28.4 two clinopyroxene compositions exist as separate grains of hedenbergite and diopside. EMP data from these sections is presented in Appendix 4.1.

Garnet is common in calc-silicates, it is golden brown when viewed in plane light and from the andradite series (Andr 0.63) (Plate 4.5), commonly it is in contact with diopside. Plagioclase is commonly sericitised and sometimes replaced by calcite. Rhombic sphene is a common accessory phase.

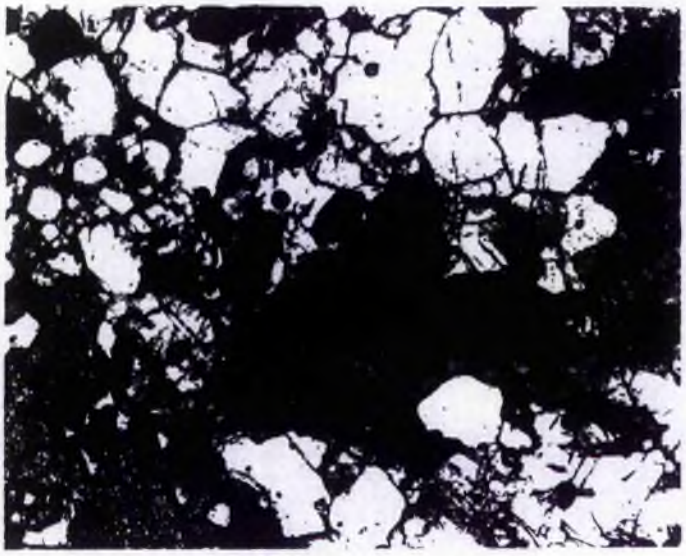

SCALE -------1mm------

Plate 4.5 Photomicrograph showing typical calc-cilicate assemblage Grt (golden brown) +Cpx (green). (Viewed in plane light)

NP15.7	Qtz+ Kfs +Cpx + Opx + Pl + Grt + Chl	Et. Fm
Texture	A granoblastic inequigranular texture. Green pleochroic Cpx grains< 4mm surrounds Opx. Poikiloblastic anhedral garnet contains orthoclase and quartz inclusions and is contact with diopside. Microcline exhibits albite blebs.	Diopside garnet granofels. GR[105,085]
NP28.4	Qtz > Pl + Bt + Hbl + 2Cpx+Fe TiO	Ar Fm
Texture	Coarse granoblastic gneiss with only minor hornblende. Biotite appears corroded containing xenoblastic quartz blebs.	GR[035,065]
NT49.1	Qtz+ Pl + Bt + Hbl + Cpx + Cal	
Texture	Polygonal texture. Xenobalstic diopside appears to be overgrown by hornblende porphyroblasts.	GR[087,121]
NT50.14	Cal + Srp + Phl + Fo+ Wo	Ar Fm?
Texture	Coarse granoblastic calcite grains surrounds anhedral wollastonite; forsterite porphyroblasts nearly all replaced by serpentine.	GR[037,074]

Table 4.8 Summary of textures and assemblages of selected calc-silicate and marble assemblages in the Namibfontein area.

Summary of Petrology

In summary it is apparant that there is no significant variation in metamorphic assemblages from basement and cover litho-types studied in the two areas. The presence of Hbl+Plag and Grt+Cpx assemblages coupled with the absence of orthopyroxene in basic lithologies suggests these rocks are compatible with upper amphibolite facies metamorphism (Kretz 1994). From the preliminary analysis it would seem that no obvious metamorphic gap exists between the basement and cover (see Chapter 5).

4.3 Reaction textures & paragenetic sequences

In this Section a tentative sequence of reactions for each litho-type is proposed. This is based on micro-textural relationships. However, in general, interpretation of thin-section textures gives equivocal results. Common boundaries between most phases (e.g. A+B) does not necessarily constitute evidence of equilibrium. Rather they can be regarded as evidence of either a consuming reaction (e.g. A+B=C) which may be forming a third phase or phase transformation (e.g.A to B) by replacement of one phase by the other. When dealing with a protracted heating event at low pressures as envisaged in the Central Zone (*cf.* Bühn *et al.* 1994 & Masberg 1996) it is likely that this is the case. Furthermore, it appears some phases have had two growth stages (e.g. garnet, see Section 4.2.3) , such that partially resorbed grains may have continued to grow, giving two generations of one mineral in a single thin-section. A second metamorphic event with similar *PT* conditions may give rise to new phases which are metamorphically compatible with the phases from the first event. Thus great care has been employed in the interpretation of thin section textures. Ideally comparison of assemblages from several litho-types should be used to gain emphatic evidence of metamorphic evolution. The scale of observation may also effect the perceived sequence of reactions, often equilibrium is not obtained at the scale of observation because diffusion limits of components control the spatial distribution of the full set of reactions (Carmicheal 1968). In this section most attention is given to the metamorphic paragenesis of pelites since these have provided most data.

4.3.1 Basement lithologies

The limited mineralogy of basement paragenesis in the Namibfontein area mitigates against the deduction of a full sequence of reactions. The main quartzo-feldspathhic phases present are stable over a range of high temperature facies and have merely undergone recyrstallisation to form more stable granoblastic-polygonal textures during metamorphism (Barker 1990). The assemblage Qtz+Bt+Kfs+Pl+Grt+Mz from sample NP43.15 however indicates that perhaps some semipelitic basement is exposed. A likely reaction is that envisaged in Section 4.3.3, e.g. (4.6): Bt+Qtz+Ms=Kfs+Grt+H20, since Ms is absent.

In contrast, in the Khan Mine area the occurrence of amphibolites and hornblende gneisses gives an indication that some mineralogical changes were coeval with metamorphism. Hornblende and plagioclase have common boundaries at 120° (e.g. KP21.16) suggesting hornblende grew during the general coarsening of the matrix. The absence of coexisting Opx and Cpx places an upper limit on the temperature obtained at *c.*700-750°C (Barker 1990).

4.3.2 Pelitic lithologies - M_1 assemblages

In this Section evidence is presented for a general paragenetic sequence of pelitic rocks for both areas. It is evident from the analysis of thin section textures that no evidence remains of the early reactions that produced cordierite (i.e. there is no obvious textural evidence of the early prograde history); therefore, several possibilities arise in defining a prograde paragenetic sequence. It has been shown that cordierite and potassium feldspar porphyroblasts are syntectonic phases enveloped and parallel to matrix biotite folia with inclusions of biotite, quartz, prismatic sillimanite and some plagioclase. Thus the early
production of these two phases may be accounted for by either of two bivariant reactions (4.1) after Jacob (1974a) or (4.2) after Nash (1971), Hoernes & Hoffer (1979) & Hartmann *et al* . (1983).

(4.1) $\quad Bt + Sil + Qtz = Crd + Kfs + H_2O$

(4.2) $\quad Bt + Qtz + Ms = Kfs + Crd + H_2O$

Nash (1971) comments that prismatic sillimanite observed in blastic cordierite suggests sillimanite growth was controlled by muscovite availible from reaction (4.2); such that (4.3) gave way to (4.2):

(4.3) $\quad Qtz + Ms = Sil + Kfs + H_2O$

The preference of cordierite production from the breakdown of muscovite and biotite in this case depends on the interpretation of prismatic sillimanite as a pre-cordierite relict inclusion phase. Prismatic sillimanite however is mainly seen in the cores of cordierite and sometimes found in quartz grains or along corroded biotite cleavage planes. Vernon (1996) comments that only phases in porphyroblasts and that are absent from the matrix are likely to be relict. Thus this may indicate that cordierite production was more likely through reaction (4.1). This reaction was investigated by Hoffer (1976) and found to initiate at about 2.5 kbar at 640° and terminate at the Ab + Or + Qtz + H2O-melt curve at 665° and 2.8kbar. Thus cordierite and potassium feldspar generation was simultaneous, consistent with textural observations.

Garnet in contrast to cordierite appears to have had at least two growth stages. Evidence supports the following three possibilities:

i) that garnet growth followed cordierite;
ii) that garnet and cordierite growth was simultaneous .
iii) that simultaneous garnet and cordierite growth was followed by second garnet growth;

In section (NP34.1) both phases appear to be in equilibrium where examples of garnet moulding cordierite and cordierite moulding garnet can be seen (NT31.4). This suggests that rather than separate growth both phases developed simultaneously. A second late-tectonic garnet growth may be invoked to explain contradictory textures in other thin sections, for example NP29.8b, where subhedral garnet porphyrobalsts have overgrown or cut biotite in optical continuity with matrix biotite.

In view of the evidence in most thin sections the main garnet porphyblastesis probably occurred through the sillimanite consuming reaction (4.4) which Jacob (1974a), Barnes (1981) and Hartmann *et al.* (1983) thought responsible for simultaneous garnet and cordierite growth. Furthermore, coronas of microcline around garnet observed in the same section are compatible with this reaction.

(4.4) $2Bt + 8Sil + 13Qtz = 3Crd + 2Ksp + 2Grt + H_20$ (Thompson 1976)

A second garnet growth phase associated with a late sillimanite overprint has recently been invoked by Nex (1997) who interprets randomly orientated fibrolite in pelites from the Goanikontes area as a product of cordierite consuming reaction (4.5), first identified by Korzhinskii (1936a). Plate 4.2 shows a typical garnet from sample KM35.11 which has an inclusion free rim, this may have arisen from a second garnet producing event. Reaction (4.5) occurs at around 4kb and 740°C (Kretz 1994) and texturally supported by garnet that contains minor prismatic sillimanite in sample NP34.7c (interpreted as evidence of their coeval growth). This would explain the textural relationship of sillimanite with cordierite.

(4.5) $Crd = Sil + Grt + H_20$

Sample N22.9 however, (Figure 4.3) contains euhedral garnet and cordierite (not shown). Garnet has an outer rim with sillimanite inclusions. This is in contact with a < 0.5mm rim of quartz on one side. The remaining garnet surface is enveloped by fibrolite and thin skeletal biotite. Cordierite has not been corroded and suggests that reaction (4.5) was unlikely. The scarcity of sillimanite in most of the observed pelitic samples from the Namibfontein area may additionally indicate reaction (4.5) has not developed to any great extent or that the composition of the pelite has controlled when and where garnet grew.

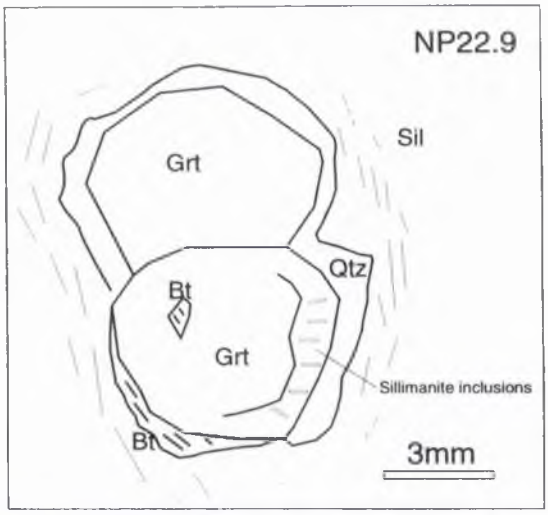

Figure 4.3 Sketch to illustrate Grt with sillimanite inclusions in rim. Grt contains bt and is enveloped by fibrolite.

An alternative to reaction (4.5) could be that garnet growth occurred by the the muscovite consuming reaction (4.6). This reaction is the same as (4.2) but produces garnet at higher pressures (Yardley 1989.p76). Thus if *P* was increasing, garnet growth would appear slightly later than cordierite.

(4.6) $\quad Bt + Qtz + Ms = Kfs + Grt + H_2O$

In summary no observable difference in peak metamorphic history between the two study areas is envisaged from the reaction textures interpreted from meta-pelitic rocks. Peak metamorphic assemblages may be explained by a sequence of prograde reactions. A possible second garnet and sillimanite stage may be invoked during metamorphic evolution.

4.3.3 Psammites and meta-arkoses

The presence of cordierite in some of the impure meta-arkoses in the Namibfontein area suggests reactions (4.1) & (4.2) may have occurred :

(4.1) $\quad Bt + Sil + Qtz = Crd + Kfs + H_2O$

(4.2) $\quad Bt + Qtz + Ms = Kfs + Crd + H_2O$

In most thin sections orientated and unorientated fibrolite is observed cutting across syn-tectonic cordierite, microcline and biotite (e.g. NP42.15) thus it clear a syn-to post-tectonic fibrolite growth occurred. Fibrolite and migmatitic textures are restricted to those samples

within about 200m of the contact between the main intrusion of 'red granite' (it is also seen in basement xenolith sample NT18.4) Interlobate grain boundaries and quartz fingers suggest that near anatexsis conditions were associated with sillimanite growth. It was suggested by Barnes (1981) that the large granite intrusions common in the Central Zone were the cause of a thermal metamorphic event. It is clear that the effects of this are most readily observed in thin sections near to the core of the twin-domes.(see Chapter 5 for a discussion).

4.3.4 Marbles and calc-silicates

Marbles in the Namibfontein area are usually pure recrystallised calcite. A single marble sample containing the assemblage Cal+Fo+Phl+Ser marble was collected from between the Arandis and Etusis Formations, N50.14 GR[037,074]. The paragenesis is in fact very similar to that observed by Mc Dermott (1986) in the Palmental area who suggested the discontinuous reaction (4.7):

(4.7) $\quad Tr + 11Dol = 8\ Fo + 13\ Cal + 9\ CO_2 + H_2O$

which occurs at 600°-670°C(Eggert & Kerrick 1981). Puhan (1983) suggested diopside-dolomite marbles in the Namibfontein area were produced through reaction (4.8) at >600°C.

(4.8) $\quad 1Tr + 3\ Cal = 4\ Di + 1\ Dol + 1CO_2 + 1H_2O.$

The presence of Fo also suggests the reaction:

(4.9) $\quad 3Tr + 5\ Cal = 11Di + 2Fo + H_2O + CO_2$

Reactions (4.7) & (4.8) define an invariant point at ~650°-700°C and XCO_2 0.8 (Eggert & Kerrick *op cit.*) (Figure 4.4).

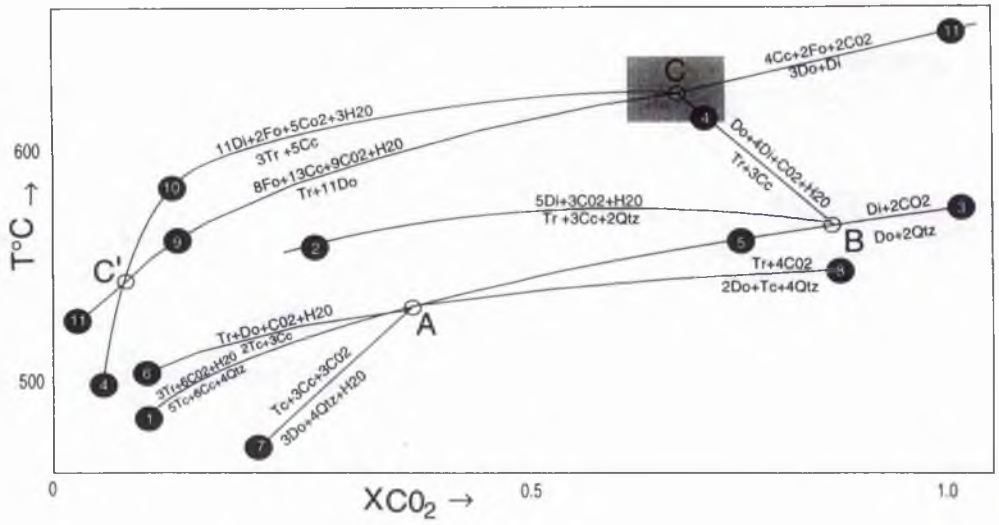

Figure 4.4 A schematic T-X_{CO2} diagram showing mixed volatile equilibria and invariant and points in the siliceous dolomite system copied from Eggert and Kerrick (1981). Reaction numbers from original paper, 4 & 10 = 4.8 & 4.9.

The presence of diopside in calc-silicates indicates that reactions have overstepped the tremolite-out isograd, equivalent to upper amhibolite facies (*cf.* Ferry 1976).

The origin of hornblende overgrowing pyroxene and the presence of two pyroxene types is more problematic. It could be suggestive of retrograde replacement. Alternatively these complex assemblages may be have been caused by skarn-type effects from late granites. Although careful sampling was undertaken this cannot be ruled out. A parallel may be drawn with the coarse patchy skarn-type mineralization seen in basic gneisses of the Khan Formation.

4.4 Quantification of *PT* conditions

From petrographic studies and field observations it is clear that metamorphic assemblages in the lowermost cover and the basement are broadly similar. It is therefore particularly important that quantitative and semi-quantitative estimates of pressure and temperature be obtained. In this section various thermombarometric calibrations have been applied to EMP data in a progressive approach. After preliminary investigation in Sections 4.4.1-4.4.3 selected EMP data has been applied to a number of computer programs to further quantify and refine estimates of PT conditions. The results are summarised in Section 4.5.
A total of 25 sections were analysed. Most of the samples analysed were from the cover, namely pelites, only 4 samples that were analysed from the basement were suitable for EMP work.

4.4.1 Garnet-biotite thermometry

A total twelve sections with coexisting garnet and biotite pairs from pelitic samples have been analysed. Estimates of temperature (C°) were initially made using the BGT spread sheet written by Rao (1995). This runs ten exchange thermometers listed in Table 4.9. A single analysis from the cover (NP10.15) and from the basement (NP43.15) were tested. The results are shown in Table 4. 9 and demonstrate that the highest temperatures where obtained from the calibration of Thompson (1976), Ferry & Spear (1978) and Indares & Martignole model B(1985). The calibration of Ferry and Spear (1978) is based on experimental data from Fe-Mg binary mixtures whilst the calibration of Thompson (1976) is based on an empirical linear relationship between ln K_D and $1/T$ from natural assemblages. These calibrations do not account for biotite non-ideality, the model B calibration of Indares & Martignole (1985) does.

Since the results from the three highest calibrations were similar it was felt justified to use the simple calibration of Ferry and Spear (1978). Even though this may give slightly elevated temperatures McDermott (1986) suggests that re-equilibration of matrix biotite during retro-grade metamorphism in the Damaran Belt to some extent compensates for the effect of Al and Ti substitution for Fe-Mg at high temperatures (a feature that is not accounted for in this calibration). Calibrations that account for Al and Ti substitution may actually yield temperatures that are too low, for example the calibration model A of Indares & Martignole (1985) gives the lowest temperature (662° at 4kbar). Thus the temperatures obtained by this method appear 'more realistic' and have the advantage of allowing comparison with previous work e.g.Nex (1997).

Calibration	SAMPLE=	10.15		43.15	
		5kb	4kb	5kb	4kb
Thompson (1976)		649°	641°	756°	746°
Holdaway & Lee (1977)		625°	621°	714°	710°
Perchuk *et al.* (1981)*		594°	594°	670°	670°
Perchuk & Lavernt' eva (1983)		606°	606°	678°	678°
Ferry & Spear (1978)		**648°**	**644°**	**795°**	**790°**
Indares & Martignole (1985)A		589°	585°	667°	662°
Indares & Martignole (1985)B		633°	630°	713°	708°
Lavrent'eva & Perchuk (1981)		617°	614°	684°	681°
Bhattacharya et al. (1992)		625°	624°	690°	689°
(T (HW) method)					
Bhattacharya et al. (1992)		631°	630°	686°	685°
(T (GS) method)					

Table 4.9 Summary of temperatures obtained from the BGT spreadsheet program.

4.1.1.i Garnet-biotite thermometry (Ferry & Spear 1978)

The calibration of Ferry & Spear (1978) was written into a spreadsheet. The calibration, for Fe^{2+} - Mg^{2+} partioning between garnet and biotite, has a maximum resolution of ±50°C. Equation (1) gives the $T°$ C (2) where $\ln K$ is given by equation (12454 - 4.662T + 0.057P + 3RT $\ln K$ = 0), where:

$$T°K = \frac{\{12454 + (0.057 \times P)\}}{\{4.662 - (5.961 \times \ln K)\}} \qquad \text{and where: } \ln K = \ln \{ (Mg/Fe_{grt} / Mg/Fe_{bt}) \}$$

The results obtained from this calibration for garnet core matrix biotite analyses are shown in Table 4.10 for the cover in the Namfontein area and Table 4.11 for the cover in the Khan Mine area. Temperature estimates using data from a Grt-Bt sample from the basement is shown in Table 4.12. Despite the shortcomings of this method the results are moderately consistent. Furthermore, they serve to illustrate that there is only a slight temperature variation in the cover around the Namibfontein dome, similar to regional scale isograd studies (Hoernes & Hoffer 1979) (see Figure 4.1). It is interesting to note that the highest temperature is recorded in the basement at the core of the Namibfontein dome, N43.15A-C.

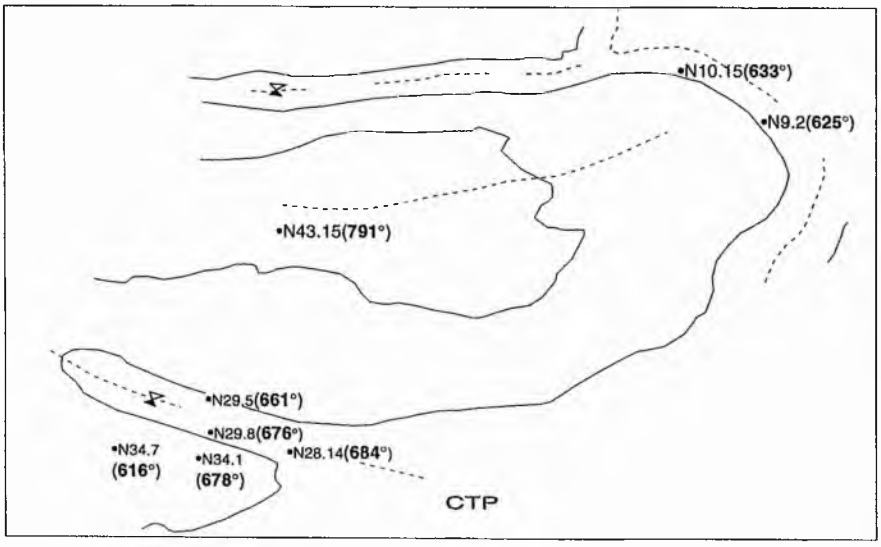

Figure 4.5 Mean garnet-bioite pair temperatures obtained for pelites in the Namibfontein area.

P	NF9.2	NF10.15	NF28.14	NF28.14A	NF28.14B	NF29.5	NF29.8B	NF34.1	N34.6	NP34.7c
4kb	633	621	693	693	686	658	646	651	642	632
	616	644	674	682	692	666	723	695	644	640
	-	-	632	692	690	660	719	689	627	606
	-	-	641	-	698	661	680	-	-	592
	-	-	699	-	717	-	614	-	-	-
5kb	637	625	697	698	689	662	650	655	646	636
	620	648	680	686	696	670	727	699	648	644
	-	-	637	696	693	665	723	694	631	610
	-	-	646	-	701	665	684	-	-	596
	-	-	704	-	720	-	618	-	-	-

Table 4.10 Summary of peak metamorphic temperatures obtained form garnet core and matrix biotite temperatures in pelitic samples using Ferry and Spear calibration (1978), Namibfontein area cover rocks.

P	NF9.2	NF10.15	NF28.14	NF28.14*a*	NF28.15	NF29.5	NF34.1	34.6	NF34.7c
4kb	521	676	608	530	501	596	548	637	471
	-	754	582	-	453	-	524	-	474
5kb	525	680	612	534	505	599	552	641	545
	-	758	586	-	457	-	528	-	449

Table 4.11 Summary of peak metamorphic temperatures obtained from garnet rim and matrix biotite for cover samples from the Namibfontein area using Ferry & Spear calibration (1978).

(A) NP43.15A		(B) NP43.15B		(C) NP43.15C	
4 kb	5 kb	4 kb	5 kb	4 kb	5 kb
572 rim	575 grt 1				
639 core	633				
666	670	806 core grt 3	811		
546	550	803 core grt 6	808	836 core grt 1	841
724	728°	791 core grt 7	796	788 core grt 6	793

Table 4.12 Summary of Grt- Bt temperatures obtained from three basement samples from the Namibfontein area using the calibration of Ferry & Spear (1978). (A)= temperatures from NP43.15A using a single garnet traverse from rim to core. (B)= NP43.15B temperatures using 3 garnet cores . NP43.15(C)= temperature using 2 garnet cores.

	sample		**rim**							**core**
(A)	KP10.1	4kb	594	574	-	-	-	-	-	675
		5kb	597	578°	-	-	-	-	-	679
(B)	KP35.11	4kb	606	641	696	734	741	739	767	755
		5kb	610°	651	700	739	746°	743°	772°	759
		4kb								684
(C)		5kb								688

Table 4.13 Summary of temperatures (C°) obtained from samples KP10.1 & KP35.11, from the cover in the Khan Mine area, using the calibration of Ferry & Spear (1978). (A) & (B) from garnet traverse and matrix biotite analyses, (C) from second garnet core, KP35.11.

4.4.1.ii Inclusion temperatures

In some of the polished sections that where analysed inclusions of biotite were found within the cores of garnet porphyroblasts (Figure 4.6). Potentially these yield the composition of biotite that was in equilibrium with garnet at the early stages of garnet growth.

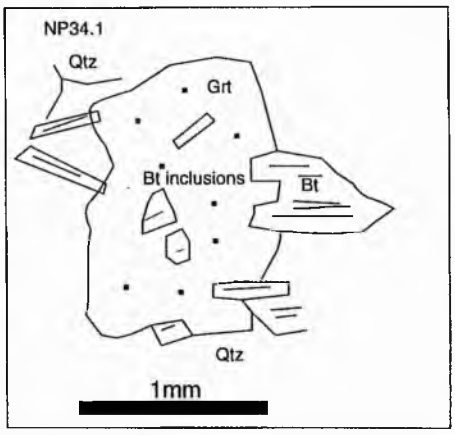

Figure 4.6 Biotite inclusion map for sample NP34.1

The results of thermometry (Table 4.14) show that only sample NP29.8b, which record temperatures of 643°, 647°, appears to record an equilibrium composition. The temperature estimates obtained from the remaining samples are lower than estimates made with matrix biotite. According to Nex (1997), who records a similar phenomena, biotite inclusions have a large surface area in contact with garnet, this actually increases the surface area of biotite in contact with garnet and promotes increased equilibration; estimates made with samples NP10.15, NP34.1, and NP31.5 may demonstrate this.

P/S	T (°C) 4kb	T (°C) 5kb	T (°C) 4kb	T (°C) 5kb
N10.15	548	550	-	-
NF34.1	566	570 grt rim	673 grt core	673
NF29.8b	643	647	577	581

Table 4.14 Summary of temperatures obtained form cover biotite inclusions and garnet cores using the calibration of Ferry and Spear (1978)

4.4.1.iii Reliability of garnet-biotite pair temperatures

In order to undertake meaningful thermometry it has been assumed that all samples are in chemical as well as textural equilibrium, however strictly this is not so. In the first instance it has been stated that matrix biotite is not necessarily in equilibrium with garnet cores. Figure 4.7 shows that a considerable range of compositions exists for matrix and inclusion biotites, despite numerous analyses of each section.

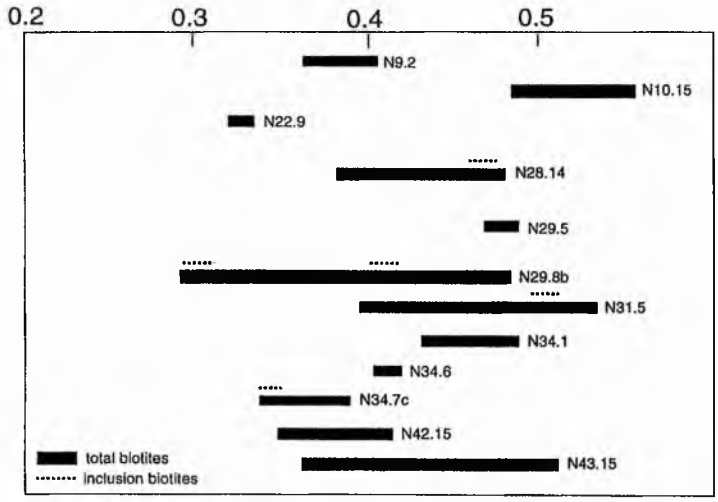

Figure 4.7 Graph to illustrate the range of XMg values for biotites.

Temperature estimations were only made using biotite samples with average X Mg values so that the degree of error caused by compositional variation would be minimised. Meaningful temperatures were obtained from most sections. The effect of weathering is unknown, analysis of fresh garnet and biotite was only made, despite this weathering of samples in the field was evident. Retrogressive effects appear to be negligible, chloritization of biotite was observed in very few sections. The distinction of Fe^{2+} & Fe^{3+} cannot made by the electron probe and was not recalculated by stoichiometric means. Making temperature estimates on total FeO gives slightly elevated temperatures.

4.4.1.iii Conclusion of garnet-biotite thermometry

Estimates of 4kb and 5kb were used for *P*. Average composition of garnet falls within the composition interval 0.80<= Fe/Fe+Mg<=1.00. The results obtained from Ferry & Spear (1978) calibration from garnet cores in the Namibfontein area show range in core temperatures from 616° to 717°C. The average temperature from 8 pelitic samples in the cover is :

662±50°C ±(arithmetic mean at 4kbar estimate) (Namibfontein area)

For two samples in the Khan Mine area:

~700±50°C (approximate estimate at 4kbar)

The average rim temperature for pelites in the cover is:

569±50°C at 4kbar (arithmetic mean).

The average rim temperature from 3 samples in the basement is:

791±50°C at 4kbar (arithmetic mean ~ 129°> than the cover)

4.4.2 Mineral Zoning

The major phases garnet, cordierite, plagioclase, amphibole and biotite were analysed from rim to core to rim in order to detect the presence of chemical zoning, only garnet samples have detectable chemical variation. The absence of chemical zoning in other phases probably reflects complete homogenisation with the surrounding matrix. Chemical variation from garnet rim to core to rim was used to deduce a thermal history of the study area. Idioblastic to sub-idioblastic garnets from most lithologies are observed to have slight reverse profiles with little compositional zonation (see Figure 4.8 and Table 4.15). The Mg, Ca and Mn contents of garnets is generally low, pyrope ranges from 10-12 mole % spessartine < 7 mole % and grossular < 2 mole % while almandine ranges from 70-80 mole %. All garnets were observed to be in contact with deep brown pleochroic biotite, Plate 4.1b shows a quartz-biotite-garnet semplectite texture suggesting that Fe-Mg exchange was occurring between these two phases. Diffusion of material into marginal biotite may have caused rim depletion or complete homogenisation of garnets. Unzoned garnets may therefore be explained by increased diffusion rates common at high temperatures (Dietvorst 1982), alternatively diffusion rates may have exceeded garnet growth rates (Woodsworth 1977). Yardley (1977) investigated the change in compositional zoning in high-grade garnets within the staurolite-sillimanite transition zone;

he observed an 'abrupt change' from bell shaped patterns to flat profiles above an homogenisation temperature of 640 ± 25°C. It is concluded from garnet profiles that temperatures in the Namibfontein area were >640°C such that internal diffusion occured.

		core	rim	core	rim	core	rim	core	rim
sample	*type of zoning*	**Py**		**Alm**		**Sps**		**Grs**	
NF22.9(1)	none	**.08**	.08	**.71**	.72	**.20**	.19	**.02**	.01
NF22.9(2)	none	**.08**	.06	**.72**	.71	**.20**	.17	**.01**	.017
NF28.14	slight reverse	**.02**	.12	**.70**	.75	**.11**	.10	**.03**	.02
NF29.8	slight reverse								
NF34.6	slight reverse	**.21**	.16	**.70**	.73	**.05**	.08	**.04**	.04
NF34.7c	slight reverse	**.15**	.1	**.77**	.81	**.05**	.07	**.03**	.02
NF43.15A	slight reverse	**.16**	.15	**.73**	.72	**.09**	.10	**.03**	.03

Table 4.15 Summary of garnet zoning and average mole end member compostions for the Namibfontein area.

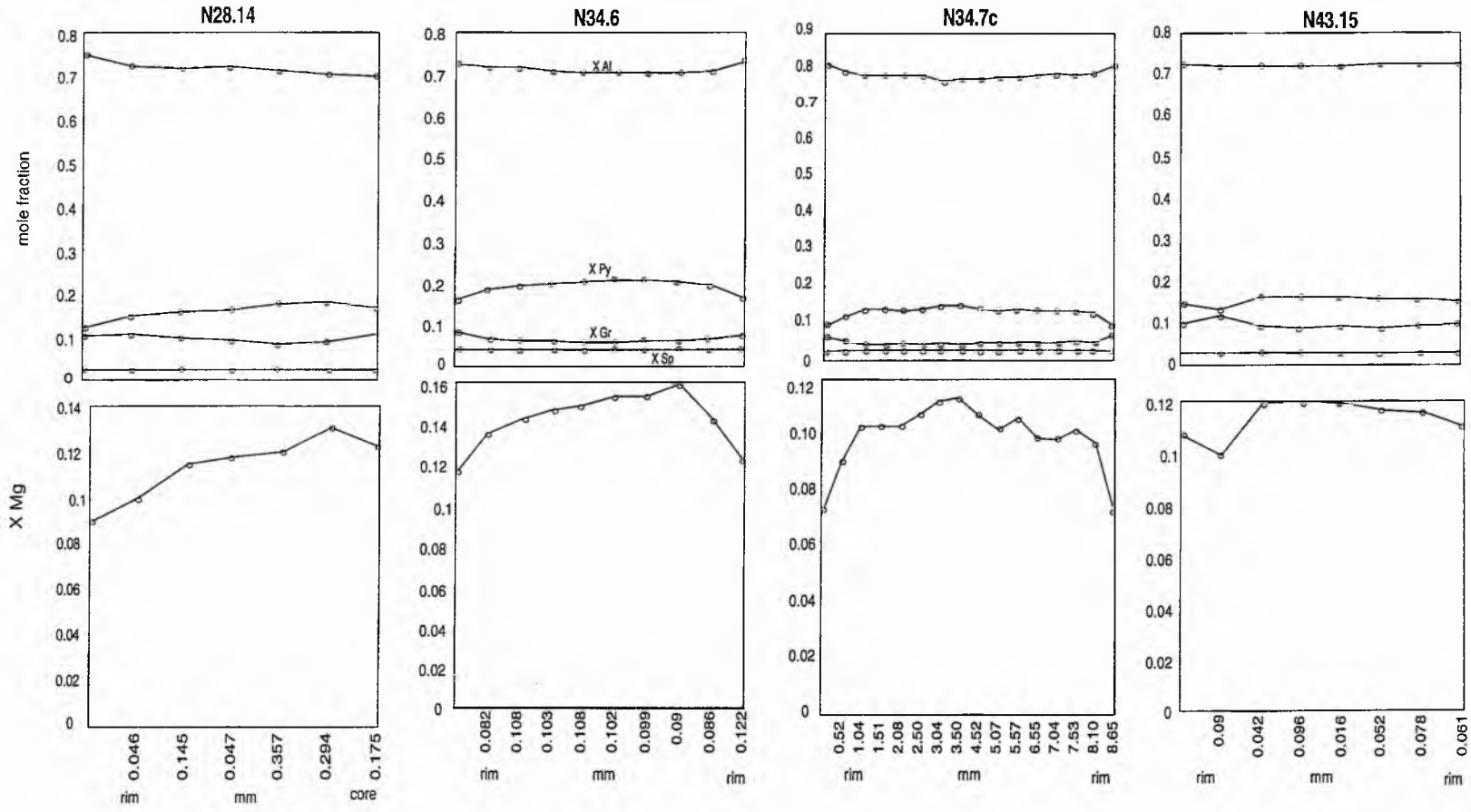

Figure 4.8 Chemical zonation profiles across garnet porphyroblasts from the Namibfontein area. (N43.15 = basement garnet).

4.4.3 Hornblende-plagioclaise thermometry

In addition to temperature estimates from garnet-biotite pairs, an assessment was made using the thermometer of Blundy & Holland (1990) for the exchange of Al^{iv} between coexisting amphibole with plagioclase. Cation exchange occurs between the T1 site of Plagioclase and the A site in hornblende, the reaction is :

Paragasite + 4Quartz = Hornblende + Albite

The thermometer (1) is accurate to ±75° assuming EMP data is recalculated for the presence of ferric iron.

$$T = \frac{0.677P - 48.98 + Y}{(-0.0429 - 0.008314)\ln K}$$

Y represents plagioclase non-ideality (2) The thermometer is sensitive to the Ca content of plagioclase.

$Y = 0$ if $X_{ab} > 0.5$

$Y = \{-8.06 + (25.5 \ (1- X^{Ab})^2 \}$ if $X_{ab} < 0.5$.

and where $K = \{ (Si^{Hbl}) / (8 - Si^{Hbl}) \}$. Plagioclase with compositions < An_{92} amphiboles with less than 7.8 Si atoms per formula unit can only be used; the results obtained are shown below in Tables 4.17 & 4.18.

Sample NP8.15

Pressure	*1 XAb .67*	*2 X Ab .67*	*3 X Ab .67*	*4 X Ab .66*	5
3.2	786°	787°	797°	796°	-
4	774°	775°	785°	784°	
6	743°	744°	754°	753°	

Sample NP28.4

Pressure	1X Ab .50	2 X Ab .50	3 X Ab .39	4 X Ab .50	5 X Ab .46
3.2	704°	704°	681°	608°	599°
4	693°	693°	670°	598°	589°
6	666°	666°	641°	577°	605°

Sample NP42.12

Pressure	1 X Ab .15	2 X Ab .15	3 X Ab .15
3.2	867°	872°	869°
4	852°	856°	854°
6	812°	816°	814°

Table 4.16 Summary of temperatures obtained from Hornblende Plagioclase thermometry for the Namibfontein area. Temperatures are shown for 3.2,4 & 6kbar. Estimates in italics corrected for Fe3+ after Droop (1987).

Sample KP38.18		Sample KP 21.16	Sample KP70	
1 XAb .57	2 X Ab .57	1 X Ab .15	1 X Ab .15	2 X Ab .14
841°	846°	848°	866°	877°
828°	833°	835°	855°	853°
796°	801°	802°	807°	810°

Table 4.17 Summary of temperatures obtained from Hornblende Plagioclase thermometry for the Khan Mine area cover amphibolites corrected for Fe3+ after Droop (1987).

Sample KP21.19

1 X Ab .42	2 X Ab .41	3 X Ab .41
850°	848°	857°
837°	835°	843°
804°	802°	810°

Table 4.18 Summary of temperatures obtained from Hornblende Plagioclase thermometry for the Khan Mine area basement. Temperatures are shown for 3.2, 4 & 6kbar corrected for Fe3+ after Droop (1987).

4.4.3.ii Summary of hornblende -plagioclase thermometry

The results from this approach have yielded uniformly high temperatures using a range of test pressures (3.2, 4, 6 kbar). The arithmetic mean from each section is taken at 4 kbar from the results of barometry shown in Section 4.5. These are:

sample	T°C	Location
NP8.15	786°C	
NP28.4	**669°C**	Namibfontein cover
NP39.2	855°C	
KP38.18	844°C	Khan Mine cover
KP70	872°C	
KP21.16	845°C	
KP21.19	846°C	Khan Mine basement

Except for sample NP28.4 the values obtained are anomalously high indicating granulite facies temperatures. They are approximately 100°C higher than the garnet-biotite temperatures in Section 4.4.1. Inspection of amphibole compositions using the classification scheme of Miyashiro (1973) (Figure 4.9) shows that the composition of sample NP28.4 is tremolitic and represents a distinctly different amphibole type. (Using the classification scheme of Leak (1978) the analyses plot between the boundary between ferro-edenitic-hornblende and edenitic-hornblende).

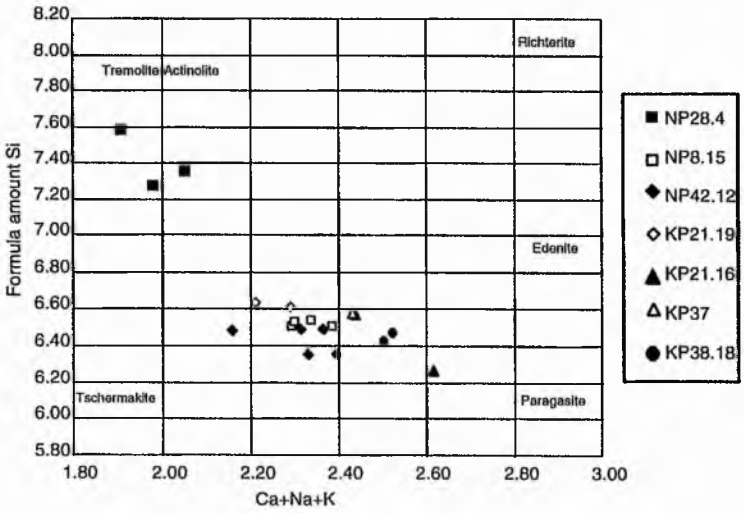

Figure 4.9 Amphibole classification after Miyashiro (1973)

The level of accuracy of this thermometer has in fact been questioned by Holland & Blundy (1994) in view of "erroneously high temperatures" obtained with garnet hornblende amphibolites. They have proposed two revised thermometers which account for hornblende

non-ideality and incorporates data from natural amphiboles which tend to be more aluminous. The mole % Al_2O_3 contents of sample NP28.4 lies between 0.35 and 0.75 while all other hornblendes have values greater than 1.6. This is consistent with the fact the calibration applied has yielded falsely high temperatures and is better suited to low aluminous hornblendes.

A simple approximation of metamorphic grade can be made from the Ti composition of amphiboles. Rasse (1974) compared the titanium contents of natural hornblendes to metamorphic grades; he identified four facies by plotting the total Ti contents calculated to 23 oxygens. In general titanium contents increases with metmorphic grade. Upper amphibolite facies lies between 0.06 and 0.22. Figure 4.10 shows that samples in this study fall in this range.

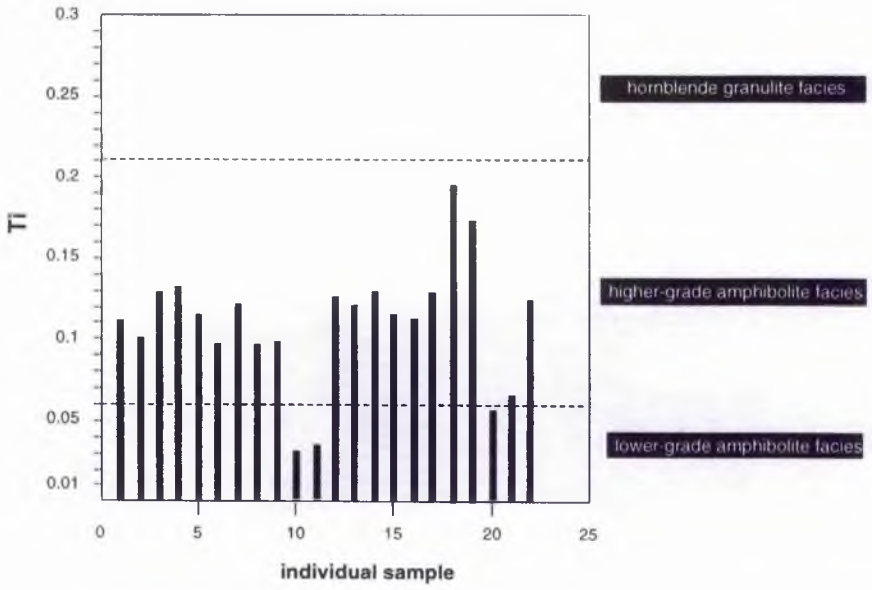

Figure 4.10 Estimation of metamorphic grade from Ti contents of all amphibole analyses in the study areas, after Rasse (1974).

4.4.4 Qualitative barometry

Estimation of peak metamorphic pressure from cover pelites was made using an integrated graphical barometer developed by Waters (1991) and later Argles (*pers. comm.*) A 'general fix' on pressure can be obtained using the barometer assemblage Grt-Crd-Sil-Qtz. This works by recording the net exchange of Fe-Mg between Grt-Crd. XMg isopleths thus correspond to pressure. Figure 4.11 shows sub-horizontal isopleths of cordierite composition constructed using data from natural pelite samples. Crd XMg composition from Namibfontein area is shown in the grey box Figure 4.11. The A total of 26 analyses indicate a range from XMg 0.238 to 0.312 with corresponding pressure in the range 3.2-3.5 kbar and an average of 3.3kbar (see Table 4.19).

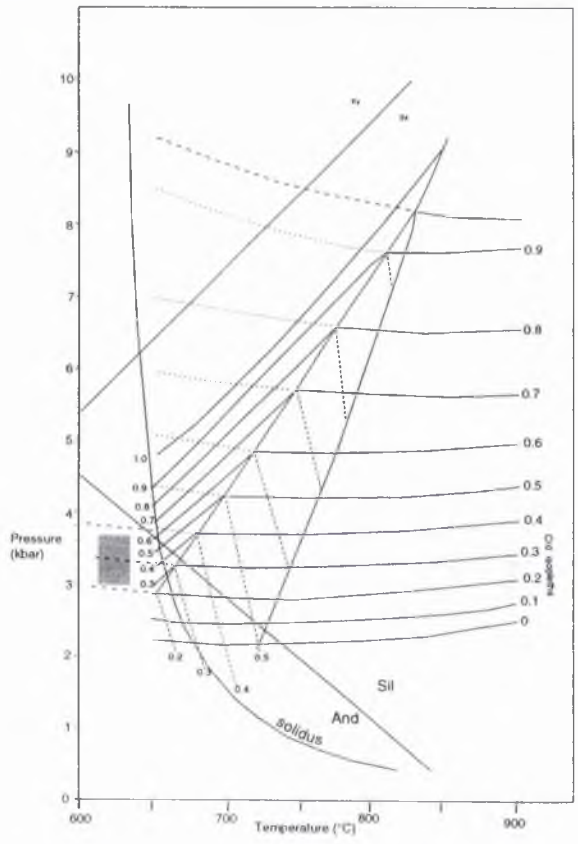

Figure 4.11 Graph showing Grt-Crd XMg isopleths developed by Argles *pers. com.* (1997) after the method of Waters (1991). Curved line (left) = Minimum melt curve Qtz-Ab-Kfs+granite melt. Sub-vertical line (left) = invariant curve Bt-Sil-Qtz - Grt-Crd-Kfs. bt-crd-sil contours = steep closely-spaced lines, grt-bt-crd contours =steep, closely-spaced contours above down left to right, grt-crd-sil contours= subhorizontal contours.

P/S	core	core	core	core	core	core	rim	rim	mean
NF9.2									
X Mg	.247	.238	.317	.236	-	-	-	-	
P (kbar)	3.2	3.1	3.5	3.2	-	-	-	-	**3.3**
NF28.14									
X Mg	.25	.253	.249	.243	.253.	.253	.253	.253	
P (kbar)	3.2	3.2	3.2	3.2	3.2	3.2	3.2	3.2	**3.2**
NF29.8b									
X Mg	.262	.262	.268	.265	.266	-	.260	.265	
P (kbar)	3.25	3.25	3.25	3.25	3.25	-	3.25	3.25	**3.25**
NF34.1									
X Mg	.277	.312	.275	-	-	-	.274	-	
P (kbar)	3.3	3.5	3.3	-	-	-	3.4		**3.4**
NF42.12c									
X Mg	.276	.269	.264	-	-	-	-	-	
P (kbar)	3.3	3.3	3.3	-	-	-	-	-	**3.3**

Table 4.19 Summary of qualitative cordierite pressures obtained for basment rocks, after Waters (1991) Argles (*pers. comm*).

4.4.5 Thermobarometry with the computer program THERMOCALC

In order to obtain additional *PT* estimates compositions of all phases in a pelitic sample NP34.1 (Qtz + Bt + Grt + Crd + Sil + FeTi O Appendix//) were run using the phase diagram mode of the computer program THERMOCALC (Powell & Holland 1988). THERMOCALC works by computing a list a reactions from the activities of given end-member fractions. Not all the activity models are well constrained such that *PT* from reactions are not always compatible. Thus it is essential to observe the textural critria of the phases in thin section before using the program.

After observation of a suitable section EMP analysis of an intermediate garnet core, cordierite rim and biotite inclusion was entered into the computer program RECALC (Powell & Holland 1988) to calculate the mixing activities of the end member fractions. This data was entered into THERMOCALC which caclulated all possible reactions within a *PT* window of 200-900°C and 1-9kbar. The results indicated six balanced reactions from eight outlined below (Figure 4.12) involved in three invariant reaction line intersections, two of which are stable:

(1) 2 Alm + 3Crd = 2Py + 3 Fcrd

(2) East + Py + 3Qtz = Phl + Crd (single data point 620° 3kbar)

(3) Ann + Py = Phl + Alm

(5) 3East + 3Alm + 9Qtz = 2Phl + Ann + 3 Fcrd

(6) 3East + Py + 2Alm + 9Qtz = 3Phl+ 3Fcrd

(7) 2Phl + 3Fcrd = 2East + 2Alm + Crd + 6Qtz

(8) 3East + 5Alm + 9Qtz = 3Ann + 2 Py + 3Fcrd

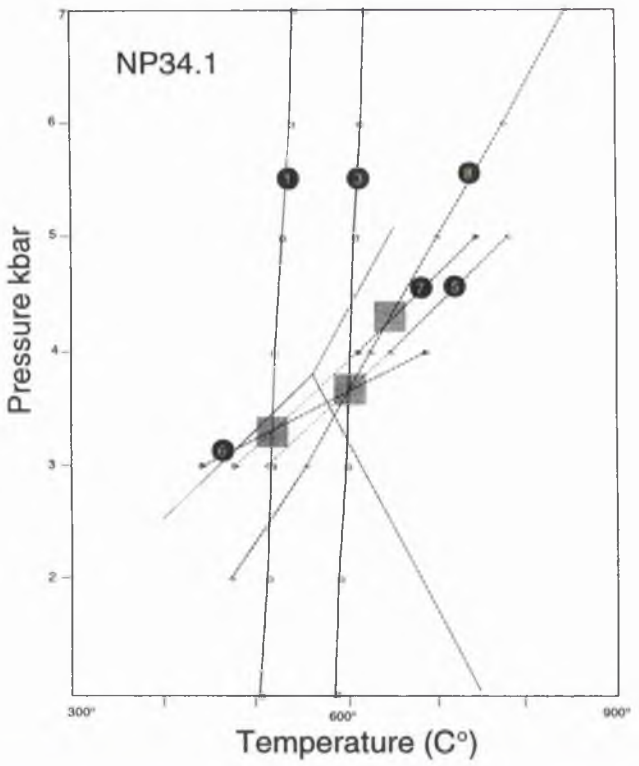

Figure 4.12. Reactions obtained from THERMOCALC plotted for sample NP34.1. (1) 2 Alm + 3Crd = 2Py + 3 Fcrd (2) east + Py + 3Qtz = Phl + Crd (single data point 620° 3kbar) (3) Ann + Py = Phl + Alm (5)3East + 3Alm + 9Qtz = 2Phl + Ann + 3 Fcrd (6) 3East + Py + 2Alm + 9Qtz = 3Phl+ 3Fcrd (7) 2Phl + 3Fcrd = 2East + 2Alm + Crd + 6Qtz (8) 3East + 5Alm + 9Qtz = 3Ann + 2 Py + 3Fcrd

The first intersection involves reactions (6) (5) (8) (3) (marked with *) where: P = 3.7 kbar and T= 604°C using values of a(H20) 0.1-0.9. The second intersection involves reactions (2) (6) (7) (1) where P=3.3 and T=521°C. The absence of andalusite suggests this intersection is unlikely. A third intersection involves reactions (7) and (8) at ~4.4 kbar and 640°C. From the presence of sillimanite in NP34.1 it is likely that intersection 1 and 3 have occurred. P is bracketed between 3.7-4.4kbar and T 604-640 °C and is in good agreement with the results of grt-bt thermometry.

4.4.6 Garnet-cordierite thermobarometry

EMP data from sample N34.1 was also run additionally to THERMOCALC on the recent computer program NICHOLS (Nichols *et al.* 1992). The program contains internally consistent gahnitic spinel-cordierite-garnet equilbria in the system FMASHZn (Nichols *et al.* 1992). Pressure and temperature is calculated from the follwing calibrations applied to the reactions (25), (26) and (27) from Nichols *et al* (1992):

Garnet-cordierite thermometry, *FMAS* 2prp+3Fe-crd=2alm+3crd

$$T = \frac{113{,}116 + 630P}{-31.87 - \mathrm{R}\ln\dfrac{(a_{\mathrm{Gnt}}^{\mathrm{alm}})^2(a_{\mathrm{crd}}^{\mathrm{Mg-crd}})^3}{(a_{\mathrm{Gnt}}^{\mathrm{prp}})^2(a_{\mathrm{crd}}^{\mathrm{Fe-crd}})^3}}$$

Garnet-cordierite barometry, *FAS* 2alm+4sil +βqtz=3Fe-crd

$$P = \frac{-151{,}416 + 182.85T - \mathrm{R}T\,\mathrm{in}\dfrac{(a_{\mathrm{crd}}^{\mathrm{Fe-crd}})^3}{(a_{\mathrm{Gnt}}^{\mathrm{alm}})^2}}{15{,}300}$$

MAS 2prp+4sil +βqtz=3crd

$$P = \frac{-38{,}300 + 151.48T - \mathrm{R}T\,\mathrm{in}\dfrac{(a_{\mathrm{crd}}^{\mathrm{Mg-crd}})^3}{(a_{\mathrm{Gnt}}^{\mathrm{prp}})^2}}{14{,}670}$$

T is accurate ±50°C and P within ± 1.4kbar. Pressure and temperature data are given in graphical and numerical form. Figure 4.13 shows the results obtained using the garnet-cordierite-sillimanite-quartz option.

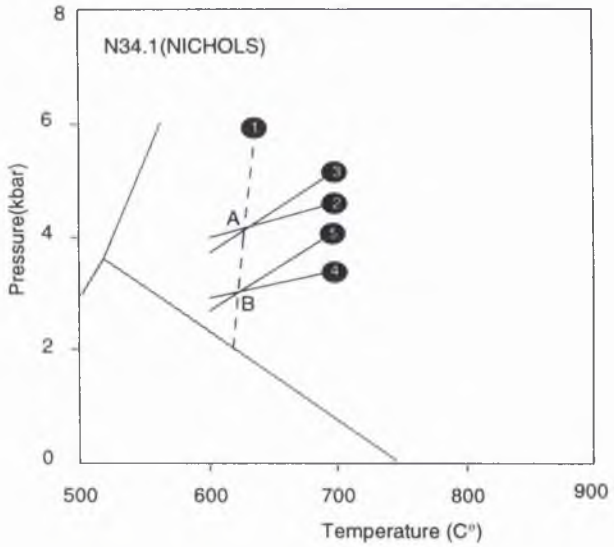

Figure 4.13 Results of thermobarometry using the computer program NICHOLS with data from NP34.1. 1=Thermometer, 2= MAS wet, 3= FAS wet, 4= MAS dry, 5= FAS dry. A= wet intersection, B= Dry intersection.

The results indicate two intersections of the thermometer with Fe-end member Mg-end member barometers. The first at 3.5 kbar and 625°C for dry conditions and the second at 4.2kbar and 660°C for wet conditions.

4.4.7 Thermobarometry with the computer program GTB

GTB(version 1.9) is a thermombarometry program based on a set of Fortran programs developed by Spear *et al.* (1991). To use the program mineral analyses are calculated to the relevant number of oxygens and entered into a mineral file. GTB gives a choice of thermobarometric calibrations from which it computes key reaction lines. In this study two thermometers and two barometers were used. Temperatures were obtained using the calibrations of Ferry & Spear (1978) (samples NP10.15, NP34.1, NP28.14 and NP43.15B, NP43.15C) and Nichols *et al.* (1992) (sample NP34.1).

Pressures were obtained from the calibrations of Nichols *et al.* (1992) for Grt-Crd assemblages (samples NP28.14 & NP9.2) and Hoisch (1990) for Grt-Bt-Pl assemblages (samples NP10.15, NP28.14, NP34.1, NP34.6, K35.11, NP43.15B & NP43.15C); this allowed estimates of pressure to be made for cover rocks in the Khan Mine area and basement in the Namibfontein area.

The calibrations of Hoisch (1990) are as follows:

R1. $\frac{1}{3}\text{Pyrope} + \frac{2}{3}\text{Grossular} + \text{Eastonite} + 2\text{Quartz}$

$\longleftrightarrow 2\text{Anorthite} + \text{Phlogopite}$

$$P = \frac{-31830.6 + 79.0281T - RT\ln K_{R1} - 26968(X^B_{Al} - X^B_{Mg}) + 32604.5X^B_{Fe} + 42855.4X^B_{Ti}}{3.8145 - \frac{2}{3}\Delta V_{gr}}$$

R2. $\frac{1}{3}\text{Almandine} + \frac{2}{3}\text{Grossular} + \text{Siderophyllite} + 2\text{Quartz}$

$\longleftrightarrow 2\text{Anorthite} + \text{Annite}$

$$P = \frac{-46707.2 + 85.5824T - RT\ln K_{R2} - 30960(X^B_{Al} - X^B_{Fe}) + 24289.6X^B_{Mg} + 37265.6X^B_{Ti}}{3.8986 - \frac{2}{3}\Delta V_{gr}}$$

Analysis of cover samples in the Namibfontein and Khan mine area are shown in Figure 4.14a plots A-G. The plots show pressure obtained from Hoisch (1990) Grt-Bt-Pl samples in red, Nichols *et al.* (1992) Grt-Crd in red and Ferry & Spear (1978) in green, except for plot G which shows a temperature range using the calibration of Indares & Martignole (1985) models A&B and Ferry & Spear (1978).

The use of the Hoisch (1990) method has given consistent estimates of *P* for the Namibfontein arae. Plots A-F show pressure in the range 3-4kbar. This was obtained using the intersection of thermometers in plots B, C & mean Grt-Bt pair temperature of 662°C from Section 4.1.1.i. In the Khan mine area P was estimated at 3-2 & 5.5 kbar, from only two analyses. This at least 1 kbar higher than the cover in the Namibfontein area, consistent with an increase in regional pressure and temperature to the west reported by Masberg *et al.* (1992).

A comparison of *PT* conditions between cover and basement rocks from the Namibfontein area is shown in plots H-I (samples N43.15B & N43.15C from the basement) & J-K (N28.14 & N34.1 from the cover) (Figure 4.14b). Eight seperate grt-bt calibrations were used to obtain minimum and maximum temperature estimates; areas of *PT* space have then been constructed (grey squares plot L) by combining these results with pressures for samples N43.15B (5.9 kbar±1) & N43.15C (7kbar±1), plots M & N after Hoisch (1992) and plots C & E . (Figure 4.14b).

Two conclusiosn may be drawn from these results Firstly, that peak metamorphic conditions in the basement were ~2kbar and 140°C higher than in the cover, this is greater than the error limits of the calibrations used and is therefore significant. Secondly, that the higher grt-bt basement temperature estimates made in Section 4.4.1iii are confirmed. The application of other grt-bt calibrations.

Figure 4.14. A. (COVER) Plots obtained from the computer program GTB.

Plot A. Sample NP9.2 from a Grt-Crd-Bt gneiss. 1=Fe end member barometer 2=Mg end member. Analyses Crd(14), Grt (16).

Plot B. Sample NP10.15 from a Grt-Bt-Pl gneiss. Analyses Grt(5),Bt(6) and Pl(12).

Plot C. Sample NP28.14 from a Grt-Crd-Pl gneiss. Analyses Pl(6), Grt(19, Bt(2), Crd(1)

Plot D. Sample NP29.8 from a Grt-Bt-Crd-Pl gneiss. Analyses Pl(22), Crd(1), Grt(8), Bt(6).

Plot E. Sample NP34.1 from a Grt-Crd-Grt-Bt-Sil gneiss. 1= Ferry & Spear (1978) estimate from section 4.1.1.i. Analyses Bt(9), Crd(5), Grt(1), Pl(13).

Plot F Sample NP34.6 from a Grt-Bt-Pl gneiss. Analyses Pl(4)&(7), Bt(6), Grt(1).

Plot G Sample NP35.11 from a Grt-Crd-Bt-Pl gneiss. Analyses Pl(1)&(4), Grt(1), Bt(2).

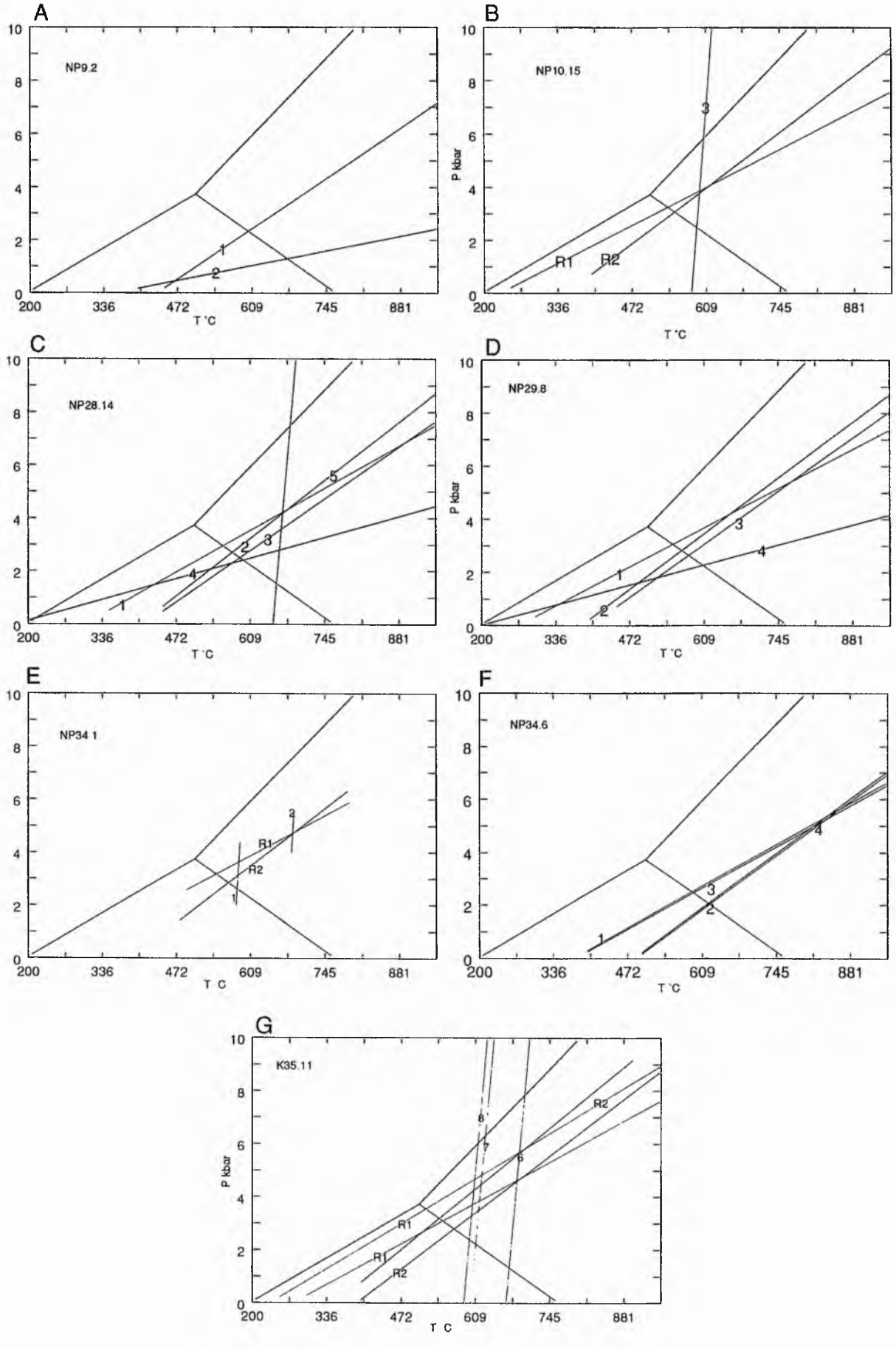
A
NP9.2
B
NP10.15
C
NP28.14
D
NP29.8
E
NP34.1
F
NP34.6
G
K35.11
P kbar
T °C
200
336
472
609
745
881
R1
R2

Figure 4.14. B. Plots obtained from the computer program GTB. Plots H-K show a range of temperatures obtained from Grt-Bt calibrations. 1=Ferry & Spear (1978), 2= Hodges & Spear (1982), 3= Ganguly & Saxena (1984) sym, 4= Ganguly & Saxena (1984) asym, 5= Perchuk & Larent' eva (1984), 6= Indares & Martignole (1985), 7=Ferry & Spear with Berman (1990) Grt, 10= Kleeman & Reinhardt (1994).

Plot H. Sample NP43.15B from a Grt-Bt-Pl basement gneiss. Analyses Grt(6),Bt(8).
(Pressure obtained from plot M)

Plot I. Sample NP43.15C from a Grt-Bt-Pl basement gneiss. Analyses Grt(4),Bt(2).
(Pressure obtained from plot N)

Plot J. Sample NP28.14 from a Grt-Crd-Grt-Bt-Sil gneiss. Grt(19, Bt(2).

Plot K. Sample NP34.1 from a Grt-Crd-Grt-Bt-Sil gneiss. Analyses Bt(9), Grt(1).
(Pressure obtained from Crd barometry)

Plot L. Plot to summarizing *PT* space for samples NP43.15, BNP43.15C(basement) and NP28.14, NP34.1(cover).
(Pressure obtained from Crd barometry)

Plot M. Sample NP43.15B from a Grt-Bt-Pl basement gneiss. Analyses Grt(7),Bt(8), Pl(1)&(4), showing pressure and temperature.

Plot N. Sample NP43.15C from a Grt-Bt-Pl gneiss. Analyses Grt(1),Bt(2), Pl(4), showing pressure and temperature

---

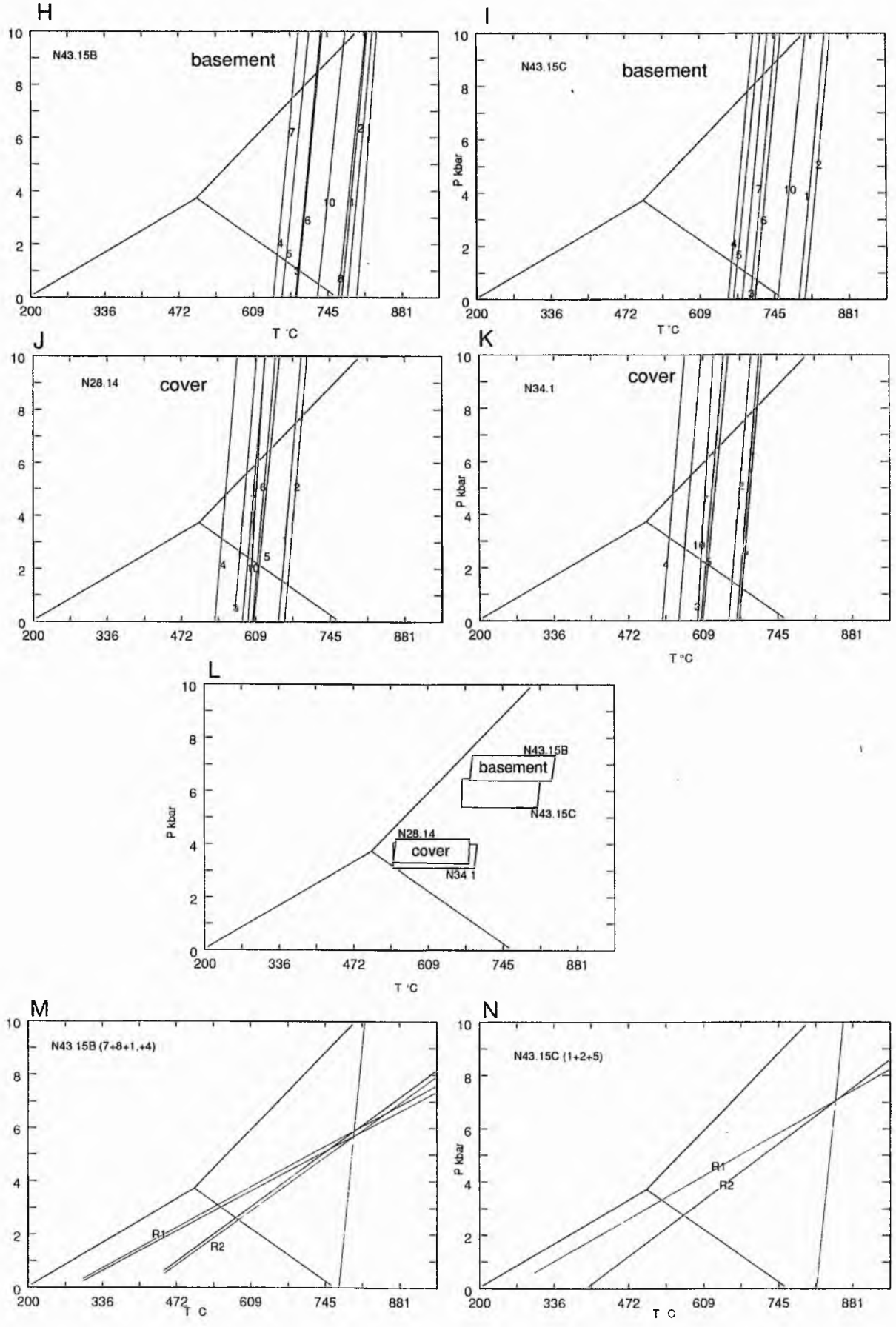
H
N43.15B
basement
I
N43.15C
basement
P kbar
T °C
J
N28.14
cover
K
N34.1
cover
L
N43.15B
basement
N43.15C
N28.14
cover
N34.1
M
N43.15B (7+8+1,+4)
R1
R2
N
N43.15C (1+2+5)
R1
R2

4.5 Summary of *PT* conditions

A summary of *PT* estimates from this study is shown in Table 4.20. The use of several approaches has given similar results, this is encouraging. For cover rocks in the Namibfontein area peak metamorphic conditions were estimated using seven methods, two were used to obtain estimates from basement rocks. In the Khan Mine area *PT* estimates were made using three methods for the cover and one for basement rocks.

In the Namibfontein area Grt+Crd+Bt+Pl gneisses from the cover record *PT* conditions for M_1 at ~662°C and 3.3-4 kbar. In the Khan Mine area Grt+Crd+Bt+Pl gneisses record *PT* conditions for M_1 ~690°C and ~5kbar. In the Namibfontein dome, basement Grt+Bt+Pl gneiss records M_1 at ~800° and ~6-7kbar, possibly as much as 140°C higher and 3kbar greater than the cover.

Table 4.20. Summary of M1 PT conditions from a variety of thermo-barometers for the Namibfontein and Khan Mine areas.

Calibration/ Method	*P* kbar	*T* °C		Description
Ferry & Spear (1978)	(4kbar)	662±50°C	COVER	arithmetic mean 4kbar(cores)
Ferry & Spear (1978)	(4kbar)	640±50°C	COVER	median 4kbar(cores)
			COVER	
Ferry & Spear (1978)	(4kbar)	569±50°C	COVER	arithmetic mean 4kbar(rims)
			COVER	
Ferry & Spear (1978)	(4kbar)	548-740±50°C	COVER	bt inclusion-grt core range
Ferry & Spear (1978)	(4kbar)	755& 675±50°C	COVER	core temperature
Ferry & Spear (1978)	(4kbar)	594 & 606±50°C	COVER	rim temperature
				KHAN MINE AREA
Garnet Profiles (qualitative)		>640°C±25	COVER	NAMIBFONTEIN AREA
Blundy & Holland (1990)		786°,669°,855° ±75	COVER	Cover arithmetic means per sample
Blundy & Holland (1990)		844°,872° ±75		Cover arithmetic means per sample KHAN MINE AREA
Argles pers comm.	3.2-3.5	(>650°)	COVER	Crd barometry
THERMOCALC	~3.7-4	604°-650°	COVER	Cover Crd-Grt (NF)
NICHOLS	3.4	622°	COVER	NP34.1 Crd-Grt (NF)
GTB	~4	~610°	COVER	NP9.2 Nichols et al. (1992)
GTB	~4	~610°	COVER	NP10.15 Hoisch (1990) Ferry & Spear (1978)
GTB	3-4.5	~650°	COVER	NP28.14 Hoisch (1990) Ferry & Spear (1978) Nichols et al. (1992) NP29.8b
GTB	3.8-4	600-670°	COVER	NP34.1 Hoisch (1990) Ferry & Spear (1978) Nichols et al. (1992)
GTB	3-4		COVER	NP34.6
Rasse (1976)		>650°		Ti content of amphiboles NAMIBFONTEIN AREA
GTB	4.6& 5.9 ±1	>600°	COVER	KP35.11 KHAN MINE AREA
GTB	5.9 ±1	~800°	BASEMENT	Sample NP43.15B Basement
GTB	7 ±1	~800°	BASEMENT	Sample NP43.15C Basement NAMIBFONTEIN AREA
Ferry & Spear (1978)	(4kbar)	791°C	BASEMENT	Basement mean core temperature NAMIBFONTEIN AREA
Ferry & Spear (1978)	(4kbar)	572°C	BASEMENT	Basement rim temperature NAMIBFONTEIN AREA
Garnet Profile		>640°C±25	BASEMENT	
Blundy & Holland (1990)		845°, 846°	BASEMENT	arithmetic means per sample KHAN MINE AREA

4.6 The relationship between deformation and metamorphism

This section discusses the timing of metamorphism with respect to deformation. M_1 or peak metamorphism in the Central Zone has been interpreted as syn-tectonic (Barnes 1981). In this study however, a progressive deformation, stage 1 to 3, is envisaged and thus metamorphism and mineral growth is placed within this scheme. The peak of deformation is regarded as stage 2 when mesoscale folds became fully developed. This provides a reference point for the relative timing of microfabric-porphyroblast relationships.

S_1 microfabric is defined in thin sections by aligned biotite and quartz parallel to S_0. Its growth must have initiated before stage 2 since it is folded i.e. it defines regional structure. There is no evidence of early pre-tectonic fabric growth recorded in either garnet or cordierite porphyroblasts, rather biotite and quartz inclusions form straight inclusion trails that are either slightly oblique or parallel to external fabrics. Straight inclusions probably represent syntectonic alignment controlled by cordierite internal structure. Barnes (1981) regards the main regional fabric in this study as axial planar to 'spectacularly heterogeneous' F_2 folds (Barnes' F_3 correspond to stage 2 F_2 folds in this study, his F_2 were not recorded in this study, see Section 6.1.1). Figure 4.15 shows folded S_1 microfabric that defines an F_2 microfold. Biotite forms a tight arc of coarse flakes.

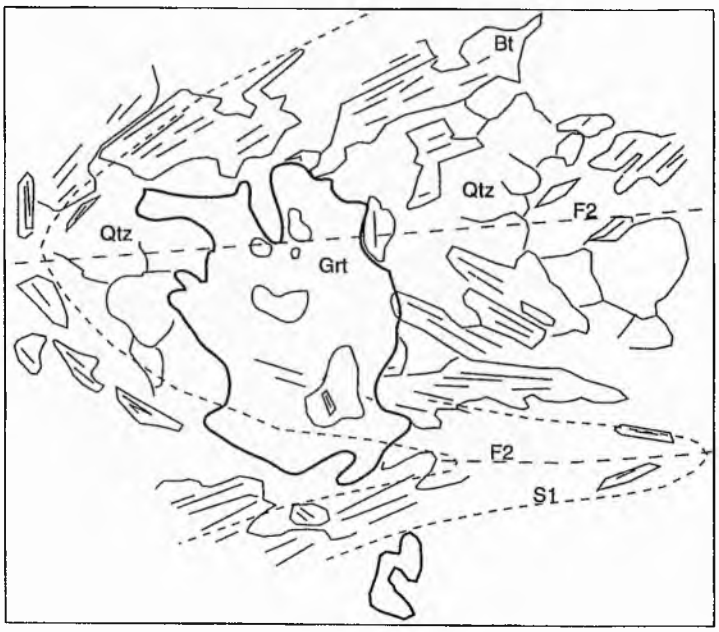

SCALE ----------1.5mm----------

Figure 4.15 F2 microfold in sample NT32.11. S1 trace is shown by dashed line, F2 axial plane by coarse dashed line.

The flakes are slightly deformed, a criteria which suggests M_1 biotite growth continued during stage 2 (strongly deformed flakes normally suggest pretectonic growth). The coarse grained textures suggest pre-tectonic mica recrystallised around folds rather than be kinked. This is consistent with the notion that S_1 is partly transposed onto S_2 during high temperature metamorphism.

Now that the regional fabric S_1 is defined it is important to place the relative growth stages of i) garnet, ii) cordierite, iii) K-feldspar and iv) sillimanite. The study of microtextures from thin section however shows two dimensional relationships of porphyroblasts. Consideration of mesoscale field relationships is essential to the complete understanding of metamorphism relative to deformation.

i) Figure 4.15 shows an anhedral garnet porphyroblast in the hinge of an F_2 microfold. The garnet appears to have overgrown biotite in the hinge. This relationship is common throughout sample NT32.11. Garnet has preferentially nucleated at the fold hinge and is indicative of syn-tectonic (stage 2) growth (Bell & Rubenach 1983). Continued tightening of the micro-fold would preserve an angular discordance between the biotite inclusions in the garnet and the external fabric. This does not appear to have occurred, thus garnet growth may have terminated with folding. Syn-tectonic pressure shadows on the limb of this F_2 micro-folds also indicate syn-tectonic garnet growth. Pressure shadows form because porphyroblasts are stiffer than the surrounding matrix (Ghosh 1993). Syn-tectonic growth of garnet is apparent in KP35.11 shown in Figure 4.16 which has developed low and high strain domains. Biotite commonly preserves the high strain domains in the coarse matrix (*cf.* Bell & Rubenach 1983), cordierite and garnet have nucleated mainly in low strain domains. It is notable that garnet also grows in the matrix high strain domains and that cordierite is confined to discrete domains above and below garnet.

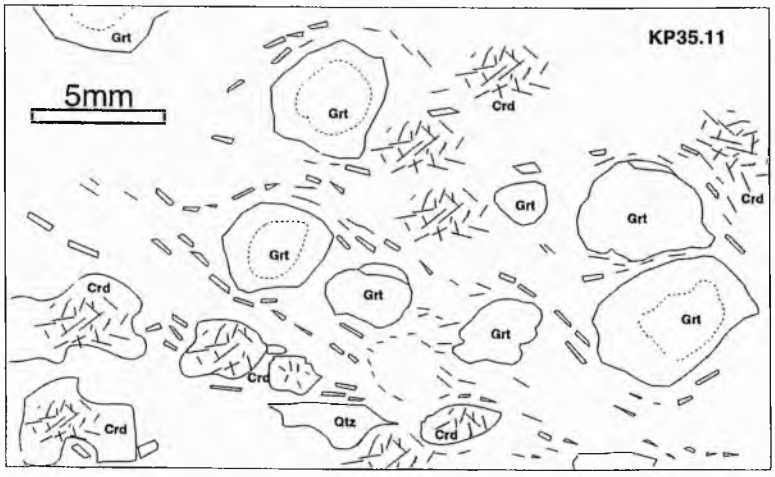

Figure 4.16. Pressure shadows and strain domains developed in sample KP35.11

ii) Cordierite growth is strictly syn-tectonic. It is always aligned sub-parallel to F_2 hinges (often as prolate-oblate porphyroblasts) on S_1 surfaces. In thin section it commonly displays pressure shadows indicative of syn-tectonic growth. It is notable that in N32.11 cordierite has nucleated at an F_2 microfold hinge in the same manner as garnet. Biotite that defines the fold can be traced through the porphyroblast. Thus cordierite growth is coeval with Stage 2 and F_2 fold development.

iii) K-feldspar is commonly found with pressure shadows e.g. NT42.5 (Figure 4.2). Its growth is interpreted as synchronous with Stage 2 and F_2 fold development.

iv) Sillimanite, as discussed in Section 4.3.2 has had two growth stages. Consumption of early biotite+Sil occurred through reactions (4.1) or (4.4) to form cordierite and garnet. Later sillimanite growth may have occurred through reaction (4.5), evidence for this is rare.

4.7 Discussion of metamorphism

In this section a brief discussion and interpretation is presented of the combined petrographic observations and thermobarometric results from this study and earlier studies. Comparison of basement and cover metamorphism, Section 4.4.7, is made in Chapter 6. Metamorphic histories may be considered as:

i) episodic (i.e. discrete multiple thermal pulses)

ii) progressive

iii) short-term and singular

Ideally it needs to be placed within the framework of *PTd* space. It has already been determined in Chapter 3 that deformation was progressive. It is not unreasonable therefore to suspect that metamorphism was also progressive (not episodic). Haugerud & Zen (1991) stated that rocks act as flight recorders and preserve evidence of part of an orogen's history. It is clear from the complex paragenetic sequence deduced from pelitic rocks that only a small part of this *PT* path evidence remains. Crude *PTd* paths for the Central Zone are shown in Figure 4.17. These were proposed by Barnes (1981) and Bühn *et al* (1994).

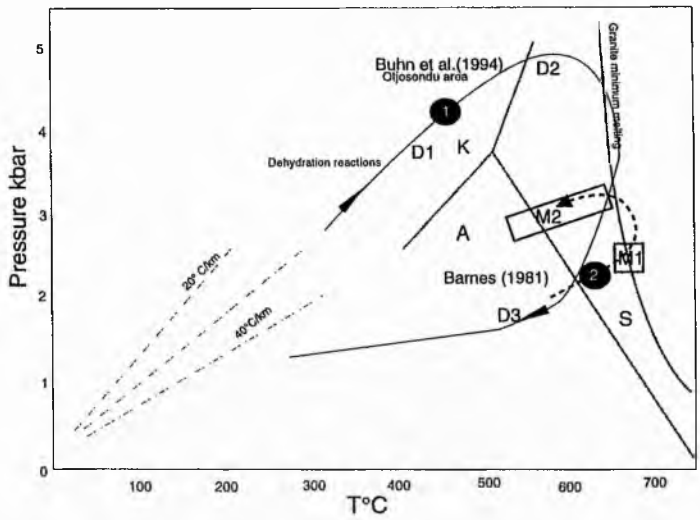

Figure 4.17 *PT* paths proposed by Bühn *et al* (1994 & 1995) (1) and (2) after Barnes (1981)

Barnes (*op. cit.*) based the early path on the restricted *PT* conditions that reaction (4.4) (i.e bt+sil=crd which occurs at 2.5kbar 640°C- 2.8kbar-665°C), he proposed an anticlockwise path. The initial part of the path is based on reactions that produced Grt+Crd+Kfs assemblages which have positive gradients. These coincide with stage 2 in this study. This is the only part of the path that can be constrained. A key stage in the *PT* path is at the probable point were the high temperatures of M_1 occured and granite intrusions occured. Barnes (1981) in his model suggests pressure increases while Bühn *et al.* (1996) suggested it decreased after M_1 i.e. a clockwise *PT* path. In fact a *PT* path may have 180° choice of trends (Vernon 1996) (Figure 4.18). Vernon (*op. cit.*) states that reactions are equivocal in *PT* path determination and that geochronological evidence is required to construct a true *P-T-t path.*

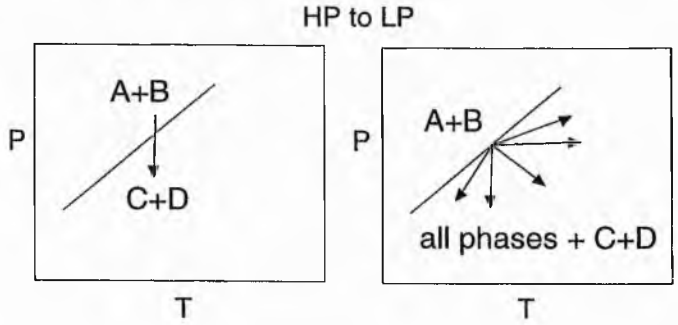

Figure 4.18 PT trends from a positive P-T slope after Vernon (1996). Left handside shows a 'usual interpreation' and right hand side 'possible interpretations'.

If post-tectonic garnet is attributed to reaction (4.6) (see Section 4.3.2) and the rocks cooled slightly before the initiation of that reaction this could be regarded as a evidence of a discrete M_2. Chemical zonation profiles, which are flat are simply explained however if *T* increased. There is, however, no means to determine if this was due to isobaric or compressional

heating. It is tempting to suggest that regional isobaric heating occurred when large amounts of granites were intruded during stage 3. Simple continuos decompression may not have occurred. *PT* space based on *PT* estimates in this study is presented in Figure 4.18. Any possible M_2 episode is thus poorly defined in terms of a *PT*.

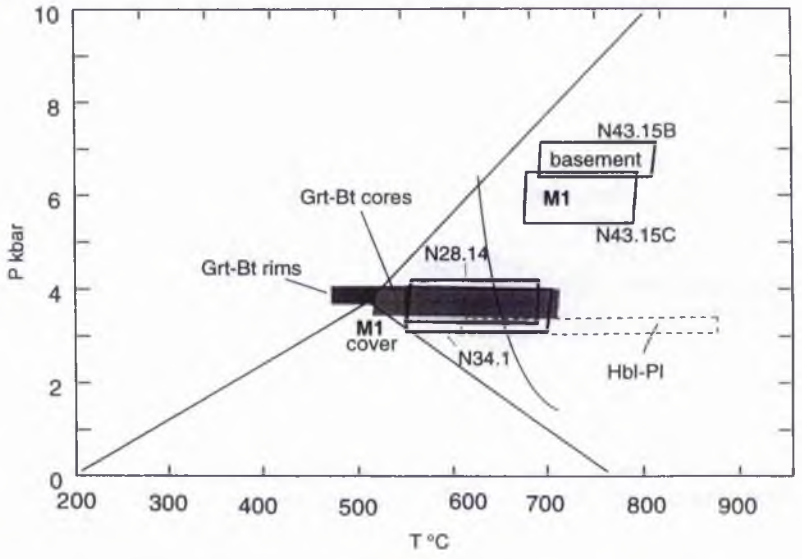

Figure 4.18 Summary of *PT* conditions obtained from this study.

High temperature low pressure metamorphism has had two petrographic effects. Firstly, it may be inferred that widespread annealing and coarsening of fabric occurred. Quartzo-feldspathic inequigranular-polygonal gniesses with abundant of lobate textures suggest that high temperatures out-lasted deformation and resulted in static recyrstallization. Secondly, it resulted in the production of random fibrolite. This has also been noted in the Goanikontes area by Nex (1997) who attributed it to an M_2 episode when the *PT* path of the rocks overstepped the minimum melt curve. These two effects, however, are coeval with the final stage orogenesis. Barton & Hanson (1989) state that extensive LP/HT terrains may result from coalescing of contact metamorphic aureoles between intrusions resulting in a general 'clockwise' *PT* path. It is clear that striking contact metamorphic effects near large granite bodies are absent in the study areas, if however such bodies added to the thermal budget of the orogen the distinction between regional thermal and local thermal metamorphism becomes a problem of scale (Puhan 1983) i.e. a single metamorphic event occurs. It is notable that samples which have late sillimanite growth are restricted to the Nosib Group arkosites immediately above the main area of red granite invasion in the Namibfontein dome. From a spatial point of view therefore, evidence of an M_2 fibrolite is locally restricted. Although it seems logical to suggest that the annealing process was caused by heat from post-tectonic granite invasion there is a strong case to argue this is not widespread (Puhan 1983). For example not all fabrics are annealed and most index minerals are aligned i.e. syn-tectonic. Stüwe and Sandiford (1994) state that

anticlockwise and clockwise *PT* paths may 'vary as a function of vertical distance from heat sources'; this is because the shear strength of the crust is heat dependant in the range 400°-800°C. Deviatoric stresses are reduced near intrusions. Thus it is probable that several *PT* paths could be derived for the Central Zone.

Summary

In reviewing the petrographic, field observation and thermobarometic data it is concluded that the rocks in study areas are characterised by one regional metamorphic event. M_1 assemblages are syn-tectonic and syn-kinematic formed from Stage 1 -Stage 2 (Table 4.21) of the proposed structural model. Pressure and temperature conditions recorded in the basement are higher than the cover. Annealing of fabrics and random growth of sillimanite suggests that the peak of metamorphism may have slightly overlapped the of peak deformation.

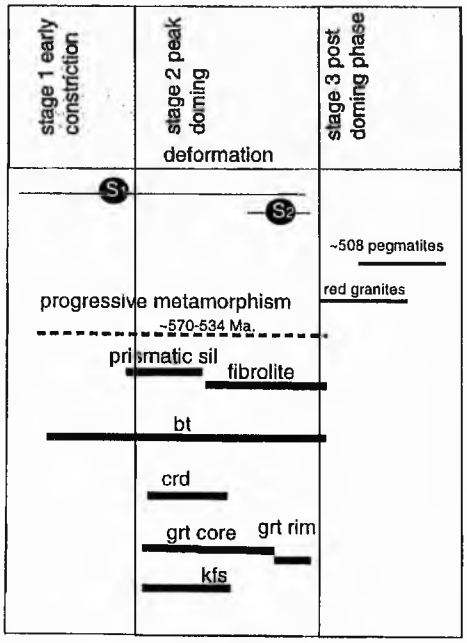

Table 4.21. Summary of growth of metamorphic phases relative to three stage structural model proposed in Section 3.10. Post-tectonic granite age and of peak metamorphism after (Brique *et al.* 1980) from Goanikontes area. Peak metamorphism from syn-metamorphic red granite.

CHAPTER 5

Granite Relations

5.1 Introduction

This Chapter briefly describes the field setting and petrology of granites in the study areas. It aims to show a simple hierarchy of Damaran granite intrusions. These have been classified into three simple groups on the basis of mineralogy, colour and intrusive relationship following the work of Smith (1965), Jacob (1974a) Brandt (1985) Mc Dermott (1986) and Nex and Kinnaird (1996). A full account of granite petrogenesis is given by Nex (1997) and Mc Dermott (1986). (Granite ages are discussed in Section 6.2.5.iii)

5.2 Field classification

Granite intrusions in the Namibfontein and Khan mine area can be divided into three chronological and petrological types:

1) Firstly, granites were found as large intrusions of red to grey unfoliated granites cross cutting and swamping i) basement rocks, ii) mylonites in the Khan River Detachment and iii) cover rocks. Coarse red gneissic granites for example form the main intrusions at the centre of the Namibfontein dome. A weak fabric is observed in red granite that intruded the Khan River Detachment at GR[075,088]. Red granites cross cut and post-date S_1.

2) Secondly, white leucogranite sheets were found throughout the stratigraphy. These exist as sheeted veins either parallel to S_1, or orthogonal to S_1. These veins are commonly gently pytgmatically folded and cut by red granites. Large bodies of leucogranite are commonly found below the Karabib Formation in the Namibfontein dome, they appear to have been impeded by the ductility of calcite marble and have formed laccolith structures. In the Khan Mine area leucogranite sheets are ubiquitous north of the Nose Structure Anticline. Leucogranites appear to be mainly syn Stage 2 and syn-to post-F_2.

3) Coarse pegmatitic veins are found throughout domes cores which cross cut leucogranite sheets and red granites. Pegmatites are post Stage 2.

5.3 Modal Analyses

Modal analysis of 24 granite thin sections were point counted (700-1000 counts per section) for all major and minor phases shown in Table 5.1.

Sample	Qtz	Kfs	Pl	Bt	Msc	Grt	Sil	Cal	Mz	Opaq.
Leucogranites										
N8.11	35.6	51.3	5.3	0.3	2	5.3	-	-	-	-
N34.5	38	37.5	31.5	6	1.5	-	-	-	-	-
N23.7	41	33	25	0.3	0.6	-	-	-	-	-
N45.4B	70	27.1	21	-	-	-	-	-	-	0.1
N3.1	46.4	25.2	28.2	0.2	-	-	-	-	-	-
N14.5L	26	68	4	0.3	-	1.6	-	-	-	-
N35.5C	43.6	20.8	35.4	-	-	-	-	-	-	0.2
N38.10G(in marble)	15	76.5	0.5	-	0.5	-	-	7.5	-	-
N26.1	27	22.8	50	-	-	0.2	-	-	-	-
Red Granites										
N50.10	32	52	15	-	0.6	-	-	-	-	-
N35.5B	26.2	40	31.5	-	1.5	-	-	-	-	0.7
N45.4	37.6	40	15.6	2	1.3	-	2.6	-	-	-
N14.11A	27.8	51.2	21	-	-	-	-	-	-	-
N37.3	35.6	61.8	1.2	0.6	0.2	-	-	-	-	0.6
N19.11	38.2	45.4	14.2	2	0.2	-	-	-	-	-
N46.15	65	12	20	0.4	0.8	-	-	-	-	-
N50.4	58	21	6	6	-	-	9	-	-	-
Grey granites										
N38.5	20.2	8.8	44.2	**25**	**0.4**	-	-	-	**0.2**	**1.2**
N38.6	**26.3**	**43.3**	**20.3**	**8**	**1.3**	-	-	-	-	**0.3**
N46.5	**23**	**18.6**	**37.8**	**18**	-	-	-	-	-	**2.6**
Late Pegmatite										
N37.3	3	87	10	-	-	-	-	-	-	-
N42.21B	17.3	71.3	9.6	1.6	-	-	-	-	-	-
N22.16	33	54.6	11	0.6	0.6	-	-	-	-	-
33.G	31	64.5	3.5	1	-	-	-	-	-	-

Table 5.1 Modal analyses of granites in the Namibfontein area

5.4 Granite Classification

The results of modal analyses show that all granites are characterised by Qtz, Kfs, Pl Msc and Bt. Grt is a common accessory phase in peraluminous leucogranites. According to Nex and Kinnaird (1996) younger granites are characterised by high Kfs contents, this is supported by the analyses of late pegmatites in Table 5.1. Older red granites appear to have lower Kfs contents. A rare and minor group of grey granites is comprised of core of the Valencia dome, e.g. N38.5 & N38.6 GR[035,015]. Sil is present in sample N45.4B GR[049,081] this is interpreted as an M_2 overgrowth phase.

The results from Table 5.1 were recalculated to 100% for comparison of samples according the Streckeisen scheme (Streckeisen 1975) shown in Figure 5.1.

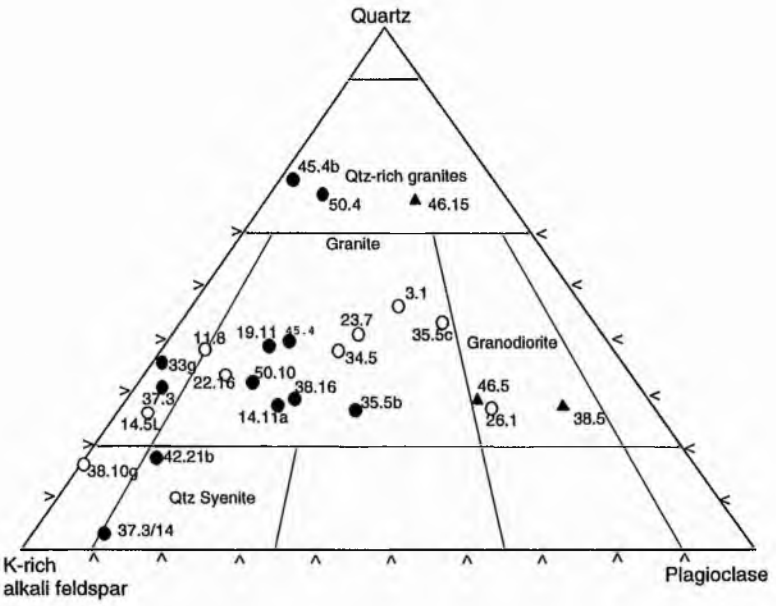

Figure 5.1 Classification granites according to the Streckeisen scheme after (Streckeisen 1975) from the Namibfontein area. (open circles=leucogranite, solid circles= red granite, solid triangles= bt granite.

Observation of Figure 5.1 shows that a sample points spread across alkali-feldspar granite to granodiorite fields; these groups may be placed in a three stage intrusion history which supports field observations:

In the first stage granite magma was emplaced throughout the deeper structural levels of the dome cores as anastamosing 2-3m wide dykes. Plate 2.8 shows an example of ubiquitous dykes found in the Khan Mine area. In this area extensive granite dyke networks cross-cut the basement cover transition around the Nose Structure Anticline. Figure 5.2 shows the trend of 23 dykes plotted as great circles on an equal area stereographic projection. Dykes have a general NE-NNE trend, this coincides with Barnes F4 trend (see Section 6.1.1). Intrusions in the Nose Structure Anticline have not formed a large coherent body that is visible at the current level of exposure.

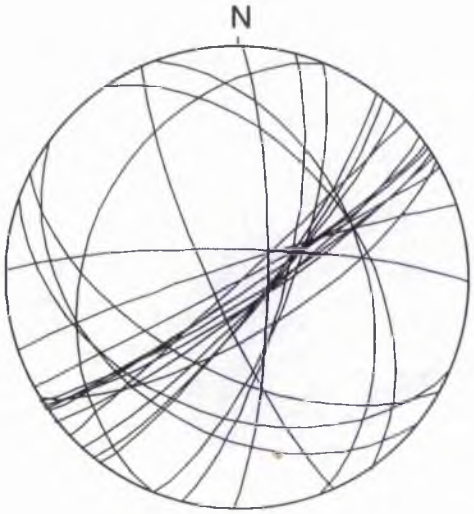

Figure 5.2 Trend of granite dykes in the Khan Mine area plotted as great circles.

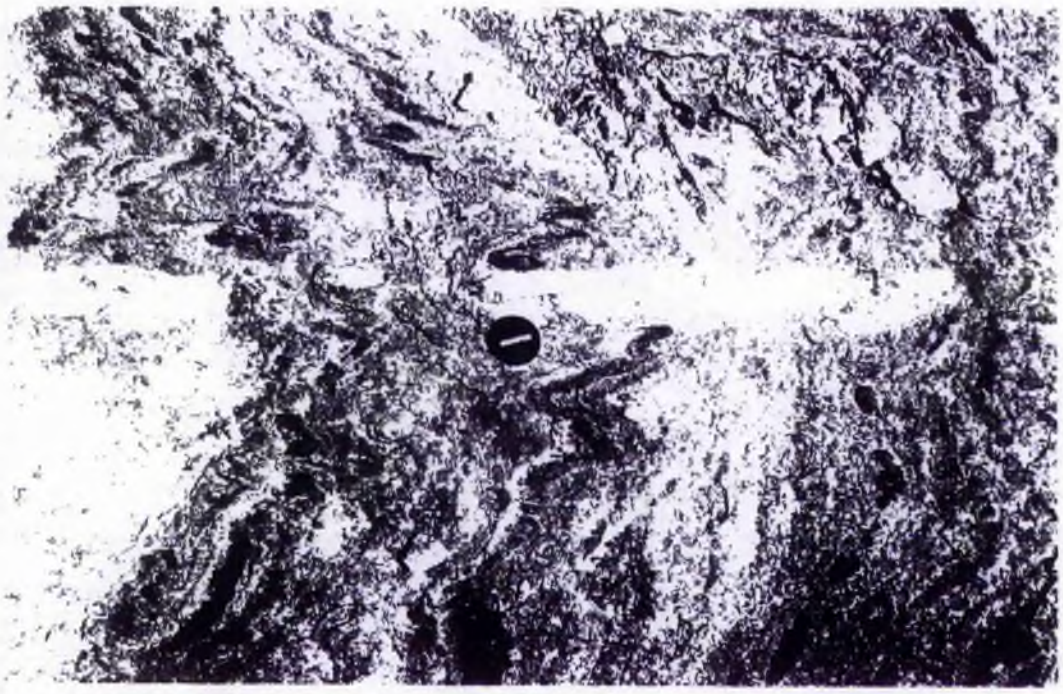

Plate 5.1 Photograph to show syn to post-tectonic granite intrusion along an F2 fold axial trace [023,095].

In the second stage, post-tectonic larger granitic laccoliths and lopoliths formed parallel to S_0/S_1. These are evident below the Karabib Marble at N33.10[012,063] & N8.6 [098,098]. Smaller 5-10cm wide veins have been intruded along the axial trace of some mesoscale folds (Plate 5.1), evidence of post-tectonic intrusion (Goodman 1994).

In the final stage the ubiquitous 'Red Granite' of Smith (1965) cross-cut reactivated basement and cover rocks such that large homogeneous bodies formed. The largest intrusion of red granite at the core of the Namibfontein dome is undeformed and contains >10m basement rafts showing a Damaran overprint. This stage was not reached in the Nose Structure Anticline, however, towards the south-west of the Khan Mine mapping area this stage was attained. Extensive out-crop of a large non-foliated coarse red granite body is clearly visible along the southern side of the Khan River from K31.17 GR[032,0102].

In summary emplacement style and granite body shape was controlled by local and regional structure. Magma has utilised anticlinal structures but not synclinal structures; little or no modification of country rock was observed. Granite emplacement is largely post-dome formation.

CHAPTER 6

Synthesis and discussion

6.1 Introduction

This chapter considers the existing geodynamic models of dome formation for the Central Zone and domes in general. The applicability of six models are evaluated; the intention is to outline and highlight features which may be synthesised in a new geodynamic model. The results of metamorphic and structural analyses from this study are used to test the various models.

6.2 The geodynamic models

The formation of large scale dome structures like those in the Central Zone have been attributed to six mechanisms.

1. Interference folding by separate sequential deformation events. (Gevers 1963, Smith 1965);
2. Interference folding by single phase progressive deformation (*cf.* Veenhof & Stel 1991) (Oliver 1994);
3. Diapiric rise of mobilised basement into cover (*cf.* Eskola 1949 and Ramberg 1972, Barnes 1981);
4. Magmatic deformation by ballooning granites (Kröner 1984) or forceful diapirs (Coward 1981);
5. Mega scale sheath folding (*cf.* Quinquis *et al.* 1978, Lacassin & Mattauer 1985, Coward 1983);
6. Metamorphic core complex development (*cf.* Coney & Harms 1984) (Oliver 1994, 1995 & 1997).

6.2.1 Polyphase folding models

Polyphase fold evolution has been reported in the Central Zone many times (Gevers 1963; Smith 1965; Jacob 1974, 1983; Blaine 1977; Barnes 1981; Downing & Coward 1981; Kasch 1988; Miller 1983b; Miller & Grote 1988; Bühn 1991; Bühn *et al.* 1994). These studies have all employed chronological notation to describe regional fold

morphology. In this study, however, regional fold descriptions (Section 3.2) are based on their morphology and spatial orientation.

The earliest model for the present study area was introduced by Smith (1965). He required successive cross folding of D_1 folds by later folds. D_1 produced flat lying structures and axial planar S_1 by shearing, subsequently D_2 obliterated S_1. Dome morphology depended on the orientation and intensity of D_2 and D_3. In this study, however, evidence of a fabric that predates the regional fabric was not found. Internal fabrics, for example inclusion trails in syn-tectonic cordierite and garnet, are always straight. According to Barker (1990) porphyroblasts "grow rapidly in geological terms (100-100,000 years)" and straight inclusion fabrics result from syn-tectonic overgrowth. Thus it seems unlikely that Smiths' D_1 structures existed. Observations in this study support this: nappe structures were not observed, rather stratigraphy is overturned at the south-west end of domes; the Karub syncline has an inverted limb. Smith's model for the Karub Syncline for example is shown in Figure 6.1(A) where it is compared to the new interpretation.

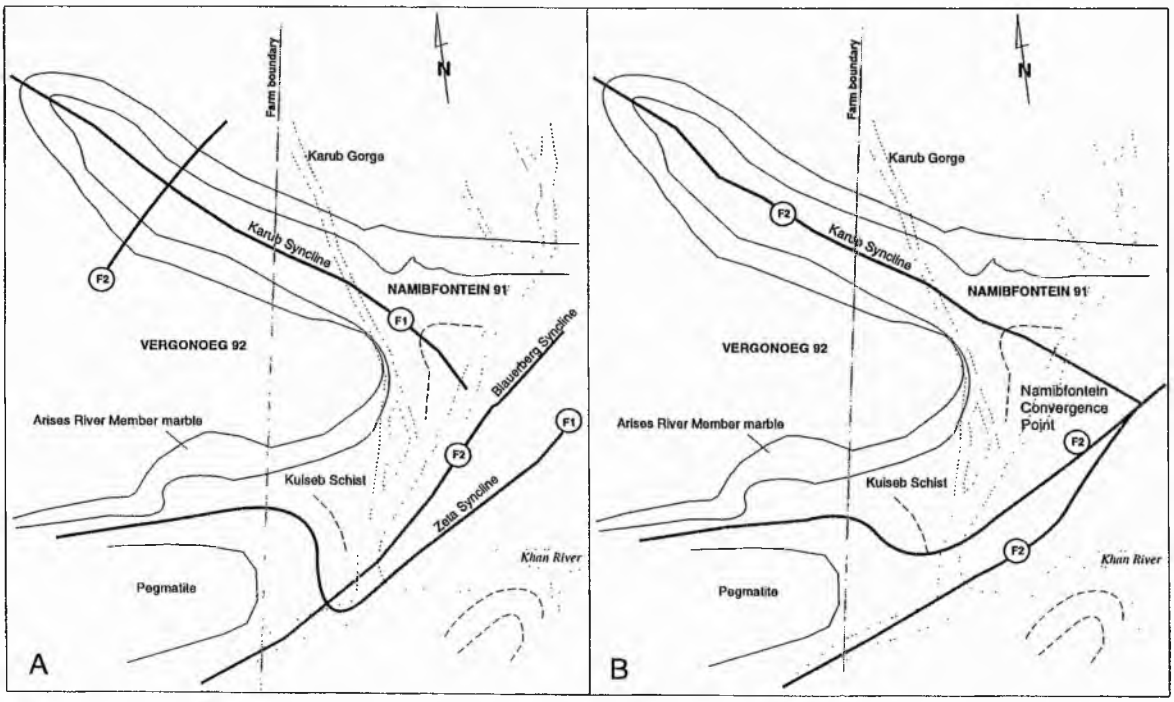

Figure 6.1 (A) Conventional polyphase interpretation of the Karub syncline after Smith (1965) and (B) new interpretation in this study.

Smith describes the Karub Syncline, domain NF(G), as an early D_1 fold which has been refolded by a north-east south-west trending D_2 fold. Field evidence from this study does

not support this. Firstly, this is because lineations in the syncline are unidirectional and plunge consistently towards ~100° (Section 3.3.5.1.ii). Secondly, no evidence of mesoscale refolding was found, instead folds appeared progressively tightened. It is notable that the Zeta Syncline (Smith's F_1) and Blauerberg Syncline (Smith's F_2) meet at the Namibfontein Convergence Point (Section 3.3.1ii). The geometry of the Zeta Syncline actually requires two of Smith's F_2 folds to explain its non-cylindrical morphology. An alternative explanation is that these synclines are contemporary (Figure 6.1 B).

Smith's model may also be tested in the Khan Mine area. It has been shown that the Karub Syncline fold trace joins a convergence point, this is also true of the domes. Barnes (1981) noted that the anticlinal crests of domes between the two areas are commonly bifurcate. Smith's (1965) interpretation of the Nose Structure Anticline and surrounding cover is shown in Figure 6.2. He shows that the Khan Dome, south of the Nose Structure Anticline, bifurcates. The northern trace meets the Blauer Heinrich Syncline at the Khan Mine Convergence Point. In total seven fold axes meet at this point, six of these are Smith's F_2 folds which radiate from the convergence point. If however they have formed by superposition of a strong coaxial D_2 event the angle between them seems unusually high. An alternative is that these folds resulted from constrictional deformation.

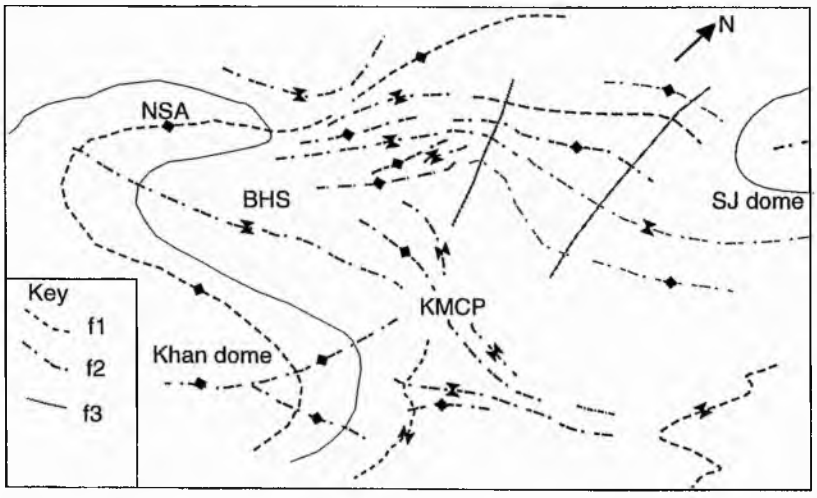

Figure 6.2 Polyphase interpretation of the Khan Mine area after Smith (1965).

Barnes (1981) made detailed morphological descriptions of most of the domes in the mapping area from the study of aerial photographs and field data (Figure 6.3). From these data he concluded that polyphase deformation formed only a small number domes e.g. the Rooikuiseb Dome and that no single mechanism could explain the variety of dome forms. In Figure 6.3 for example dome 1/2 corresponds to the Namibfontein and Vergenoeg domes. Barnes determined that the axes of the twin-domes in particular the 'arrow head' Vergenoeg dome was not parallel to the his main F_3-D_3 fold phase. He

proposed either: i) a 90° rotation of principle compression; or ii) locally produced deformation field (caused by diapirism). Thus the deviation of the long axes of the Vergenoeg dome cannot be explained solely by fold interference. Instead this could be explained by heterogeneous strain systems caused by progressive constriction.

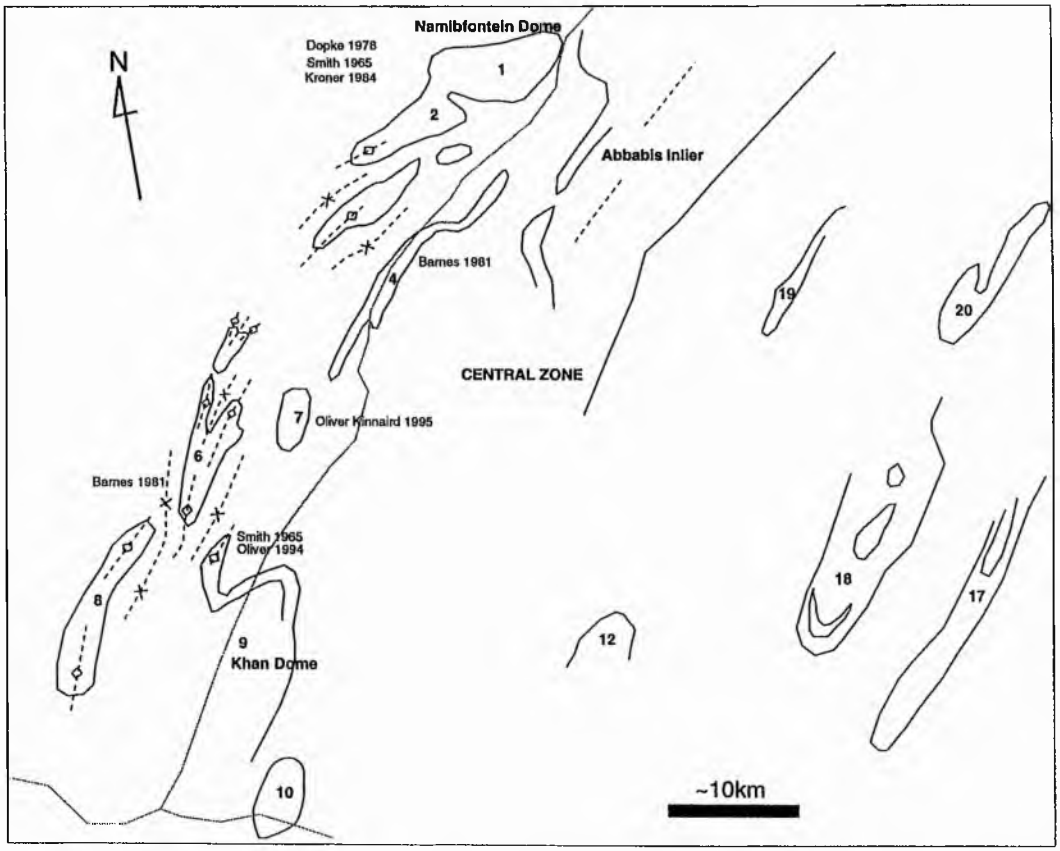

Figure 6.3 Map showing the domes studied by Barnes (1981). Other workers names are shown for some areas. Domes 1 & 2 = the Namibfontein and Vergenoeg domes, 4= Valencia Dome, 9 = The Khan dome, 10=Ida Dome. 7= SJ Dome, 12= Rote Adlerkuppe Dome 17=Rooikuiseb Dome. 18,19,20=unamed.

Finally, Bühn (1991) and Bühn *et al.* (1993b) proposed that deformation in the Central Zone was controlled by the variety of polyform D_1 folds. They examined the Otjosondo area, 100km east of Okahandja, on the basis of deformation styles they identified three D_1 fold types:

i) recumbent folds that formed 'crescent-mushroom shapes', i.e. Ramsay (1967) type two interference,

ii) upright open folds which were rotated into the D_2 trend (Ghosh *et al.* 1992), see Figure 6.4,

iii) and upright inclined folds which were resisted refolding and preserved their original orientation.

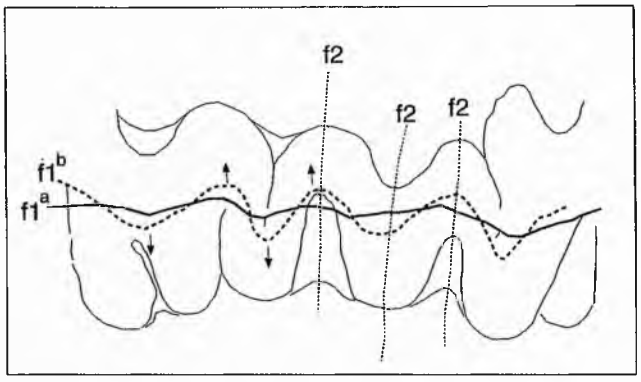

Figure 6.4 Diagram to illustrate fold hinge transposition of early fold phase by progressive second deformation (after Ghosh *et al.* 1992).

Their model predicts that some of the early fold hinges were 'reused' during D_2. This requires a heterogeneous D_1 event i.e. to produce early folds with diverse shapes. In this new model the origin of diverse F_1 shape could be explained by the amoeboidal nature of constrictional folding (Ghosh 1995) (see Section 6.4). Furthermore domes are unlikely to form from coaxial D_1 and D_2 folding. The Nose Structure Anticline has previously been interpreted by Smith (1965) as a Bühn *et al.* (1993b) type ii) situation. The three dimensional morphology of the Nose structure Anticline described in this study suggests it is a more complex pronounced tubular dome. This may be explained more adequately by constriction than an orthogonal buckling D_2 event.

6.1.2 Domes from single phase deformation

In addition to simple polyphase deformation, Barnes (1981) suggested that at least some of the non-planar regional folds both in the cover envelopes and the domes where the result of progressive deformation, either from simple or pure shear. Often it is difficult to detect progressive deformation. Peterson and Robinson (1993), who studied the Pelham Dome in Massachusetts, an orogen parallel structure, stated that time separated structures may be caused by i) changes in the stress field ii) strain environment (i.e. rate of strain transport direction) and iii) physical conditions. Evidence of any of these criteria may be used to differentiate between progressive and separate discrete events. It is evident that in

this study that the finite X direction, recorded by L_1, was constant and resulted in a moderately plunging (NE-SW) orogenic trend. Variation of L_1 at the domain scale from the overall trend represents local changes in the stress field in the new model rather than subsequent deformations.

Domal structures have been reported by Veenhof and Stel (1991) as the result of a single deformation from the Sveco-Finnides, Finland. They studied the Mustio dome noting that diversely orientated cleavages resulted from gravity collapse of a 'sink' structure. The intensity and orientation of S_2 reflected its position within the regional structure. Diverse S_2 fabrics are otherwise explained by D_3 folding. This would result in π girdle distributions of poles plotted to S_2 surfaces. In the new model S_2 fabrics are contemporary and reflect partitioning of high strain at the sub-domain scale.

6.2.3 Diapiric rise of basement

Models that depend on diapiric rise of buoyant basement were extensively studied by Eskola (1949) Ramberg (1972). These models require 'positive active boundaries' (Ramberg 1968a), i.e. a buoyant Newtonian basement, and involve amplification of deflections caused by gravity over time. In this study the mineralogy of both the basement and the Nosib Group is quartzo-feldspathic and suggests that only small density contrasts existed.

Barnes (1981) mapped domes in the Central Zone (Figure 6.3) in particular domes 4, 6 and 8 between the two areas were studied. He found that evidence of S_1 was rare or non-existent and probably destroyed by shearing; he invoked two pre-dome forming deformation events, D_1 which formed recumbent structures and D_2 which formed nappes and thrusts. These were not responsible for dome formation but 'destroyed simple density stratification'; this propagated gravity instabilities and diapirism (see Section 6.1.2). Field evidence from this study shows that domes have a simple stratification. Furthermore, a diapiric model fails to explain several of the morphological characteristics of the domes. Firstly, domes are overturned therefore there is a probability that there was no longer a density contrast; for example the western flank of the Namibfontein dome dips moderately to the north-east. Second, domes have a strong structural trend which is parallel to domain decametre and centimetre scale fold axes. An upward ascent of basement should result in concentric fabrics and radial domes. Third, domes are characterised by sharp anticlinal crests and broadly regional tubular fold geometries (Figure 6.5a/b). Diapir theory predicts S_1 should have a shallow trajectory with flat dome roofs (Cruden 1988, Bouhallier *et al.* 1995). In conclusion it appears unlikely that diapirism in the Central Zone was a major dome forming mechanism.

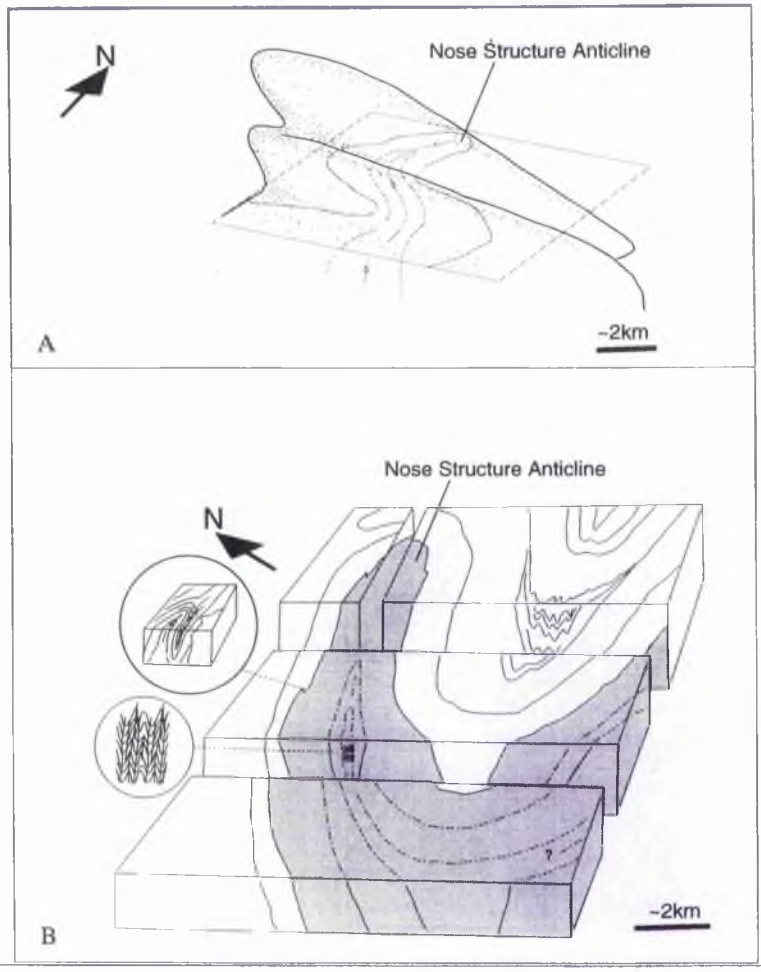

Figure 6.5a 3D interpretation of the regional geometry of the Nose Structure Anticline, part of the Khan Dome.

Figure 6.5b Block cross-section diagram showing structure through the Nose Structure Anticline and Blauer Heinrich Syncline. Syn-kinematic folds in the Khan River Detachment are shown in upper circle. Crenulations at the core of the Nose structure anticline are shown in lower circle.

6.2.4 Magmatic models

In the Central Zone various magmatic related models have been proposed, these are subdivided into three groups:

i) Ballooning of granites (Barnes & Downing 1979, Barnes 1981) (*cf.* Brun & Prons 1981)
ii) The diapiric rise of magma (Coward 1980, Barnes 1981, Kröner 1984)
iii) The interaction of forceful granitoids with regional deformation (Barnes 1981, Kröner 1984);

Models which involve regional deformation around rigid granite bodies (Paterson *et al.* 1991) are excluded from this discussion since granites in this study were intruded after the dome forming events.

i) Forceful granitoid plutons are quite distinct from diapirs which are strictly an ascent mechanism (England 1990, Paterson & Vernon 1995); diapirs, however, may balloon after intrusion. Inspection of the strain environment at the flanks of, and within the largest granite intrusion of the Namibfontein area and Khan Mine area domes (Figures 3.33a & b) does not show radially distributed sub-vertical oblate strain markers typical of forceful granite intrusions (Cruden 1988) e.g. The Burguillos Anticline Sierra Morena (Brun & Prons 1981), the Flamanville Granite north-west France (Brun *et al.* 1990). Barnes (1981) noted that 'the absence of significant flat lying areas suggests the final stages of dome configuration were not attained'. This work has shown domes have sharp crests and record prolate strains. According to Guglielmo (1993) prolate strains are more likely to occur at the ends of intrusions at cleavage triple points, between three or more interfering domes and in diapiric necks. In the Central Zone prolate strains are widespread and they are not confined to these settings.

ii) The diapiric rise of magma suggested by Coward (1980) Barnes (1981) and Kröner (1984) as the ascent mechanism in the current study seems inconsistent with field observations and theoretical considerations. The ascent of magma in the Khan River area has occurred through extensive sheeted dyke complexes (Berning 1986). In detail at least three stages of granite emplacement have occurred in the study areas i.e. i) early folded veins ii) large post-tectonic bodies and lastly iii) pegmatites.

Theoretical controls which apply to diapirism have recently been studied by Clemens & Petford (1995) and Petford (1996). They suggest that rising magma diapirs expend thermal energy softening their surrounding rocks. Consideration of the 'Hot Stokes Model' (Marsh 1982) means that the ascent of the magma occurs when viscous drag is overcome by creating a ductile envelope through which it ascends. This would cause

magma temperature to drop such that at depths of ~14km crystallization would start. Estimates of peak metamorphic conditions in the Central Zone (Chapter 4) indicate pressures for the cover around ~4kb which is equivalent to a depth of 12km, 2km above probable diapir crystallization depth. Furthermore in this model the effect of heating should record pre-tectonic porphyroblast growth (e.g. the North Arran Granite, England 1988). However, garnet, cordierite and sillimanite in this study are syn-tectonic. The ascent of granite melt therefore appears most likely to have been by rapid dyke propagation (*cf.* Clemens 1995), this is consistent with structural and metamorphic field observations.

Although extensive granite intrusion has occurred in the Central Zone, it was not responsible for dome formation due to the following reasons:

i) only a small number of domes in the Central Zone are cored by granite (Barnes 1981 and Jacob *et al.* 1983). The Nose Structure Anticline and Valencia dome for example are composed almost entirely of pre-Damara basement; doming in these areas cannot be attributed to a forceful granite body.
ii) Where granite is present, as in the Namibfontein and Vergenoeg domes for example, radial expansion, i.e. ballooning has not occurred, indicated by an absence of both internal fabrics and radially distributed oblate fabrics at the margins.
iii) Large granite bodies were emplaced entirely passively and are largely post-tectonic, their form is controlled by pre-existing structures, in particular domes.

6.2.4 Sheath folding

Coward (1983) made the important observation that the geometry of domes resembled 'telescoped sheath folds', suggesting that early upright structures formed domes within a regional scale simple shear zone. Sheath folds as defined by Quinquis *et al.* (1978) and Lacassin & Mattauer (1985) form by passive amplification of curved hinge lines, tending to be planar. Domes and mesoscale sheath folds in this study are strongly *non-planar* . The large amplitude of domes, implied in Figure 6.4, resulting from passive rotation and flattening is not supported by shear sense criteria or finite strain data. Although a simple shear component could explain dome asymmetry, quantitative strain analysis suggests dome amplification is principally a result of general constriction. Strain markers generally indicate prolate irrotational strains.

6.2.5 Core-complex models

Domes in the Central Zone were first compared to metamorphic core complexes by Oliver (1994). Perhaps the most important characteristic feature of a metamorphic core complex is a zone of intense high temperature mylonites that separates brittle extending upper crust from deep exhumed crust (Brun & Van den Driessche 1994). A typical internal zone of a core-complex is shown in Figure 6.6.

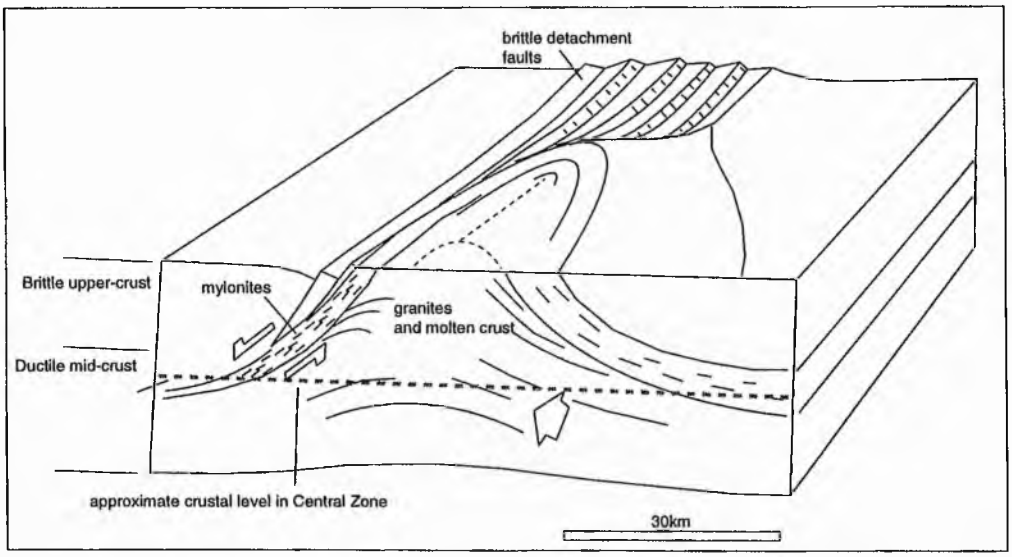

Figure 6.6 Sketch to show the brittle-ductile transition in a 'typical' Cordilleran Metamorphic core complex after Brun and Van den Driessche (1994). Approximate exposure level in the Central Zone is shown by grey dashed line.

At first glance it is clear that the detachment geometry and thickness of the mylonite zone is similar to the Khan River Detachment described in Section 3.9. The Cordilleran detachment surfaces are commonly folded with fold axes parallel and perpendicular to regional extension, this is in turn cut by post-tectonic granites (Reynolds and Lister 1990, Fletcher and Bartley 1996). This is similar to the geodynamic sequence of events in this study. Examination of fold axis trajectories in Chapter 3, for example, strongly suggested a fold mechanism that produced fold axis parallel extension. Furthermore, granites in the study are post-tectonic.

Yin (1991), in an experimental study of core-complexes stated that 'domal and basinal geometries of detachment faults controlled the exposure of mid-crustal rocks' a situation that is apparent in this study. Since deformation in the study areas is entirely ductile a direct comparison to American core complexes may suggest that domes in this study represent a deeper equivalent to Cordilleran core complexes (Oliver 1996). Mylonites are ductile, cataclasis was not observed. Domes in the Central Zone are notably

overturned (to the south-west) a feature which is easily explained if the rock mass had a high ductility. Overturning is not reported in Cordilleran core complexes it has however been reported other core complex domes e.g. the Nyahuku Dome (Crow & Siman'go 1990).

Inspection of the internal zone and mesoscale structures of core complexes shows that early structures are progressively modified by continued shearing at the detachment surface (Critteden *et al.* 1980). Furthermore, the detachment history may be sequential such that extensional duplex systems develop; thus only the latest fault is seen (Davis & Lister 1989). Only minor shear bands were associated with the Khan River detachment (K14.4), these could be interpreted as anastomising and as duplex initiation.

The origin of core complex detachment faults is 'controversial', it is unclear why detachments are folded. Many mechanisms have been proposed, John (1987) suggested simultaneous folding and isostatic recovery. Yin (1991) used the results of experimental modelling to proposed doming of the detachment was controlled by either 1) the vertical force of uncompensated crustal roots or 2) by the effect of buoyant diapirs and/or 3) buckling due to compression perpendicular to extension. Wernicke *et al.* (1988) suggested that a constrictional regime was associated with detachment folding. More recently Fletcher and Bartley (1996) stated that constriction may be a fundamental part of the Mojave core complex, they suggest folds which are parallel to regional extension are formed in crustal regime where $\sigma 1$ is vertical, $\sigma 2$ horizontal and perpendicular to fold axes and $\sigma 3$ oblique to the extension direction and horizontal. Mean lineation plunges are $< 20°$ and mylonitic foliations are horizontal. Lineation recorded around the domes in this study, however, plunge more steeply at ~45°. Orientation of $\sigma 3$ in this study is steeper and would represent more vertical crustal flow than the Cordilleran case. In addition strong zones of simple shear are absent.

In summary similarities between domes in this study and Cordilleran Metamorphic core complexes are represented by:

i) A close similarity of kilometre-scale morphological character;

ii) fold axis parallel extension around the exhumed dome cores;

iii) exposure of mid-crust basement controlled by detachment geometry and erosion level;

iv) folding of a regional kilometre-scale detachment;

v) similarity of the constrictional finite strain regime;

vi) the presence of post-tectonic granites that cut the detachment surface.

6.2.5.ii Testing for a metamorphic basement-cover gap

In section 5.1.5 it was noted that the structural geometry and structural features of the domes in the Central Zone may represent an 'Incipient Metamorphic core complex' setting (*cf.* Bozkurt *et al.* 1994, Oliver 1995). In the North American Cordillera the metamorphic history appears to be complex. Metamorphism is generally in the upper greenschist to upper amphibolite facies (Hodges & Walker 1990). The unroofing history of the Funeral Mountain core complex during Cenozoic extension, for example, resulted in a stepped equilibration of rocks during progressive exhumation. This records a decompression of 4-6kbar from peak conditions of 8-10kbar at 527°-577°C and is supported by lower temperatures in Grt rims away from late stage granites (Hodges & Walker *op. cit.*).

Comparison of the metamorphic situation in the Namibfontein dome shows a metamorphic gap of 3kbar and 140°C between basement and cover. An estimate of peak metamorphic conditions of ~800° and ~6kbar is based on three separately analysed samples from one location N43.15 at the core of the dome. This may be interpreted in three ways. Firstly, the results could be in error. The consistency of results from three samples hopefully confirms that the are meaningful. Furthermore, the observed microtextures reveal a considerable amount of information. The ductile deformation of plagioclase and microcline described in Chapter 3 is undisputed and requires temperatures during dynamic metamorphism to have been in the range >700°C (Mainprice & Berhmann 1987). Secondly, they may represent pre-Damaran metamorphism. Structural analyses in the sample area shows a strong Damaran structural trend. Thirdly, the higher temperature and pressure may reflect a profound unroofing and elevation of deep crust from a palaeodepth of at least 25km.

6.2.5.iii Age of metamorphism and exhumation

Oliver (1994) has reviewed the age of peak metamorphism and has bracketed it between Lower and Middle Cambrian. This is given by an unabraided U-Pb concordant zircon age of 534±7 Ma from post-tectonic red granite and unabraided U-Pb concordant zircon and monazite ages of 508±2 from post-tectonic/M_1 pegmatitic granitoids (Briqueu *et al.* 1980). This is similar to a Rb-Sr whole rock age *c.*515± for granite near the Valencia Dome (Allsop *et al.* 1983). Dating of zircon rim from the core of the Khan Dome gave a syn-metamorphic U-Pb SHRIMP date of 571±64 Ma (Kröner *et al.* 1991). This suggests at least 63 Ma of regional metamorphism. There is therefore little constraint on the rate of exhumation. However ,Tack *et al.* (1994) have provided Ar/Ar plateau age dates for 'unaligned' hornblende and biotite flakes from mylonitic cover gneisses in the Ida dome

(Figure 6.3), in addition they provide an overview of radiometric dates for the late Damaran (Table 6.1). It is notable that Ar-Ar hornblende and biotite plateau ages are similar, 465±2 and 461±9 respectively. Tack *et al.* (*op. cit.*) have interpreted this as the age of a thermal M_2 episode associated with late granite intrusion. Alternatively, very rapid uplift could account the near identical hornblende and biotite ages. (This is discussed in Section 6.5).

429±17	K- Ar biotite	Khan Mine pelite	Haack and Hoffer, 1976
452±22	K- Ar biotite	Khan Canyon Kuiseb gneiss	Clifford, 1967
466±25	K- Ar biotite	Khan Canyon Kuiseb gneiss	Clifford, 1967
448-465	R- Sr biotite	Khan River micaschists	Hawkesworth *et al.*, 1983
458±8	R- Sr 7WR	Rössing alaskites	Hawkesworth *et al.*, 1983
468±8	R- Sr 7WR	Late Rössing alaskites	Misson 1995
485±7	R- Sr 9WR	Late Rössing alaskites	Misson 1995
495±12	R- Sr 13WE	Valencia alaskite	Hawkesworth *et al.*, 1983
542±33	R- Sr 10WR	Ida alaskite emplacement	Marlow, 1983
461±9	K- Ar biotite	Khan Formation gneiss	Tack *et al.* 1995
465±1	K- Ar biotite	Khan Formation gneiss	Tack *et al.* 1995
465±2	K- Ar hornblende	Khan Formation gneiss	Tack *et al.* 1995
528±14	K- Ar hornblende	Khan Formation gneiss	Tack *et al.* 1995
508±2	U-Pb monazite	Goanikontes alaskite	Briqueu et al. 1980
518±7	U-Pb zircon	Goanikontes alaskite	Briqueu et al. 1980
509±1	U-Pb uraninite	Goanikontes primary U mineralisation	Briqueu et al. 1980
510±3	U-Pb monazite	Goanikontes Khan Fm.	Briqueu et al. 1980
510±40	U-Pb monazite/daviite	Rössing U-mineralisation	Nicolaysen, 1962

Table 6.1. Overview of available late Damara radiometric age dates (after Tack *et al.* 1995)

6.3 Summary

The objective of this Section is to describe a new model which broadly fits into model 2. Comparison of field observations with polyphase and magmatic geodynamic models for the Central Zone in Section 6.2 has shown a number of observations which require a revised model :

i) Kilometre scale folds which bifurcate and domes with sharp crests are unlikely to result from ballooning and/or diapirism. Interference of large granite intrusions with regional deformation may be ruled out because large granite bodies are post-tectonic.

ii) The distribution and abundance of prolate (k >1) strains does not support magmatic or polyphase folding models. Finite strains of a flattening type (k <1) are expected from these models.

iii) Domes show a variety of styles and morphologies with a general trend and domain scale heterogeneity. These features are not explained by chronological and incremental fold trends. Outcrop scale mapping of metre-scale folds indicates non-sequential contemporary fold development.

The main structural features in this study are therefore incompatible with polyphase and magmatic models. Further examination is necessary of the proposed three stage single phase constrictional deformation model.

The differences between the new model and polyphase models are shown in Figure 6.7. Domes are interpreted as having an elongated tubular geometry, shown diagramatically with the approximate 45° plunge of dome axes (Figure 6.7). In the polyphase interpretation domes are less pronounced and more flat lying. Finite strain estimates from prolate pebbles of up to 300% elongation are applied to the model to obtain the geometry seen in Figures 6.5 and cross-sections from maps 1,2 & 3(see Appendix).

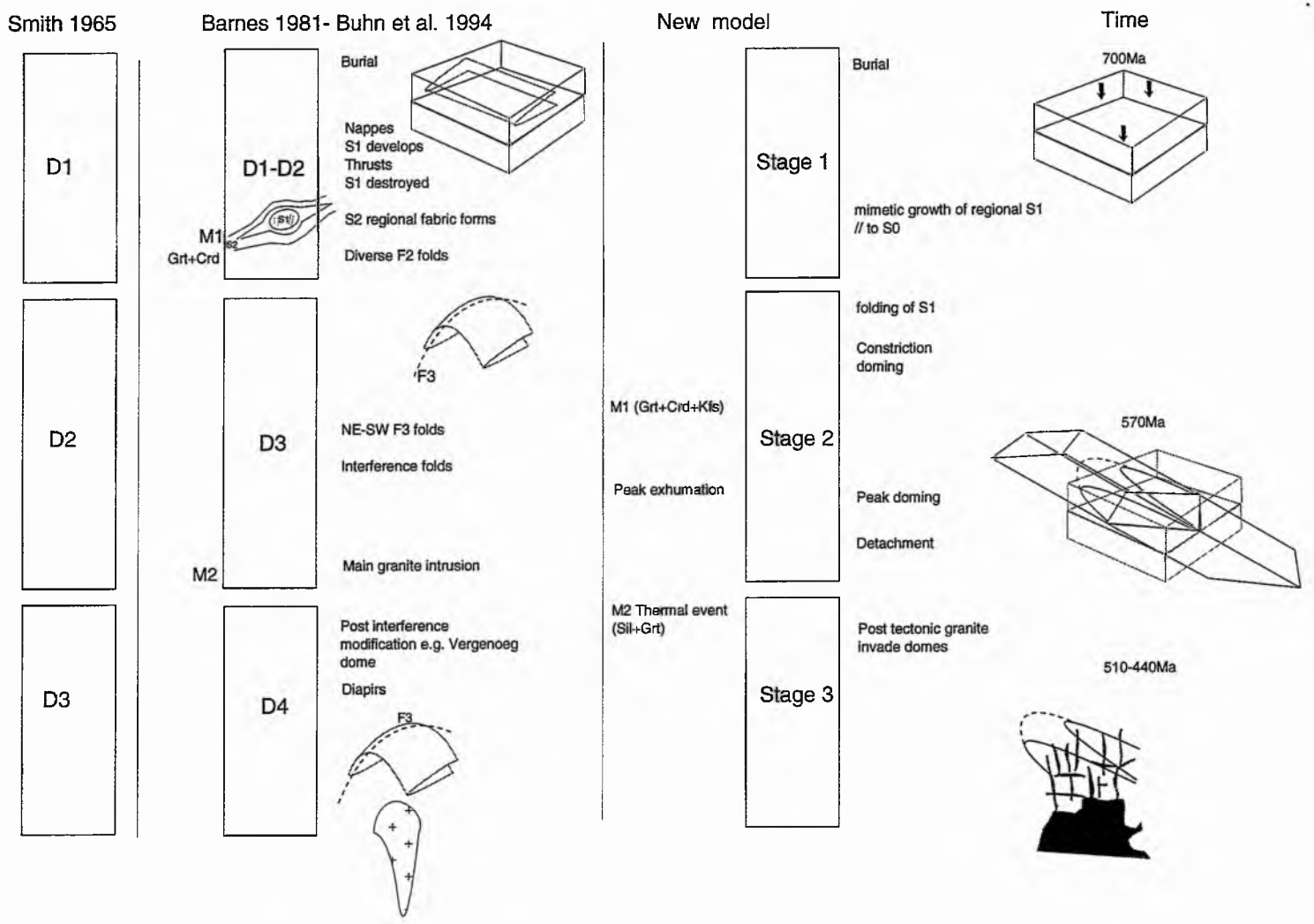

Figur 6.7 Conceptual diagram comparing proposed model and early polyphase models for the Central Zone.

This is supported by the theory of constriction (Ghosh and Ramberg 1968; Ghosh 1970 & Ghosh *et al.* 1995). Ghosh and Ramberg (*op. cit.*) devised experiments with putty and clay layers that were subjected to one period of deformation, these were:

i) 'simultaneous buckle folding at uniform compression' defined as pure constriction
ii)'unequal simultaneous buckle folding at uniform compression' defined as general constriction.

They tested this against models with two episodes of deformation, varying the angle between the two compression directions. In a pure constrictional deformation the combined effect of simultaneous shortening produces domes that have larger fold arcs than folds produced by unidirectional deformation. Superposition of subsequent deformation event resulted in secondary folds with a similar amplitude to the primary folds. High amplitude domes in the Central Zone are therefore consistent with single phase constriction.

The formation of domes is also complicated by the physical behaviour of the crust. Ghosh (1970) stated that the crust may behave in a viscous or elastic manner during general constriction. In the elastic case, a critical yield stress must be exceeded to initiate synchronous folding (constriction), otherwise one fold set will develop first according to the direction of maximum stress. In the elastic case two fold sets may give the impression that polyphase folding took place: field criteria will essentially be the same as that of superposition. In the viscous case, general constriction does not have the constraint of a critical stress and so simultaneous folding will occur. Oliver (1994) suggested that the Central Zone may have behaved in a combination of viscous and elastic behaviour, similar to Smith's (1979) notion that in nature the division of the two is not clear. It is assumed that because no evidence of D_2 overprinting on mesoscale F_1 folds is found that the viscous case applied to the Central Zone.

Ghosh *et al.* (1995) established common criteria from constriction experiments which may help identify constrictional deformation in nature. These experiments expanded the earlier work on general and pure constriction (Ghosh and Ramberg 1968). By subjecting layers to varying amounts of constriction they determined that in a general constrictional deformation of >20% shortening, amoeboid domes and basins form which are parallel to the direction of maximum shortening. The amoeboid forms are illustrated in Figure 6.8 which shows a plan view of the pure constriction model. Figure 6.9 shows a plan view of the Central Zone divided anticlinal and synclinal domains for comparison. The domes of the Central Zone have similarities to the model, notably curvilinear and bifurcating hinge lines with 'hairpin bends' and amoeboid fold patterns. Continued general constriction results in tightening of domes (Ghosh *et al.* 1995). Progressive folding of the

axial trace of regional folds may allow open synclines to form which have axial surfaces that bend sharply. Domains NF(D),(A) and (B) reflect this type of structure. The Khan mine and Namibfontein Convergence Points represent areas where contemporary near horizontal non-cylindrical fold hinges meet. These are abundant in the constrictional model (Figure 6.8).

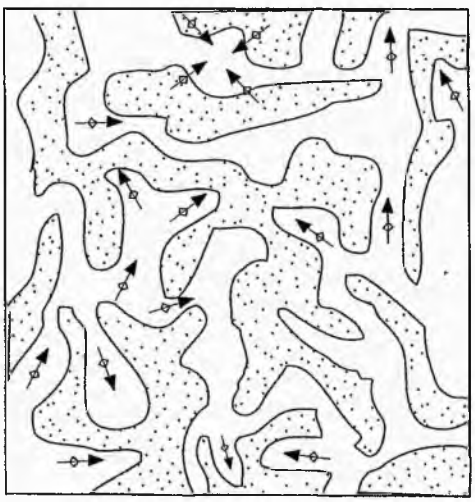

Figure 6.8 Plan view of a clay model showing the plunge of antiformal and synformal domains in pure constriction after >20% shortening, from Ghosh *et al.* (1995).

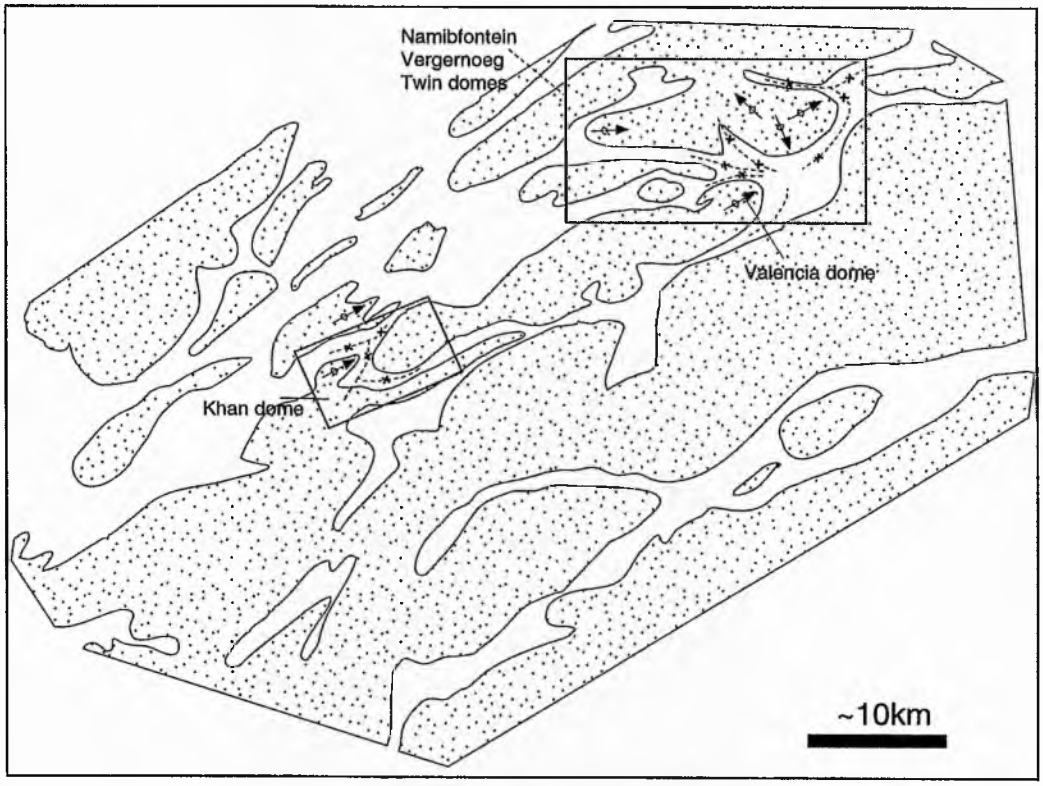

Figure 6.9 Plan view of part of the Central Zone showing antiformal (stippled) and synformal domains (blank).

The orientation of the intermediate and maximum strain axes in steep layers may, under increasing strain switch because the mechanical possibility of more shortening is easier along the direction that underwent initially less strain (Ghosh *et al.* 1995). A stage of pure constriction will occur in this transition. Strain estimates from deformed pebbles in this study indicate at least 20% shortening has occurred. It is interesting to note that 20km north of the Namibfontein area domes around the Omaruru lineament trend north south (Figure 1.1), perhaps reflecting a switching effect. Furthermore switching may have occurred at the domain scale where L_1 does not reflect the general trend e.g. Map 1 GR[025,065]. This is attributed to changing orientation of strain axes.

Observation of mesoscale folds shows overprinting relationships are rare. According to De Beer (1995) areas which do show mesoscale fold interference may result from episodic variations in relative magnitude of strain and the relative importance of the maximum and intermediate shortening directions. Areas where 'polyphase fold patterns' and folded boudins occur could be attributed to this. The complex folds near the basement cover-transition in the Khan Mine area, for example, may partly be explained by strain magnitude variation. Alternatively, Ghosh & Sengupta (1984 & 1987) state that 'differential translatory movements of well foliated rocks may give rise to small zones of shortening'; these may cause spin or local body rotation (Lister & Williams 1983).

Finally, it has been stated that mesoscale folds and S_2 fabrics reflect domain scale strains during constriction. It is notable that F_1 folds commonly plunge more steeply than regional fold hinges. De Beer (1995) noted a similar relationship in the Cape Fold Belt Ceres Arc, an example attributed to thin-skinned constriction. He suggested that this may result from constriction rather than subsequent rotation of early fold axes. Polyphase folding may result in refolded mesoscale folds which plunge less than and are oblique to the domain scale folds.

6.4 Speculation on the causes of regional general constriction

A consideration of the plate boundary conditions and plate motions holds the key to unravelling the field geology of the study areas. A key question which tests the new model is "did the plate tectonic setting of Damara orogeny permit single phase constrictional deformation?"

Breakup and drifting of Archean cratons formed Pan-African oceans before Pan-African-Brasiliano orogenic belts formed between 725-500Ma (Trompette 1994; Unrug 1992 & 1997). There are, however, several interpretations of the number of Neoproterozoic cratons and controversy regarding the timing of their break up (Unrug 1997). Reconstructions of Rodinia at 750Ma (Dalziel 1991, 1992, 1995; Powell 1995; Unrug 1992, 1997) indicates

that at least three cratons were involved in Damara orogenesis (Figure 6.10). Prave (1996) details evidence of NW derived sediments from palaeocurrents in the Northern Branch placing the docking of the Rio de la Plata craton with the Congo craton before the closure of the Congo and Kalahari cratons. Collision resulted in sinistrally transpressive shear parallel to the Northern Branch (Dürr & Dingeldey 1996). Limited kinematic data from the Northern and Southern Zones of the Damara belt show that nappe transport was oblique to the craton margins (Ahrendt *et al.* 1978; Coward 1981; Kasch 1983; Ahrendt *et al.* 1983; Oliver 1994). Figure 6.11a &b shows the approximate position and relative plate motions involved in Damara orogenesis: the Central Zone was affected by complex sinistral transcurrent shear and shortening motions. Transcurrent shear zones appear to post-date thrusting by at least 50Ma in the Ribiera Belt (Ebert *et al.* 1996). However, a tripartite sinistrally transpressive collision involving oblique collisions between the Congo, Rio de la Plata and Kalahari cratons, with a small component of simple shear appears a reasonable interpretation which is consistent with palaeographical reconstructions.

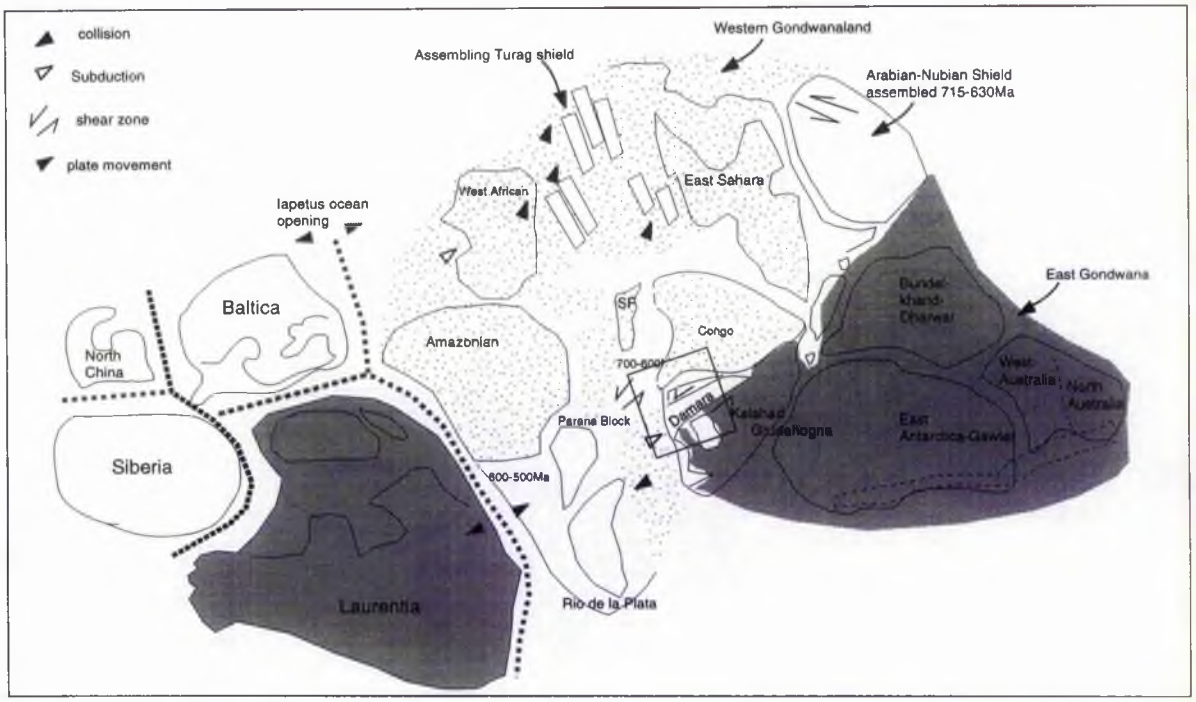

Figure 6.10. Map showing East Gondwanaland (stippled), assembley of West Gondwanaland (dark grey) from 700-500Ma (after Unrug 1997).

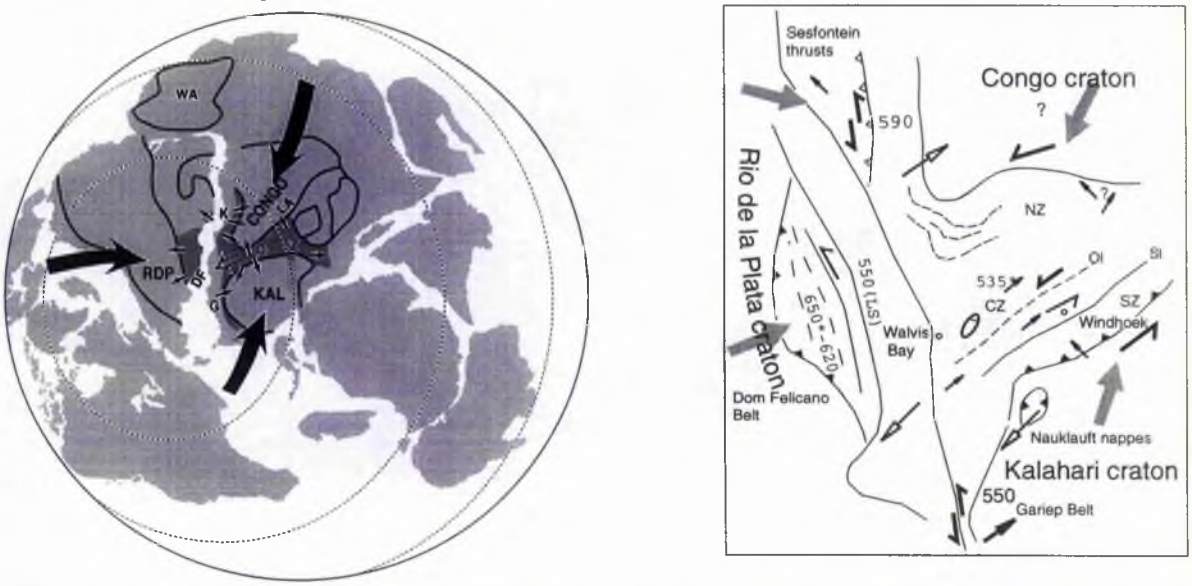

Figure 6.11a Map showing reconstruction of relative plate positions and motions during Pan-African assembly (after Trompette 1994, Coward 1981, 1983, Coward & Daly 1984; Dürr & Dingeldey 1996).
Domes indicated by small ellipse.Small arrows= structural lineation. Large arrows= plate movement vectors. Numbers= dates of main tectonic events. (LS)= Late transcurrent shearing event.
Open arrows = thrust directions. Other symbols see Fig.1.

Figure 6.11b. Plate reconstruction of Pannotia for 580Ma based on Fig.1 in Dalziel et al (1994) with the Damara Belt moved to the centre of the projection. (Large arrows indicate plate movement vectors). WA= west African craton. KAL= Kalahari Craton. RDP = Rio de la Plata craton. DF = Dom Felicano Belt. D= Damara Belt. LA= Lufilian Arc. Z=Zambezi Belt. K=Koako Belt. G= Gariep Belt.

How then were asymmetrical domes formed in the Central Zone? Why are higher grade basement rocks found at the core of these domes? How do these features relate to constriction? Examples of constrictional deformation in nature are apparently rare. Large scale geodynamic models which discuss constriction are confined to extensional divergent plate settings. Extensional collapse of orogens nucleated on thickened crust e.g. the Caledonides of south-west Norway (Dewey *et al.* 1993) and Cenozoic extension in Basin and Range province (Dewey 1988, 1995) have resulted in the production of linear pure-shear fabrics and explain the exhumation of high-grade rocks in the foot-wall of extensional faults. Fletcher and Bartley (1994) have documented prolate strains and horizontal constriction in the Mojave Metamorphic core complex; they state that 'constriction may be common in Core Complexes'. It has already been shown that there are similar structural and metamorphic features in the Central Zone and Cordilleran metamorphic more complexes, however, two features mitigate against this. Firstly, the Central Zone does not have a divergent plate setting, rather the belt has thrusted margins and compressional features (Coward 1983). Secondly, the orientation of L_i in the study areas is moderately plunging, lineation in the Basin and Range province is nearly horizontal. This suggests that exhumation of the mid-crust is not controlled by shallowly plunging footwall exposure of a regional detachment. Exhumation appears to have been through sub-vertical elevation of the mid-crust.

Fossen and Tikoff (1997) present theoretical models that show mid-crustal exhumation may be intimately associated with prolate fabrics during transpressional collisons. They divised five reference models of constant volume transpression and transtension, type A-E, shown in Figure 6.12. the principal strains x, y, z vary in these models, transtension involves extension rather than compression:

Type A: equal shortening of x, y and z stretched

Type B: equal shortening x, y, z not stretched (Sanderson and Marchini 1984 model)

Type C: flattening of shear plane, equal stretching of x, z

Type D: constant vertical height

Type E: coaxial component causes vertical shortening equal to shear zone normal

In these models resultant strain types and their trajectories depend on the proportion of simple shear and pure shear applied in the deformation. The particle movement paths of the deformed rock mass is shown in Figure 6.12. These 'flow apophyses' are directions of maximum, intermediate and minimum flow. In both transtension and transpression 'the one flow apophysis which is horizontal and (in general) oblique to the x-axis marks the convergence direction' (Fossen and Tikoff *op. cit.*). It is notable that type A transpression and type E transtension show overall vertical apophyses which could explain the exhumation of mid-crustal rocks in the Central Zone. In order to deduce which 'type'

applies consideration of the expected mesoscale features of the models is necessary. Four features strongly suggest transpression:

i) the shape of the finite strain ellipsoid (see Figure 6.12) shows that, depending on the amount of simple shear applied, prolate $k>1$ constrictional strains result from transpression but not transtension;

ii) that linear markers plunge from near horizontal to vertical in transpression but are mainly horizontal in transtension e.g. the Sierra Nevada Batholith (Tikoff & Greene 1997);

iii) that in constriction planar markers e.g. foliation, may have any strike. In transtension foliation is parallel to shear zone margin.

iv) and finally that during type A and B transpression maximum and intermediate strains may switch, thus allowing for heterogeneous domains such seen in the field in NFG.

Overall these factors indicate type A transpression can be satisfactorily applied to the Damara Belt.

An example of constriction during transpression in nature has recently been shown for the Iberian-Amorican arc. Dias & Ribeiro (1994) document constrictional fabrics which may have been produced by complex transpression between two colliding continents where both lateral escape and volume change occur. Application of theoretical models to the Central Zone suggest a slightly more simple case were domes formed by sub-vertical extrusion of the Damaran crustal material to the SW by type A transpression (Fossen & Tikoff 1997). Partitioning of strain at the orogen scale may have allowed the separate mechanisms of thrusting at the margins and constriction at the orogen core to operate simultaneously. According to Teyssieir *et al.* (1995), partitioning depends on the convergence angle of the colliding plates. When the convergence α is low, 20° for example, partitioning is profound. When $\alpha > 20°$ less partitioning occurs. Since the Central Zone is bounded to its south by two zones i.e. the Okahandja Lineament and Southern Zones and only one in the North i.e. the Northern Zone, it is probable that the plate motion vector for the Congo craton was greater than the Kalahari craton such that less partitioning occurred (A crude estimation of α 30° for the Kalahari craton may be implied from the transport direction of the Naukluft Nappes in Figure 6.11). It is interesting to note that $\alpha < 70.5°$ in transtension produces mainly horizontal planar fabrics with $k>1$ (Dewey 1995). The presence of steep planar surfaces at the flank of domes in the Central Zone may provide another line of evidence which supports transpression.

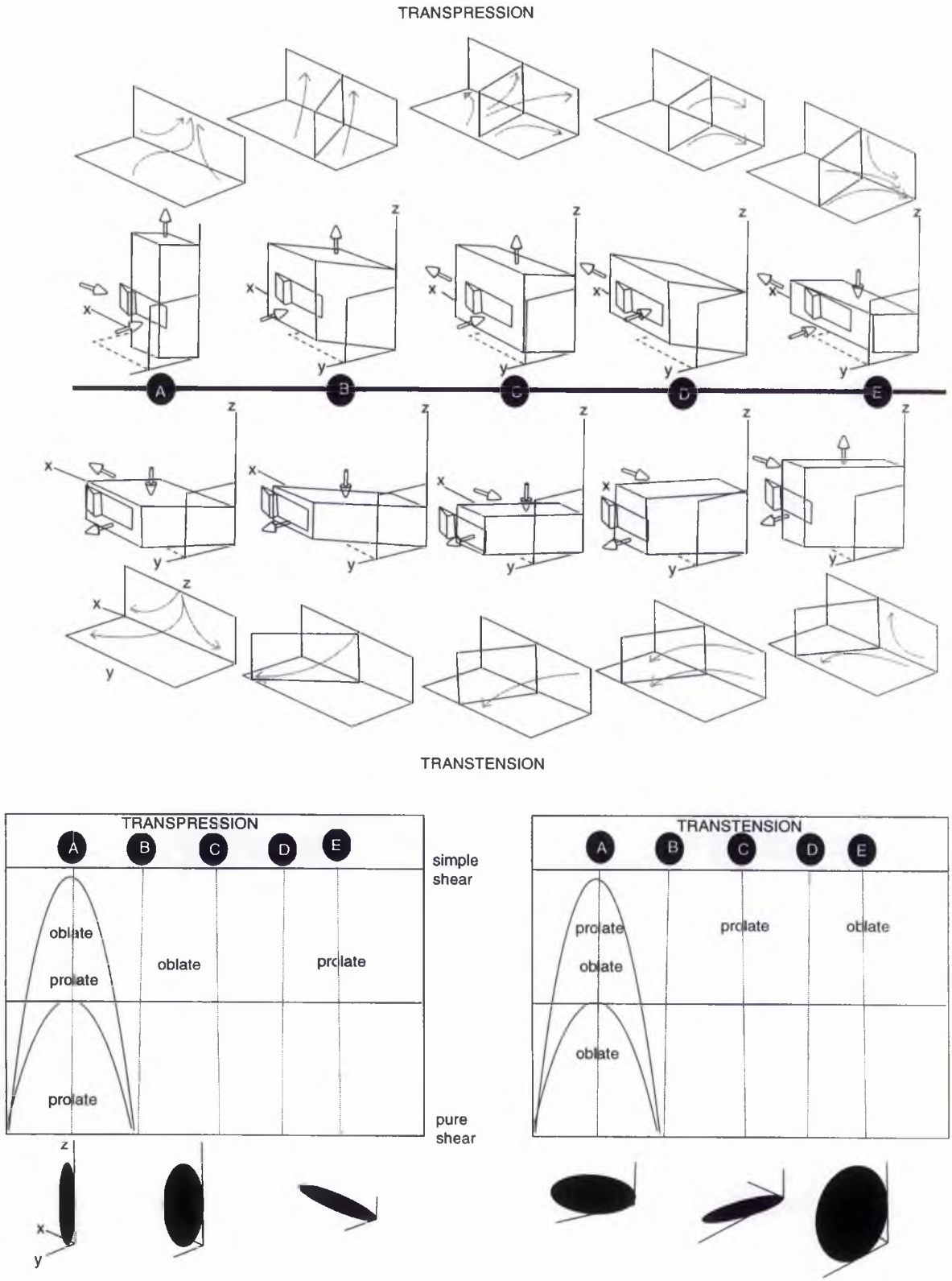

Figure 6.12 The spectrum of transpressional and transtensional deformations after Fossen and Tikoff (1997).

6.5 Damaran orogenic model.

In the previous section it has been shown that the structural features of the Central Zone may be generated by transpression during continental plate-plate collision. The objective of this final section is to develop a revised geodynamic model for the Damara orogen from early collision to suturing (*cf.* Wilson 1965). This must explain:

1. the exposure of mid-crust in domal structures at the present erosion level;
2. the presence of a metamorphic gap between the basement and cover;
3. the observed changes in *PT* conditions from the Central Zone to the marginal Southern Zone.

1. Thompson *et al.* (1997a) have recently modelled elevation of lower-crustal rocks through vertical extrusion of the crust. They suggest that lower crustal rocks at the orogen core become 'thermally softened' and 'weakened' during collision (Figure 6.13). Because the core is bounded by rigid lithospheric 'pistons' compression causes vertical extrusion. The rate of extrusion is dependent on orogenic width. Rocks in a relatively narrow belt e.g. 60km, similar to the Damara Belt, may reach the kyanite-sillimanite boundary rapidly in ~16 m.y. (Thompson *et al. op. cit.*) state that this produces isothermal *P-T-t* paths in which "heat is advected rapidly to the surface". This results in rapid cooling from 600°to 350°C in 3m.y. for 100km belt and different minerals will record similar blocking temperatures. This mechanism may account for the similar blocking ages of biotites and hornblende in the Ida Dome *c.*465 Ma. (Tack *et al.* 1995). Such rapid uplift rates are reported in present day collision belts e.g. southern Tibet 1-100mm$\cdot$yr^{-1} (Copeland *et al.* 1987). Rapid cooling is also reported in extensional settings .e.g. Metamorphic core complexes in the D'Entrecasteaux islands, where combined K/Ar, Ar40/Ar39 and fission track ages of ~2.7 to 3.0 Ma. record cooling rates of >>100°C//m.y. (Baldwin *et al.* 1993).

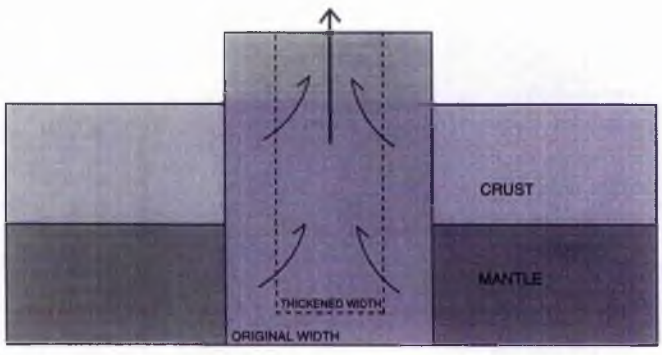

Figure 6.13. Schematic two dimensional diagram showing block of thickened weak crust enclosed between rigid crust and mantle. Black arrows indicate vertical extrusion. Lower dark grey block = lithospheric mantle.

In addition Thompson *et al.* (1997) present a series of 'thermal evolution paths' for orogens of between 100 and 300km width. The thermal history for extrusional uplift in the Central Zone is predicted from these curves, is shown in Figure 6.14. This is estimated from an approximate width of 200km and an initial thermal peak of ~800°C using M_1 temperatures from the basement. It is notable that the temperatures pass through the sillimanite field and are compatible with conditions of M_1 recorded in this study.

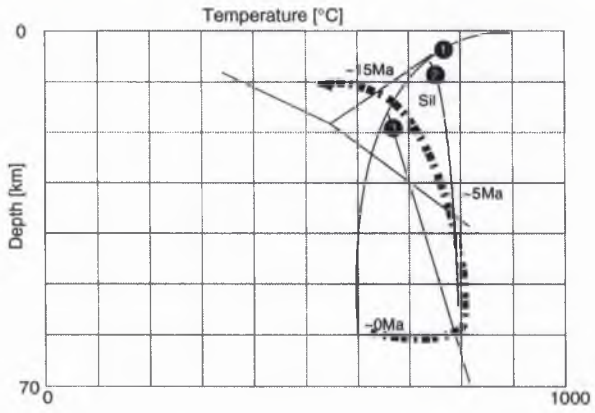

Figure 6.14. Proposed thermal history of the thickened crust for the Central Zone constructed for ~200km orogen width, (after Thompson et al. 1997) 1= WSP water saturated pelite curve 2= msc melt curve, 3= bt melt curve.

2. & 3. Several models currently exist which account for the main regional structural features of the Damara orogen e.g. Miller (1983), De Kock (1992) and Henry *et al.* (1990). Explanation of the Central Zone is rather poor in these models. Miller (1983) & Bühn *et al.* (1994) suggested that the Central Zone has been up thrown so that exposure of high temperature metamorphic facies occurred. Oliver (1994) suggested a Core Complex situation whereby crustal material was driven to the south-west by gravity collapse after the peak of deformation. However, brittle-ductile extensional detachments and syn-extensional grabens are not evident in Namibia, rather exposure of mid-crust occurs below an entirely ductile shear zone formed in a compressional regime. Thus, an alternative model is required for the Central Zone.

In this study the main structural and metamorphic features of the Central Zone are interpreted as a result of extrusion during general constriction. Figure 6.15 shows a revised geodynamic model for the evolution of the orogen:

1) Early Damaran; Rift, Rift-Drift Stage.

After rifting and deposition of Nosib Group on the passive margin of the Congo craton subduction of wide ocean occurs. the location of the Congo craton is not well constrained. Evidence of "rift-drift" transition suggested from U-Pb discordant upper intercept zircon age of 746±2 from rhyolite lavas in the Upper Nosib Group (Hoffmann *et al.* 1996) and a Rb-Sr whole rock isochron age 764±60Ma. (Hawkesworth *et al.* 1983) from the first Damaran intrusive granitoids in Pre-Damara Kamanjab Inlier. (The Lofdal Nepheline Syenite).

2) Mid-Damaran; 650-580Ma. Accretion Phase.

Congo and Rio de la Plata collide. Northward subduction of oceanic crust occurs below the Congo Craton (see Figure 6.15). Onset of post-rift/ pre-molasse Otavi Group foreland basin deposition Hoffmann (1995). Accretion of the Khomas Terrane starts. In the Central Zone thickening initiates the development of regional S_0/S_1 fabrics. At this stage the Central Zone is ~150km wide.

3) Early collision; ca. 580 Ma

Congo-Kalahari collide obliquely. The Central Zone is thickened and thermally softened, regional isotherms start to fold.

4) Early-Middle Cambrian; late collision. ca.570-530 Ma.

The Khomas Terrane is now subducted. Material of oceanic affinity is thrust south, deformed pillow lavas and gabbros are preserved as the Matchless Amphibolite (Kukla & Stanistreet 1991). Maximum extrusion in the Central Zone occurs; this has two important effects:

i) The distance between basement and cover isotherms is reduced. A 300% sub-vertical strain in the Central Zone (assumed from deformed pebbles) reduces the distance between the 650°C and 800°C isotherms from *c.*6km to *c.*2km. (calculated from a geothermal gradient of 25°C/km). Inhomogenous pure strain, compared by Thompson *et al.* (1997) to 'toothpaste in a tube', has the effect of thinning the mid-crust along the basement-cover interface (see right inset Figure 6.15). As isotherms fold they do not recover, higher temperature mid-crustal basement ~800°C is juxtaposed against lower temperature 650°C cover.

ii) Domes in the Central Zone reach their greatest amplitude. Broad synclines surround dome structures. These structures reflect the separate process of extrusion and constrictional deformation which is buffered by the Okahandja Lineament Zone, Southern

and Northern Zones. The later two zones experience polyphase deformation and are thrust outwards onto the Northern Platform and Southern Foreland.

Peak deformation and metamorphism occurs in the Central Zone ca. 570 Ma.. Ages of 548.8±30 Ma to 539.4±1 from ash beds between sediments in the Nama Basin (Grotzinger *et al.* 1995) indicate uplift and erosion. Further to the east the Lufilian Arc was pushed out towards to the north (Unrug 1992) and the eastern Zambesi belt in Zimbabwe extruded towards the north-east (Figure 6.11). It is significant that both these latter areas are dominated by dome structures (Barr 1978; Talbot 1978 & Daly 1988).

5) Middle Ordovician; Post collision ca. 530 Ma.- 465 Ma.

Post-tectonic granite intrusion occurs ca. 508±2 (Briqueu *et al.* 1980). Age of the post-tectonic Donkerhuk Granite 521±15 Ma. (Blaxland *et al.* 1979).

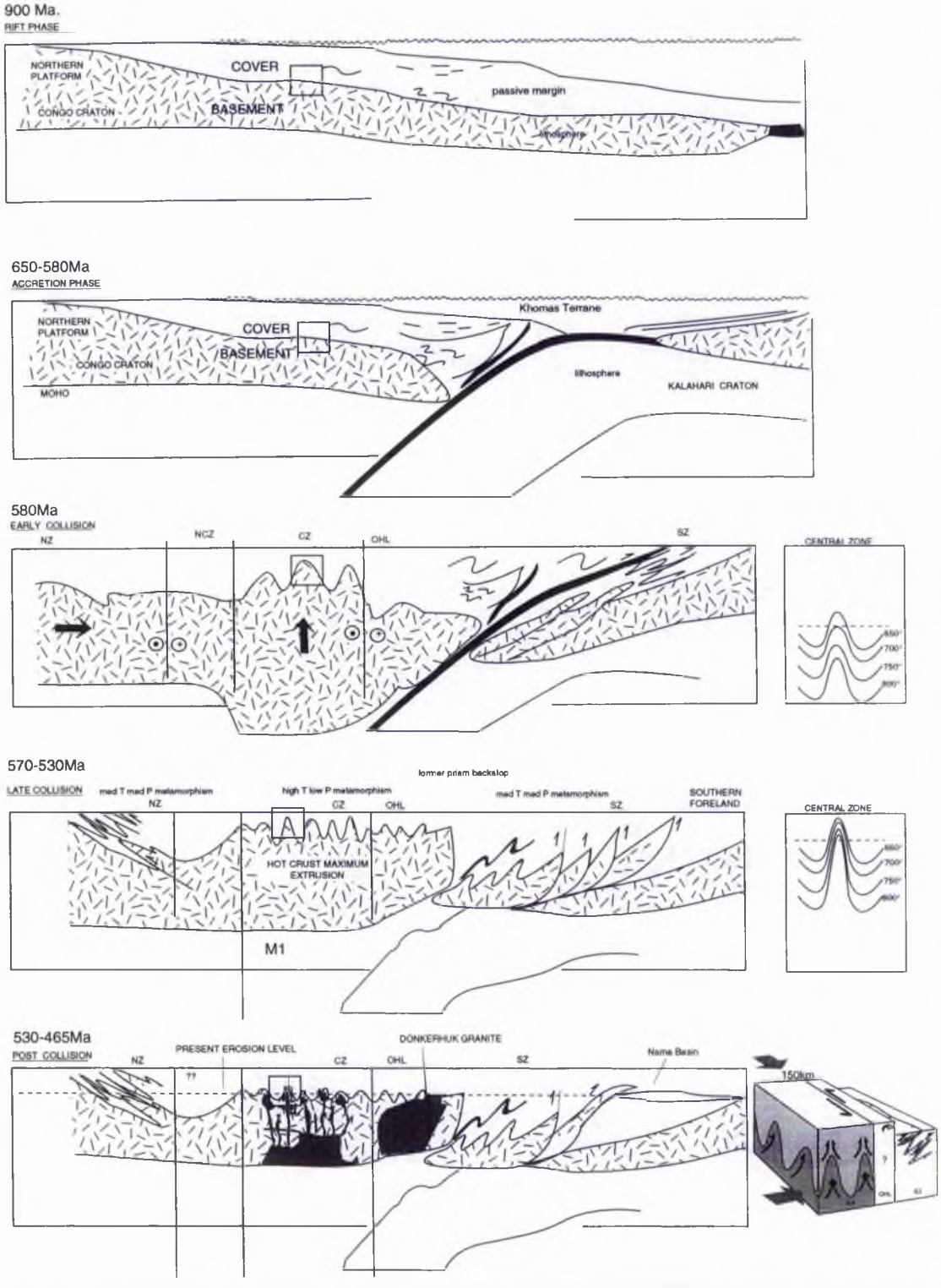

Figure 6.15. A Geodynamic model for the structural and metamorphic evolution of the Damara Orogen from the Vendian to Middle Ordovician modified from Miller (1983), Kukla & Stanistreet (1991). Five stages are shown. 1) Rift stage 2)Accretion phase. 3) Early collision phase 4)Late collision right inset demonstrates strain partitioning between tectonic zones; the Central Zone is compressed by cooler margins and extruded. 5) Post collision. Granite invasion phase.

6.6 Application of the Damara model.

Domal structures are a common feature of the internal zone of many orogens, for example, Schneider *et al.* (1996) have reported thermal weakening and extrusion in the Watersmeet Gneiss Dome, northern Michigan. Other examples include the Limpopo Belt, Zimbabwe (Roering *et al.* 1992), the Mary Kathleen Fold Belt, Mt. Isa Inlier northern Australia (Holcombe *et al.* 1991), the Dharwar craton (Bouhallier *et al.* 1995) and the Williamantic Dome New England (Getty and Gromet 1992).

CHAPTER 7

Conclusions

7.1 Conclusions

The conclusions of this research are summarised in point form below. Data from fieldwork and laboratory studies, Chapters 2-5, have been used to address the main aims in Chapter 1. These have been tested against existing and theoretical models in Chapter 6. Further research is suggested following this.

1. A new three stage structural model is proposed in Chapter 3 for the development of domes in the Central Zone. This is based on consideration of data from field mapping and laboratory studies. Stage 1 produced a regional parallel S_0/S_1 fabric. During Stage 2 folding produced domes, local S_2 foliations and aberrant fold patterns. Stage 3 is characterised by late granite intrusion.

2. Detailed analysis of small scale and regional structures has shown several common features i) NE-SW trending amoeboidal domes and sinuous bifurcating synclines ii) inconsistent mesoscale fold relations and iii) synclinal convergence points. This highlights a discrepancy between existing models of dome formation and observed geological structures. Early models do not adequately explain them. Domes are interpreted to have formed contemporaneously by a single progressive deformation (i.e. Stage 1- Stage 3) and not discrete deformation events.

3. Finite strain determination from a variety of methods shows general constriction $k>1$ in both study areas. A moderately plunging constrictional field is the likely cause of structures in the Central Zone.

4. Strain has been concentrated at the basement-cover contact during Stage 2. High temperature ductile mylonites formed in response to these distributed higher strains in a zone termed the Khan River Detachment.

5. Pressure and temperature conditions of peak M_1 metamorphism have been estimated from a variety of thermobarometers for cover gneisses in Namibfontein and Khan Mine

area. Grt-Bt thermometers give temperatures ~662±50°C in the Namibfontein area and ~700°C in the Khan Mine area. A combination of barometers gives pressure ~3.2-4kbar±1 in the Namibfontein area and 4.6-5.9kbar±1 in the Khan Mine area.

6. Pressure and temperature conditions of peak M_1 metamorphism have been estimated from a variety of thermobarometers for three basement gneiss samples in Namibfontein area. Grt-Bt thermometers give temperatures ~791±50°C and a Grt-Bt-Pl barometer gives pressures of 5.9 & 7kbar±1.

7. Cover and basement gneisses record distinct *PT* conditions. The presence of a metamorphic gap is confirmed. This is interpreted as a result of the dome forming process. A 300% inhomogeneous strain of the crust has extruded high temperature gneisses at dome cores. Syn-tectonic folding and thinning of crustal geotherms during Stage 2 resulted in a metamorphic gap ~150°C ~ 2kbar separated by the Khan River detachment.

8. A three stage granite intrusion history is documented in both areas. The main granite intrusions post-date dome formation and cross cut the Khan River Detachment.

9. Extrusion of the Central Zone during single phase progressive constriction was caused by collision of the Congo, Kalahari and Rio de la Plata cratons during Pan-African assembly. A new 5 stage geodynamic model is proposed (Chapter 6) in which the Central Zone is buffered by cooler marginal tectonic zones. Domes formed during final collision and suturing. This may represent a common geological process.

7.2 Suggestions for further research

1. Systematic dating of shear zone fabric, e.g. radiometric and isotopic methods, in the Khan River Detachment is required. This would date the peak of deformation i.e. dome formation in the Central Zone. This would also test the observation that metamorphism is syn-kinematic.

2. Orogen wide dating of granites and the regional metamorphic fabrics in the Central Zone, Southern and Northern Zones by a variety of methods would help constrain the timing of the rate of extrusion in the proposed geodynamic model.

3. Study of small scale geological structures in the Central Zone, Okahandja Lineament Zone and Southern Zones (especially lineations in marginal zones) would

help determine i) the kinematics of plate motions during Damaran orogenesis and ii) highlight changes in the strain gradients across the orogen.

4. Further thermobarometric investigation of the basement in other basement areas. This would test the findings of this study. Petrographic investigation of basement in the Abbabis inlier for example may identify evidence of pre-Damaran metamorphic assemblages.

References

Ahrendt, H., Hunziker, C.H. & Weber, K. 1978. Age and degree of metamorphism and time of nappe emplacement along the southern margin of the Damara Orogen, Namibia. *Geologische Rundschau*, **67/7**, 19-742.

Ahrendt, H., Behr, H.J., Clauer, N., Hunziker, J.C., Porada, H. & Weber, K., 1983. The Northern Branch: depositional Development and the timing of the structural and Metamorphic Evolution within the framework of the Damara Orogen. In: Martin, H. and F.W. Eder (eds), *Intracontinental Fold Belts*. Springer Verlag, 723-743.

Alsop, G.I. and Holdsworth, R.E. 1993. The distribution, geometry and kinematic significance of Caledonian buckle folds in the western Moine Nappe, northwestern Scotland. *Geological Magazine*, **130**, 353-362.

Alsop, G.I. 1994. Relationships between distributed and localized shear in the tectonic evolution of a Caledonian fold and thrust zone, northwest Ireland, *Geological Magazine*, **131**, 123-136.

Alsop, G. I., Bryson, R. & D.H.W. Hutton 1996. Ductile transpression and localisation along tectonic boundaires in the Caledonides of northwestern Ireland. Abstract, *Tectonic Studies Group.*

Allsopp, H.L. Barton, E.S., Kröner, H.J., Welke, A.J. & Burger A.J. 1983. Emplacement versus inherited isotopic age patterns: A Rb-Sr U-Pb study of Salem-type granites from the Central Damara Belt. In Miller, R.McG. (ed) *Evolution of the Damara Orogen of South West Africa Namibia.* Special Publication of the Geological Society of South Africa., **11**, 281-289.

Anhaeusser, C.R. 1969a. A comparison of pebble and fold deformations in: The Nelspruit Granite Contact Aureole, Barberton Mountain Land. *Transactions of the Geological Society of South Africa*, **72**, 49-60.

Argand, E. 1922. La tectonique de' l' Asie. *International Geological Congress, 13th Session, Brussels*, 171-372.

Badenhorst, F.P. 1992. The lithostratigraphy of area 2115B and D in the Central zone of the Damara Orogen, Namibia: with emphasis on the facies changes and regional correlations. M. Sc. thesis (unpubl.), Uniiversity Port Elizabeth, 124p.

Barker, A.J. 1990. *Metamorphic textures and microstructures*. Blackie & Son, Glasgow, 162p.

Barnes, F.H. and Downing, N. 1979. Origin of domes in the central Damaran Belt, Namibia. *Revue de geologie dynamique et de Geographie physique*, **21**, FASC. 5, 383-386.

Barnes, J.F.H. 1981. Some aspects of the Tectonic history of the Khan-Swakop region of the Damara Belt, Namibia.. Ph. D thesis (unpubl.) University of Leeds.

Barnes, F.H. & Sawyer, E.W. 1980. An alternative model for the Damara mobile Belt: ocean crust subduction and continental convergence. *Precambrian Research*, **13**, 297-336.

Barr, M.W.C. 1976. Crustal shortening in the Zambezi belt. P*hilosophical Transactions of the Royal Society London*, A, **280**, 555-567.

Barton, C.M, Carney, J.N., Crow, M.J., Dunkley, P.N.,Simango, S. and Evans, J.A. 1991. The Geology of the Country Around Rushinga and Nyamapanda. Bulletin 92, *Zimbabwe Geological Survey*.

Barton, M.D. and Hanson, R.B. 1989. Magmatism and the development of low pressure metamorphic belts: implications from the western United States and thermal modelling. *Geological Society of America Bulletin*, **101**, 1051-1065.

Bell, T.H. & Rubenach, M.J., 1983 Sequential porphyroblast growth and crenulation cleavage development during progressive deformation. *Tectonophysics*, **78**. 23-506.

Berning, J., Cooke, R., Hiemstra, S.A. and Hoffman, U. 1976. The Rössing uranium deposit, South West Africa. *Economic Geology*, **71**, 351-368.

Berning, J. 1986. The Rössing Uranium deposit, South West Africa Namibia. In: Annhaeusser, C.R. and Maske, S. (eds.) *Mineral deposits of southern Africa,* Geological Society of South Africa, Johannesburg, 1819-1832.

Bhattacharya, A., Mohanty, L., Maji, A., Sen, S. K., and Raith, M. 1992, Non-ideal mixing in the phlogopite-annite binary: constraints from experimental data on Mg-Fe partitioning and a reformulation of the biotite-garnet geothermometer: *Contributions to Mineralogy and Petrology*, **111**, 87-93.

Berman, R.G. (1988). Internally-consistent thermodynamic data for minerals in the system Na_2O-K2O-CaO-MgO-FeO-Fe_2O_3-Al_2O_3-SiO_2-TiO2-H_2O-CO_2. *Journal of Petrology*, **29**, 445-522.

Black, R & Liegeois, J.P. 1993. Cratons, mobile belts ,alkaline rocks and the continental lithospheric mantle: the Pan-African testimony.*Journal Geological Society London*, **150**, 89-98.

Blaine, J.L. 1977. Tectonic evolution of the Waldau ridge structure and the Okahandja Lineament in part of the Central Damaran Orogen, west of Okahandja, south West Africa, *Bulletin of the Precambrian Research Unit*, University of Cape Town, **21**, 99.

Blaxland, A., Gohn, E., Haack, U and hoffer, E. 1979. Rb/Sr ages of late tectonic granites in the Damara orogen, South West Africa Namibia. *Neues. Jb. Mineral Mh*, **11**, 489-508.

Blundy, J.D. and Holland, T. 1990. Calcic amphibole equilibria and a new amphibole-plagioclase geothermometer. *Contributions to Mineral Petrology,* **104**, 208-224.

Bouhallier, H. Dominique, C. and Choukroune, P. 1995. Strain patterns in Archean dome-and-basin structures: The Dharwar craton (Karnataka, South India). *Earth and Planetary Science Letters*, **135**, 57-75.

Bozkurt, E. and Park, R.G. 1994. Southern Mendres Massif: an incipient metamorphic core complex in western Turkey. *Journal of the Geological Society London*, **151**, 213-216.

Bühn, B., Stanistreet, I.G. & Charelsworth, E.G. 1991. Multiple deformation patterns in the Otjosondu Manganese mining area, eastern Damara Belt, Namibia. *Communications of the Geological Survey of Namibia*, **7**, 15-19.

Bühn, B., Stanistreet, I.G. and Charlesworth, E.G. 1993b. Fold shape variation controlling interference mechanisms and patterns of during oblique fold superpositions in the Damara orogen, eastern Namibia. *Annales Tectonicae*, **7**, 113-128.

Bühn, B., Okrusch, M., Woermann, E., Lehnert, K., and Hoernes, S. 1995. Metamorphic evolution of neoproterozoic manganese formations and their country rocks at Otjosondu, Namibia. *Journal of Petrology*, **36**, 463-496.

Bühn, B., Haussinger, H., Kramm, U., Kukla, C., Kukla, P.A. & Stanistreet, I.G.1994. Tectonometamorphic patterns developed during Pan-African continental collision in the Damara Inland Belt, Namibia. *Chemie Der Erde-Geochemistry*, **54**, 329-354.

Brandt, R. 1985. Preliminary report on the stratigraphy of the Damara Sequence and the geology and geochemistry of the Damaran granites between Walvis Bay and Karabib.*Communications of the Geological Survey Namibia*, **1**, 31-45.

Brandt, R. 1987. A revised stratigraphy for the Abbabis Complex in the Abbabis Inlier, Namibia. *South African Journal of Geology*, **90**. 314-323.

Briqueu, L., Lancelot, J.R., Valois, J-P. and Walgenwitz, F. 1980. Geochronologie U=Pb et genèse d'un type de minéralisation uranifère: les alaskites de Goanikontes (Namibie)et leur encaissant. Bulletin *Cêntre Récherche Exploration-Production Elf-Aquitaine*, **4**, 759-811.

Brun, J-P. and Pons, 1981. Strain patterns of pluton emplacement in acrust undergoing non-coaxial deformAtion, Serra Morena, Southern Spain, *Journal of Structural Geology*, **5**, 321-327.

Brun, J-P. and Van Den Driessche 1994. Extensional gneiss domes and detachment fault systems: structure and kinematics. *Bulletin Societie Géologie France*, **165**, 519-530.

Carmichael, D.M. 1969. On the mechanism of prograde metamorphic reactions in quartz-bearing pelitic rocks. *Contributions to Mineralogy & Petrology*, **20**, 244-267.

Clemens, J.D. and Petford, N. 1995. Ascent mechanisms of granitic magmas: Causes and consequences. Abstract, Deformation-enhanced Melt Segregation and Metamorphic Fluid Transport, conference 1995.

Coney, P.J. and Harms, T. A. 1984. Cordilleran metamorphic core complexes: Cenozoic extensional relics of Mesozoic compression. *Geology*, **12**, 550-554.

Coward, M.P. 1981a. The junction between Pan African mobile belts in Namibia - its structural history. *Tectonophysics*, **76**, 59-73.

Coward, M.P. 1981. Diapirism and gravity tectonics - Report of a Tectonic Studies Group Conference Held At Leeds-University, 25-26 March. *Journal of Structural Geology*, **3**, 89-90.

Coward, M.P.1981. Pan-African Gneiss domes, diapirs and sheath folds *Journal of Structural Geology*, **3**, 89-95.

Coward. M.P., Daly.M.C. 1984. Crustal lineaments and shear zones in Africa -Their relationship to plate movements. *Precambrian Research*, **24**, 27-45

Clifford, T.N.1967. The Damara episode in South West Africa. *Geological Society of America Special paper*, **92**.

Coward, M.P. 1983. The Tectonic History of the Damara Belt. In: Miller, R.McG. (ed) *Evolution of the Damara Orogen of South West Africa Namibia.* Special. Publication of the Geological Society of South Africa, **11**, 409-423.

Crittenden, M.D., Jr., Coney, P. J. and Davies, G. H. 1980. Cordilleran metamorphic core complexes. *Memoir,* **153**, 490p. *Geological Society America*, Washington, USA.

Cruden, A.R. 1988. Deformation around a rising diapir modelled by creeping flow past a sphere. *Tectonics,* **7**, 1091-229.

Daly, M.C. 1986. Crustal shear zones and thrust belts: their geometry and continuity in Central Africa. Philosophical. *Transactions Royal Society London.* A, **317**, 111-128.

Davis, G.A. and Lister, G. S. 1989. The origin of metamorphic core complexes and detachment faults formed during Tertiary continental extension in the northern Colorado River region, USA. *Journal of Structural Geology*, **11**, 65-94.

Dievorst, E.J.L. 1982. Retrograde Garnet Zoning at Low Water Pressure in Metapelitic Rocks from Kemiö, SW Finland. *Contributions to Mineralogy and Petrology,* **79**, 37-45.

Downing, K.N. and Coward, M. P. 1981. The Okahandja Lineament and its significance for Damaran tectonics in Namibia. *Geologische Rundschau*, **70**, 972-1000.

Dalziel, I.W.D. 1991. Pacific Margins of Laurentia and East Antarctica Australia as a conjugate rift pair - evidence and implications for an Eocambrian Supercontinent. *Geology*, **19**, 598-601.

Dalziel. I.W.D. 1992. On the organisation of American plates in the Neoproterozoic and the breakout of Laurentia. GSA Today, **2**, 237-241.

Dalziel, I.W.D. 1995. Earth Before Pangea. *Scientific American*, **272**, 58-63.

Dalziel, I.W.D., Dallasalda, L.H., Gahagan, L.M. 1994. Paleozoic Laurentia-Gondwana interaction and the origin of the Appalachian-Andean mountain system. *Geological society of America Bulletin*, **106**, 243-252.

De Beer, C.H. 1995. Fold interference from simultaneous shortening in different directions: the Cape Fold Belt Syntaxis. *Journal of African Earth Sciences. Pre print.*

De Kock, G.S. 1992. Fore-arc evolution in the Pan African Damara Belt, central Namibia: the Hureb Formation of the Khomas Zone. *Precambrian Research*, **57**, 169-194.

De Paor, D.G. 1980. Some limitations of the R_f/ϕ technique of strain analysis. *Tectonophysics*, **64** , 29-31.

Dewey, J.F. 1988. Extensional collapse of orogens. *Tectonics*, **7**, 1123-1139.

Dewey, J.F., Ryan, P.D. and Anderson, T.B. 1993. Orogenic uplift and collapse, crustal thickness, fabrics and metamorphic phase changes: the role of ecolgites, In: Prichard, H.M., Alabaster, T., Harris, N.B.W. and Neary, C.R. (eds) Magmatic processes and Plate Tectonics, *Geological Society of London Special Publication*, **76**. 325-343

Dewey, J.F. 1995. Transtension in extensional core complex/detachment systems. Abstract Tectonic Studies Group conference.

Dias, R. & Ribeiro, A. 1994. Constriction in a transpressive regime: an example in the Iberian branch of the Ibero-Amoricain arc. *Journal of Structural Geology*, **16**, 1543-1554.

Döpke, H.H. 1978. Zur Geologie und Tektonik des Namibfontein Vergenoeg-Zwillingsdomes, Namibia (Südwest-Afrika). M.Sc. thesis (upubl.), Univiversity Mainz, 60p.

Downing, K.N. & Coward, M.P. 1981. The Okahandja Lineament and its significance for Damaran tectonics in Namibia. *Geologische Rundschau*, **70**, 972-1000.

Dürr, S.B. & Dingledey, D.P. 1996. The Koako belt (Namibia): Part of a late Neoproterozoic continental-scale strike slip system. *Geology*. **24**, 503-506.

Droop, G.T.R. 1987. A general equation for estimation Fe^{3+} concentrations in ferromagnesian silicates and oxides from microprobe analyses, using stoichiometric criteria, *Mineral Magazine*, **51**, 431-435.

Edbert, H.D., Chemiale, F., Babinski, J.R., Artur, A.C. & Van Schmus, W.R. 1996. Tectonic setting and U/Pb zircon dating of the plutonic Soccorro Complex in the Transpressive Rio Paraíba do Sul shear Belt, SE Brazil. *Tectonics,* **15**, 688-699.

Eggert, R.G. and Kerrick, D.M. 1981. Metamorphic equilibria in the silceous dolomite system: 6 kbar experimental data and geologic implications. *Geochimica et Cosmochimica Acta*, **45**, 1039-1049.

England, R.W. 1988. The ascent sand emplacement of granitic magma: the Northern Arran granite. Ph. D thesis, University of Durham.

England, R.W. 1990. The identification of granite diapirs. *Journal of the Geological Society, London*, **147**, 931-933.

Eskola, P. 1949. The problem of mantled gneiss domes. *Quarterly Journal Geological Society London.*, **104**, 461-476.

Ferry, J.M. and Spear, F.S. 1978. Experimental calibration of the partitioning of Fe and Mg between biotite and garnet. *Contributions to Mineralogy and Petrology*, **66**, 113-117.

Ferry, J.M. 1976. P, T, f_{CO2} and f_{H2O} during metamorphism of calcareous sediments in the Waterville-Vassalboro area, south-central Maine. *Contributions to Mineral Petrology*, **57**, 119-143.

Ferguson, C.C. 1981. A strain reversal method for estimating extension from fragmented rigid inclusions. *Tectonophysics*, **79**, 43-52.

Fletcher. J.M. & Bartley J.M. 1994. Constrictional strain in a non-coaxial shear-zone: implications for fold fabric development, central Mojave metamorphic core complex, California. *Journal of Structural Geology*, **16**, 555-570.

Flinn, D. 1956. On the Deformation of the Funzie conglomerate, Fetlar, Shetland. *Journal of Geology*, **64**, 480-505.

Flinn, D. 1965. On the symmetry principle and the deformation ellipsoid. *Geological Magazine*, **102**, 36-45.

Fossen, H and Tikoff, B. 1997. Extended models of transpression/ transtension and application to tectonic settings. *Continental Transpressional and Transtensional Tectonics, Pre-print*, Geological Society Special Publication in press.

Freeman, B. and Lisle, R.J. 1987. The relationship between tectonic strain and the three-dimensional shape fabrics of pebbles in deformed conglomerates. *Geological Society London*, **144**, 635-639.

Ganguly, J. and Saxena, S. K. 1984. Mixing properties of aluminosilicate garnets: constraints from natural and experimental data, and applications to geothermo-barometry. *American Mineralogist*, **69**, 88-97.

Gevers, T.W. & Frommurze, H.F. 1929. Geology of North-Western Damaraland, in South West-Africa. *Transactions of the Geological Society South Africa*, **32**, 31-55.

Gevers, T.W. 1963. Geology along the north-western margin of the Khomas highlands between Otjimbingwe-Karabib and Okahandja, South West Africa. Transactions Geological Society South Africa., **66** 199-251.

Getty, S.R. and Gromet, L.P. 1992. Geochronological constraints on ductile deformation, crustal extension, and doming about a basement-cover boundary, New England Appalachians. *American Journal of Science,* **292**, 359-397.

Ghosh, S.K. and Ramberg, H. 1968. Buckling experiments on intersecting fold patterns. *Tectonophysics,* **5**, 89-105.

Ghosh, S.K.1970. A theoretical study of intersecting fold patterns. *Tectonophysics.* **9**, 557-569.

Ghosh, S.K. and Sengupta, S. 1984. Successive development of plane noncylindrical folds in progressive deformation. *Journal of Structural Geology*, **6**, 703-709.

Ghosh, S.K. and Sengupta, S. 1987. Progressive development of the structures in a ductile shear zone. *Journal of Structural Geology*, **9**, 277-88

Ghosh, S.K., Mandal, N., Khan, D., and Deb, S. 1992. Modes of superposed buckling in single layers controlled by intial tightness of early folds. *Journal of Structural Geology,* **14**, 381-394.

Ghosh, S.K. 1993. *Structural Geology*: Fundamentals and Modern Developments. Pergamon Press.

Ghosh, S.K., Khan, D., & Sengupta, S. 1995. Interfering folds in constrictional deformation. *Journal of Structural Geology,* **17**, 1361-1373.

Goodman, S. 1994. Igneous rocks as time-markers in structural sequences-a hierachy of evidence. Abstract, Tectonic Studies Group conference.

Gresse, P.G.1989. Pan African orogenesis in southern Africa as reflected in the late Proterozoic/ early Cambrian Nama foreland basin. *Etudes récentes sur la Géologie de l' Afrique.* 117-119

Grotzinger, J.P., Bowring, S.A., Saylor, B.Z., and Kaufman, A.J. 1995. Biostratigraphic and geochronologic constraints on early animal evolution, *Science*, **270**, 598-604.

Guglielmo, J.R. 1993. Interference between pluton expansion and non-coxial tectonic deformation: three-dimensional computer model and field implications. *Journal of Structural Geology.* **17**, 593-608.

Haack, U & Hoffer, E. 1976. K/Ar ages of biotites from the damara-orogen, South West Africa.*Transactions of the Geological Society South Africa,* **76**, 213-216.

Haack, U. and Martin, H. 1983. Geochronology of the Damara Orogen-A review. In: Martin, H. and F.W. Eder (eds), *Intracontinental Fold Belts*. Springer Verlag, 839-846.

Hartmann, O. Hoffer, E., Haack, U. 1983. Regional metamorphism in the Damara Orogen: interaction of crustal motion and heat transfer. In Miller, R.McG. (ed) *Evolution of the Damara Orogen of South West Africa Namibia.* Special Publication of the Geological Society of South Africa., **11**, 233-241.

Haugerud, R.A. and Zen, E-an. 1991. Essay on metamorphic path studies or Cassandra in P-T-t space. In: L.L Perchuk (eds) *Progress in Metamorphic and Magmatic Petrology*, Cambridge University Press, 323-351.

Hawkesworth, C.J. Gledhill, A.R. Roddick, J.C. Miller, R. McG. and Kröner, A. 1983. Rb-Sr and 40Ar/39Ar studies bearing on models for the thermal evolution of the Damara Belt, Namibia. In: Miller, R.McG. (ed) *Evolution of the Damara Orogen ofSouth West Africa Namibia.* Special. Publication of the Geological Society of South Africa. **11**, 323-338.

Hawkesworth, C.J., Menzies, M.A. & Calestra, P .1986. Geochemical and tectonic evolution of the Damara belt, Namibia. *Collision tectonics.* Geological Society Special Publication, **19**, 305-319.

Henry, G., Stanistreet, I.G. and Maiden, K.J. 1986. Prelimenary results of a sedimentological study of the Chuos Formation in the Central Zone of the Damara Orogen: evidence for mass flow processes and glacial activity. *Communications of the Geological Survey Namibia.* **2**, 75-92.

Henry, G., Clendenin, C.W., Stanistreet, I.G. and Maiden, K.J. 1990. Multiple detachment model for th early rifting stage of the Late proterozoic Damara orogen in Namibia. *Geology*, **18**. 67-71.

Henry, G. 1992. The sedimentary evolution of the Damara Sequence in the lower Khan River valley, Namibia. Ph. D. thesis (unpubl.), Univiversity Witwatersrand, 217p.

Heubeck, C. and Lowe, D.R. 1994. Late syndepositional deformation and detachment tectonics in the Barberton Greenstone Belt, South Africa. *Tectonics*, **13**, 1514-1536.

Hodges, K.V. and Spear, F.S. 1982. Geothermometry, geobarometry and the Al2SiO5 triple point at Mt. Moosilauke, New Hampshire. *American Mineralogist*, **67**, 1118-1134.

Hodges, K.V. and Walker, J.D. 1990. Petrologic Constraints on the Unroofing History of the Funeral Mountain Metamorphic Core Complex, California. *Journal of Geophysical Research*, **95**, 8437-8445.

Hoernes, S. and Hoffer, E. 1979. Equilibrium Relations of Prograde Metamorphic Mineral assemblages, (A stable Isotope Study of Rocks of the Damara Orogen, from Namibia). *Contributions to Mineralogy and Petrology*, **68**, 377-389.

Hoisch, T.D. 1990. Empirical calibration of six geobarometers for the mineral assemblage quartz +muscovite +biotite plagioclase +garnet. *Contributions to Mineralogy and Petrology*, **104**, 225-234

Hoffman, A.B. 1984. *An excursion guide to the geology of the Rössing uranium Mine.* Manuscrip (unpubl.) 50pp.

Hoffer, E. 1976. The reaction sillimanite +biotite +quartz⇔ cordierite +K-feldspar+H2O and partial melting in the system K_2O-FeO-$MgOAl_2O_3$-SiO_2-H_2O. *Contributions to Mineralogy & Petrology*, **55**, 127-130.

Hoffer, E. 1977. Petrologische Untersuchungen zur Regionalmetamorphose Al-reicher Metapelite im südlichen Damara-Orogen (Südwest-Afrika). Habilitationsschrift, University Gottingen, 150pp.

Hoffman, F. 1991 Did the breakout of Gondwana turn Laurentia inside-Out?. *Science*. **252**, 1409-1412.

Hoffmann, K.H. 1994. New constraints on the timing of continental breakup and collision in the Damara belt. In: Niall, M., and McManus, C. (eds). Abstracts, Conference on Proterozoic Crustal and Metallogenic Evolution, Windhoek, Namibia: *Geological Society and Geological Survey of Namibia,* p. 30.

Holcombe, R.J., Pearson, P.J. and Oliver, N.H.S. 1991. Geometry of a Middle Proterozoic extensional décollement in northern Australia. *Tectonopyhsics*, **191**, 255-274.

Holdaway, M.J. and Lee, S.M. 1977. Fe-Mg cordierite stability in high grade pelitic rocks based on experimental, theoretical and natural observations: *Contributions to Mineral Petrology,* **63**, 175-198.

Holland, T. and Blundy, J. 1994. Non-ideal interactions in calcic amphiboles and their bearing on amphibole-plagioclase thermometry. *Contributions to Mineral Petrology,* **116**, 433-447

Horstmann, U.E., Ahrendt, H., Clauer, N. and Porada. 1990. The metamorphic history of the Damara Orogen based on K/Ar data of detrital white micas from the Nama Group, Namibia, *Precambrian Research*, **48**, 41-61.

Hutton, D.H.W. 1979. The strain history of a Dalradian slide: Using pebbles with low flucations in axis orientation. *Tectononphysics*, **55**, 261-273.

Hunt, G., Mühlhaus, H. Hobbs, B. Ord, A. 1996. Localized folding of viscoelastic layers. *Geologische Rundschau,* **85**, 58-64.

Indares, A. and Martignole, J.1985. Biotite-Garnet thermometry in the granulite facies: the influence of Ti and Al in biotite. *American Mineralogist*, **70**, 272-278.

Jacob, R.E. 1974a. Geology and metamorphic petrology of part of the Damara orogen along the lower Swakop river, South West Africa. Bulletin **17**, *Chamber of Mines, Precambrian Research Unit*, University of Cape Town.

Jacob, R.E., Snowden, P.A. & Bunting, F.J.L. 1983. Geology and Structural development of the Tumas basement dome and its cover rocks. In: Miller, R.McG. (eds) *Evolution of the Damara Orogen of south West Africa Namibia.* Special. Publication of the Geological Society of South Africa. **11**, 157-173.

John, B.E. 1987. Geometry and evolution of mid-crustal extensional fault system: Chemehuevi Mountains, southeastern California, In: M. P. Coward, J.F. Dewey and P.L. Hancock (eds), *Continental Extensional Tectonics*, Geological Society Special Publication, London, **28**, 313-335.

Kasch, K.W.1983a. Regional P-T Variations in the Damara Orogen with particular reference to early high-pressure metamorphism along the Southern Margin. In: Miller, R.McG. (ed) *Evolution of the Damara Orogen of Ssouth West Africa/ Namibia.* Special Publication of the Geological Society of South Africa. **11**, 243-255.

Kasch, K.W.1983b. Folding and thrust tectonics in the south eastern portion of the Damara Orogen around Omitara, Namibia. In: Miller, R.McG. (ed) *Evolution of the Damara Orogen of South West Africa/ Namibia.* Special. Publication of the Geological Society of South Africa. **11**, 175-185.

Kasch, K.W. 1988. Lithostratigraphy and structural geology of the upper Swakop River area east of Okahandja, SWA/Namibia. *Communications of the geological survey of South West Africa/ Namibia,* **4**, 59-66.

Kennedy, W.Q.1964. *8th Annual Report of the Research Institute for African Geology.* Univeristy of Leeds, 48-49.

Kleeman, U. and Reinhardt, J. 1994. Garnet-biotite thermometry revisted: The effect of Al^{VI} and Ti in biotite. *European Journal of Mineralogy*, **6,** 925-941.

Korzhinskii, D.S. 1936a. Paragenetic analysis of quartz-bearing low-calcium schists of Archean complex of Southern Pribaikalje. *Zapiski Mineral Obschestva*, **65**, 247-280.

Kröner, A. 1982.Rb-Sr geochronolgy and tectonic evolution of the Pan-African Damara Belt, Southwestern Africa. *American Journal of Science*. **282**, 1471-1507.

Kröner, A. 1984. Dome structures and basement reactivation in the Pan-African Damara belt of Namibia. In: A. Kröner and R. Grieiling (eds) *Precambrian Tectonics Illustrated.*

Kröner, A., Retief, E.A., Compston, W., Jacob, R.E. & Burger, A.J. 1991. Single-Age and conventional zircon dating of remobilised basement gneisses in the central Damara belt of Namibia. *South African Journal of Geology,* **94**,379-387.

Kobberger, G. & Zulauf, G. 1995. Experimental folding and boudinage under pure constrictional conditions. *Journal of Structural Geology*, **17**, 1055-1063.

Kretz, R. 1983. Symbols for rock-forming minerals. *American Mineralogist*, **68**, 277-279.

Kretz, R. 1994. *Metamorphic Crystallization*, John Wiley and Sons, Chichester.

Kukla, P.A. and Stanistreet, I.A. 1991. Record of the Damaran Khomas Hochland accretionary prism in central Namibia: Refutation of an "ensialic" origin of a Late Proterozoic orogenic belt. *Geology,* **19**, 473-476.

Lacassin, R. & Mattauer, M. 1985. Kilometre-scale sheath fold at Mattmark and implications for transport direction in the Alps. *Nature*, **315**, 739-741.

Lavrent' eva, I.V. and Perchuk, L.L. 1981 Phase correspondence in the system biotite-garnet: experimental data: *Doklady Akademii Nauk* (USSR), **260**, 731-734.

Lehtonen, M.I., Manninen, T.E.T. & Schreiber, U.M. 1993. The Geology of the area between the Khan river and the Coast, and in the vincinity of Omdel Dam. Mapping Report and geochemical study, *Finnish-Namibian Geological mapping and maps project.* Map 2215A.

Lehtonen, M.I., Manninen, T.E.T. & Schreiber, U.M. 1996. Report: lithostratigraphy of the area between the Swakop, Khan and lower Omaruru Rivers, Namib Desert. *Communications of the Geological Survey Namibia,* **11**, 65-75.

Leake, B.E. 1978. Nomenclature of Amphiboles, *Mineralogical Magazine*, **42**, 533-563.

Lisle, R.J. 1991. Strain estimation from flattened buckle folds. *Journal of Structural Geology*, **14**, 369-371.

Lister, G.S. & Williams, P.F. 1983. The partitioning of deformation in flowing rock masses. *Tectonopyhsics,* **92**, 1-23.

Mainprice, D. and Behmann, J.H. 1987. Deformation Mechanisms in a high-temperature quartz feldspar mylonite-evidence of superplastic flow in the lower continental crust. *Tectonophysics,* **140**, 297-305.

Martin, H.1983a. Overview of the geosynclinal, structural and metamorphic development of the intracontinental branch of the Damara Orogen. In: Martin, H. and F.W. Eder (eds), *Intracontinental Fold Belts*. Springer Verlag, 913-945.

Martin, H., Porada, H. and Walliser, O.H. 1985. Mixtite deposits of the Damara Sequence, Namibia, problems of interpretation. *Palaegeography, Palaeoclimatology and Palaeoecology*, **51**, 159-196.

Marsh, B.D. 1982. On the mechanics of igneous diapirism, stoping and zone melting. *American Association of Petroleum Geologists*, **71**, 1068-1093.

Masberg, P. 1996. Multiple migmatization in the the HT/LP central Damara ororgen, Namibia.. *Neues Jahrbuch Fur Mineralogie-Abhandlungen*, **170**, 257-289.

Masberg, H.P.Hoffer, E. and Hoernes, S. 1992. Microfabrics indicating granulite-facies metamorphism in the low-pressure central Damara orogen, Namibia. *Precambrian Research*, **55**, 243-257.

Marlow, A.G.M. 1981. Remobilisation and Primary Uranium Genesis in the Damaran Orogenic Belt. Ph. D. thesis (unpubl.) University of Leeds.

Marlow, A.G.M. 1983. Geology and Rb-Sr geochronolgy of mineralised and radioactive granites and alaskites, Namibia. In: Miller, R.Mcg. (ed) *Evolution of the Damara Orogen of South West Africa Namibia.* Special. Publication of the Geological Society of South Africa, **11**, 289-298.

Mawer, C.K. 1987. Shear criteria in the Grenville Province, Ontario, Canada. *Journal of Structural Geology*, **9**, 531-539.

Mc Dermott, P.F. 1986. Granite petrogenesis and crustal evolution studies in the Damara Pan-African orogenic belt, Namibia.. Ph. D thesis(unpubl.) The Open University.

Mestres-Ridge, D. 1992. An investigation into the controls on the distribution of betafite in the SH Area, Rössing Uranium Mine, Namibia.. Msc thesis (unpubl) University of St Andrews.

Miller, R.McG. and Hoffmann, K.H. 1981. *Guide to the excursion through the Damara Orogen.* Geocongress 81, 103pp. Geological Society south Africa, Windhoek, South-West Africa.

Miller, R.Mcg. 1983a *Evolution of the Damara Orogen of south West Africa Namibia.* Special. Publication of the Geological Society of South Africa, **11**.

Miller, R.Mcg. 1983b. The Pan African Damara Orogen of South West Africa / Namibia. In: Miller, R.Mcg. (ed) *Evolution of the Damara Orogen of south West Africa Namibia.* Special. Publication of the Geological Society of South Africa, **11**, 431-515.

Miller, R.McG & Grote, W. 1988. Geological Map of the Damara Orogen, S W Africa; 1: 500 000. Geological survey of Namibia, Government Printer. Windhoek.

Misson, C. 1995. A radiogenic istotopeevaluation of the pegmatite granites of the Damaran orogen within the Central zone, Namibia, Africa. BSc dissertation (upubl.) University St Andrews.

Miyashiro, A. 1973. *Metamorphism and metamorphic belts.* George Allen and Unwin, London.

Nash, C.R. 1971. Metamorphic petrology of the SJ area Swakopmund district South West Africa. Bulletin, **9**, *Chamber of Mines, Precambrian Research Unit University of Cape Town.*

Nex, P. 1997. Tectonometamorphic setting and evolution of granitic rocks in the Goanikontes area, Namibia.. Ph.D thesis (unpubl) National University of Ireland.

Nex, P. and Kinnaird, J. A. Granites and their mineralisation in the Swakop River area around Goanikontes, Namibia. *Communications of the Geological Survey Namibia*, **10**, 51-56.

Nichols, G.I., Berry, R.F., and Green, D.H. 1992. Internally consistent gahnitic spinel-cordierite-garnet equilibria in the FMASHZn system: geothermobarometry and applications. *Contributions to Mineralogy and Petrology*, **111**, 362-377.

Nicolaysen, L. 1962. Stratigraphic interpretation of age measurements in southern Africa. In. Engel, A., James, H. and Leonard, B. (eds), *Petrologic studies*, Geological Society of America, Buddington volume, 569-598.

Oliver, G. J. H. 1993. Mid-crustal detachment in the central zone of the Damaran orogen, Namibia. An example of regional crustal extension in a transpressive orogen, In: Serrane, M. and Malavielle, J. (eds) *Late Orogenic Extension in mountain Belts* Document BRGM Fr. No. 219 p155.

Oliver, G.J.H.1994. Mid-crustal detachment and domes in the central zone of the Damaran orogen, Namibia. *Journal of African Earth Science*, **19**, 331-344.

Oliver, G.J.H. 1995. The Central Zone of the Damara Orogen, Namibia, as a deep metamorphic core complex. *Communications of the Geological Survey Namibia*, **10**, 33-41.

Oliver, G.J.H. and Kinnnaird, J.A. 1996. The Rössing-SJ Dome, Central Zone, Damara Belt, Namibia: an example of mid-crustal extensional ramping. *Communications of the Geological Survey Namibia*, **11**, 53-64.

Passchier, C.W. and Simpson, C. 1986. Porphyroclast systems as kinematic indicators. *Journal of Structural Geology*, **8**, 831-843.

Peterson, V.L. and Robinson, P. 1993. Progressive evolution from uplift to orogen-parallel transport in late-arcadian upper amphibolite-to-granulite-facies shear zone, South Central Massachusetts. *Tectonics*, **12**, 550-567.

Paterson, S.R., Brudos, T., Fowler, K., Carlson, C., Bishop, K. and Vernon, R.H. 1991. Papoose Flat pluton: Forceful expansion or postemplacement deformation? *Geology*, **9**, 324-327.

Paterson, S.R. and Vernon, R.H. 1995. Bursting the bubble of balloning plutons: A return to nested diapirs emplaced by multiple processes. *Geological Society of America Bulletin*. **107**, 1356-1380.

Perchuk, L.L. and Lavrent'eva, I. V. 1981 Experimental investigation of exchange equilibria in the system cordierite-garnet-biotite. In: Saxena, S. K., (eds). Kinetics and Equilibrium in Mineral Reactions. Springer Verlag, pp. 199-240.

Perchuk, L.L. and Lavrent'eva, I. V. 1983. Experimental investigation of exchange equilibria in the system cordierite-garnet-biotite. In: Saxena, S. K., (eds). Kinetics and Equilibrium in Mineral Reactions. Springer Verlag, pp. 199-239.

Perchuk, L.L., Aranovich, L. Y., Podlesskii, K. K., Lavrant'eva, I. V., Gerasimov, V. Y., Fed'Kin, V. V., Kitsul, V. I., Karasakov, L. P., and Berdnikov, N. V. 1985. Precambrian granulites of the Aldan shield, eastern Siberia, USSR. *Journal of Metamorphic Geology*, **3**, 265-310.

Petford, N. 1996. Dykes or diapirs? *Transactions of the Royal society of Edinburgh*: Earth Sciences, **87**, 105-114.

Porada, H. 1979. The Damara-Ribiera orogen of the Pan -African Brasiliano cycle in Namibia (SouthWest Africa) and Brazil as interpreted in terms of continental collision. *Tectononopyhsics*, **57**, 237-265.

Porada, H. 1989. Pan-African rifting and orogenesis in southern to equatorial Africa and eastern Brazil. *Precambrian Research*, **44**, 103-136.

Powell, & Holland, T. 1988. An internally consistent dataset with uncertainites and correltations: 3. Applications to geobarometry, worked examples and a computer program. *Journal Metamorphic Geology*, **6**, 173-204.

Powell, C.M. 1995. Are the Neoproterozoic glacial deposits preserved on the margins of Laurentia related to the fragmentation of 2 Supercontinents-comment. *Geology,* **23**, , 1053-1054.

Prave. A.R. 1996. Tale of three cratons: Tectonostratigraphic anatomy of the Damara orogen in northwestern Namibia and the assembly of Gondwana. *Geology*, **24**, 1115-1118.

Puhan, D. 1983. Temperature and Pressure of metamorphism in the Central Damara Orogen. In: Miller, R.McG. (ed) *Evolution of the Damara Orogen of south West Africa Namibia.* Special. Publication of the Geological Society of South Africa, **11**, 219-223.

Quinquis, H., Audren, C., Brun, J.P. & Cobbold, P.R. 1978. Intense progressive shear in Ile de Groix blueschists and compatibility with subduction or obduction. *Nature,* **273**, 43-45.

Ramberg, H. 1968a. Instability of layered systems in the field of gravity. I, II. *Physical Earth Planet Interiors*, **1**, 427-447.

Ramberg, H. 1972. Theoretical models of density stratification and diapirism in the Earth. *Journal Geophysical Reviews*, **77**, 877-889.

Ramsay, J.G. 1967. *Folding and fracturing of Rocks*, Mc-Graw-Hill New York.

Ramsay, J.G. 1980. Shear zone geometry: a review. *Journal of Structural Geology*, **2**, 83-99.

Ramsay, J.G. & Huber, M.I. 1987a *The Techniques of modern Structural Geology*. Volume 1 : Strain analysis, Academic press London.

Ramsay, J.G. & Huber, M.I. 1987b *The Techniques of modern Structural Geology*. Volume 2 : Folds and fractures, Academic press London.

Rasse, P. 1974. Al and Ti contents of hornblende, indicators of pressure and temperature of regional metamorphism. *Contributions to Mineral Petrology*, **45**, 231-236.

Rao, D.R. 1995. BGT-The macros driven spreadsheet program for biotite-garnet thermometry. *Computers and Geoscience*, **21**, 593-604.

Reynolds, S.J. 1990. Folding of mylonitic zones in Cordilleran metamorphic core complexes: Evidence from near the mylonitic front. *Geology*, **18**, 216-219.

Roering, C. van Reenen, D.D., Smit, C.A., Barton Jr, J.M. De Beer, J.H., De Wit, M.J., Settler, E.H., Van Schalkyk, J.F., Stevens, G. and Pretorius, S. 1992. Tectonic model for the evolution of the Limpopo Belt. *Precambrian Research*, **55**, 539-552.

Sanderson, D.J and Marchini, W.R.D. 1984. Transpression. *Journal of Structural Geology*, **6**, 449-458.

Sander, B. 1970. *An introduction to the study of fabrics in geological bodies*. Translated by F. C. Phillips and G. Windsor. Pergamon Press, 641pp.

Schermerhorn, L.J.G. 1974. Late Precambrian mixtites: glcial and/or nonglacial. *American Journal of Science*, **274**, 673-824.

Schermerhorn, L.J.G. 1975. Tectonic framework of Late-Precambrian supposed glacials. In: Wright, E.A. and Mosely, F (eds), *Ice ages, ancient and modern*. Geological Journal. Special Issue, **6**, 241-274.

Schneider, D., Holm, D. and Lux, D. 1996. On the origin of Early Proterozoic gneiss domes and metamorphic nodes, northern Michigan. *Canadian Journal of Earth Sciences*, **33**, 1053-1063.

Schwerdtner, W.M., Bennet, P.J. & Janes, T.W.1977. Application of L-S fabric scheme to structural mapping and paleostrain analysis. *Canadian Journal Of Earth Sciences*, **14**, 1021-1032.

Shimamoto, T. 1989. The origin of S-C mylonites and a new fault zone model. *Journal of Structural Geology*, **11**, 51-64.

Skjernaa, L. 1989. Tubular folds and sheath folds: definitions and conceptional model for their development, with examples from the Grapesvare area, northern Sweden. *Journal of Structural Geology*, **11**, 689-703.

Smith, D.A.M. 1965. The geology of the area around the Khan and Swakop Rivers in S W Africa. Memoir **3**, 113. *Geological Survey South Africa*, Windhoek, South West Africa.

Smith, R.B. 1979. The folding of a strongly non-Newtonian layer. *American Journal of Science*, **279**, 272-287.

South African Committee for Stratigraphy (SACS) 1980. Stratigraphy of South Africa, I. (Compiler L.E. Kent). Lithostratigraphy of the Republic of the South Africa, south West Africa/ Namibia, and Republics of Bophutshatswana, Transkei and Venda. Geological Survey South Africa. Handbook **8**.

Spear, F.S., Peacock, S. M., Kohn, M. J., Florence, F. P. and Menard, T. 1991. Computer programs for petrologic P-T-t path calculations. *American Mineralogist,* **76**, 2009-2012.

Stanistreet, I.G. Kukla, P.A. & Henry, G.1991. Sedimentary basinal responses to a Late Precambrian Wilson Cycle: the Damara orogen and Nama Foreland, Namibia. *Journal of African Earth Sciences*, **13**, 141-156.

Steven, N.M. 1992. A study of epigenetic mineralisation in the Central Zone of the Damara Orogen, Namibia with special reference to gold, tungsten tin and rare earth elements. Ph. D. thesis (unpubl) University of Cape Town.

Steven, N.M and Moores, J.M. 1995. Tourmaline mineralisation in the late Proterozoic Kuiseb schist formation of the Damara orogen, Central Namibia. *Economic Geology*, **90**, 1098-1117.

Streckeisen, A. 1975. To each plutonic rock it's proper name. Earth Science Review, **12**, 1-33.

Stüwe, K and Sandiford, M. 1994. Contribution of deviatoric stresses to metamorphic P-T paths: an example appropriate to low-P, High-T metamorphism. *Journal Metamorphic Geology*, **12**, 445-454.

Tack, L., Boven, A., Bowden., P and Oliver, G. 1994. The significance of 40Ar/39Ar ages on a mylonitic cover gneiss from the contact shear zone of the Ida Dome, Central Damaran Belt, Western Namibia. *Musee Royal de l'Afrique centrale*, Tervvuren Belgium. Départment de Géologie et Mineralogie. Rapp. Annales, 159-172.

Talbot, C.J. 1978. The Geology at the Eastern end of the Zambezi Orogenic belt, Rhodesia. *Geological Society of South Africa,* **76,** 113-133.

Tikoff, B. & Greene, D. 1997. Stretching lineations in transpressional shearzones; an example from the Sierra Nevada Batholith, California. *Journal of Structural Geology,* **19**, 29-39.

Teyssier, C., Tikoff, B. and Markley, M. 1995. Oblique plate motion and continental tectonics. *Geology,* **23**, 447-450.

Thompson, A.B. 1976. Mineral reaction in pelitic rocks. Calculation of some P-T-X (Fe-Mg) phase relations. *American Journal of Science*, **276**, 425-454.

Thompson, A.B., Schulmann, K. and Jezek, J. 1997. Extrusion tectonics and elevation of lower crustal metamorphic rocks in convergent orogens. *Geology*, **25**, 491-494.

Tobisch, O.T. & Paterson, S.T. 1988. Analysis and interpretation of composite foliation in areas of progressive deformation. *Journal of Structural Geology*, **10**, 745-754.

Trompette, R. 1994. (ed) *Geology of Western Gondwana (2000-500.Ma) Pan African - Brasiliano aggregation of south America and Africa*. Translated by A.V. Carozzi. A.A. Balkema/Rotterdam/ Brookfield.

Tullis, J. & Yund, R. A. 1991. Diffusion creep in feldspar aggregates: experimental evidence. *Journal of Structural Geology*, **13**, 987-1000.

Turner, F.J. & Weiss, L.E. 1963. *Structural Analysis of Metamorphic Tectonites*, New York: McGraw-Hill. 545pp.

Unrug, R. 1992. The supercontinent cycle and Gondwanaland assembly - component cratons and the timing of suturing events. *Journal of Geodynamics*, **16**, 4, 215-240.

Unrug, R. 1997. Rodinia to Gondwana: The Geodynamic Map of Gondwana Supercontinent Assembly. *GSA Today*, **7**, 1-5.

Veenhof, R.P, Stel, H. 1991. A cleavage triple point and its meso-scopic structures: the Mustio Sink (Sveckofennides of SW Finland). *Precambrian Research*, **50** 269-282.

Vernon, R.H. 1996. Problems with inferring *P-T-t* paths in low-*P* granulite facies rocks. *Journal Metamorphic Geology*, **14**, 143-153.

Waters, D.J. 1991. Hercynite-quartz relations and implications for crustal processes. *European Journal of Mineralogy*, **3**, 367-386.

Weiss, L.E. 1955. Fabric analysis of a triclinic tectonite. *American Journal of Science*, **253**, 225-236.

Wells, M.L. and Allmendinger, R. W. 1990 An early history pure shear in the upper plate of the Raft river metamorphic core complex. *Journal of Structural Geology*, **12**, 851-867.

Wernicke, B. and Axen, I.B. 1988. On the role of isostacy in the evolution of normal fault systems, *Geology*, **16**, 848-851.

White, S.H. & Knipe, R.J. 1978. Transformation-and-reaction-enhanced ductility in rocks. *Journal of Geological Society London*, **135**, 513-516.

Wilkinson, M.J. 1990. Palaeoenvironments in the Namib Deserts: the lower Tumas Basin in the Late Cenozoic. University of Chicago research paper, **231**, Committee on Geographical Studies, Chicago, U.S.A.

Wilson, G. 1961. Tectonic significance of small-scale structures and their importance to geologists in the field. *Annales Societe Géologique de Belgique*. **84**, 423-548. Revised as *Introduction to small-scale geological structures*. George Allen & Unwin, 128pp.

Woodsworth, G.J. 1977. Homogenization of zoned garnets from pelitic schists. *Canadian Mineralogist*, **15**, 230-242.

Yardley, B.W.D. 1977a. An empirical study of diffusion in garnet. *American Mineralogist*, **62**, 793-800.

Yardley, B.W.D. 1989. *An introduction to metamorphic Petrology*. Longman Earth Science series. New York.

Yin, A. 1991 Mechanisms For The Formation of Domal and Basinal Detachment Faults - A 3-Dimensional Analysis. *Journal of Geophysical Research-Solid Earth and Planets*, **96**, 14577-14594.

APPENDIX 3.1 Observed fold axis and lineation data from the Namibfontein area

Location	fold axis	L1	Location	fold axis	L1
N4.9	22 037	30 072	N28.4(353m)	40 137	40 127
N5.8	15 275	10 062	N28.15	30 062	40 057
N10.15	38 077	40 007	N29.5	42 002	45 082
N11.4	40 317	70 032	N29.7	40 089	40 089
N11.4	72 002	70 032	N29.7	30 342	10 322
	68 355	28 052	N29.11	15 177	18 141
	65 027	28 052	N30.1	40 079	40 085
	65 027	28 052		42 082	40 085
	70 027	28 052		45 082	40 085
	86 077	28 052		44 083	40 085
N14.4	68 182	50 177		34 097	40 085
	58 177	50 177	N30.2	20 092	40 085
	52 179	50 177		60 089	40 085
N15.4	40 237	*	N32.5	30 067	32 047
N16.3	5 250	*	N33.4-6	25 122	25 092
N16.6	50 067	30 079		25 132	25 092
	45 097	30 079	N33.4-6b	24 122	20 107
N18.4	20 072	20 020	N33.4-6c	20 182	20 107
	38 072	20 020		20 122	20 107
	10 097	20 020	N33.7a	25 082	20 107
	15 257	20 020		24 089	20 107
N19.2	10 007	25 020	N33.7b	18 145	20 107
N19.3	20 042	20 020	N33.17b	28 112	15 122
N19.17	15 357	10 017		28 117	28 117
	18 001	40 017		20 125	28 117
N20.9	5 137	*		15 122	28 117
	5 287	45 022		25 119	28 117
N21.10.	15 082	60 032		45 092	28 117
	20 065	60 032	N33.17b	24 137	28 117
	24 262	60 032		20 072	28 117
N22.12	36 027	35 027		20 102	28 117
N22.23	52 347	28 357		40 079	28 117
N23.1	24 175	84 217		44 097	28 117
N23.9	72 007	70 042		24 121	28 117
N23.12	25 112	40 062		32 122	28 117
	56 257	25 062	N36.3	24 062	35 085
N24.8	45 065	20 071	N36.14	40 079	38 079
N24.11	5 257	20 071		24 142	38 079
	10 060	20 071	N38.19	24 071	22 073
N25.2	60 077	36 042	N42.23	5 252	5 277
N25.4	89 107	48 079	N43.6	5 287	*
N25.8	80 107	34 082		5 015	5 317
	80 107	34 082	N43.1	5 107	10 037
	80 109	34 082	N44.15	40 062	28 085
N28.2	24 322	26 057	N45.5	40 152	35 082
	20 319	26 057	N49.1	68 082	85 157
N28.4(353m)	40 327	40 127			

APPENDIX 3.2 Strain data from the Namibfontein area (mm)

Location	Observed shape		
	x	y	z
N4.4	20	10	5
N9.6	41	6	4
N14.11	180	80	15
N15.5	25	10	10
	45	25	10
	70	30	15
	50	30	20
	10	5	5
	40	40	10
	35	20	7
	55	30	10
	10	10	5
	35	25	7
	60	30	5
	50	40	7
	50	40	10
	50	40	7
	50	40	10
	60	30	7
	50	40	10
	30	20	10
	55	40	40
	60	50	20
	50	30	7
	120	70	40
	40	20	10
	40	20	10
	150	100	40
	40	30	10
	60	50	20
	50	30	30
	60	55	20
	40	20	10
N16.6	40	20	7
	10	8	2
	45	20	1
	20	20	3
	10	10	7
	10	5	1
	12	8	1
	40	20	2
	30	20	2
	70	40	2
	70	35	5
	70	30	2
	10	7	1
	20	10	2
	20	10	2
N18.7	40	30	20
N19.4	20	10	1
N19.5	60	30	1
N19.9	50	50	2
N19.14	60	20	12
	60	20	13
N20.8	40	40	2
N22.4	40	30	2
N23.14	10	10	6
N23.16	56	20	15
N24.4	80	8	5
	200	10	10

Location	Observed shape		
	x	y	z
	80	5	5
	90	8	8
	150	20	8
	180	25	5
	130	15	5
	100	15	10
	100	10	5
	200	20	10
	80	10	5
	80	5	5
	150	25	10
	90	8	5
	250	10	10
	80	15	5
	120	10	10
	40	20	10
	60	15	10
	250	25	10
	110	15	10
	140	15	5
	80	15	10
	140	10	5
	400	40	10
	70	15	10
	130	10	8
	180	20	10
	120	15	8
	150	15	10
	300	20	15
N25.5	15	8	5
N26.7	10	10	1
	40	20	5
N27.5	90	10	10
	120	10	10
	150	50	15
N27.7	15	10	2
N27.8	20	20	2
N27.9	45	20	20
	25	20	10
	30	20	10
	25	12	10
	30	12	10
	12	10	5
	40	25	20
	40	25	10
	60	17	25
	30	17	10
	25	15	10
	30	15	10
	30	25	20
	34	20	10
	20	15	10
	25	15	10
	40	17	9
	40	20	12
	25	10	10
	20	12	10
	40	25	10
	30	17	10
	25	15	12

Location	Observed shape		
	x	y	z
	15	15	5
	25	15	10
	20	12	10
	25	12	10
	25	15	12
	40	22	17
	30	15	7
N28.12	6	3	1
	10	5	4
N34.8	150	100	30
N35.8	20	6	5
	15	7	3
	50	30	9
	80	40	20
	20	10	3
	20	7	3
	40	8	3
	20	7	5
	30	10	1
	40	15	10
	70	20	8
	20	10	3
	30	10	1
	10	5	2
	20	15	3
	6	5	1
N35.10	10	5	2
N37.3	40	20	5
N38.18	30	12	5
Ababbis	60	30	15
farm	25	15	5
pebbles	70	20	15
	40	25	15
	100	80	30
	35	20	10
	30	8	8
N42.11	8	5	3
N42.15	40	10	1
N42.20	20	10	10
N42.21	40	30	30
	20	20	15
	60	30	20
	70	30	20
	40	20	15
	80	25	20
	40	40	10
	80	30	20
	30	20	15
	60	35	30
	30	15	15
pebblesB	30	15	2
	40	15	2
	30	30	2
	50	15	2
	20	10	2
	40	30	2
	40	20	2
	70	20	2
	30	10	3
N43.3	6	3	2

Location	Observed shape		
	x	y	z
N43.10	5	5	5
	30	30	5
N44.3	7	4	3
N44.14	20	15	2
N45.1	60	15	15
	50	20	20
	15	7	2
	25	15	10
	50	15	10
	25	15	10
	40	20	15
	50	30	15
	50	30	15
	20	10	5
	40	10	5
	25	10	5
	30	15	10
	30	15	5
	30	10	10
	30	15	4
	30	25	10
	50	30	20
	80	25	20
	70	20	20
	30	15	10
	50	18	15
	50	20	12
	50	20	14
	80	20	15
	40	20	8
	80	30	8
	50	15	15
	40	20	9
	40	20	6
N46.10	20	15	12
	20	10	5
	30	8	5
	30	10	6
	40	18	10
	60	10	8
	60	15	9
	20	5	5
	50	15	8
	60	20	10
	30	12	5
	40	10	8
	70	10	8
	40	8	5
	45	12	8
	50	30	15
	45	10	5
	30	15	5
	70	18	5
	40	12	5
	50	7	7
	60	12	6
	30	8	8
	30	12	8
	40	8	8
	40	12	9

Location	Observed shape		
	x	y	z
	45	12	10
	52	12	8
	50	12	8
	60	18	12
N48.2	50	25	10
	40	25	10
	18	12	5
	60	40	20
	30	20	8
	80	80	30
	12	12	3
	25	15	15
	30	25	5
	15	15	5
	15	12	6
	40	12	12
	70	35	20
	80	50	30
	40	35	10
	30	25	10
	50	30	12
	15	12	5
	60	25	15
	60	40	18
N48.3	8	8	1
	15	8	2
	15	8	2
	8	8	2
	6	6	1
	8	6	2

APPENDIX 3.3 Strain data from the Khan Mine area (mm)

Location	Observed Clast shape		
	x	y	z
K8.1	40	6	2
	26	3	2
	17	3	2
	72	11	3
	45	7	3
	15	10	2
	20	11	2
	70	9	2
	65	7	2
	62	7	2
	110	10	3
	90	7	3
	200	14	3
	156	14	4
	151	12	4
K10.1	35	10	5
	60	8	4
	50	9	3
	52	9	3
	52	9	3
	40	8	4
	80	8	3
	95	8	4
	83	8	3
	102	8	6
K11.1	12	10	2
	12	11	2
	22	8	2
	33	9	2
	17	8	2
	18	7	1
	13	11	1
	34	12	2
	18	12	2
	15	9	2
K11.2	150	40	25
	50	17	7
	45	12	7
K11.3	110	7	2
	70	5	2
	37	10	2
	75	9	2
	62	4	1
	30	5	2
	50	15	3
	85	8	2
	25	8	2
	40	6	6
K11.8	130	30	15
	90	25	20
	52	45	45
	140	105	30
	80	35	20
	80	20	11
	78	50	20
	60	22	12

Location	Observed shape		
	x	y	z
	262	54	12
	62	45	11
	170	25	7
	61	32	11
	68	20	10
	58	20	11
	110	40	9
	112	42	10
	100	12	11
	98	7	7
	52	20	8
	36	25	22
	42	32	20
	180	62	30
	80	50	12
	112	40	21
	70	21	20
	60	30	25
	48	40	23
	49	38	20
	64	19	10
	65	23	20
K11.9	35	22	10
	50	22	9
	30	30	6
	50	29	8
	40	30	12
	40	20	10
	35	20	10
	51	30	8
	30	12	12
	65	30	17
	13	9	5
	15	7	3
	52	20	9
	35	22	5
	36	25	7
	59	28	7
	27	15	5
	45	35	8
	55	22	9
	32	15	9
	50	25	20
	25	12	5
	45	11	6
	70	25	11
	40	20	11
	30	22	6
	55	12	8
	25	10	9
	30	24	12
	32	15	14
K11.11	12	10	2
	12	11	2
	22	8	2
	33	9	2

Location	Observed shape		
	x	y	z
	17	8	2
	18	7	1
	13	11	1
	34	12	2
	18	12	2
	15	9	2
K14.2	31	13	3
	30	14	3
	35	17	3
	42	13	3
	36	11	2
	40	15	3
	30	9	3
	42	12	3
	32	7	3
	42	8	3
	21	7	2
	33	7	2
	25	10	3
	25	11	3
	26	11	3
	6	5	1
	22	10	3
	22	11	3
	24	15	3
	25	15	3
	15	7	2
	16	9	2
	40	11	2
	62	9	3
	27	9	3
	28	10	4
	62	13	3
	32	11	3
	30	12	2
	31	12	3
14.6	42	12	3
	55	15	8
	35	8	3
	52	9	4
	95	10	8
	95	15	4
	75	12	4
	92	7	6
	65	6	5
	77	11	5
	135	13	5
	45	4	4
	43	5	4
	45	5	3
	117	15	5
16.1	89	11	3
	75	5	3
	82	6	4
	40	11	3
	25	6	2

Location	Observed shape		
	x	y	z
	65	18	5
	65	9	4
	89	9	3
	60	12	3
	32	11	5
	17	7	3
	15	4	2
	17	10	3
	40	15	3
	30	9	2
	70	10	3
	65	9	4
	70	9	5
	70	10	3
	95	10	4
	60	9	3
	70	6	6
	35	5	5
	102	11	6
	62	5	4
K16.3	50	25	3
	40	14	3
	42	15	3
	60	14	6
	95	13	7
	85	13	6
	55	9	4
	60	9	4
	63	7	5
	72	8	5
	68	8	4
	40	4	2
16.5	30	8	3
	52	22	4
	50	7	4
	50	15	5
	52	7	5
16.6	36	3	3
	22	4	2
	55	4	4
	31	11	5
	35	7	5
	50	9	7
	35	5	5
	35	6	5
	27	10	3
	40	11	9
	39	10	4
	35	14	7
	30	9	7
	45	9	9
	31	15	5
	28	7	4
	30	9	7
	27	4	4
	22	3	3

Location	Observed shape		
	x	y	z
	22	9	5
K18.2	80	50	15
	220	50	15
	62	41	25
	182	48	20
	160	35	17
	65	30	12
	110	55	22
	180	70	29
	30	30	15
	120	45	12
K18.16	35	15	5
	30	9	6
	35	9	5
	34	7	6
	90	11	5
	52	11	5
	55	5	5
	60	6	5
	70	5	4
	30	4	4
	40	4	3
	73	4	3
	62	7	4
	80	12	5
	55	5	5
	70	3	3
	20	6	3
	80	12	8
	63	4	4
	33	5	4
K18.18	170	20	15
	110	7	5
	172	25	17
	120	4	3
	66	7	5
	72	12	7
	80	7	6
	66	5	4
	65	15	8
	60	12	4
	55	12	5
	60	11	4
	70	11	5
	90	5	5
	110	6	5
	85	7	5
	55	7	5
	70	10	4
	77	8	7
	125	8	6
K18.20	15	10	3
	14	9	3
	15	11	3
	12	7	2
	11	8	2

Location	Observed shape		
	x	y	z
K18.20	13	7	2
	7	6	2
	20	15	5
	16	15	3
	20	16	4
	15	5	2
	17	7	5
	27	7	4
	30	12	4
	25	9	4
	15	10	4
	9	7	3
	20	9	4
	21	9	4
	15	10	3
K19.1a	21	4	3
	25	4	2
	25	6	3
	20	4	2
	21	4	3
	25	3	3
	35	4	3
	24	5	2
	25	5	2
	20	4	2
	20	7	4
	30	6	3
	35	4	3
	31	5	4
	13	4	3
K19.1b	45	5	5
	35	6	4
	42	6	4
	21	3	2
	45	8	3
K19.9	18	10	2
	18	12	3
	20	10	3
	22	10	3
	23	15	4
	37	8	3
	55	12	3
	30	13	3
	12	8	3
	37	9	3
	20	6	2
	22	11	3
	21	18	3
	25	8	2
	15	2	1
	10	4	2
	11	4	2
	37	10	3
	52	15	2
	37	11	3
	32	11	4

Location	Observed shape		
	x	y	z
	33	11	4
	77	12	4
	56	17	3
	48	12	3
	40	10	4
	25	13	3
	45	9	2
	49	9	3
	20	7	2
K20.4	15	6	6
	14	6	6
	30	7	5
	32	12	7
	33	10	5
	30	10	9
	45	14	14
	55	10	6
	25	9	5
	25	10	6
	32	8	5
	65	15	7
	30	12	11
	42	9	4
	40	12	5
K21.6	25	5	4
	25	4	4
K22.32	60	6	3
	20	3	3
	70	6	5
	45	4	4
	40	12	8
	30	7	5
	195	8	8
	40	4	4
	60	5	4
	90	4	4
	42	7	7
	102	20	11
	25	5	4
	30	3	2
	30	6	5
	120	15	10
	45	15	10
	110	15	5
	115	5	5
	67	11	5
	75	7	5
	60	5	4
	70	4	4
	35	5	4
	70	5	4
K22.36	27	17	4
	42	20	7
	32	17	4
	27	14	7
	30	20	5

Location	Observed shape		
	x	y	z
	40	20	13
	32	13	5
	32	12	6
	37	12	11
	40	15	5
	50	5	5
	52	6	5
	45	4	4
	46	5	4
	50	22	4
	22	7	5
	62	7	5
	54	6	4
	50	6	4
	37	20	3
K22.36b	70	10	4
	72	10	4
	62	11	3
K22.57	62	7	4
	65	7	1
	65	7	4
	62	6	4
	59	5	5
	75	4	4
	64	5	4
	95	8	6
	45	6	4
	120	7	6
	70	5	4
K25.73	45	10	4
	90	7	3
	85	6	3
	35	9	3
	70	7	3
	30	7	3
	37	7	3
	35	7	3
	12	7	2
	28	6	2
	30	7	3
	40	8	3
	42	8	3
	70	4	4
	72	4	3
K25.78	9	3	1
	8	2	1
	8	3	1
	10	6	2
	10	5	2
	8	4	2
	20	7	2
	25	7	2
	11	7	2
	22	8	2

Location	Observed shape		
	x	y	z
K25.81	90	7	6
	102	6	5
K26.1	15	5	2
	40	12	3
	17	5	3
	45	7	3
	16	6	2
	35	7	2
	42	4	3
	60	4	4
	28	7	2
	40	5	4
	42	12	3
	47	4	4
	43	4	3
	40	7	5
	42	7	5
	63	11	5
	52	12	4
	33	7	4
	37	6	3
	41	5	4
K26.16	35	8	6
	37	5	4
	40	5	4
	35	7	6
	45	15	5
	70	8	4
	70	12	4
	82	9	4
	80	7	5
	73	6	4
K26.18	45	6	3
	27	4	3
	50	9	4
	20	5	3
	28	4	3
	23	3	3
	15	10	6
	30	4	3
	25	4	2
	14	9	3
K26.22	35	9	4
	34	5	4
	25	10	6
	35	7	4
	37	9	4
	27	14	5
	27	13	5
	30	17	7
	36	12	5
	20	4	2
	45	7	3
	65	8	4
	112	12	4
	115	12	4
	58	7	3
	102	5	4

Location	Observed shape		
	x	y	z
	52	7	3
	50	5	4
	62	5	4
	25	8	4
	65	7	4
K27.1	45	7	3
	65	8	4
	112	12	4
	115	12	4
	58	7	3
	102	5	4
	52	7	3
	50	5	4
	62	5	4
	25	8	4
	65	7	4
K29.1	78	8	4
	60	7	4
	63	5	4
	70	15	8
	65	9	5
	63	9	5
	60	8	4
	61	22	6
	68	8	4
	45	8	6
	72	8	4
	65	15	7
	145	15	10
	95	8	7
	85	8	6
K29.5	85	9	4
	47	12	3
	60	8	4
	32	8	5
	42	5	5
	62	5	4
	33	1	5
	43	6	5
	111	10	7
	32	6	4
	35	6	6
	47	7	7
	33	6	5
	41	6	6
	55	8	8
K30.1	75	8	7
	67	3	3
	135	7	6
	112	7	7
	137	7	6
	95	10	8
	102	7	6
	130	10	8
	105	7	7
	88	9	8
	106	7	6
	82	8	7

Location	Observed shape		
	x	y	z
	92	8	7
	65	7	7
	72	7	6
K30.6	80	10	8
	60	4	4
	55	6	4
	60	10	9
	67	9	8
	55	6	5
	66	8	5
	73	7	6
	140	11	6
	135	10	7
	100	5	4
	75	7	7
	57	4	4
	42	4	3
	62	5	5
K31.3	90	12	8
	110	15	8
	75	8	6
	50	6	4
	70	8	5
K31.19	20	7	5
	150	11	10
	27	7	6
	97	5	4
	77	11	5
K32.1	80	8	5
	32	7	5
	35	7	5
	135	12	7
	63	8	7
K33.1	21	7	3
	52	13	5
	32	9	4
	22	15	8
	18	6	4
	11	6	2
	33	14	6
	59	11	10
	28	8	5
	29	5	4
	43	4	4
	187	30	20
	57	23	9
	51	8	3
	107	31	16
	59	11	9
	38	19	4
	28	9	3
	62	12	4
	81	11	8
	106	19	6
	69	16	10
	61	9	5
	69	9	7
	51	8	4

Location	Observed Class shape		
	x	y	z
	82	21	12
	24	5	4
	71	13	4
	84	15	9
	24	13	3
	31	7	3
K34.1	160	15	9
	145	15	14
	67	40	30
	54	30	19
	74	21	11
	123	32	24
	105	53	30
	71	30	29
	71	24	23
	82	32	31
	61	34	22
	53	41	21
	70	24	18
	53	27	24
	57	20	13
	55	31	22
	71	39	26
	94	33	19
	97	19	13
	122	42	17
	84	29	18
	118	24	19
	89	25	13
	94	43	35
K34.2	44	15	9
	75	29	23
	83	15	9
	66	27	12
	27	9	8
	55	10	10
	72	25	20
	43	8	7
	112	32	23
	48	11	8
	175	52	45
	47	27	19
	77	30	22
	113	40	34
	58	30	28
	68	25	17
	64	25	25
	57	29	19
	75	16	14
	13	5	4
	30	13	7
	42	25	10
	60	27	13
	49	12	10
	82	25	12
	95	19	12
	42	22	19
	18	9	7

Location	Observed shape		
	x	y	z
	30	9	7
	49	25	11
K34.3	200	19	17
	49	17	12
	79	18	11
	210	34	21
	63	10	9
	74	13	14
	90	17	7
	101	13	7
	45	12	10
	37	7	5
	54	10	7
	84	25	19
	50	12	8
	35	15	7
	84	4	4
	57	9	6
	55	12	9
	70	24	15
	40	15	12
	122	15	12
	74	18	12
	100	11	10
	72	11	10
	47	20	18
	50	12	10
	25	9	9
	46	5	5
	53	15	13
	120	20	13
	72	23	18
K34.4	260	38	35
	50	25	20
	55	15	13
	250	82	60
	270	140	130
	154	62	37
	75	18	9
	62	20	20
	43	25	15
	152	64	30
	80	42	31
	82	20	15
	430	130	120
	103	42	25
	610	34	34
	350	52	24
	141	42	34
	125	32	23
	92	30	20
	67	25	18
	410	130	55
	170	60	57
	420	52	50
	320	107	50
	85	120	90
	127	34	30

Location	Observed shape		
	x	y	z
	1050	310	250
	470	241	200
	108	40	34
	121	24	22
K34.5	78	21	18
	57	22	12
	83	42	24
	83	19	12
	109	22	20
	96	23	17
	32	12	10
	40	10	8
	51	15	13
	24	8	5
	29	8	6
	51	24	18
	42	18	12
	28	10	9
	106	24	21
	64	20	14
	32	23	19
	34	9	9
	88	13	9
	50	14	12
	36	18	10
	64	20	9
	65	20	14
	38	21	9
	73	31	23
	67	22	13
	142	34	22
	50	19	16
	41	11	10
	58	25	18
K34.6	29	5	5
	39	16	14
	49	22	19
	44	10	8
	76	20	16
	54	23	17
	32	24	20
	22	12	9
	44	14	12
	30	9	8
	41	8	8
	55	9	8
	63	15	14
	29	9	8
	20	7	6
	31	15	9
	40	12	10
	47	15	11
	56	15	12
	73	20	17
	63	19	15
	49	19	15
	26	16	10
	58	18	15

Location	Observed shape		
	x	y	z
	61	24	16
	83	24	19
	18	10	8
	29	16	12
	27	18	14
	40	18	12
K34.10	140	42	29
	32	14	12
	33	7	6
	16	9	5
	28	11	9
	28	15	11
	105	23	20
	32	10	8
	39	18	10
	33	5	4
	69	24	17
	69	20	15
	40	27	13
	82	35	22
	114	27	13
	35	24	17
	53	16	10
	155	52	36
	64	5	5
	64	10	9
	42	9	8
	33	16	12
	61	10	10
	39	10	8
	47	15	12
	32	14	11
	60	22	16
	122	49	27
	25	13	12
	65	29	14
K35.4	61	8	8
	42	4	4
	125	55	50
	102	11	10
	23	9	8
	82	33	29
	32	22	19
	40	22	15
	35	15	12
	29	12	9
	34	19	16
	47	19	14
	31	6	4
	69	18	12
	45	10	8
	162	32	16
	158	42	33
	43	8	8
	50	27	22
	48	16	13
K35.5	65	10	6
	44	20	13

Location	Observed shape		
	x	y	z
	41	24	11
	57	12	8
	67	37	18
	26	10	7
	30	15	11
	56	15	11
	43	22	11
	84	40	35
	51	10	8
	34	17	10
	50	29	14
	34	19	14
	41	15	9
	43	11	9
	26	4	4
	167	88	75
	23	14	12
	26	5	4
	108	50	39
	35	16	15
	46	9	8
	61	17	7
	51	15	13
	16	13	13
	24	16	14
	19	11	8
	38	18	14
	10	7	5
K35.6	71	35	11
	81	14	12
	21	11	8
	27	13	6
	116	25	13
	20	11	10
	97	35	21
	108	15	7
	61	9	7
	70	10	9
	46	17	15
	34	16	10
	94	12	11
	19	16	12
	95	32	26
	67	12	10
	44	6	5
	214	19	8
	67	23	15
	26	10	9
	51	20	12
	63	27	12
	23	11	7
	73	32	19
	111	58	18
	66	17	9
	39	11	9
	32	20	12
	42	11	8
	27	14	9

Location	Observed shape		
	x	y	z
K35.7	62	11	8
	133	60	56
	39	13	7
	38	9	4
	32	14	5
	52	19	12
	27	11	10
	26	10	6
	67	14	14
	65	20	12
	72	27	20
	15	3	2
	45	21	14
	33	15	12
	19	4	3
	36	14	9
	38	10	6
	40	14	7
	25	14	4
	54	15	9
	56	12	9
	67	35	17
	65	15	9
	13	11	4
	10	7	5
	6	3	3
	37	12	10
	17	9	8
	14	11	9
	60	11	9
K35.8	145	103	47
	52	23	11
	111	38	19
	21	7	6
	67	24	17
	19	8	7
	10	4	3
	31	16	7
	47	14	8
	72	50	23
	13	5	5
	54	9	7
	22	14	12
	21	17	9
	38	18	14
	54	26	15
	55	27	18
	18	7	5
	23	16	11
	162	25	14
	14	9	6
	63	12	9
	31	24	12
	34	15	9
	34	8	7
	15	9	7
	20	18	14
	25	18	12
	25	9	6
	32	12	8
K35.9	53	12	9
	9	3	2

Location	Observed shape		
	x	y	z
	25	13	10
	24	12	11
	24	11	7
	23	5	4
	43	22	9
	27	13	12
	27	17	9
	45	17	15
	31	21	19
	39	10	7
	15	7	5
	29	13	9
	42	19	12
	18	4	3
	21	10	8
	16	3	3
	10	3	3
	18	3	2
	30	27	14
	86	40	25
	34	21	17
	38	27	20
	26	7	5
	33	13	11
	10	2	2
	8	3	2
	34	12	9
	42	19	17
K35.10	32	16	14
	21	9	7
	20	9	6
	19	15	7
	24	15	8
	44	14	9
	7	3	2
	87	42	16
	42	9	8
	75	9	8
	25	12	8
	18	14	6
	40	8	8
	19	8	6
	55	11	7
	16	7	6
	43	19	15
	55	11	9
	41	26	14
	21	13	5
	19	13	8
	26	12	11
	45	9	8
	24	6	5
	51	5	5
	20	10	8
	58	11	8
	33	8	5
	11	4	4
	28	6	5
K35.11	83	25	16
	34	6	5
	24	8	6
	40	5	4

Location	Observed shape		
	x	y	z
	135	27	12
	69	19	12
	24	5	5
	152	35	27
	56	5	4
	28	6	5
	46	8	6
	26	13	9
	17	4	4
	37	10	8
	37	8	6
	86	10	12
	154	42	33
	29	7	5
	85	18	7
	162	40	32
	89	40	12
	91	18	8
	54	32	16
	95	13	12
	71	20	12
	17	5	4
	35	17	10
	78	32	16
	89	33	15
	62	31	8
K35.12	37	5	4
	47	30	25
	20	5	4
	19	9	6
	42	10	8
	42	12	9
	42	27	24
	48	22	12
	57	19	13
	11	8	7
	12	10	9
	15	9	7
	26	12	4
	37	18	6
	87	44	19
	86	12	7
	63	14	9
	57	30	13
	58	6	5
	29	12	5
	39	18	9
	33	12	9
	34	15	10
	13	5	5
	15	9	6
	41	12	10
	48	11	9
	25	15	12
	32	2	2
	19	4	4
K36.2	52	19	13
	32	12	7
	28	9	6
	79	14	12
	32	11	8
	57	35	14

Location	Observed shape		
	x	y	z
	69	37	19
	36	11	6
	64	17	5
	28	20	12
	22	8	5
	35	25	12
	38	20	8
	43	32	20
	42	22	10
	36	26	10
	25	13	7
	27	12	5
	30	8	5
	49	27	8
K38.17	20	6	3
	50	11	4
	22	6	3
	35	10	4
	50	11	5
	30	10	8
	32	8	6
	52	12	8
	30	15	8
	32	6	5
	40	14	8
	26	5	4
	65	4	4
	60	5	5
	65	12	7
	77	21	7
	53	10	7
	110	12	7
	38	5	4
	27	9	4
	130	23	10
	72	8	3
	78	11	4
	32	9	2
	62	9	4
	31	6	3
	65	5	3
	60	6	4
	40	10	5
K39.12	80	9	7
	92	9	8
	53	8	5
	75	11	8
	65	9	8
	83	7	5
	59	6	5
	76	7	5
	25	8	4
	49	13	6
	57	11	5
	54	10	8
	135	7	7
	75	14	11
	57	9	5
	62	14	4

4.1: Microprobe analysis equipment, conditions of analysis:

1) JEOL JCXA-733 SUPERPROBE: Machine specifications

Acc. voltage	15kV
Beam current	15nA
Beam diameter	~1μm

2) Standards

Ca	wollastonite
Si	rutile
Ti	corundum
Al	metal
Fe	metal
Mn	metal
Mg	periclase
Na	jadeite
K	orthoclase

APPENDIX 4.2 Results from Microprobe analyses for the Namibfontein area

SAMPLE N8.15

	kfs	pl host	Hbl	Pl core	Hbl rim	hbl core	spinel	ilm	mag	hbl rim	hbl core	pl
SiO2	65.062	60.137	45.257	59.549	45.392	45.242	0.142	0.209	0.193	45.307	45.385	59.277
TiO2	0.069	0.008	1.104	0.028	10.076	1.134	16.846	59.691	0.023	1.023	1.017	0.018
Al2O3	18.533	25.729	9.241	25.157	9.343	9.252	0.168	0.000	91.092	9.421	9.273	25.797
FeO	0.096	0.084	13.977	0.213	13.558	14.073	72.558	38.522	0.063	13.951	14.035	0.142
MnO	0.003	0.017	0.471	0.023	0.429	0.481	1.855	0.696	0.000	0.405	0.465	0.000
MgO	0.000	0.002	13.060	0.025	13.427	13.283	0.000	0.000	0.007	13.468	13.568	0.000
CaO	0.000	6.677	12.051	6.655	11.950	11.820	0.006	0.126	0.000	12.162	11.900	7.063
Na2O	0.720	8.149	1.190	7.623	1.125	1.406	0.000	0.000	0.000	1.009	1.110	7.960
K2O	16.294	0.358	0.801	0.341	0.808	0.937	0.013	0.010	91.488	0.821	0.854	0.379
Total	100.778	101.156	97.151	99.613	97.107	97.627	91.589	99.253	91.488	97.567	97.607	100.635
	11.954	10.624	6.731	10.670	6.733	6.707	0.162	0.005	0.080	6.704	6.716	10.548
	0.010	0.000	0.124	0.004	0.120	0.127	14.366	1.094	0.007	0.114	0.113	0.002
	4.013	5.357	1.620	5.313	1.633	1.617	0.225	0.000	0.054	1.643	1.618	5.411
	0.015	0.012	1.739	0.032	1.682	1.745	68.809	0.785	31.719	1.727	1.737	0.021
	0.001	0.003	0.059	0.003	0.054	0.060	1.782	0.014	0.022	0.051	0.058	0.000
	0.000	0.001	2.895	0.006	2.969	2.935	0.000	0.000	0.000	2.971	2.993	0.000
	0.000	1.264	1.921	1.278	1.900	1.877	0.008	0.003	0.003	1.928	1.887	1.347
	0.257	2.791	0.343	2.648	0.323	0.404	0.000	0.000	0.000	0.290	0.319	2.746
	3.819	0.081	0.152	0.078	0.153	0.177	0.019	0.003	0.000	0.155	0.161	0.086
Total	20.068	20.133	15.583	20.033	15.568	15.649	100.000	1.904	31.885	15.582	15.602	20.161
no. [O]	32	32	23	32	23	23	20	3	32	23	23	32
An		0.31		0.31								0.32
Ab		0.67		0.67								0.66

SAMPLE N9.2

	1	2	3	4	5	6	7	8	9	10	11	12	13	14	15	16
	grt	bt	crd	bt	crd	bt	pl	crd	ilm (Grt)	ilm (Grt)	bt rim (Tm)	kfs core	pl core	crd	bt (crd)	grt core
SiO2	37.897	35.303	45.963	35.454	49.067	36.308	62.000	48.607	35.533	35.663	35.435	62.346	63.104	47.685	35.821	37.431
TiO2	0.008	2.390	0.000	2.789	0.041	2.542	0.028	0.021	0.716	0.779	3.345	0.099	0.012	0.000	2.214	0.028
Al2O3	21.692	19.577	33.165	19.996	32.921	20.304	24.295	32.832	30.287	33.141	19.411	17.825	25.250	32.731	21.179	21.914
FeO	29.016	18.355	8.569	18.438	7.987	17.594	0.031	8.277	6.171	5.822	18.788	0.084	0.012	8.043	18.323	29.350
MnO	6.910	0.172	0.552	0.313	0.648	0.245	0.000	0.368	0.070	0.037	0.167	0.017	0.000	0.515	0.302	7.828
MgO	3.327	10.073	7.992	9.265	7.692	9.777	0.000	7.877	6.437	6.430	9.411	0.000	0.000	7.559	10.508	2.419
CaO	0.955	0.010	0.006	0.000	0.008	0.030	5.450	0.009	1.087	1.075	0.030	0.000	5.545	0.041	0.017	0.915
Na2O	0.000	0.025	0.277	0.221	0.319	0.213	8.967	0.195	1.749	1.867	0.065	1.473	9.472	0.235	0.000	0.000
K2O	0.000	9.702	0.020	9.387	0.000	9.407	0.192	0.007	0.035	0.030	9.396	14.703	0.325	0.037	8.530	0.000
Total	99.804	95.608	96.543	95.864	98.682	96.420	100.963	98.195	85.087	84.843	96.048	96.546	103.721	96.845	96.894	99.885
	6.053	5.336	4.855	5.337	5.035	5.394	10.920	5.015	4.901	4.321	5.333	11.929	10.844	4.991	5.285	6.012
	0.001	0.272	0.000	0.322	0.003	0.284	0.004	0.002	0.065	0.071	0.379	0.014	0.002	0.000	0.246	0.003
	4.084	3.488	4.129	3.548	3.982	3.556	5.044	3.992	4.749	4.733	3.443	4.020	5.115	4.038	3.683	4.149
	3.876	2.320	0.757	2.321	0.685	2.186	0.004	0.714	0.625	0.590	2.365	0.013	0.002	0.704	2.261	3.943
	0.935	0.022	0.049	0.040	0.056	0.031	0.000	0.032	0.007	0.004	0.021	0.003	0.000	0.046	0.038	1.065
	0.792	2.270	1.259	2.079	1.177	2.165	0.000	1.751	1.162	1.161	2.111	0.000	0.000	1.179	2.311	0.579
	0.163	0.002	0.001	0.000	0.001	0.005	1.028	0.001	0.141	0.140	0.005	0.000	1.021	0.005	0.003	0.157
	0.000	0.007	0.057	0.064	0.063	0.061	3.063	0.039	0.410	0.438	0.019	0.547	3.156	0.048	0.000	0.000
	0.000	1.871	0.003	1.803	0.000	1.783	0.043	0.001	0.005	0.005	1.804	3.589	0.071	0.005	1.606	0.000
Total	15.904	15.588	11.110	15.514	11.003	15.466	20.107	11.547	11.466	11.463	15.479	20.115	20.211	11.016	15.431	15.909
no. [O]	24	22	18	22	18	22	32	18	18	18	22	32	32	18	22	24

SAMPLE N15.7

	dp(grt)	grt	hbl	cpx (hbl)	kfs	augite	cpx
SiO2	50.102	35.990	36.722	49.880	64.934	53.312	51.731
TiO2	0.090	0.780	0.027	0.057	0.093	0.045	0.093
Al2O3	2.622	3.531	19.881	3.511	19.113	3.487	2.328
FeO	9.036	23.158	14.372	10.279	0.037	10.836	8.923
MnO	0.325	0.925	0.143	0.363	0.000	0.385	0.379
MgO	12.572	0.018	0.195	11.640	0.000	17.807	13.256
CaO	23.904	34.868	23.007	24.062	0.000	12.694	24.456
Na2O	0.917	0.000	0.000	0.796	0.174	0.852	0.784
K2O	0.031	0.000	0.024	0.003	16.593	0.291	0.016
Total	99.599	99.279	94.370	100.592	100.944	99.660	101.965
	0.114	6.309	5.796	1.884	11.902	1.958	1.913
	0.000	0.103	0.003	0.002	0.013	0.001	0.003
	0.007	0.729	3.698	0.156	4.129	0.151	0.101
	0.017	3.394	1.897	0.325	0.006	0.333	0.276
	0.001	0.137	0.019	0.012	0.000	0.010	0.012
	0.043	0.005	0.046	0.655	0.000	0.975	0.731
	0.058	6.547	3.891	0.974	0.000	0.500	0.969
	0.004	0.000	0.000	0.058	0.062	0.061	0.056
	0.000	0.000	0.005	0.000	3.880	0.034	0.001
Total	0.244	17.224	15.355	4.066	19.991	4.002	4.062
no. [O]	6	24	23	6	32	6	6

SAMPLE N28.14

	1	2	3	4	5	6	7	8	9	10	11	12	13	14	15	16
	crd	bt inc (Crd)	bt core	crd core	crd	pl	bt	crd rim	crd	bt-(Crd)	crd rim	grt rim	crd core	grt rim	bt rim	bt rim
SiO2	48.880	36.189	36.660	49.353	48.217	62.797	36.557	48.914	48.712	35.961	48.401	38.219	47.873	37.589	35.568	36.156
TiO2	0.000	2.671	2.608	0.017	0.000	0.000	2.677	0.030	0.038	2.263	0.000	0.300	0.019	0.000	1.241	0.966
Al2O3	32.433	19.451	19.220	32.987	33.025	24.563	19.290	32.656	32.595	19.315	32.815	21.389	33.269	22.001	20.099	20.193
FeO	7.489	17.255	18.338	7.692	7.829	0.059	17.695	7.826	7.907	17.571	7.734	31.005	7.788	31.184	15.840	16.307
MnO	0.296	0.184	0.130	0.324	0.271	0.000	0.156	0.213	0.303	0.075	0.280	5.438	0.349	4.029	0.142	0.119
MgO	8.063	10.249	10.466	8.255	7.997	0.000	10.365	8.208	7.812	9.940	8.194	3.300	8.197	3.144	12.412	12.055
CaO	0.041	0.038	0.000	0.027	0.019	5.376	0.000	0.011	0.021	0.065	0.052	0.898	0.006	1.064	0.009	0.000
Na2O	0.134	0.172	0.094	0.174	0.154	8.130	0.000	0.255	0.074	0.170	0.283	0.000	0.104	0.000	0.000	0.177
K2O	0.000	8.681	8.851	0.025	0.027	0.169	7.824	0.008	0.000	8.533	0.010	0.000	0.024	0.019	8.332	9.086
Total	97.336	94.891	96.374	98.854	97.539	101.093	94.563	98.122	97.432	93.833	97.769	101.248	97.628	99.629	93.642	95.059
	5.062	5.438	5.449	5.039	4.996	10.992	5.485	5.036	5.049	5.462	5.005	6.017	4.960	6.018	5.369	5.406
	0.000	0.302	0.292	0.001	0.000	0.000	0.302	0.002	0.001	0.259	0.000	0.000	0.001	0.000	0.141	0.109
	3.959	3.445	3.367	3.970	4.034	5.068	3.412	3.963	3.982	3.464	4.000	4.155	4.063	4.152	3.577	3.559
	0.649	2.169	2.279	0.657	0.678	0.009	2.220	0.674	0.685	2.236	0.669	4.082	0.675	4.175	2.000	2.039
	0.026	0.023	0.017	0.028	0.024	0.000	0.020	0.019	0.027	0.010	0.024	0.725	0.031	0.628	0.018	0.015
	1.245	2.296	2.319	1.256	1.235	0.000	2.318	1.260	1.207	2.254	1.263	0.775	1.266	0.750	2.793	2.687
	0.005	0.006	0.000	0.003	0.002	1.008	0.000	0.001	0.002	0.011	0.006	0.151	0.001	0.182	0.001	0.000
	0.027	0.050	0.027	0.034	0.031	2.759	0.000	0.051	0.015	0.050	0.057	0.000	0.021	0.000	0.000	0.051
	0.000	1.664	1.678	0.003	0.004	0.038	1.498	0.001	0.000	1.656	0.001	0.000	0.003	0.004	1.605	1.733
Total	10.972	15.394	15.428	10.993	11.004	19.873	15.255	11.006	10.967	15.401	11.025	15.906	11.020	15.908	15.504	15.599
no.[O]	18	22	22	18	18	32	22	18	18	22	18	24	18	24	22	22

SAMPLE N28.14

	17	18	19	20	21	22	23	24	25	26	27	28	29	30	31	32
	grt rim	bt	grt core	bt rim	bt	grt rim	bt rim	bt rim	grt rim	bt rim	grt	grt core	kfs	grt	bt rim	grt
SiO2	37.16	35.91	37.928	36.585	36.631	38.344	36.089	35.571	38.076	36.428	37.889	37.944	47.726	37.574	36.317	37.787
TiO2	0.037	2.068	0.052	3189	3.282	0.049	2.025	2.519	0.036	1.3	0	0.023	0.04	0.019	1.559	0.008
AlO2O3	21.782	19.919	22.176	18.996	18.779	22.017	20.109	19.17	21.758	19.768	21.861	22.083	36.67	21.531	19.49	21.562
FeO	31.216	17.713	31.336	18.73	19.024	31.788	16.421	16.517	31.49	15.592	31.521	31.917	0.816	31.631	17.011	31.908
MnO	5.001	0.112	3.861	0.116	0.08	5.308	0.161	0.154	5.201	0.115	4.712	5.002	0	4.614	0.137	5.307
MgO	2.771	11.186	4.254	11.255	11.092	3.069	11.313	10.48	2.536	12.377	3.313	2.497	0.765	2.521	11.659	2.637
CaO	1.01	0.028	0.893	0.006	0	0.982	0.067	0.012	0.962	0.05	0.878	0.896	0.051	0.831	0	0.877
Na2O	0	0.283	0	0	0.048	0	0.13	0.002	0	0.098	0	0	0.553	0.031	0.116	0
K2O	0.009	8.601	0.033	9.297	9.607	0.013	8.889	8.871	0	8.481	0	0.008	8.404	0.008	8.518	0
Total	98.987	95.819	100.534	98.174	98.543	101.569	95.203	93.315	100.059	94.207	99.992	100.37	95.023	98.754	94.806	100.085
	6.008	5.355	5.991	5.365	5.369	6.038	5.387	5.431	25.346	5.455	6.047	6.048	9.084	6.081	5.446	6.056
	0.005	0.232	0.006	0.352	0.362	0.006	0.227	0.289	0.018	0.146	0.000	0.003	0.006	0.002	0.176	0.001
	4.151	3.501	4.129	3.283	3.245	4.087	3.538	3.450	17.072	3.489	4.112	4.149	8.227	4.107	3.445	4.073
	4.221	2.209	4.140	2.297	2.332	4.187	2.050	2.109	17.530	1.953	4.207	4.254	0.130	4.282	2.133	4.277
	0.685	0.014	0.517	0.014	0.010	0.708	0.020	0.020	2.932	0.015	0.637	0.675	0.000	0.633	0.017	0.720
	0.668	2.487	1.002	2.460	2.424	0.720	2.517	2.385	2.517	2.768	0.745	0.593	0.217	0.608	2.606	0.630
	0.175	0.004	0.151	0.001	0.000	0.166	0.011	0.002	0.686	0.008	0.150	0.153	0.010	0.144	0.000	0.151
	0.000	0.082	0.000	0.000	0.014	0.000	0.038	0.007	0.009	0.028	0.000	0.000	0.204	0.010	0.034	0.000
	0.002	1.636	0.007	1.739	1.797	0.003	1.693	1.728	0.000	1.620	0.000	0.002	2.041	0.000	1.630	0.000
Total	15.913	15.521	15.942	15.512	15.552	15.914	15.482	15.422	100.000	15.478	15.897	15.876	19.919	15.868	15.487	15.907
no. [O]	24	22	24	22	22	24	22	22	24	22	24	24	32	24	22	24

33	34	35	36
bt inc	grt core	grt core	grt
36.783	37.529	37.565	37.358
1.798	0.044	0.000	0.000
19.950	21.592	21.980	21.757
16.376	32.503	32.139	31.498
0.054	5.001	4.175	4.908
11.897	2.910	3.992	2.883
0.060	0.894	0.857	0.890
0.136	0.000	0.000	0.000
8.510	0.021	0.000	0.000
95.562	100.494	100.707	99.294
5.444	6.004	5.960	6.020
0.200	0.005	0.000	0.000
3.480	4.071	4.110	4.133
2.027	4.348	4.264	4.245
0.007	0.678	0.561	0.670
2.625	0.694	0.944	0.692
0.009	0.153	0.146	0.154
0.039	0.000	0.000	0.000
1.607	0.004	0.000	0.000
Total 15.439	15.958	15.985	15.914
no. [O] 22	24	24	24

SAMPLE N28.4

	1	2	3	4	5	6	7	8	9	10	11	12	13
	hbl core	pl	pl core	pl rim	hbl rim	hbl core	pl core	pl rim	cpx	pl core	pl rim	cpx	hbl
SiO2	51.888	55.651	55.575	53.083	51.706	54.116	55.837	55.210	51.338	56.040	55.115	52.623	52.452
TiO2	0.273	0.011	0.038	0.015	0.306	0.126	0.000	0.000	0.463	0.034	0.000	0.067	0.137
Al2O3	4.328	28.957	28.367	30.285	3.898	2.094	29.407	29.142	4.877	28.261	28.695	0.327	2.690
FeO	13.343	0.022	0.056	0.224	13.468	13.907	0.022	0.112	14.530	0.074	0.180	10.130	13.414
MnO	0.426	0.003	0.000	0.013	0.396	0.471	0.017	0.007	0.513	0.000	0.000	0.475	0.350
MgO	15.163	0.000	0.000	0.000	14.391	15.147	0.000	0.040	14.341	0.000	0.000	12.503	15.196
CaO	12.475	10.745	10.257	12.703	12.529	12.422	10.776	10.809	12.164	10.137	10.859	24.121	12.814
Na2O	0.285	6.055	5.791	4.578	0.358	0.154	6.067	5.282	0.361	5.760	5.587	0.239	0.246
K2O	0.185	0.276	0.279	0.080	0.252	0.009	0.043	0.172	0.365	0.284	0.097	0.109	0.157
Total	98.366	101.719	100.363	10.981	97.304	98.447	102.169	100.772	98.952	100.591	100.533	100.595	97.456
	7.472	9.888	9.980	9.541	7.537	7.770	9.863	9.786	1.930	10.030	9.896	1.979	7.630
	0.029	0.002	0.005	0.002	0.034	0.014	0.000	0.000	0.013	0.004	0.000	0.002	0.015
	0.735	6.065	6.004	6.416	0 670	0.354	6.123	6.144	0.216	5.962	6.073	0.014	0.461
	1.607	0.008	0.008	0.034	1.642	1.670	0.003	0.017	0.457	0.011	0.027	0.319	1.632
	0.052	0.001	0.000	0.002	0 049	0.057	0.003	0.001	0.016	0.000	0.000	0.015	0.043
	3.255	0.000	0.000	0.000	3.128	3.242	0.000	0.011	0.804	0.000	0.000	0.701	3.295
	1.925	2.046	1.974	2.446	1.957	1.911	2.040	2.071	0.490	1.944	2.089	0.972	1.997
	0.080	2.086	2.017	1.596	0.101	0.043	2.078	1.832	0.026	1.999	1.945	0.017	0.069
	0.034	0.062	0.064	0.018	0.047	0.002	0.010	0.039	0.018	0.065	0.022	0.005	0.029
Total	15.188	20.152	20.052	20.055	15.165	15.062	20.120	19.900	3.970	20.016	20.052	4.024	15.173
no.[O]	23	32	32	32	23	23	32	32	6	32	32	6	23
X An		0.49	0.49	0.60			0.49	0.53		0.49	0.51		
X Ab		0.50	0.50	0.39			0.50	0.46		0.50	0.48		

SAMPLE N29.5

	grt core	grt rim	grt core	bt rim	grt core	bt rim	grt core
SiO2	38.292	37.975	38.716	36.180	38.960	36.807	37.947
TiO2	0.000	0.000	0.000	1.420	0 000	1.945	0.014
Al2O3	22.124	22.667	22.699	18.805	22.417	19.417	22.433
FeO	29.886	29.574	30.143	16.579	30.127	17.012	29.949
MnO	3.962	4.689	3.866	0.111	4.139	0.090	5.626
MgO	5.130	4.304	5.274	12.786	5.206	12.638	3.510
CaO	1.583	1.660	1.542	0.000	1.737	0.000	1.814
Na2O	0.014	0.000	0.000	0.000	0.000	0.045	0.000
K2O	0.025	0.002	0.000	9.345	0.000	9.354	0.000
Total	101.015	100.872	102.240	95.226	102.385	97.309	101.291
	5.990	5.960	5.973	5.425	5.999	5.397	5.970
	0.000	0.000	0.000	0.160	0.000	0.215	0.002
	4.079	4.193	4.128	3.323	4.068	3.356	4.159
	3.910	3.882	3.889	2.079	3.879	2.086	3.940
	0.525	0.623	0.505	0.014	0.540	0.011	0.750
	1.196	1.007	1.213	2.858	1.195	2.763	0.823
	0.265	0.279	0.255	0.000	0.287	0.000	0.306
	0.004	0.000	0.000	0.000	0.000	0.013	0.000
	0.005	0.000	0.000	1.788	0.000	1.750	0.000
Total	15.975	15.944	15.963	15.647	15.967	15.591	15.949
no. [O]	24	24	24	22	24	22	24

SAMPLE N29.5

	1	2	3	4	5	6	7	8	9	10	11	12	13	14	15	16
	crd core	crd	crd	crd	crd rim	bi rim	bt core	grt core	grt core	bt inc(Grt)	bt inc (Crd)	crd(Bt inc)	pl	bt inc(Bt)	crd rim(Bt)	bt core
SiO2	48.445	48.041	47.884	48.035	48.043	35.843	35.483	37.539	38.527	35.824	37.078	48.530	58.688	35.841	48.874	34.986
TiO2	0.000	0.000	0.015	0.036	0.017	2.592	0.000	0.000	0.000	1.994	2.453	0.023	0.059	2.210	0.002	3.919
Al2O3	33.242	33.009	32.814	33.207	33.052	18.341	20.329	21.859	21.868	18.963	18.671	33.095	26.394	18.895	33.361	19.086
FeO	6.826	7.498	7.290	7.150	7.267	17.939	30.951	31.988	32.693	17.418	16.944	6.813	0.528	18.094	7.626	20.809
MnO	0.162	0.248	0.157	0.196	0.154	0.113	3.233	3.251	2.370	0.047	0.160	0.225	0.034	0.130	0.198	0.103
MgO	8.389	8.511	8.685	8.592	8.364	10.861	4.454	4.181	5.115	12.727	11.022	8.573	0.000	11.570	8.779	7.798
CaO	0.016	0.025	0.031	0.101	0.037	0.000	1.248	1.300	1.218	0.000	0.000	0.039	7.292	0.000	0.027	0.003
Na2O	0.364	0.225	0.203	0.248	0.130	0.086	0.000	0.000	0.012	0.041	0.077	0.261	7.625	0.108	0.140	0.201
K2O	0.020	0.020	0.028	0.038	0.403	8.924	0.135	0.000	0.003	7.201	7.523	0.000	0.100	7.454	0.000	0.822
Total	97.464	97.577	97.107	97.583	97.467	94.699	95.833	100.118	101.806	94.215	93.928	97.559	100.720	94.302	99.014	87.727
	4.995	4.970	4.973	4.965	4.980	5.432	5.436	5.972	6.000	5.384	5.568	5.004	3.340	5.406	4.978	5.337
	0.000	0.000	0.001	0.003	0.001	0.295	0.000	0.000	0.000	0.226	0.277	0.002	0.003	0.251	0.000	0.450
	4.040	4.025	4.017	4.046	4.038	3.276	3.671	4.099	4.014	3.359	3.305	4.022	1.770	3.359	4.006	3.432
	0.589	0.649	0.633	0.616	0.630	2.274	3.966	4.256	4.258	2.189	2.128	0.588	0.025	2.283	0.650	2.655
	0.014	0.022	0.014	0.017	0.014	0.015	0.420	0.438	0.313	0.006	0.020	0.020	0.002	0.017	0.017	0.013
	1.289	1.313	1.345	1.324	1.293	2.454	1.017	0.992	1.188	2.851	2.467	1.318	0.000	2.602	1.333	1.773
	0.002	0.003	0.003	0.011	0.004	0.000	0.205	0.222	0.203	0.000	0.000	0.004	0.445	0.000	0.003	0.000
	0.073	0.045	0.041	0.050	0.026	0.026	0.000	0.000	0.004	0.012	0.022	0.052	0.841	0.032	0.028	0.059
	0.003	0.003	0.004	0.005	0.053	1.725	0.026	0.000	0.001	1.381	1.441	0.000	0.007	1.434	0.000	1.600
Total	11.003	11.028	11.030	11.037	11.039	15.496	14.741	15.978	15.981	15.407	15.229	11.009	6.433	15.383	11.014	15.319
no. [O]	18	18	18	18	18	22	22	24	24	22	22	18	32	24	18	24

	17	18	19	20	21	22	23	24	25
	kfs	grt rim	grt(Bt)	bt(Crd)	crd cl	pl	bt rim	grt	grt
SiO2	63.000	38.424	38.572	36.193	48.325	58.386	35.461	37.924	37.652
TiO2	0.049	0	0	2.411	0.019	0	2.912	0	0.033
Al2O3	18.780	22.412	22.283	19.016	33.064	26.653	17.986	22.097	21.975
FeO	0.025	30.88	32.036	16.752	7.22	0.019	17.716	32.373	32.165
MnO	0.003	2.442	2.74	0.06	0.27	0	0.114	3.5329	2.935
MgO	0.000	5.02	4.968	11.18	8.528	0	11.244	3.893	4.572
CaO	0.000	1.366	1.306	0	0.012	7.791	0.039	1.343	1.333
Na2O	1.214	0	0	0.096	0.286	7.734	0.106	0	0
K2O	14.425	0	0.048	9.501	0.027	0.159	8.917	0.035	0
Total	97.496	100.544	101.954	95.21	97.752	100.742	94.515	101.194	100.665
	11.868	5.01488	5.98944	5.43444	4.9869	10.38592	5.38956	5.9784	5.95128
	0.007	0	0	0.27136	0.00144	0	0.33352	0	0.00384
	4.170	4.13544	4.07832	3.36556	4.02174	5.58848	3.22212	4.10592	4.09416
	0.004	4.0428	4.16016	2.10364	0.62316	0.00288	2.25192	4.26816	4.25208
	0.001	0.32376	0.36024	0.0077	0.02358	0	0.01452	0.47112	0.39288
	0.000	1.17144	1.15008	2.5025	1.31184	0	2.5476	0.91488	1.07736
	0.000	0.2292	0.2172	0	0.00126	1.4848	0.00968	0.2268	0.22584
	0.443	0	0	0.02706	0.05724	2.66784	0.03124	0	0
	3.467	0	0.00648	1.82006	0.0036	0.03616	1.72898	0.00696	0
Total	19.960	15.918	15.962	15.538	11.031	20.166	15.589	15.972	15.997
no. [O]	32	24	24	22	18	32	22	24	24

SAMPLE N34.1

	1	2	3	4	5	6	7	8	9	10	11	12	13
	grt rim	bt rim	grt core	bt rim mag	crd	bt (crd)	crd	bt	bt inc	crd rim	crd	bt	pl
SiO2	38.159	36.862	38.766	36.911	48.231	36.240	49.150	35.697	36.613	49.064	48.824	36.483	59.692
TiO2	0.012	2.252	0.041	2.077	0.000	2.412	0.073	2.218	2.598	0.013	0.006	2.594	0.011
AlO2O3	22.307	20.599	22.717	19.263	33.557	19.188	33.977	19.788	19.576	33.870	34.022	19.611	26.119
FeO	28.365	26.383	28.410	16.915	6.767	18.190	6.616	17.011	15.596	6.655	6.835	16.545	0.081
MnO	7.237	0.211	6.246	0.166	0.387	0.277	0.467	0.307	0.194	0.438	0.518	0.142	0.036
MgO	3.730	13.134	4.977	12.479	9.142	11.801	9.316	12.283	11.835	9.087	9.200	12.093	0.002
CaO	1.220	0.000	1.293	0.000	0.010	0.000	0.022	0.000	0.000	0.035	0.033	0.000	7.461
Na2O	0.000	0.620	0.000	0.085	0.103	0.065	0.166	0.000	0.004	0.144	0.179	0.071	7.648
K2O	0.000	9.315	0.025	9.438	0.016	9.402	0.000	9.011	8.595	0.016	0.000	9.451	0.260
Total	101.031	97.818	102.476	97.333	98.214	97.575	99.788	96.316	95.012	99.323	99.616	96.990	101.311
	6.006	5.363	5.978	5.414	4.946	5.346	4.957	5.297	5.440	4.970	4.940	5.364	10.538
	0.001	0.246	0.005	0.229	0.000	0.268	0.006	0.248	0.290	0.001	0.001	0.287	0.002
	4.138	3.361	4.129	3.330	4.056	3.337	4.039	3.461	3.428	4.044	4.058	3.399	5.435
	3.733	1.993	3.664	2.075	0.580	2.244	0.018	2.111	1.938	0.564	0.578	2.035	0.012
	0.965	0.026	0.958	0.021	0.034	0.035	0.040	0.039	0.024	0.038	0.044	0.018	0.005
	0.875	2.848	1.144	2.728	1.398	2.595	1.401	2.717	2.621	1.372	1.388	2.651	0.000
	0.206	0.000	0.214	0.000	0.011	0.000	0.002	0.000	0.000	0.004	0.004	0.000	1.412
	0.000	0.017	0.000	0.024	0.020	0.019	0.032	0.000	0.001	0.028	0.035	0.020	2.618
	0.000	1.729	0.005	1.766	0.002	1.769	0.000	1.706	1.629	0.002	0.000	1.773	0.059
	15.924	15.583	16.097	15.587	11.047	15.612	10.494	15.578	15.371	11.022	11.048	15.546	20.081
no. [O]	24	22	24	22	18	22	18	22	22	18	18	22	32
An													.34 An
Ab													.64 Ab

SAMPLE N34.6

	1	2	3	4	5	6	7
	grt core	grt core	bt rim	pl	grt core	bt rim 6	pl
SiO2	38.129	38.155	35.861	61.954	38.038	35.612	61.846
TiO2	0.000	0.000	3.780	0.000	0.000	3.727	0.031
AlO2O3	21.525	21.564	17.643	24.781	21.736	17.568	24.655
FeO	34.615	35.251	17.923	0.019	35.675	17.920	0.057
MnO	1.899	1.872	0.013	0.010	1.934	0.063	0.000
MgO	4.218	4.313	10.215	0.004	4.178	10.269	0.000
CaO	0.901	0.904	0.031	5.414	0.923	0.000	5.663
Na2O	0.000	0.000	0.174	8.194	0.000	0.000	8.401
K2O	0.013	0.000	8.131	0.213	0.000	8.967	0.167
Total	101.300	102.059	100.000	100.589	102.484	94.126	100.820
	6.015	5.989	5.471	10.915	5.959	5.374	10.892
	0.000	0.000	0.434	0.000	0.000	0.423	0.004
	4.002	3.990	3.172	5.146	4.014	3.122	5.118
	4.567	4.627	2.287	0.003	4.674	2.033	0.008
	0.254	0.249	0.002	0.002	0.257	0.008	0.000
	0.992	1.009	2.323	0.001	0.976	1.313	0.000
	0.152	0.152	0.005	1.022	0.155	0.000	1.068
	0.000	0.000	0.051	2.799	0.000	0.000	2.869
	0.003	0.000	1.582	0.048	0.000	2.624	0.037
Total	15.985	16.016	15.327	19.936	16.034	14.896	19.997
no. [0]	24	24	22	32	24	22	32

SAMPLE N34.7c

	bt inc(grt)	bt rim(grt)	grt core	bt inc(grt)	sil inc(grt)
SiO2	35.395	36.615	37.554	35.315	37.114
TiO2	4.186	4.603	0.066	4.308	0.000
AlO2O3	19.039	18.659	21.730	18.546	62.410
FeO	18.575	18.926	35.591	20.236	1.158
MnO	0.000	0.103	2.654	0.095	0.045
MgO	9.735	9.715	2.848	8.697	0.000
CaO	0.025	0.043	0.882	0.000	0.000
Na2O	0.063	0.141	0.085	0.222	0.000
K2O	8.074	7.752	0.007	7.401	0.017
Total	95.092	95.557	101.417	94.824	100.744
	5.332	5.342	5.972	5.365	0.999
	0.474	0.519	0.008	0.492	0.000
	3.381	3.299	4.073	3.321	1.981
	2.340	2.374	4.734	2.571	0.026
	0.000	0.013	0.358	0.013	0.001
	2.186	2.172	0.675	1.970	0.000
	0.004	0.007	0.150	0.000	0.000
	0.018	0.041	0.026	0.065	0.000
	1.552	1.483	0.001	1.435	0.001
Total	15.288	15.252	15.997	15.232	3.008
no. [O]	22	22	24	22	5

SAMPLE N42.12

	hbl core	pl	hbl rim	Ilmenite	ulvospinel	hbl	bt	hbl	bt	hbl core	hbl rim	pl rim	hbl core	hbl	pl rim	pl rim
SiO2	45.245	46.656	45.719	0.225	0.124	44.379	37.514	44.922	38.867	43.532	44.180	47.650	44.885	45.671	45.493	46.992
TiO2	0.974	0.008	0.889	42.745	10.829	1.130	2.825	1.092	1.237	1.149	0.916	0.000	0.843	0.825	0.020	0.000
AlO2O3	10.094	33.881	10.068	0.001	0.000	10.727	15.120	10.327	15.066	10.208	10.129	33.286	9.770	9.836	34.272	34.201
FeO	15.426	0.220	15.197	50.388	81.268	15.628	16.502	15.392	15.177	15.287	15.327	0.124	14.211	14.406	0.377	0.185
MnO	0.353	0.000	0.500	0.404	0.817	0.404	0.152	0.435	0.173	0.357	0.410	0.000	0.493	0.373	0.017	0.000
MgO	12.560	0.000	12.138	0.000	0.000	11.884	14.558	12.154	16.211	11.800	12.052	0.006	12.285	12.480	0.000	0.014
CaO	10.906	17.752	11.523	0.117	0.000	12.144	0.000	11.771	0.000	11.675	12.039	17.084	12.173	11.637	18.342	17.968
Na2O	1.350	1.395	1.431	0.000	0.000	1.465	0.133	1.408	0.139	1.272	1.232	2.043	1.218	1.166	1.372	1.598
K2O	0.631	0.005	0.666	0.019	0.050	0.765	9.634	0.697	9.346	0.862	0.650	0.010	0.555	0.658	0.054	0.018
Total	97.539	99.917	98.131	93.901	93.088	98.527	96.437	98.199	96.217	96.143	96.935	100.202	96.432	97.051	99.946	100.974
	6.708	8.591	6.742	0.006	0.006	6.565	5.580	6.643	5.726	6.595	6.629	8.735	6.725	6.779	8.417	8.571
	0.109	0.001	0.099	0.898	0.382	0.126	0.316	0.121	0.137	0.131	0.113	0.000	0.095	0.092	0.003	0.000
	1.764	7.353	1.750	0.000	0.000	1.870	2.651	1.800	2.616	1.823	1.791	7.192	1.725	1.721	7.474	7.353
	1.913	0.034	1.874	1.177	3.190	1.934	2.053	1.904	1.870	1.937	1.923	0.019	1.781	1.788	0.058	0.028
	0.044	0.000	0.063	0.010	0.032	0.051	0.019	0.055	0.022	0.046	0.052	0.000	0.063	0.047	0.003	0.000
	2.776	0.000	2.668	0.000	0.000	2.621	3.228	2.679	3.560	2.665	2.696	0.002	2.744	2.761	0.000	0.004
	1.733	5.681	1.821	0.004	0.000	1.925	0.000	1.865	0.000	1.895	1.936	3.356	1.954	1.851	3.636	3.512
	0.388	0.446	0.409	0.000	0.000	0.420	0.039	0.404	0.040	0.374	0.359	0.726	0.354	0.335	0.492	0.565
	0.119	0.002	0.125	0.001	0.003	0.144	1.828	0.132	1.756	0.167	0.124	0.002	0.106	0.125	0.013	0.004
Total	15.555	22.108	15.551	2.096	3.613	15.657	15.712	15.603	15.727	15.632	15.623	20.032	15.547	15.499	20.096	20.037
no. [O]	23	32	23	3	4	23	22	23	22	23	23	32	23	23	32	32
X An		0.93										0.82			0.88	0.86
X Ab		0.07										0.18			0.12	0.14

SAMPLE N42.15

	1	2	3	4	5	6	7	8	9	10
	kfs	crd	Kfs	pl rim	bt rim	crd	bt	pl (bt)	pl	crd (bt)
SiO2	63.254	46.683	63.192	61.577	35.544	48.174	35.267	62.830	61.002	48.682
TiO2	0.055	0.000	0.026	0.003	1.927	0.033	3.523	0.094	0.000	0.074
Al2O3	19.005	33.436	19.536	24.862	19.695	33.417	18.096	25.490	25.867	33.636
FeO	0.184	6.737	0.128	0.285	18.204	7.157	19.757	0.202	0.048	5.997
MnO	0.000	0.737	0.000	0.000	0.211	0.731	0.370	0.000	0.000	0.683
MgO	0.000	9.044	0.000	0.000	10.361	8.928	8.746	0.020	0.000	8.503
CaO	0.000	0.055	0.000	5.070	0.000	0.000	0.012	4.923	4.861	0.079
Na2O	0.978	0.149	1.391	9.143	0.174	0.081	0.110	9.211	9.090	0.211
K2O	15.937	0.000	15.017	0.063	9.775	0.000	10.108	0.217	0.232	0.634
Total	99.413	96.841	99.290	101.003	95.892	98.523	95.988	102.988	101.099	98.499
	11.805	4.873	11.757	10.845	5.354	4.942	5.378	10.844	10.729	4.982
	0.008	0.000	0.004	0.000	0.218	0.003	0.404	0.012	0.000	0.006
	4.181	4.114	4.284	5.161	3.497	4.040	3.253	5.185	5.362	4.057
	0.029	0.588	0.020	0.004	2.293	0.614	2.520	0.029	0.007	0.513
	0.000	0.065	0.000	0.000	0.027	0.064	0.048	0.000	0.000	0.059
	0.000	1.407	0.000	0.000	2.326	1.365	1.988	0.005	0.000	1.297
	0.000	0.006	0.000	0.957	0.000	0.000	0.002	0.910	0.916	0.009
	0.354	0.030	0.502	3.123	0.051	0.016	0.032	3.083	3.100	0.042
	3.795	0.000	3.564	0.014	1.878	0.000	1.967	0.048	0.052	0.083
Total	20.171	11.085	100.000	100.000	15.644	11.044	15.591	20.116	20.165	11.047
no. [O]	32	18	32	32	22	18	22	32	32	18

SAMPLE N43.15

	bt rim	grt core	grt rim	grt core	bt inc (grt)	grt core	bt rim	grt rim	pl core	grt core	grt rim	bt rim(grt)	grt core	grt rim
SiO2	36.365	38.508	38.718	38.594	36.728	38.442	35.91	37.421	62.414	38.132	37.888	36.862	38.326	37.872
TiO2	1.939	0.006	0	0	4.826	0.008	3.995	0.011	0	0	0.026	3.598	0.006	0.024
Al2O3	19.051	22.327	22.032	21.969	18.038	22.026	17.763	21.476	24.901	21.672	21.774	17.996	21.711	21.598
FeO	17.707	33.876	33.572	32.77	14.814	34.947	18.193	36.131	0.04	34.526	35.187	17.383	32.414	31.74
MnO	0	3.793	3.48	2.903	0.093	1.768	0.016	2.346	0	1.861	2.109	0.049	4.055	6.252
MgO	11.249	3.791	4.414	4.718	13.084	4.87	9.806	3.179	0	4.621	3.517	10.208	4.041	2.808
CaO	0.037	0.874	0.988	0.975	0.01	0.938	0.029	0.952	5.848	0.951	0.936	0.082	1.065	0.928
Na2O	0.201	0	0	0	0.182	0	0	0	8.856	0	0.06	0.214	0	0.114
K2O	10.11	0	0	0	9.22	0.021	9.778	0.008	0.249	0.042	0	9.693	0.007	0
Total	96.659	103.175	103.204	101.93	97.197	103.014	95.491	101.526	102.319	101.804	101.498	96.084	101.624	101.336
	5.42058	5.97672	5.99304	6.0156	5.33678	5.95848	5.43532	5.9556	10.86016	5.98272	5.98896	5.50814	6.02136	6.0156
	0.21736	0.00072	0	0	0.52932	0.00096	0.45474	0.0012	0	0	0.00312	0.40436	0.00072	0.00288
	3.34708	4.08456	3.95496	4.03632	3.1009	4.02408	3.16888	4.02888	5.10688	4.008	4.05696	3.16954	4.02048	4.04352
	2.20726	4.39728	4.34592	4.27176	1.80686	4.53024	2.30296	4.80936	0.00576	4.53048	4.65168	2.17228	4.25904	4.21632
	0	0.49848	0.45624	0.38328	0.01144	0.23136	0.00198	0.31632	0	0.2472	0.28248	0.00616	0.53952	0.8412
	2.49964	0.87696	1.01832	1.09632	2.8446	1.12536	2.21254	0.75408	0	1.08072	0.82872	2.27392	0.94632	0.6648
	0.00594	0.1452	0.16368	0.16296	0.00154	0.15576	0.00484	0.16224	1.09024	0.1584	0.1584	0.0132	0.17928	0.15792
	0.05808	0	0	0	0.10802	0	0	0	2.99136	0	0.01848	0.06182	0	0.03528
	1.92258	0	0	0	1.716	0.00408	1.88826	0.00168	0.05586	0.0084	0	1.84778	0.0012	0
Total	15.68	15.98	15.93	15.97	15.48	16.03	15.47	16.03	20.11	16.02	15.99	15.46	15.97	15.98
no. [O]	22	24	24	24	22	24	22	24	32	24	24	22	24	24

SAMPLE N43.15b

	1	2	3	4	5	6	7	8
	pl	pl	grt r/c	pl	bt	grt rim	grt core	bt
SiO2	61.044	61.203	38.029	60.370	35.185	38.435	38.623	35.514
TiO2	0.000	0.006	0.021	0.000	3.623	0.015	0.012	3.706
Al2O3	24.782	24.533	21.605	25.066	18.079	21.758	21.103	17.776
FeO	0.036	0.033	32.325	0.269	20.071	31.790	32.270	19.993
MnO	0.045	0.036	3.376	0.000	0.108	3.892	3.404	0.079
MgO	0.000	0.000	4.236	0.000	8.639	4.141	4.199	8.794
CaO	5.453	5.516	0.941	5.699	0.000	0.820	0.851	0.000
Na2O	8.536	8.720	0.000	8.455	0.016	0.000	0.000	0.000
K2O	0.363	0.258	0.025	0.410	9.434	0.003	0.000	9.247
Total	100.259	100.305	100.558	100.270	95.155	100.855	100.462	95.110
	10.833	10.858	6.024	10.741	5.392	6.057	6.114	5.432
	0.000	0.001	0.002	0.000	0.418	0.002	0.001	0.426
	5.184	5.130	4.034	5.257	3.265	4.042	3.937	3.205
	0.005	0.005	4.282	0.040	2.572	4.190	4.272	2.558
	0.007	0.005	0.453	0.000	0.014	0.520	0.456	0.010
	0.000	0.000	1.000	0.000	1.973	0.973	0.991	2.005
	1.037	1.049	0.160	1.087	0.000	0.138	0.144	0.000
	2.937	3.000	0.000	2.917	0.005	0.000	0.000	0.000
	0.082	0.059	0.005	0.093	1.844	0.000	0.000	1.804
Total	20.085	20.106	15.960	20.135	15.483	15.921	15.916	15.441
no. [O]	32	32	24	32	22	24	24	22

SAMPLE N43.15c

1	2	3	4	5	6	7
grt	bt	mag- inc grt	pl	grt core	grt	bt
38.453	35.314	2.893	61.295	38.546	38.457	35.316
0.000	3.479	0.020	0.006	0.040	0.000	3.415
21.870	18.029	0.498	24.858	21.827	21.967	18.054
32.220	20.206	77.405	0.036	32.663	32.536	19.982
3.420	0.136	0.476	0.000	3.628	3.441	0.175
4.394	8.585	0.259	0.016	4.262	4.345	8.861
0.929	0.000	0.525	5.414	0.889	0.954	0.000
0.000	0.158	0.089	8.599	0.048	0.000	0.106
0.000	9.373	0.065	0.306	0.000	0.000	8.855
101.287	95.280	82.230	100.530	101.902	101.699	94.763
6.033	5.407	1.270	10.840	6.027	6.018	5.414
0.000	0.401	0.007	0.001	0.005	0.000	0.394
4.045	3.254	0.257	5.182	4.023	4.052	3.262
4.228	2.588	28.412	0.005	4.272	4.258	2.562
0.455	0.018	0.177	0.000	0.480	0.456	0.023
1.028	1.960	0.169	0.004	0.993	1.014	2.025
0.156	0.000	0.247	1.026	0.149	0.160	0.000
0.000	0.047	0.076	2.949	0.015	0.000	0.031
0.000	1.831	0.036	0.069	0.000	0.000	1.732
15.944	15.505	30.651	20.076	15.964	15.957	15.443
24	22	32	32	24	24	22

APPENDIX 4.3 Results from Microprobe analyses for the Khan Mine area

SAMPLE K10.1

	1	2	3	4	5
	grt core	bt inc	grt rim	grt rim	bt
SiO2	38.744	37.03	37.405	38.694	36.421
TiO2	0	2.821	0	0	2.17
Al2O3	22.296	18.251	21.351	22.293	18.161
FeO	29.888	15.121	31.359	31.329	17.085
MnO	3.427	0.056	4.92	5.079	0.23
MgO	4.847	13.057	2.776	3.891	11.955
CaO	1.441	0	1.496	1.494	0.034
Na2O	0	0.05	0	0	0
K2O	0	7.778	0.01	0.009	8.534
Total	100.643	94.164	99.318	102.789	94.59
	6.05472	5.5143	6.03696	6.0024	5.48812
	0	0.31592	0	0	0.24596
	4.10688	3.20342	4.06176	4.07616	3.22564
	3.90624	1.8832	4.09632	4.0644	2.15314
	0.4536	0.00704	0.67248	0.66744	0.02948
	1.1292	2.89828	0.66792	0.89976	2.68532
	0.2412	0	0.25872	0.24816	0.0055
	0	0.0143	0	0	0
	0	1.47774	0.00216	0.00192	1.64054
Total	15.892	15.314	15.796	15.960	15.474
no. [O]	24	22	24	24	22

SAMPLE K35.11

	1	2	3	4	5	6	7	8	9	10	11	12	13	14	15	16
	bt rim	grt rim	grt	grt	grt	grt	grt	grt	grt core	kfs	kfs	kfs	pl	grt	bt	pl
SiO2	36.385	38.52	37.966	38.627	39.139	39.094	38.938	39.303	38.885	49.509	49.271	48.95	62.131	38.382	36.878	60.652
TiO2	2.181	0.008	0	0	0.021	0.69	0.03	0.018	0	0.015	0	0	0	0	2.573	0.013
Al2O3	19.597	22.692	22.184	22.735	22.84	22.895	22.768	23.932	22.658	36.116	36.174	36.217	24.223	21.843	18.75	25.266
FeO	17.752	32.808	32.55	32.217	31.751	31.762	31.541	30.932	31.161	2.258	1.93	1.938	0.078	32.06	18.301	0.106
MnO	0.095	3.077	3.105	2.507	2.567	2.464	2.75	2.327	2.436	0.014	0	0.037	0.01	2.977	0.115	0
MgO	11.536	4.145	4.514	5.096	5.455	5.542	5.53	5.687	5.585	2.948	2.727	2.703	0	4.594	11.088	0
CaO	0	0.972	0.928	1.048	1.083	1.051	1.766	1.655	1.981	0.563	0.492	0.545	4.782	0.946	0	5.812
NaO	0.123	0	0	0	0.018	0	0	0.046	0	0.104	0.031	0.127	9.251	0	0.261	8.586
K2O	9.027	0.005	0.011	0.011	0.028	0.029	0	0	0.019	4.791	4.162	4.747	0.163	0	8.88	0.147
Total	96.692	102.227	101.258	102.241	102.904	102.906	102.849	103.023	102.726	96.318	94.789	95.264	100.637	100.802	96.847	100.581
	5.383	5.986	5.966	5.972	5.993	5.983	5.967	5.988	5.966	9.160	9.199	9.141	10.963	6.037	5.459	10.739
	0.243	0.001	0.000	0.000	0.002	0.008	0.004	0.002	0.000	0.002	0.000	0.000	0.000	0.000	0.286	0.002
	3.417	4.156	4.109	4.143	4.122	4.130	4.112	4.140	4.098	7.876	7.961	7.972	5.038	4.050	3.271	5.273
	2.196	4.264	4.278	4.165	4.066	4.065	4.042	3.941	3.999	0.349	0.301	0.303	0.012	4.218	2.266	0.016
	0.012	0.405	0.413	0.328	0.333	0.319	0.295	0.300	0.317	0.002	0.000	0.006	0.002	0.397	0.015	0.000
	2.544	0.960	1.057	1.174	1.245	1.264	1.250	1.292	1.278	0.813	0.759	0.752	0.000	1.077	2.447	0.000
	0.000	0.162	0.156	0.174	0.178	0.172	0.290	0.270	0.326	0.112	0.099	0.109	0.904	0.159	0.000	1.103
	0.035	0.000	0.000	0.000	0.006	0.000	0.000	0.013	0.000	0.037	0.012	0.046	3.165	0.000	0.075	2.948
	1.703	0.001	0.002	0.002	0.006	0.006	0.000	0.000	0.004	1.131	0.991	1.131	0.036	0.000	1.677	0.033
Total	15.534	15.935	15.981	15.958	15.950	15.947	15.960	15.947	15.986	19.484	19.322	19.460	20.11936	15.93768	15.49504	20.11296
no. [O]	22	24	24	24	24	24	24	24	24	32	32	32	32	24	22	32

SAMPLE K21.16

	1	2
	pl core	hbl core
SiO2	59.557	42.452
TiO2	0.012	1.085
Al2O3	25.416	10.19
FeO	0.161	14.392
MnO	0.02	0.743
MgO	0	12.677
CaO	6.798	11.866
Na2O	8.048	1.618
K2O	0.194	1.506
Total	100.206	96.529
	10.621	6.451
	0.002	0.124
	5.343	1.825
	0.024	1.829
	0.003	0.096
	0.000	2.872
	1.299	1.932
	2.783	0.477
	0.044	0.292
Total	20.119	15.897
no. [O]	32	23
XAn	0.31	
XAb	0.67	

SAMPLE K21.19

	1	2	3	4	5
	hbl c	pl c	FeO TiO	pl c	hbl c
	47.092	58.503	0.344	53.183	46.672
	0.493	0.013	8.021	0.000	0.587
	9.223	30.386	0.050	29.843	9.113
	9.257	0.220	81.682	0.245	9.734
	0.740	0.000	0.147	0.010	0.697
	16.284	0.005	0.000	0.000	16.035
	11.631	11.958	0.011	12.178	12.227
	1.056	4.847	0.040	4.654	0.966
	0.942	0.129	0.000	0.110	0.981
	96.718	101.062	90.294	100.223	97.013
	6.857	9.590	0.422	9.616	6.810
	0.054	0.002	7.417	0.000	0.064
	1.583	6.420	0.072	6.360	1.567
	1.127	0.033	83.997	0.037	1.188
	0.091	0.000	0.153	0.002	0.086
	3.534	0.001	0.000	0.000	3.487
	1.815	2.297	0.014	2.351	1.912
	0.298	1.684	0.096	1.632	0.273
	0.175	0.029	0.000	0.026	0.183
	15.594	20.056	100.000	20.024	15.570
	23	32		32	23
		0.57		0.59	
		0.42		0.41	

SAMPLE K37

	1	2	3	4
	hbl c	Pl c	hbl c	Pl c
SiO2	45.862	46.47	46.098	46.201
TiO2	0.497	0.01	0.583	0
Al2O3	9.333	34.67	9.316	34.455
FeO	11.632	0.264	11.553	0.318
MnO	0.57	0	0.405	0.023
MgO	14.62	0	14.749	0
CaO	12.448	16.909	12.472	17.584
Na2O	1.144	1.596	1.124	1.615
K2O	1.164	0.009	1.138	0.02
Total	97.27	99.928	97.378	100.216
	6.754	8.539	6.762	8.495
	0.055	0.001	0.064	0.000
	1.620	7.509	1.613	7.468
	1.433	0.041	1.419	0.049
	0.071	0.000	0.050	0.004
	3.210	0.000	3.229	0.000
	1.964	3.329	1.963	3.465
	0.327	0.569	0.320	0.576
	0.219	0.002	0.213	0.005
Total	15.653	19.990	15.634	20.061
no. [O]	23	32	23	32
XAn		0.85		0.86
XAb		0.15		0.14

SAMPLE K38.18

	pl c	hbl rim	hbl core	pl c
	57.348	44.186	44.104	57.968
	0.005	1.726	1.583	0
	27.115	9.797	10.091	27.262
	0.16	14.685	14.965	0.249
	0	11.95	0.223	0.054
	0.03	0.266	11.881	0
	9.053	12.128	11.876	8.907
	6.786	1.31	1.422	6.967
	0.302	1.347	1.351	0.4
	100.799	97.394	97.496	101.807
	10.236	6.611	6.595	10.252
	0.001	0.194	0.178	0.000
	5.704	1.728	1.779	5.683
	0.024	1.837	1.872	0.037
	0.000	0.034	0.028	0.008
	0.008	2.665	2.648	0.000
	1.731	1.944	1.903	1.688
	2.348	0.380	0.412	2.389
	0.069	0.257	0.258	0.090
	20.121	15.650	15.672	20.146
	32	23	23	32
	0.42			0.41
	0.57			0.57

APPENDIX 4.4 Results from Microprobe analyses for Grt profiles

SAMPLE N43.15 (basement)

(mm)	0	0.09	0.042	0.096	0.016	0.052	0.078	0.061
SiO2	38.091	37.263	37.713	37.422	37.561	37.767	37.660	37.704
TiO2	0.124	0.006	0.037	0.000	0.028	0.037	0.046	0.000
AlO2O3	21.625	21.580	21.852	21.745	21.405	21.511	21.823	21.885
FeO	31.412	30.852	31.570	31.622	31.800	32.092	32.144	31.687
MnO	4.305	4.913	4.056	3.853	4.143	3.888	3.976	4.333
MgO	3.572	3.253	4.002	4.035	4.008	3.903	3.863	3.714
CaO	0.962	0.967	0.969	0.940	0.954	0.971	0.928	0.949
Na2O	0.091	0.092	0.000	0.000	0.000	0.000	0.093	0.000
K2O	0.007	0.114	0.000	0.000	0.000	0.023	0.009	0.007
Total	100.189	99.040	100.199	99.617	99.900	100.192	100.542	100.279
	6.055	6.009	5.996	5.987	6.005	6.018	5.978	5.994
	0.015	0.001	0.004	0.000	0.003	0.004	0.006	0.000
	4.052	4.102	4.095	4.100	4.034	4.040	4.083	4.101
	4.176	4.161	4.198	4.231	4.252	4.277	4.267	4.213
	0.580	0.671	0.546	0.522	0.561	0.525	0.535	0.584
	0.846	0.782	0.948	0.962	0.955	0.927	0.914	0.880
	0.164	0.167	0.165	0.161	0.163	0.166	0.158	0.162
	0.028	0.000	0.000	0.000	0.000	0.000	0.029	0.000
	0.001	0.019	0.000	0.000	0.000	0.005	0.002	0.001
Total	15.918	15.911	15.952	15.963	15.974	15.961	15.971	15.936
no. [O]	24	24	24	24	24	24	24	24

SAMPLE N34.7c

(mm)	0.00	0.52	1.04	1.51	2.08	2.50	3.04	3.50	4.52	5.07	5.57	6.55	7.04	7.53	8.10	8.65
SiO2	37.051	37.404	37.261	37.629	37.418	37.536	37.689	36.322	37.564	37.715	37.924	37.553	37.278	37.457	37.316	37.618
TiO2	0.021	0.049	0.006	0.005	0.000	0.005	0.031	0.017	0.043	0.029	0.006	0.005	0.081	0.003	0.060	0.060
AlO2O3	21.745	21.871	21.787	21.847	21.748	21.606	21.737	21.804	21.741	21.922	21.807	21.902	21.894	21.889	21.660	21.542
FeO	36.535	35.751	34.932	34.942	35.787	35.783	33.584	34.484	35.354	35.435	35.981	34.586	35.657	35.892	35.466	35.771
MnO	2.898	2.494	1.993	2.037	2.195	2.075	2.050	1.957	2.312	2.305	2.131	2.095	2.108	2.342	2.181	2.932
MgO	2.400	3.045	3.472	3.477	3.513	3.652	3.743	3.771	3.567	3.483	3.653	3.335	3.383	3.485	3.322	2.387
CaO	0.845	0.925	0.938	1.009	0.953	0.944	1.018	0.952	0.994	1.047	1.046	1.019	0.949	0.986	1.015	0.886
NaO	0.000	0.019	0.000	0.063	0.000	0.000	0.000	0.000	0.000	0.000	0.005	0.000	0.096	0.000	0.000	0.000
K2O	0.000	0.000	0.025	0.000	0.000	0.035	0.018	0.044	0.000	0.065	0.058	0.000	0.000	0.000	0.002	0.000
Total	101.495	101.558	100.414	101.010	101.615	101.636	99.870	99.351	101.675	102.024	102.611	100.496	101.446	102.054	101.022	101.196
	5.913	5.941	5.956	5.974	5.934	5.949	6.007	5.872	5.942	5.946	5.947	5.984	5.914	5.919	5.948	6.006
	0.003	0.006	0.001	0.000	0.000	0.000	0.004	0.002	0.005	0.003	0.001	0.001	0.010	0.000	0.072	0.007
	4.091	4.094	4.105	4.088	4.065	4.036	4.084	4.154	4.054	4.074	4.031	4.114	4.224	4.077	4.070	4.054
	4.876	4.749	4.670	4.640	4.746	4.743	4.477	4.662	4.677	4.672	4.719	4.610	4.731	4.744	4.728	4.776
	0.392	0.336	0.270	0.274	0.295	0.279	0.277	0.268	0.310	0.308	0.283	0.283	0.283	0.313	0.294	0.396
	0.571	0.721	0.827	0.823	0.830	0.863	0.889	0.909	0.865	0.819	0.854	0.792	0.800	0.821	0.789	0.568
	0.144	0.157	0.161	0.172	0.162	0.160	0.174	0.165	0.168	0.177	0.176	0.174	0.161	0.167	0.173	0.152
	0.000	0.006	0.000	0.019	0.000	0.000	0.000	0.000	0.000	0.000	0.001	0.000	0.030	0.000	0.000	0.000
	0.000	0.000	0.005	0.000	0.000	0.007	0.004	0.005	0.000	0.013	0.010	0.000	0.000	0.000	0.000	0.000
Total	15.990	16.009	15.994	15.991	16.033	16.036	15.915	16.037	16.021	16.011	16.023	15.958	16.1532	16.0418	16.0752	15.96
no. [O]	24	24	24	24	24	24	24	24	24	32	32	32	32	24	22	32

SAMPLE N34.6

(mm)	3.49	3.41	3.30	3.20	3.09	2.99	2.89	2.80	2.71	2.59
SiO2	37.924	37.652	38.213	37.920	38.222	38.124	38.257	38.088	37.934	37.756
TiO2	0.000	0.033	0.007	0.000	0.045	0.030	0.051	0.000	0.034	0.027
AlO2O3	22.097	21.975	22.191	21.963	22.346	22.348	22.238	21.884	22.079	21.696
FeO	32.373	32.165	32.450	32.050	31.596	31.557	32.163	31.608	32.268	32.761
MnO	3.529	2.935	2.602	2.642	2.493	2.378	2.616	2.607	2.849	3.203
MgO	3.893	4.572	4.868	4.972	5.105	5.216	5.313	5.056	4.903	4.098
CaO	1.343	1.339	1.345	1.281	1.328	1.289	1.287	1.327	1.311	1.343
Na2O	0.000	0.000	0.000	0.052	0.000	0.024	0.000	0.000	0.000	0.000
K2O	0.035	0	0.002	0.005	0.021	0.002	0.016	0	0.009	0
Total	101.194	100.665	101.673	100.885	101.156	100.963	101.941	100.570	101.387	100.884
	5.978	5.951	5.963	5.961	5.969	5.965	5.948	5.994	5.947	5.976
	0.000	0.004	0.001	0.000	0.005	0.004	0.006	0.000	0.004	0.003
	4.106	4.094	4.081	4.069	4.113	4.121	4.075	4.059	4.080	4.048
	4.268	4.252	4.235	4.214	4.126	4.129	4.182	4.160	4.231	4.337
	0.471	0.393	0.344	0.352	0.330	0.315	0.345	0.348	0.378	0.430
	0.915	1.077	1.131	1.165	1.188	1.217	1.231	1.186	1.146	0.967
	0.227	0.226	0.225	0.216	0.222	0.216	0.215	0.224	0.220	0.228
	0.000	0.000	0.000	0.016	0.000	0.007	0.000	0.000	0.000	0.000
Total	15.965	15.997	15.981	15.992	15.953	15.974	16.002	15.971	16.007	15.987
no. [O]	24	24	24	24	24	24	24	24	24	24

SAMPLE N28.14

(mm)	0.00	0.05	0.20	0.25	0.61	0.90	1.07
SiO2	37.707	38.278	37.686	38.553	38.434	38.012	38.316
TiO2	0.000	0.000	0.000	0.029	0.000	0.038	0.000
AlO2O3	21.820	21.696	21.888	21.970	21.957	21.906	21.999
FeO	32.925	31.768	31.654	31.869	30.468	30.615	31.482
MnO	4.535	4.622	4.327	4.030	3.596	3.845	4.423
MgO	2.989	3.637	3.871	3.986	4.225	4.399	3.560
CaO	0.814	0.805	0.876	0.879	0.900	0.911	0.817
Na2O	0.000	0.000	0.000	0.073	0.000	0.000	0.000
K2O	0.000	0.023	0.002	0.000	0.011	0.000	0.000
Total	100.790	100.829	100.303	101.389	99.591	99.726	100.598
	6.005	6.056	5.993	6.047	6.089	6.033	6.029
	0.000	0.000	0.000	0.003	0.000	0.005	0.000
	4.096	4.046	4.103	4.062	4.100	4.098	4.063
	4.386	4.203	4.210	4.181	4.037	4.064	4.160
	0.612	0.619	0.583	0.535	0.483	0.517	0.653
	0.710	0.858	0.918	0.932	0.998	1.041	0.987
	0.139	0.137	0.149	0.148	0.153	0.155	0.156
	0.000	0.000	0.000	0.022	0.000	0.000	0.000
	0.000	0.005	0.000	0.000	0.002	0.000	0.000
Total	15.947	15.924	15.956	15.930	15.862	15.913	16.047
no. [O]	24	24	24	24	24	24	24

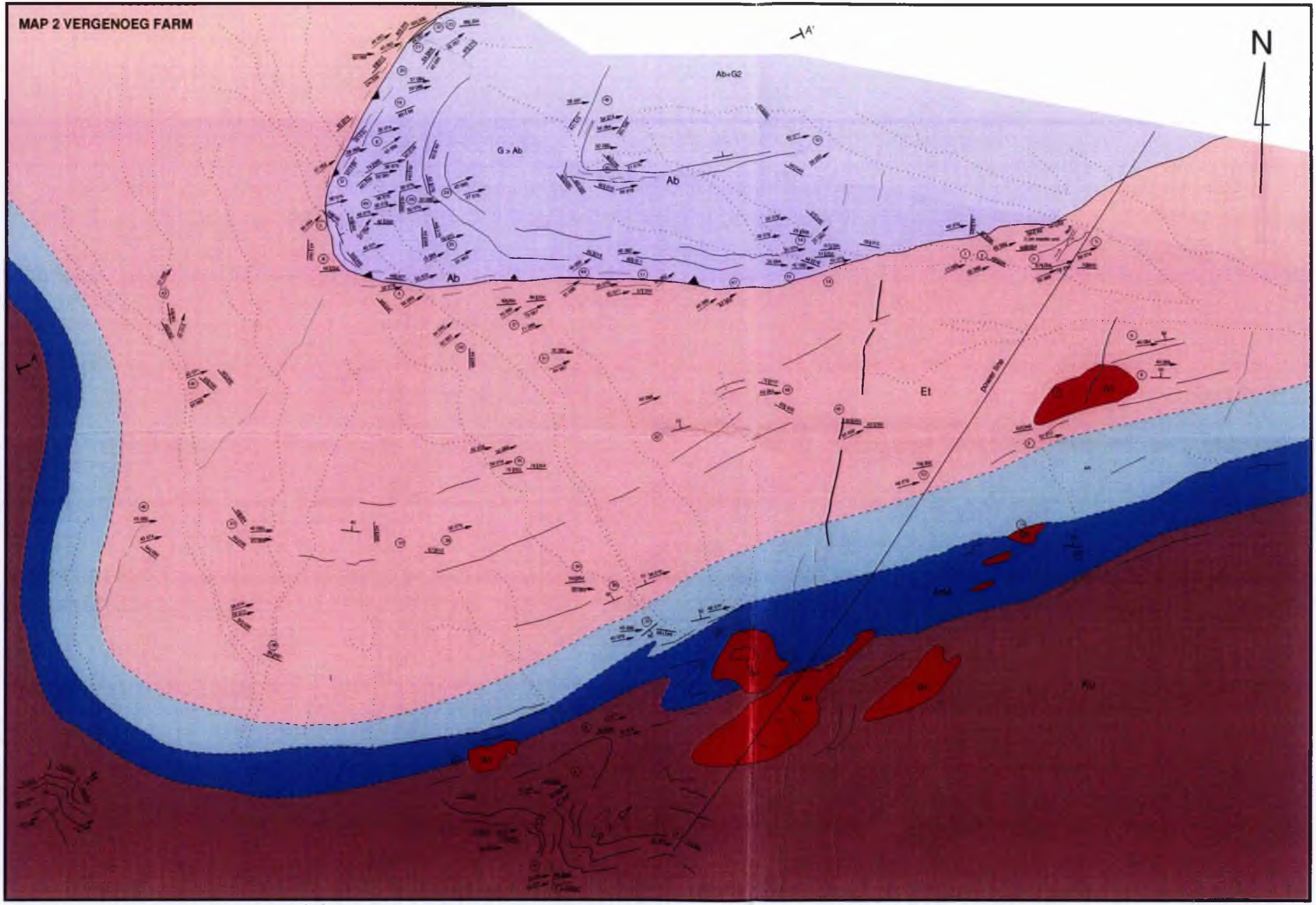
MAP 2 VERGENOEG FARM
A'
N
Ab+G2
G > Ab
Ab
Ab
Ab
Et
Dowser Zone
KEY
GEOLOGICAL
Swakop Group
Ar
R
Ch
Nosib Group
Kh
Et
Ab
STRUCTURAL
0m
SCALE = 1:30

Map 2 [Vergenoeg Area]

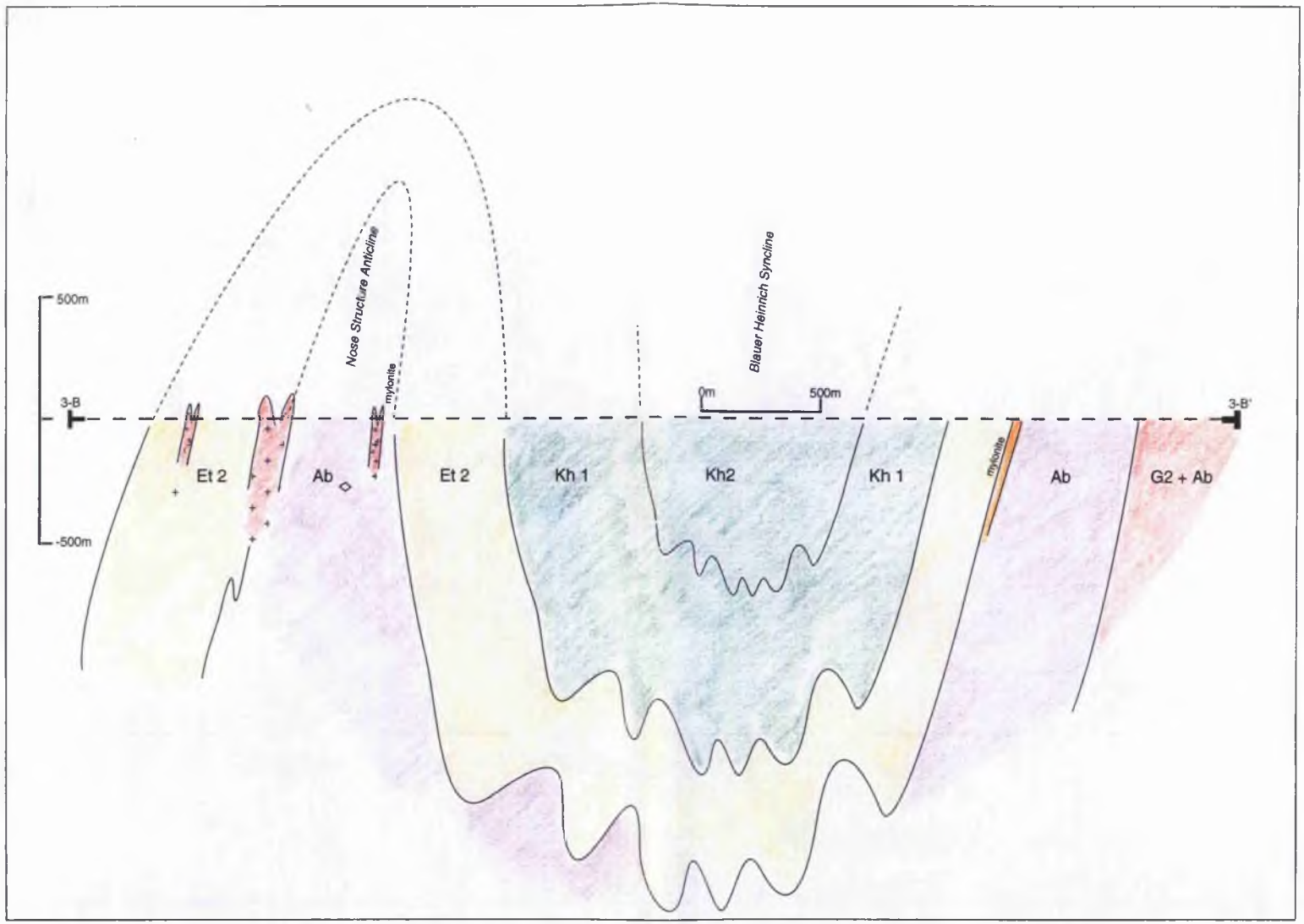

Cross-section Khan Mine area [Map 3] B- B' (stratigraphic symbols as main map)

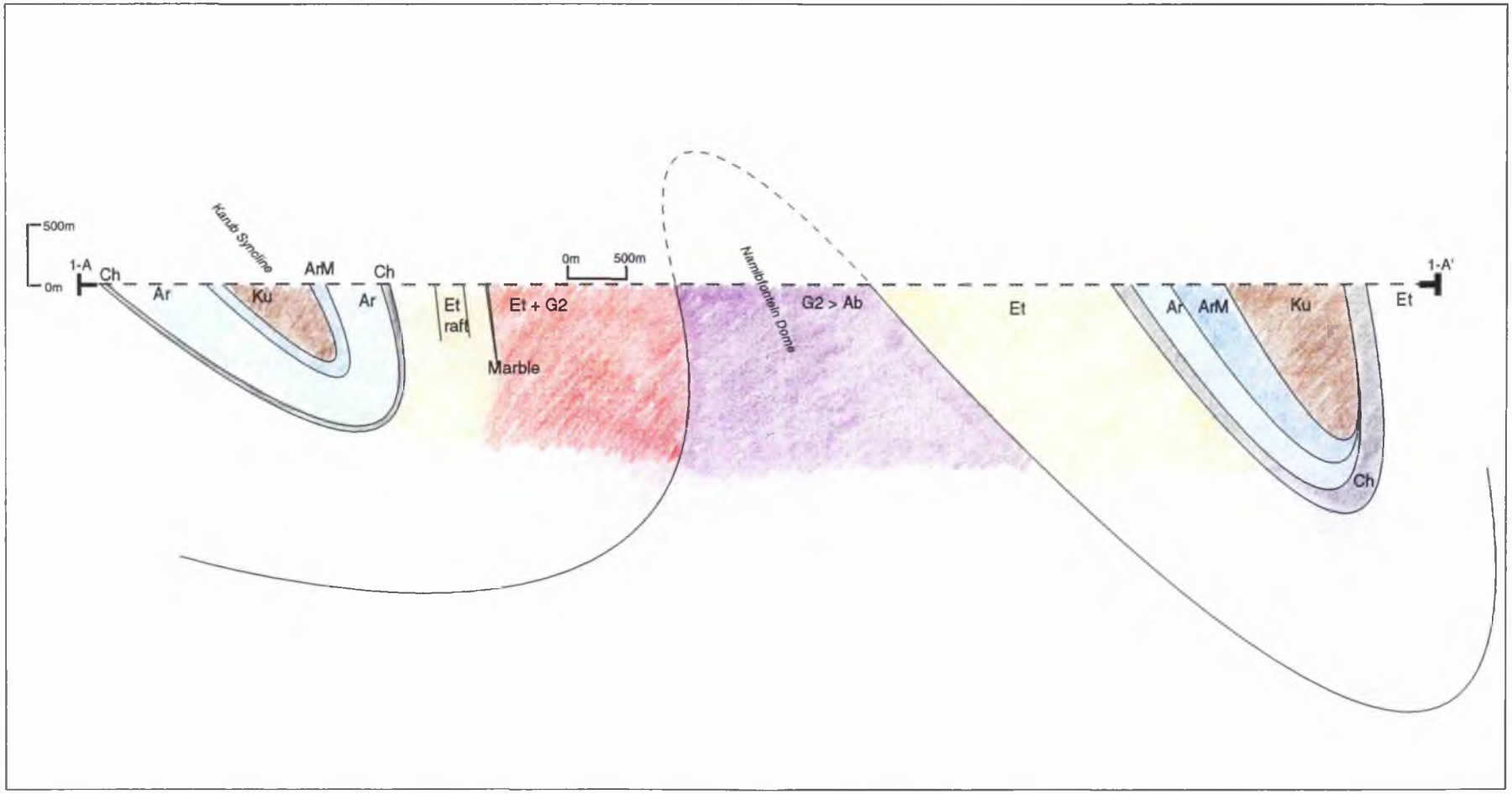

Cross-section Namibfontein area [Map 1] A-A' (stratigraphic symbols as main map)

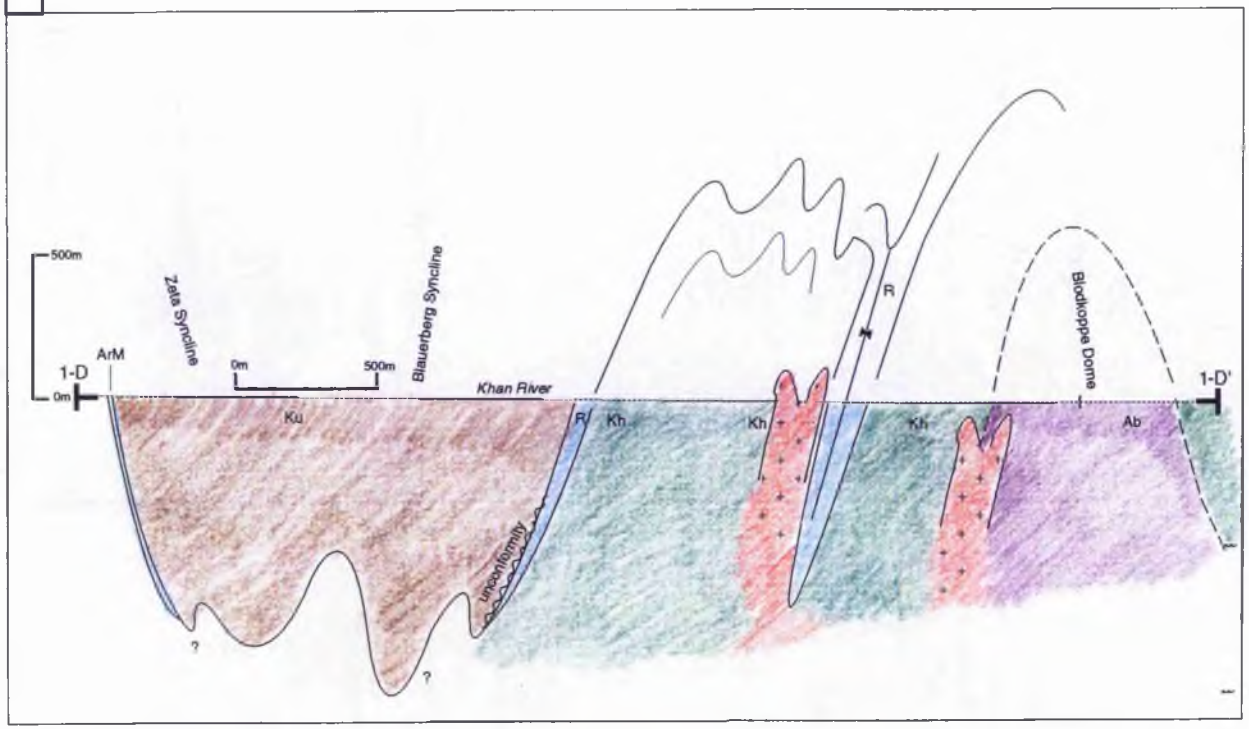

Cross-section Namibfontein area [Map 3] D-D' (stratigraphic symbols as main map)

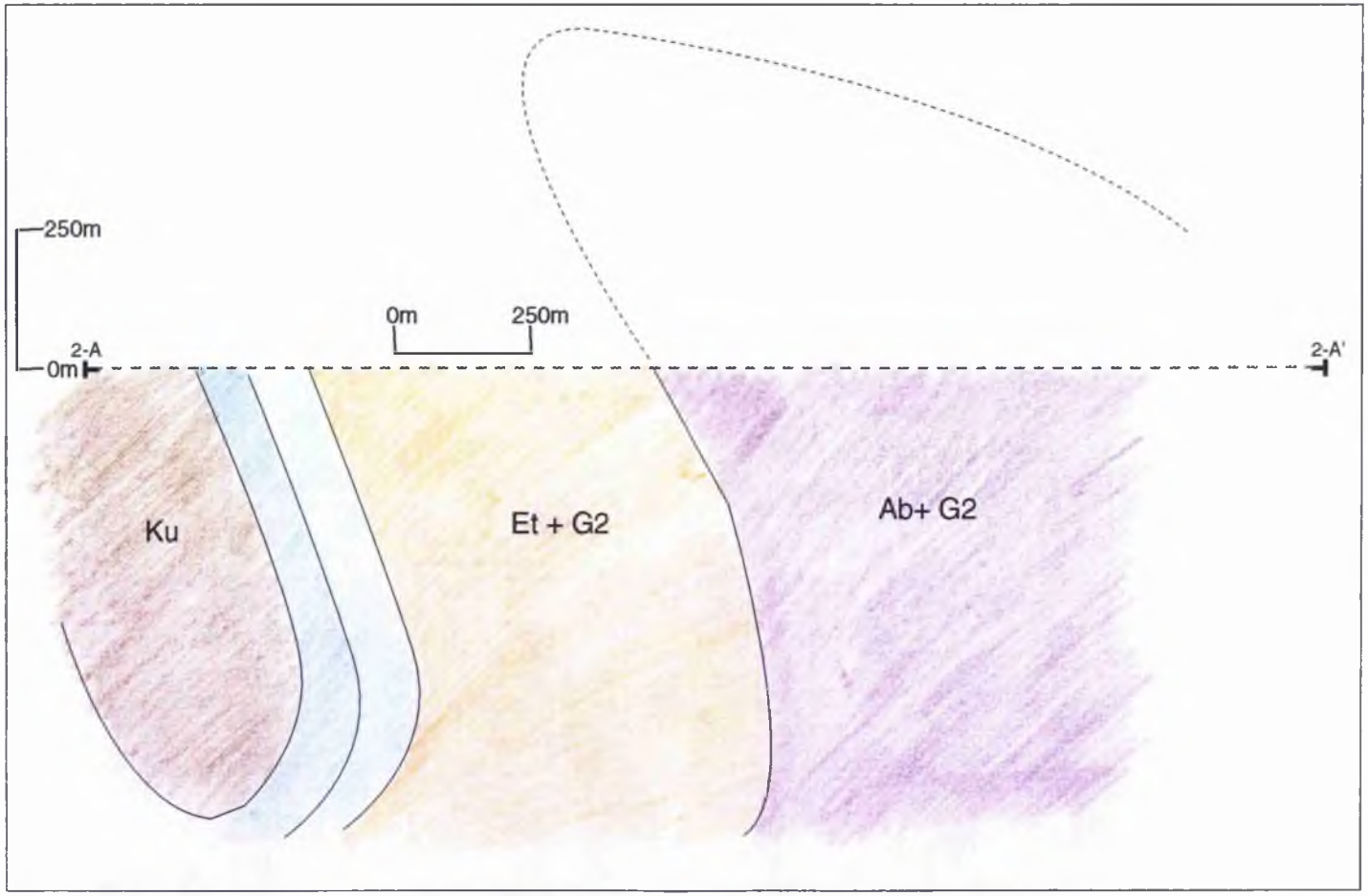

Cross-section Vergenoeg area [Map 2] A-A'(stratigraphic symbols as main map)

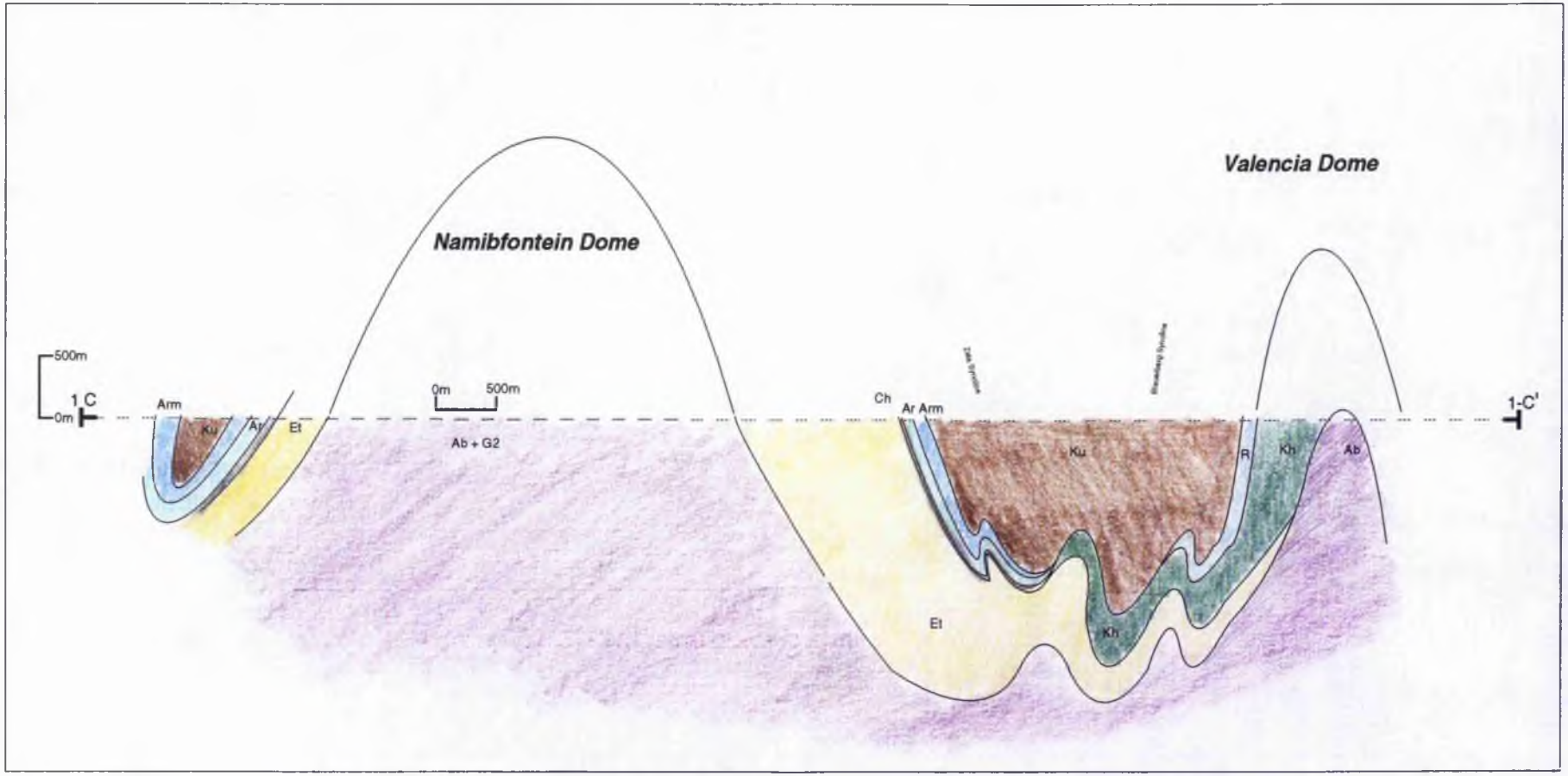

Cross-section Namibfontein area [Map 3] C-C' (stratigraphic symbols as main map)

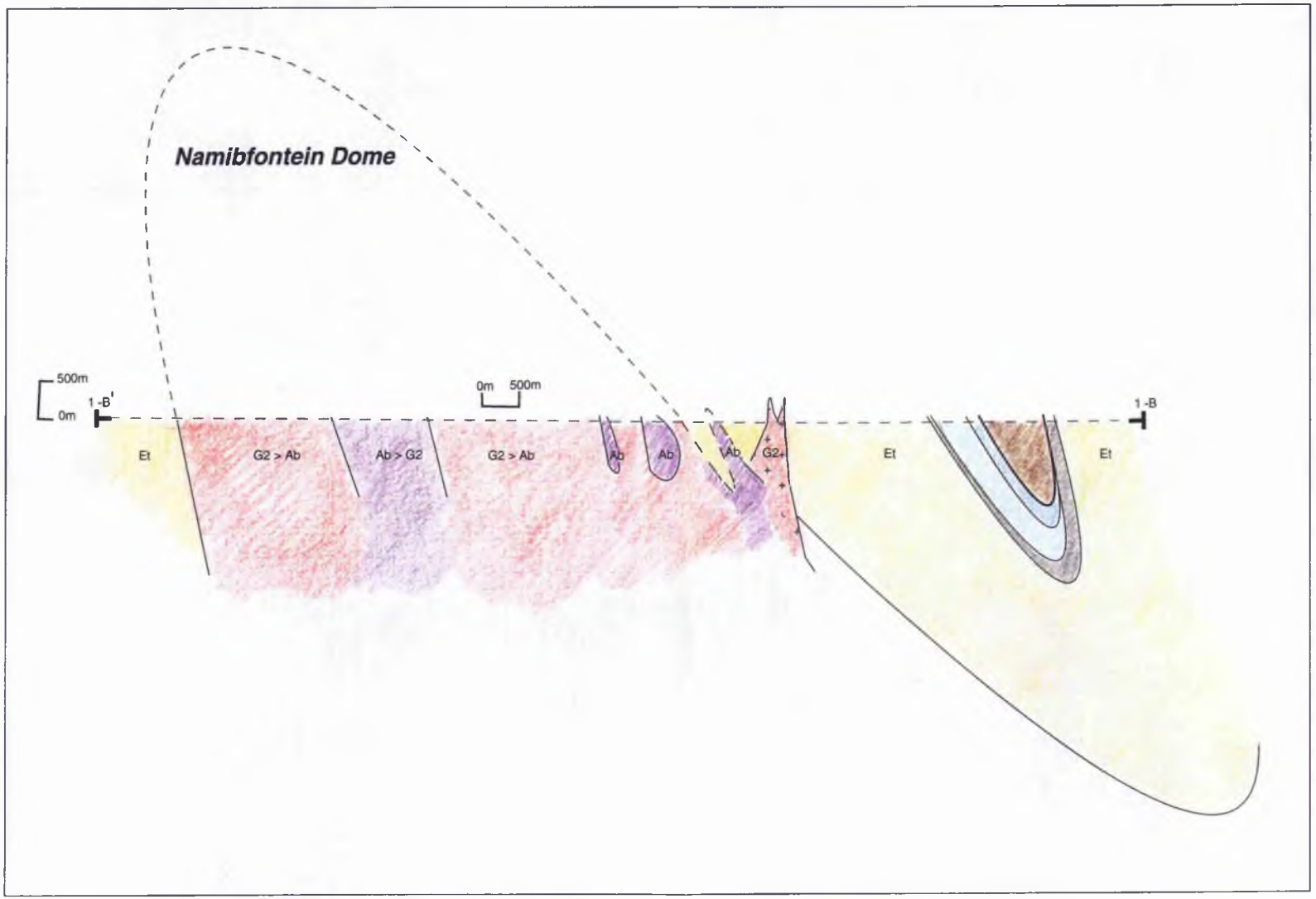

Cross-section Namibfontein area [Map 1] B-B' (stratigraphic symbols as main map)

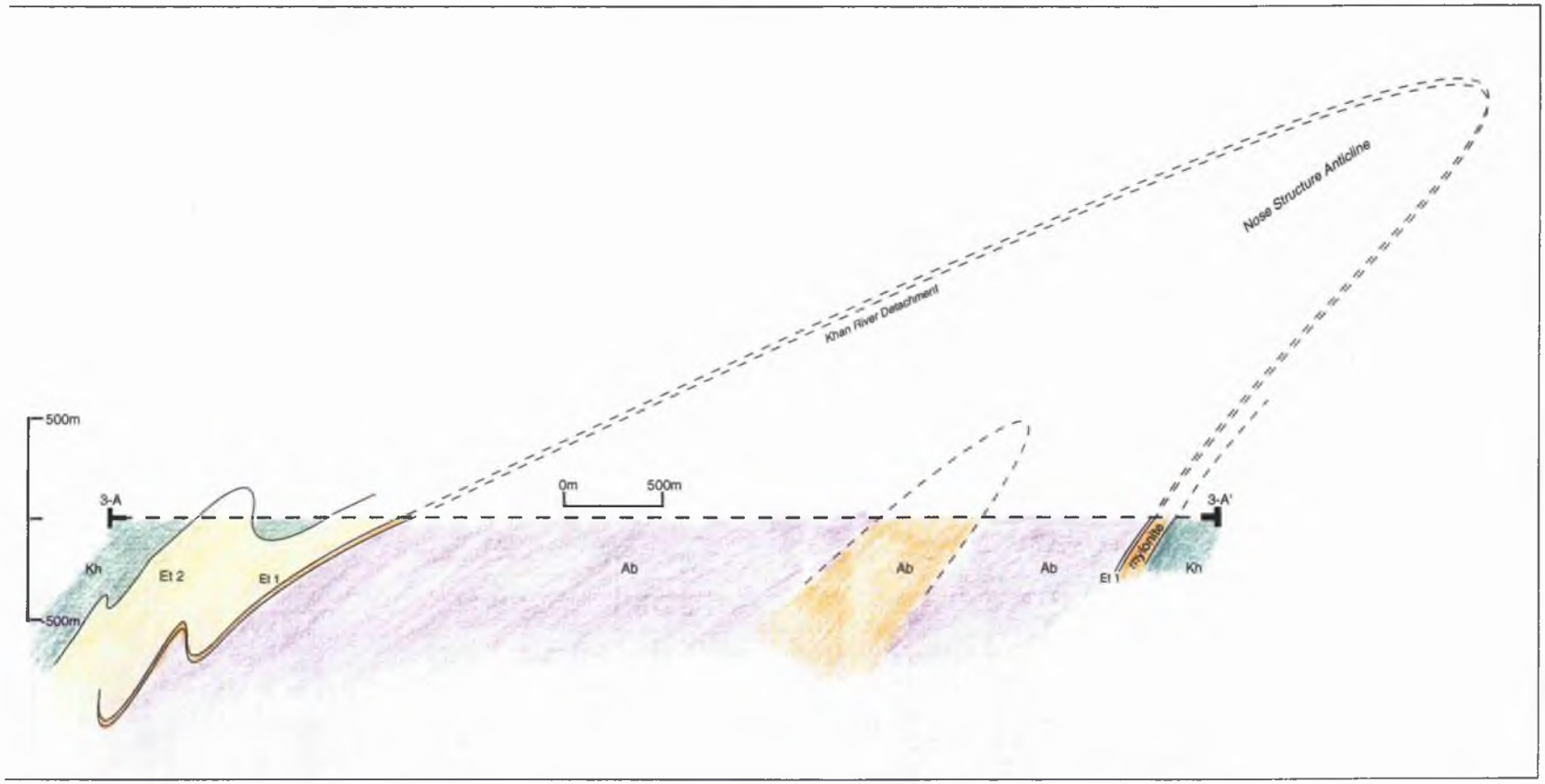

Cross-section Khan Mine area [Map 3] A-A' (stratigraphic symbols as main map)

Map 1 [Namibfontein Area]
Part 1

MAP 1 NAMIBFONTEIN AREA

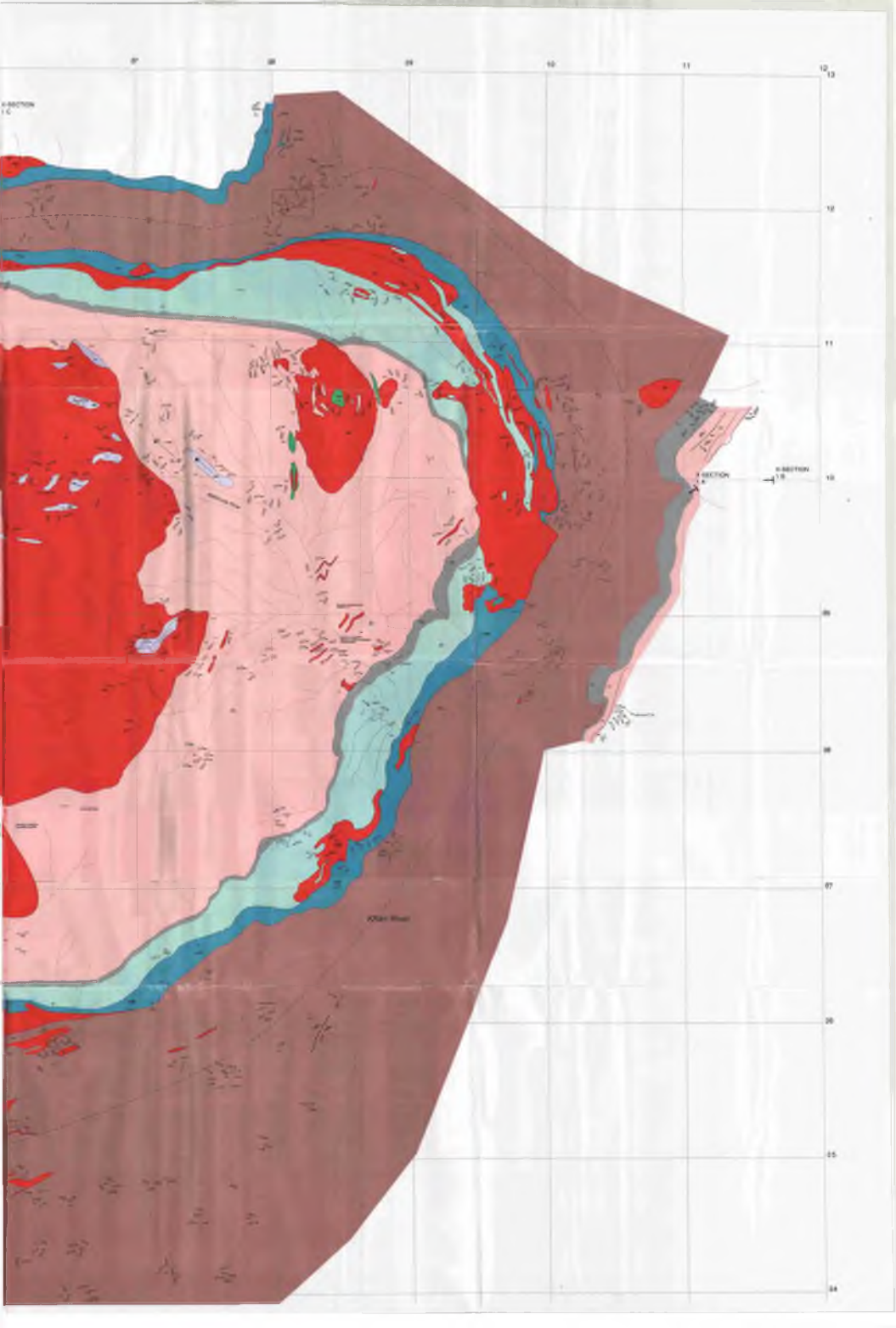

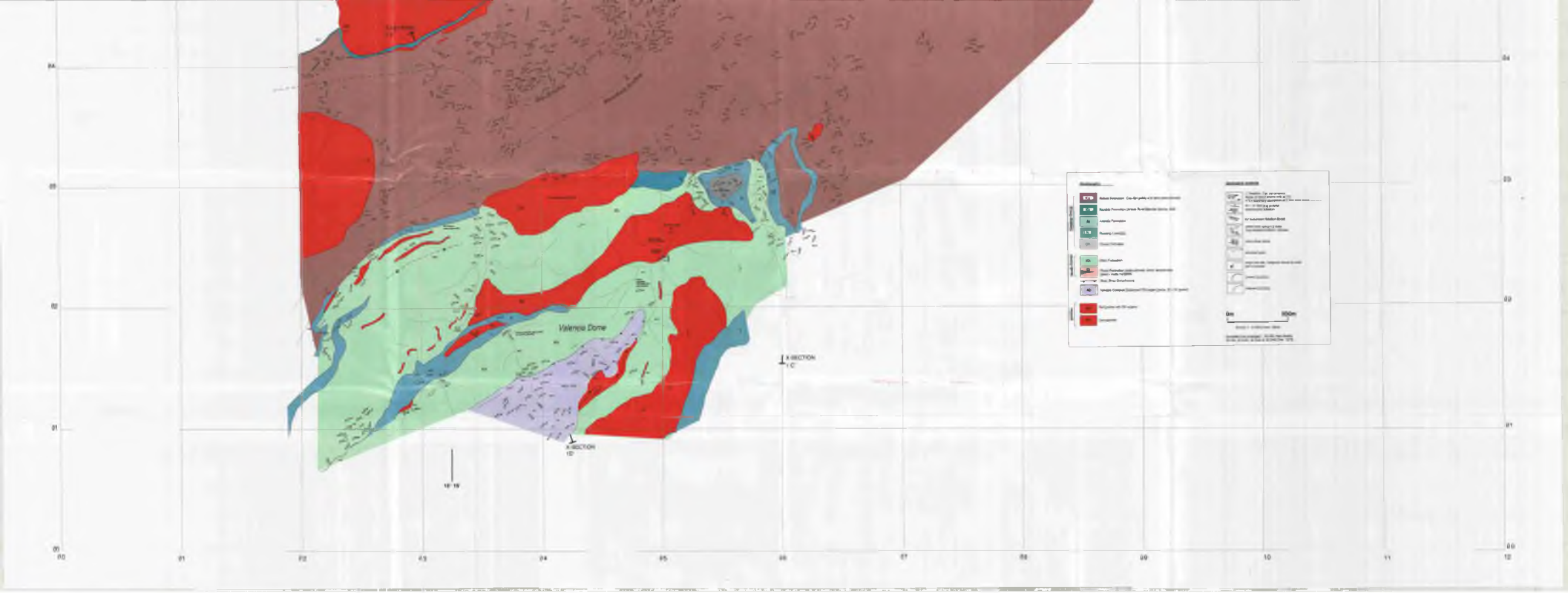
Valencia Dome
X-SECTION
1 C'
X-SECTION
1 D'
18° 19'

Map 1 [Namibfontein Area]
Part 2

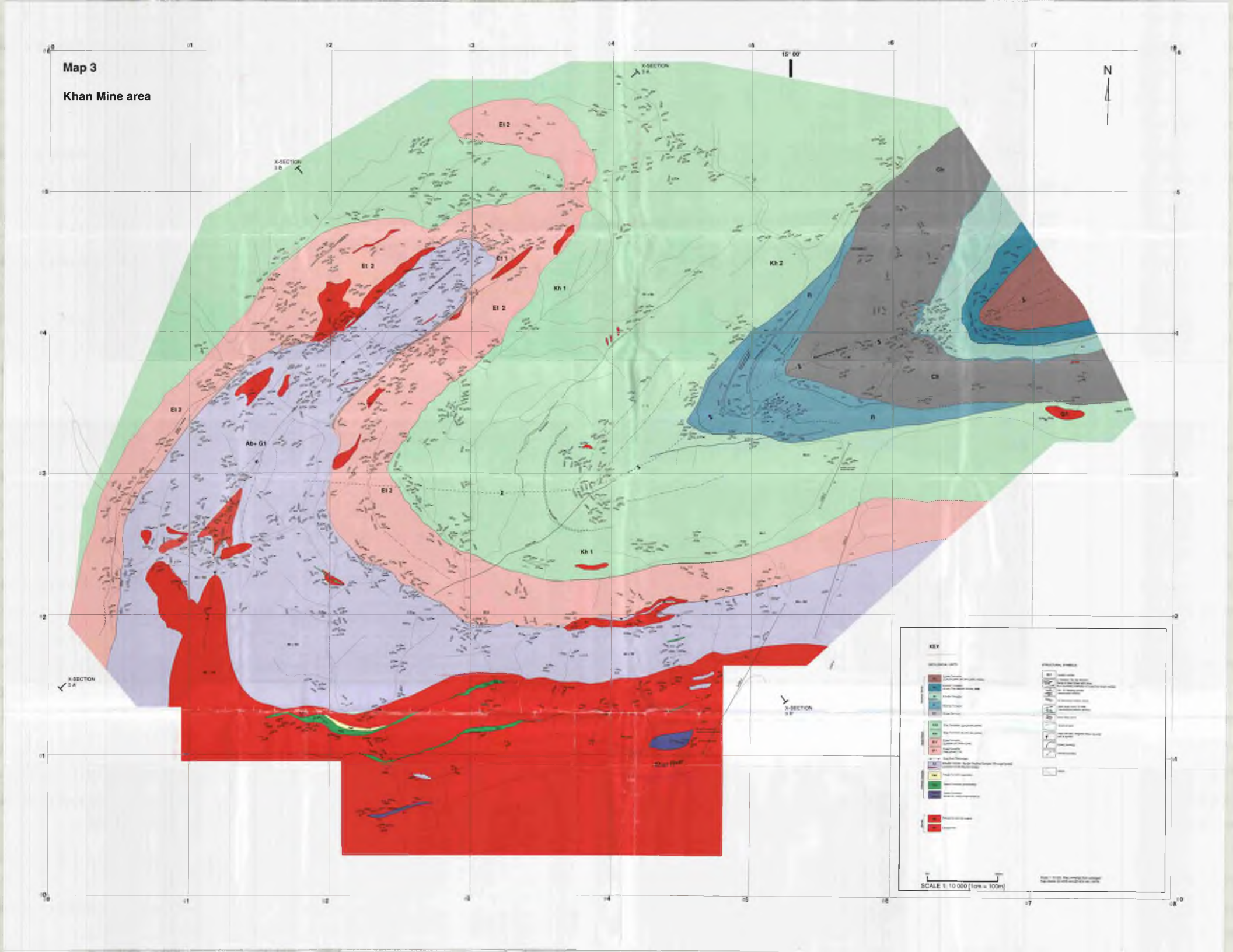
Map 3
Khan Mine area
15° 00'
N
X-SECTION 3 A
X-SECTION 3 B
X-SECTION 3 A'
X-SECTION 3 B'
El 2
El 1
Kh 1
Kh 2
Ch
Ab+ G1
KEY
SCALE 1: 10 000 [1cm = 100m]

Map 3 [Khan Mine Area]